



Universidade do Estado do Rio de Janeiro

Centro de Tecnologia e Ciências

Faculdade de Engenharia

Deborah Souza Castanheira

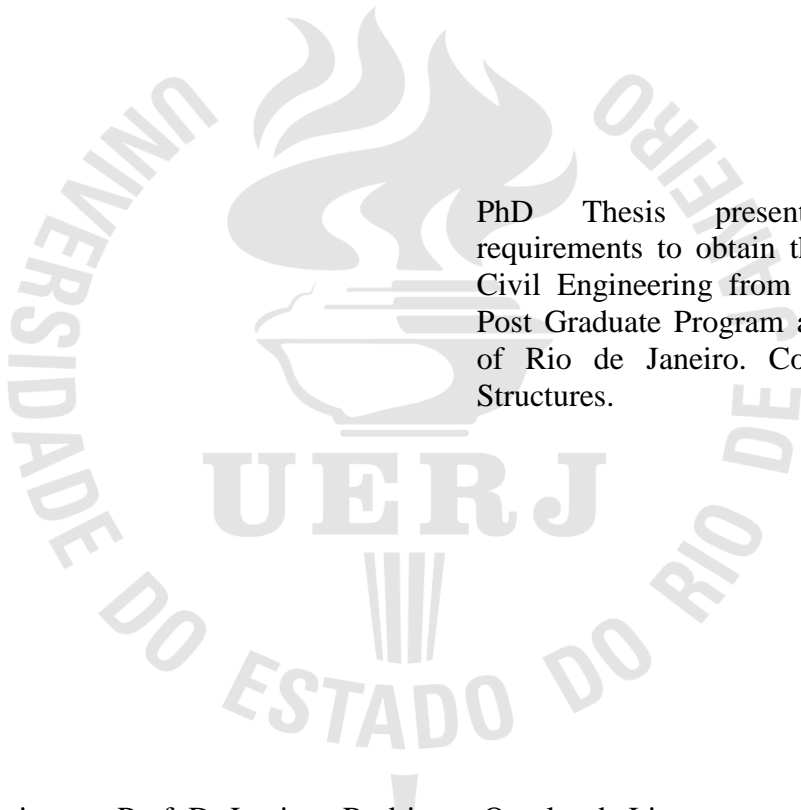
**Behaviour of concrete-filled double-skin stub columns with recycled
aggregate concrete subjected to concentric and eccentric load**

Rio de Janeiro

2021

Deborah Souza Castanheira

**Behaviour of concrete-filled double-skin stub columns with recycled aggregate concrete
subjected to concentric and eccentric load**



PhD Thesis presented as partial requirements to obtain the PhD Degree in Civil Engineering from Civil Engineering Post Graduate Program at State University of Rio de Janeiro. Concentration Area: Structures.

Supervisors: Prof. Dr Luciano Rodrigues Ornelas de Lima
Prof. Dr Pedro Colmar Gonçalves da Silva Vellasco
Prof. Dr Leroy Gardner

Rio de Janeiro

2021

CATALOGAÇÃO NA FONTE
UERJ / REDE SIRIUS / BIBLIOTECA CTC/B

C346 Castanheira, Deborah Souza.
Behavior of concrete-filled double-skin stub columns with recycled aggregate concrete subjected to concentric and eccentric load / Deborah Souza Castanheira. – 2021.
217f.

Orientadores: Luciano Rodrigues Ornelas de Lima, Pedro Colmar Gonçalves da Silva Vellasco, Leroy Gardner.
Tese (Doutorado) – Universidade do Estado do Rio de Janeiro, Faculdade de Engenharia.

1. Engenharia civil - Teses. 2. Colunas - Teses. 3. Construção mista - Teses. 4. Análise estrutural (Engenharia) - Teses. 5. Análise numérica - Teses. I. Lima, Luciano Rodrigues Ornelas de. II. Vellasco, Pedro Colmar Gonçalves da Silva. III. Gardner, Leroy. IV. Universidade do Estado do Rio de Janeiro, Faculdade de Engenharia. V. Título.

CDU 624.016

Bibliotecária: Júlia Vieira – CRB7/6022

Autorizo, apenas para fins acadêmicos e científicos, a reprodução total ou parcial desta tese, desde que citada a fonte.

Assinatura

Data

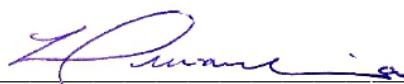
Deborah Souza Castanheira

**Behaviour of concrete-filled double-skin stub columns with recycled aggregate concrete
subjected to concentric and eccentric load**

Presented thesis as partial requirement for obtaining the title of Doctor in Civil Engineering, at the Post-Graduation program in Civil Engineering at the State University of Rio de Janeiro. Concentration area: Structures.

Aprovado em: 14 de outubro de 2021

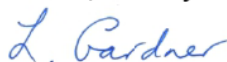
Banca Examinadora:




Prof. Luciano Rodrigues Ornelas de Lima (Supervisor), DSc
Structural Engineering Department, Faculty of Engineering – UERJ



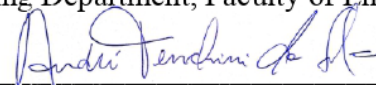
Prof. Pedro C. G. da S. Vellasco (Supervisor), PhD
Structural Engineering Department, Faculty of Engineering – UERJ



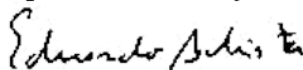
Prof. Leroy Gardner, (Supervisor), PhD
Civil and Environmental Engineering Department – Imperial College, London



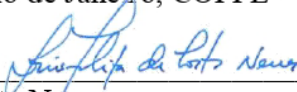
Profa Maria Elizabeth da Nóbrega Tavares
Structural Engineering Department, Faculty of Engineering – UERJ



Prof. André Tenchini da Silva
Structural Engineering Department, Faculty of Engineering – UERJ



Prof. Eduardo de Miranda Batista
Federal University of Rio de Janeiro, COPPE – UFRJ



Prof. Luis Filipe da Costa Neves
Civil Engineering Department, University of Coimbra, Portugal

Rio de Janeiro

2021

DEDICATION

This work is dedicated to my parents, Christina and Marco Antonio.

ACKNOWLEDGEMENTS

My parents Christina and Marco Antonio who always provided financial and emotional support, encouraging me to pursue my life dreams. Nothing would be possible without your love.

My supervisor Prof. Dr Luciano Rodrigues Ornelas de Lima for all the knowledge during all my academic life (undergraduate, master and doctorate), guidance, encouragement, strong support, friendship, patience and specially the time invested in meetings and WhatsApp messages. Thank you for helping me whenever I needed.

My second supervisor Prof. Dr Pedro Colmar Gonçalves da Silva Vellasco for all the knowledge transfer and time spent in my thesis' writing revisions, knowing how to push me to my limit.

My third supervisor Prof. Dr Leroy Gardner to whom I am very grateful for the opportunity to be part of his research group during my stay at Imperial College London. My sincere gratitude for all the support and inspiration.

To Prof. Dr Maria Elizabeth da Nóbrega Tavares for teaching me so much about recyclable concrete and experiments. The quick chats over afternoon coffee breaks helped and motivated me to conclude my doctoral degree.

To Prof. Dr Katherine Cashell who has been supportive on the development of my conference and journal papers.

My boyfriend Marcus. I don't have words to express how grateful I am for all your support and patience (specially for encouraging my GTA work).

My friends Paulo Barreto and Bruno Costa who always encourage me, sometimes while working in the laboratory and sometimes just having a good laugh.

My friends Raphael Carneiro, Stephane Nascimento and Arthur Menezes who have always been there to hear me complain about the doctorate or to help me with any other questions.

The financial support from the Rio de Janeiro government through FAPERJ during the doctoral degree in Brazil and the Brazilian government via CAPES during the year spent at Imperial College London.

RESUMO

CASTANHEIRA, Deborah Souza. *Avaliação de pilares tubulares de aço preenchidos com concreto*. 2021. 217f. Tese (Doutorado em Engenharia Civil) – Faculdade de Engenharia, Universidade do Estado do Rio de Janeiro, Rio de Janeiro, 2021.

Colunas tubulares tipo *double-skin* preenchidas com concreto (CFDST) são um tipo relativamente novo de elemento estrutural e seu uso vem se tornando cada vez mais popular. Uma de suas vantagens é tornar a construção mais leve e menos cara devido à menor quantidade de material e utilização de formas. Hoje em dia, o emprego de aço inoxidável e concreto reciclável de agregado graúdo (RAC) em elementos mistos é extremamente tópico devido à obtenção do agregado reciclável ser mais barata e às questões de sustentabilidade, uma vez que ambos os materiais são totalmente recicláveis. Esta tese apresenta um estudo experimental e numérico sobre o comportamento de colunas curtas tipo *double-skin* (CFDST). Os experimentos foram submetidos a carga axial concêntrica e os numéricos foram submetidos a carga axial concêntrica, excêntrica e flexão pura. Quatro ensaios de compressão axial foram realizados em colunas curtas tipo *double-skin* preenchidas com concreto reciclável e posteriormente comparadas com colunas CFDST preenchidas com concreto convencional, encontrados na literatura. As colunas tinham seções transversais tubulares circulares e cada uma compreendia um tubo externo de aço inoxidável austenítico e um tubo interno de aço carbono com dimensões variáveis. A substituição de 50% do agregado graúdo natural (NCA) por agregado graúdo reciclado (RCA) foi adotada nos testes de RAC. Durante os ensaios foi observado que o comportamento estrutural das colunas com concreto convencional e concreto reciclado era semelhante e os modos de ruptura se mostraram idênticos. Um modelo de elementos finitos foi desenvolvido no ABAQUS e validado em relação aos experimentos e dados da literatura para investigar melhor o comportamento de colunas CFDST. O modelo de elementos finitos foi empregado em um estudo paramétrico para avaliar a influência de diferentes geometrias, resistência à compressão do concreto (f_c), concreto reciclável de agregado graúdo e aplicação de carga excêntrica no comportamento de colunas CFDST. O diagrama de interação N-M é desenvolvido para comparar com os procedimentos de projeto disponíveis para colunas curtas CFDST e vigas-colunas. Finalmente, um estudo de confiabilidade foi conduzido para avaliar as equações propostas de diagrama de interação N-M. No geral, os resultados demonstraram que as colunas curtas CFDST com concreto reciclável de agregado graúdo atingem uma capacidade de carga final muito semelhante a membros com concreto convencional, no entanto, as expressões atuais de projeto existentes na literatura fornecem alguns resultados inseguros. O fator de confinamento desenvolvido para o concreto, a equação de capacidade de carga axial, a equação de flexão pura e o diagrama de interação N-M propostos demonstram estar em boa concordância com os experimentos e resultados de FE avaliados.

Palavras-chave: Colunas mistas; Colunas tipo *double-skin*; Aço inoxidável; Concreto reciclável de agregado graúdo; Diagrama de interação de pilares N-M; Eurocode 4.

ABSTRACT

CASTANHEIRA, Deborah Souza. *Behaviour of concrete-filled double-skin stub columns with recycled aggregate concrete subjected to concentric and eccentric load*. 2021. 217f. Tese (Doutorado em Engenharia Civil) – Faculdade de Engenharia, Universidade do Estado do Rio de Janeiro, Rio de Janeiro, 2021.

Concrete-filled double-skin tubular (CFDST) columns are a relatively new type of structural element, and their use is becoming very popular. One of their advantages is light and less expensive construction due to less material and formwork. Nowadays, the employment of stainless steel and recycled aggregate concrete (RAC) in composite elements is hugely topical due to less expensive manufacturing and sustainability issues since both materials are fully recyclable. This thesis presents an experimental and numerical study into the behaviour of CFDST stub columns. In contrast, the experiments were subjected to concentric axial load, and the numerical were subjected to concentric, eccentric axial load and pure bending. Four axial compression tests were carried out filled with recycled aggregate concrete and afterwards compared with CFDST columns filled with conventional concrete found in the literature. The columns had circular tubular cross-sections, and each comprised an austenitic stainless steel outer tube and a carbon steel inner tube with variable dimensions. A replacement ratio of 50% of natural coarse aggregate (NCA) by recycled coarse aggregate (RCA) was adopted in the RAC tests. During the tests, similar structural behaviour was observed in the columns with conventional or recycled aggregate concrete, while the failure modes proved to be identical. To further investigate the behaviour, a finite element model was developed in ABAQUS and was validated against the experiments and the literature's data. The finite element model was employed to conduct a parametric study to assess the influence of different geometric, concrete compressive strength (f_c), the recycled coarse aggregate concrete and eccentricity load application on the behaviour of CFDST stub columns. An N-M interaction diagram is generated to compare with available design procedures for CFDST stub columns and beam-columns. Finally, a reliability study was conducted to assess the proposed N-M interaction diagram. Overall, the results demonstrated that the CFDST stub columns with recycled aggregate concrete achieve a very similar ultimate load capacity to similar members with conventional concrete. However, current design expressions provide some unsafe results. The developed concrete confinement factor, axial load capacity, pure bending moment and N-M interaction diagram demonstrate to be in good agreement with the experiments and FE results evaluated.

Keywords: Composite columns; Double-skin columns; Stainless steel; Recycled coarse aggregate concrete; N-M interaction diagram; Eurocode 4.

FIGURES

Figure 1 - Cross-section of a CFDST column.	26
Figure 2 - CFDST columns used in an offshore platform [5].	27
Figure 3 - CFDST cross-section in a submarine pipeline structure [11].	28
Figure 4 - CFDST pole and transmission tower [12].	28
Figure 5 - CFDST columns in a high-rise building, Office Building Palestra, London [13]. ...	28
Figure 6 - Residual stress distribution [19].	33
Figure 7 - Stress <i>versus</i> strain curve of carbon and stainless steel [20].	34
Figure 8 - Stress <i>versus</i> strain curves for stainless and carbon steels, adapted from [21].	34
Figure 9 - Radial pressure in the composite column due to the concrete confinement effect [17].	35
Figure 10 - Triaxial stresses in the infilled concrete of a CFDST column [25].	36
Figure 11 - Recycled coarse aggregates (RCA) from old structural concrete with various deleterious materials and sizes [26].	37
Figure 12 - Failure mode of the RAC CFST columns [30].	39
Figure 13 - Behaviour of confined RAC [36].	39
Figure 14 - Grading curves of coarse aggregates [40].	40
Figure 15 - Experimental and numerical deformations of columns with CHS 89 x 3, 1200 of length and RCA replacement ratio of 0%, 35% and 70% [40].	41
Figure 16 - Cross-section of the CFDST columns [44].	42
Figure 17 - Failure modes [44].	42
Figure 18 - CFDST columns cross-section [45].	43
Figure 19 - Failure modes of stub columns, beam-columns and beams [45].	44
Figure 20 - CFDST columns cross-sections [46].	45
Figure 21 - CFDST columns configurations [46].	45
Figure 22 - Typical failure modes for the straight CFDST columns [46].	46

Figure 23 - CFDST column cross-section [9].	47
Figure 24 - CFDST columns failure modes [9].....	47
Figure 25 - Failure modes of the CFDST columns [47].....	48
Figure 26 - CFDST stub columns failure modes [48].	50
Figure 27 - Axial load <i>versus</i> hollow ratio parameter (χ) influence using the same outer tube diameter [49].	50
Figure 28 - Stress distributions from Uenaka and Kitoh [55].	57
Figure 29 - Stress distributions with neutral axis located above the inner tube, Fouché <i>et al.</i> [56].	60
Figure 30 - Stress distributions with the neutral axis located across the inner tube, Fouché <i>et al.</i> [56].	62
Figure 31 - Eurocode 4 (EC4) [18] CFST columns simplified interaction curve and stress distributions.....	64
Figure 32 - CFDST cross-sections before casting.....	67
Figure 33 - View of the crushed concrete to make the RAC.....	71
Figure 34 - Steel coupons geometry (mm).	72
Figure 35 - Stress <i>versus</i> strain of the four tensile specimens for the outer stainless steel tube.	72
Figure 36 - Geometric imperfection measurement.....	73
Figure 37 - Measured geometric imperfections along the stainless steel tubular column length.	73
Figure 38 - Test layout and instrumentation.....	74
Figure 39 - Deformed specimens after testing showing outward-only local buckling of the outer stainless steel tube.	75
Figure 40 - Specimen RAC1 after testing showing an inward-only local buckling of the carbon steel inner tube.....	76
Figure 41 - Axial load <i>versus</i> axial displacement curves for the CFDST columns.	77
Figure 42 - CFDST columns axial load <i>versus</i> mean axial strain curves.....	78

Figure 43 - Typical failure modes of CFST columns with RAC [39].	83
Figure 44 - Axial load <i>versus</i> axial displacement curves [39].	83
Figure 45 - Longitudinal cut of the CFST stub columns with RAC [39].	84
Figure 46 - Stress <i>versus</i> strain curves from tensile tests [48].	85
Figure 47 - Failure modes [48].	86
Figure 48 - Axial load <i>versus</i> mean axial strain for the CFDST columns [48].	87
Figure 49 - Failure mode [46].	88
Figure 50 - Axial load <i>versus</i> axial displacement [46].	89
Figure 51 - Failure mode [5].	90
Figure 52 - Axial load <i>versus</i> mid-span deflection [5].	91
Figure 53 - Failure mode [77].	92
Figure 54 - Axial load <i>versus</i> axial displacement [77].	93
Figure 55 - Axial load <i>versus</i> mid-span deflection [77].	93
Figure 56 - Test set-up [87].	95
Figure 57 - Failure mode [88].	96
Figure 58 - Axial load <i>versus</i> mid-span deflection [88].	97
Figure 59 - Typical failure mode of a CFDST beam [77].	98
Figure 60 - Failure mode [77].	98
Figure 61 - Moment <i>versus</i> mid-span deflection of the CFDST beam under pure bending [77].	99
Figure 62 - Geometry of the FE model in ABAQUS [16].	101
Figure 63 - Boundary conditions.	102
Figure 64 - Stress <i>versus</i> strain relationship for confined concrete in compression [76].	104
Figure 65 - Axial load <i>versus</i> axial displacement for the NAC CFDST columns.	106
Figure 66 - Axial load <i>versus</i> axial displacement for the RAC CFDST columns.	106
Figure 67 - Axial load <i>versus</i> axial strain for the NAC CFDST columns.	107

Figure 68 - Axial load <i>versus</i> axial strain for the RAC CFDST columns.	107
Figure 69 - Comparison of failure mode.	108
Figure 70 - Comparison of failure mode [48].....	109
Figure 71 - Axial load <i>versus</i> mean axial strain for the CFDST columns from Wang <i>et al.</i> [48].	110
Figure 72 - Axial load <i>versus</i> axial displacement for the CFDST columns from Han <i>et al.</i> [46].	112
Figure 73 - Comparison of failure mode [46].....	112
Figure 74 - Axial load <i>versus</i> mid-height deflection for CFDST columns with L = 887 mm.	115
Figure 75 - Axial load <i>versus</i> mid-height deflection for CFDST columns with L = 1770 mm.	115
Figure 76 - Comparison of failure mode [76].....	116
Figure 77 - Axial load <i>versus</i> axial displacement for CFDST beam-columns.....	117
Figure 78 - Axial load <i>versus</i> mid-height deflection for CFDST beam-columns.	117
Figure 79 - Comparison of failure mode [77].....	118
Figure 80 - Axial load <i>versus</i> mid-height deflection for CFDST beam-columns.	121
Figure 81 - Comparison of failure mode [88].....	122
Figure 82 - Moment <i>versus</i> mid-span deflection for the CFDST beam under pure bending.	123
Figure 83 - Comparison of failure mode [77].....	123
Figure 84 - Tests axial compression load <i>versus</i> FE axial compression load.	126
Figure 85 - Cross-sections: CFDST beam-columns and beams CFDST stub columns.	135
Figure 86 - CFDST stub columns axial load <i>versus</i> axial displacement response varying the inner tube diameter.	137
Figure 87 - Influence of tube diameter on the normalized axial load <i>versus</i> normalized concrete cross-sectional area response.	138
Figure 88 - Influence of hollow ratio on the axial load <i>versus</i> axial displacement response for CFDST columns with an outer diameter of 168.3 mm.	140

Figure 89 - Lateral confining pressure along with the columns' height, measured through ABAQUS [16].	140
Figure 90 - Normalized axial capacity <i>versus</i> hollow ratio.	141
Figure 91 - Influence of tube slenderness over the axial load <i>versus</i> axial displacement response for CFDST columns with different inner tube geometries.	142
Figure 92 - Influence of the local slenderness of the inner steel tube over the normalized ultimate axial load, for in a constant value of $t_{so} = 2.8$ mm (all values in the legend are in mm).	143
Figure 93 - Axial load <i>versus</i> axial displacement response for CFDST columns with the outer and inner tube thicknesses of 5 mm and variable outer diameters.	144
Figure 94 - Longitudinal stress and deformed shape of CFDST beam-columns for the selected key points defined in Figure 93 b).	146
Figure 95 - Influence of the outer tube diameter over the axial load <i>versus</i> normalized concrete cross-sectional area response.	147
Figure 96 - Axial load <i>versus</i> axial displacement response for CFDST columns with outer and inner tube thicknesses of 5 mm and different hollow ratio.	149
Figure 97 - Axial load <i>versus</i> normalized hollow ratio.	150
Figure 98 - Axial load <i>versus</i> axial displacement response for CFDST columns with outer and inner tube thicknesses of 5 mm and various inner tube geometries.	152
Figure 99 - Influence of the outer steel tube's local slenderness over the normalized ultimate axial load (all values in mm).	153
Figure 100 - Normalized axial load <i>versus</i> outer tube slenderness for a 33 MPa f_c concrete compressive strength.	154
Figure 101 - Normalized axial load <i>versus</i> outer tube slenderness for an 80 MPa f_c concrete compressive strength.	155
Figure 102 - Axial load <i>versus</i> eccentricity ratio (e/D).	156
Figure 103 - Axial load <i>versus</i> concrete strength (f_c) (MPa).	159
Figure 104 - Longitudinal stress and deformation of the outer steel tube.	159
Figure 105 - Existing design formula accuracy assessment.	163

Figure 106 - Proposed N-M interaction curve and current design methods (Han <i>et al.</i> [12], Uenaka and Kitoh [55] and Fouché <i>et al.</i> [56]), for concrete strength (f_c) of 30 MPa.	170
Figure 107 - Proposed N-M interaction curve and current design methods (Han <i>et al.</i> [12], Uenaka and Kitoh [55] and Fouché <i>et al.</i> [56]), for concrete strength (f_c) of 80 MPa.	173
Figure 108 - CFDST sections stress distributions under combined axial load and bending moment.....	175
Figure 109 – Ratio of the confined compressive concrete strength and the compressive concrete strength f_{cc}/f_c <i>versus</i> important parameters.....	180
Figure 110 - Ratio of the confined compressive concrete strength and the compressive concrete strength f_{cc}/f_c <i>versus</i> the parameter.	181
Figure 111 - Pure compression load and pure bending moment experiments and FE results divided by the proposed equations with confinement <i>versus</i> new parameter for $f_c \leq 50$ MPa.	184
Figure 112 - $N_{Experiments}$ and N_{FE} divided by $N_{u,theoretical}$ <i>versus</i> $N_{Experiments}$ and N_{FE} for all the concentric load CFDST cross-sections studied with $f_c \leq 50$ MPa.....	185
Figure 113 - Pure compression load and pure bending moment FE results divided by the proposed equations with η <i>versus</i> new parameter for $50 < f_c \leq 90$ MPa.....	186
Figure 114 - Pure bending calculated through PNA and pure bending estimated formula accuracy assessment.	188
Figure 115 - Proposed N-M interaction curve and FE results for concrete strength (f_c) of 33 MPa.	192
Figure 116 - Proposed N-M interaction curve and experiments from the literature.	193
Figure 117 - Proposed N-M interaction curve and FE results for concrete strength (f_c) of 80 MPa.	196
Figure 118 - Predicted capacity and definition of H_u and $H_{u,pred}$	197
Figure 119 - Proposed conservative N-M interaction curve for all the FE and experiments evaluated.....	199

Figure 120 - Proposed conservative N-M interaction curve for all the FE and experiments
evaluated without considered the studied class 4 cross-sections. 199

TABLES

Table 1 - Stub column specimens' geometry and results.	67
Table 2 - Concrete mix proportion details.....	68
Table 3 - Concrete compressive strength (after 28 days).	68
Table 4 - Fine aggregate grain composition.	69
Table 5 - Natural coarse aggregate (NCA) grain composition.....	70
Table 6 - Recycled coarse aggregate (RCA) grain composition.	70
Table 7 - Characteristics of the coarse aggregates.	71
Table 8 - Mechanical properties of the grade 1.4307 stainless steel.	72
Table 9 - Mechanical properties of the carbon steel with diameter of 153 mm [39].	80
Table 10 - Mechanical properties of the carbon steel with diameter of 178 mm [39].	80
Table 11 - Concrete mix proportion details [39].	82
Table 12 - CFST column specimens' results [39].	84
Table 13 - Geometric details and experimental ultimate loads [48].	86
Table 14 - Geometric details and ultimate experimental loads [46].	88
Table 15 - Specimen label, dimensions, eccentricity and ultimate capacities [5].	90
Table 16 - Specimen label, dimensions, eccentricity and ultimate capacities [77].	92
Table 17 - Specimen label, dimensions, eccentricity and ultimate capacities [87].	94
Table 18 - Specimen label, dimensions, eccentricity and ultimate capacities [88].	96
Table 19 - Summarized references used in the FE's validation for CFDST columns.	105
Table 20 - Comparison of the ultimate loads from the experimental and the FE model.	107
Table 21 - Comparison of the ultimate loads from the experimental from Wang <i>et al.</i> [48] and the FE model.	109
Table 22 - Comparison of the ultimate experimental loads from Han <i>et al.</i> [46] and the FE model.	111
Table 23 - Summarized references used in the CFDST beam-columns FE's validation.	113

Table 24 - Specimen label, eccentricity and ultimate capacities from Tao <i>et al.</i> [5].	113
Table 25 - Specimen label, eccentricity and ultimate capacities from Li <i>et al.</i> [77].	117
Table 26 - Specimen label, concrete compressive strength, eccentricity and ultimate capacities from Ibañez <i>et al.</i> [87].	119
Table 27 - Specimen label, eccentricity and ultimate capacities from Zao <i>et al.</i> [88].	120
Table 28 - Specimen label and bending capacities from Li <i>et al.</i> [77].	123
Table 29 - Experimental and FE model ultimate load comparison.	124
Table 30 - Cross-sections geometrical properties - CFDST columns.	129
Table 31 - Cross-sections geometrical properties - CFDST beam-columns and beams.	131
Table 32 - Analysed slenderness ratio.	157
Table 33 - Longitudinal stress deformation.	157
Table 34 - Han <i>et al.</i> 's [12] method limitations.	166
Table 35 - Coefficient of variation (CoV) of pure compression and pure bending proposed equations for $f_c \leq 50$ MPa.	184
Table 36 - Coefficient of variation (CoV) of pure compression and pure bending proposed equations for $50 < f_c \leq 90$ MPa.	186
Table 37 - Coefficient of variation (CoV) for pure bending calculated by PNA and estimated.	187
Table 38 - $H_u/H_{u,pred}$ coefficient of variation (CoV) for FE results of eccentricity parametric analysis with $f_c = 33$ MPa.	197
Table 39 - $H_u/H_{u,pred}$ coefficient of variation (CoV) for experiments.	198
Table 40 - $H_u/H_{u,pred}$ coefficient of variation (CoV) for FE results of concentric parametric analysis with $f_c = 33$ MPa.	198
Table 41 - $H_u/H_{u,pred}$ coefficient of variation (CoV) for FE results of eccentricity parametric analysis with $f_c = 80$ MPa.	198
Table 42 - $H_u/H_{u,pred}$ coefficient of variation (CoV) for all the FE and experiments results.	198
Table 43 - $H_u/H_{u,pred}$ coefficient of variation (CoV) for all the FE and experiments evaluated considering the proposed conservative N-M interaction curve.	200

Table 44 - CFDST columns subjected to concentric axial compression evaluated by Eurocode 0 (EC0) [14].	202
Table 45 - CFDST columns subjected to concentric axial compression evaluated by AISI [15].	203
Table 46 - CFDST columns subjected to eccentric axial compression evaluated by Eurocode 0 (EC0) [14].	203
Table 47 - CFDST columns subjected to eccentric axial compression evaluated by AISI [15].	203

ABBREVIATION AND ACRONYMS

CFDST	Concrete-filled double-skin tubular
CFST	Concrete-filled steel tubular
RCA	Recycled coarse aggregate
RAC	Recycled aggregate concrete
NCA	Natural coarse aggregate
NAC	Natural aggregate concrete
FE	Finite element
EC0	Eurocode 0 - Basis of structural design
AISI	North American Cold-Formed Steel Specification
EC4	Eurocode 4 – European Committee for Standardization – Design of composite steel and concrete structures
EC3	Eurocode 3 – European Committee for Standardization – Design of Steel Structures – General rules and rules for buildings
ACI	Building Code Requirements for Structural Concrete – American Concrete Institute
AIJ	The standard for Structural Design of Reinforced Concrete Boxed-Shaped Wall Structures – Architectural Institute of Japan
AISC-LRFD	Specification for Structural Steel Buildings – American Institute of Steel Construction
BS5400	British Standard – Steel, concrete and composite bridges.
DBJ1351	Technical Specification for concrete-filled steel tubular structures – The Construction Department of Fujian Province, Fuzhou, China
CoV	Coefficient of variation
RACFSST	Recycled aggregate concrete-filled stainless steel tube
CHS	Circular hollow steel
UERJ	State University of Rio de Janeiro
LVDT	Linear variable differential transducer
CDP	Concrete damage plasticity
PNA	Plastic neutral axis

NOTATIONS

b	Test or FE to design model resistance mean ratio
d	Inner steel tube thickness
d_{\max}	Maximum coarse aggregate size
e	Load eccentricity
e_f	ABAQUS [16] eccentricity
f_{b0}/f_c	ABAQUS [16] compressive strength ratio under biaxial and uniaxial loading
f_c	Concrete compressive cylinder strength
f_{cc}	Proposed confined compressive concrete strength
f_{cu}	Concrete compressive cubic strength
f_{mean}	ABAQUS [16] shear stress limit
f_{osc}	Combined strength of the outer steel tube and concrete infilled
f_r	Concrete residual stress at the end of the softening branch
f_{sui}	Inner steel ultimate stress
f_{suo}	Outer steel ultimate stress
f_{syi}	Inner steel yield stress
f_{syo}	Outer steel yield stress
$f_{0.2\%}$	Proof strength of the stainless steel at 0.2%
f_l	Hassanein <i>et al.</i> 's [51] lateral confining pressure
h	Location of the plastic neutral axis
k	Concrete equivalent stress block
$k_{d,n}$	Eurocode 0's [14] reliability analysis design fractile factor
parameter	Proposed confinement effect parameter
r	Inner steel tube radius
$r_{(i - \text{tsi})}$	Hollow cross-section radius
t_{si}	Inner steel tube thickness
t_{so}	Outer steel tube thickness
$w_{\text{eff}/c}$	Effective water-to-cement ratio
$y_{c,c}$	Concrete resultant compressive force application point
$y_{c,\text{comp}}$	Proposed concrete resultant compressive force application point
$y_{i,c}$	Inner steel tube resultant compressive force application point
$y_{i,t}$	Inner steel tube resultant tensile force application point
$y_{o,c}$	Outer steel tube resultant compressive force application point

$Y_{o,t}$	Outer steel tube resultant tensile force application point
Y_{syi_comp}	Proposed inner steel tube resultant compressive force application point
Y_{syo_comp}	Proposed outer steel tube resultant compressive force application point
Y_{syi_ten}	Proposed inner steel tube resultant tensile force application point
Y_{syo_ten}	Proposed outer steel tube resultant tensile force application point
A	Concrete peak stress at the strain ϵ_{c0}
A_c	Cross-section area of the infilled concrete
A_{ce}	Equivalent cross-sectional area of the infilled concrete as the full area enclosed by the outer tube
A_{osc}	Sum of the cross-sectional areas of the outer steel tube and the concrete infilled
A_{si}	Cross-section area of the inner steel tube
A_{so}	Cross-section area of the outer steel tube
B	Concrete peak stress at the strain ϵ_{cc}
C_1	Outer steel tube confinement coefficient
C_2	Concrete infilled confinement coefficient
D	Outer steel tube diameter
E_c	Natural aggregate concrete Young's modulus
E_{c_RAC}	Recycled aggregate concrete Young's modulus
E_{si}	Inner steel Young's modulus
E_{so}	Outer steel Young's modulus
$(EI)_{eff}$	Effective flexural stiffness
F_{c_comp}	Theoretical concrete compressive resistance
F_{syi_comp}	Theoretical inner steel tube compressive resistance
F_{syi_ten}	Theoretical inner steel tube tensile resistance
F_{syo_comp}	Theoretical outer steel tube compressive resistance
F_{syo_ten}	Theoretical outer steel tube tensile resistance
G_f	ABAQUS [16] energy fraction
I_c	Concrete infilled second moment of area
I_{si}	Inner steel tube second moment of area
I_{so}	Outer steel tube second moment of area
K_c	ABAQUS [16] stress invariant on the tensile meridian to compressive meridian
K_e	Correction factor
L	Length of the column

$M_{u,FE}$	Bending capacity of the FE models
$M_{u,Fouché}$	Fouché <i>et al.</i> 's [56] theoretical bending resistance
$M_{u,Han}$	Han <i>et al.</i> 's [12] theoretical bending resistance
$M_{u,pred}$	Predicted bending moment capacity
$M_{u,test}$	Bending capacity of the experimental tests
$M_{u,Uenaka}$	Uenaka and Kitoh's [55] theoretical bending resistance
$N_{c,c}$	Resultant compressive force on the concrete
N_{cr}	Elastic axial load capacity critical value
$N_{i,t}$	Resultant tensile force on the inner tube
$N_{i,u}$	Han <i>et al.</i> 's [46] theoretical load capacity of the inner steel tube
$N_{o,c}$	Resultant compressive force on the outer tube
$N_{osc,u}$	Han <i>et al.</i> 's [46] theoretical load capacity of the outer steel tube and concrete combined
$N_{o,t}$	Resultant tensile force on the outer tube
$N_{pl,Rd}$	Eurocode's [18] plastic axial load
$N_{u,CFDST}$	Uenaka <i>et al.</i> 's [54] theoretical load capacity
$N_{u,EC4}$	Eurocode's [18] theoretical ultimate load capacity
$N_{u,FE}$	Axial load capacity of the FE models
$N_{u,Fouché}$	Fouché <i>et al.</i> 's [56] theoretical ultimate load resistance
$N_{u,Han}$	Han <i>et al.</i> 's [46] theoretical load capacity
$N_{u,Hassanein}$	Hassanein <i>et al.</i> 's [51] theoretical load capacity
$N_{u,pred}$	Predicted axial load capacity
$N_{u,test}$	Axial load capacity of the experimental tests presented in the thesis
$N_{u,theoretical}$	Theoretical load capacity
$N_{u,Uenaka}$	Uenaka and Kitoh's [55] theoretical ultimate load resistance
P_m	AISI's [15] reliability analysis test or FE to the theoretical resistance ratio
R	Outer steel tube radius
R_c	Concrete radius
V_P	AISI's [15] reliability analysis coefficient of variation
V_δ	Test or FE relative to the theoretical resistance CoV
W_{osc}	Flexural modulus of the A_{osc}
W_{si}	Flexural modulus of the inner steel tube
α_{cc}	Reduction concrete confinement factor

α_i	Angle between horizontal centroid axis and inner steel tube radius
α_o	Angle between horizontal centroid axis and outer steel tube radius
β_i	Angle between horizontal centroid axis and inner steel tube radius
β_o	Angle between horizontal centroid axis and outer steel tube radius
β_0	AISI's [15] reliability analysis target reliability index
γ_c	Hassanein <i>et al.</i> 's [51] concrete strength reduction factor
γ_{m1}	Probability partial factor of W_{osc}
γ_{m2}	Probability partial factor of the inner steel tube
γ_{M0}	Eurocode 0's [14] partial safety factor
γ_{si}	Hassanein <i>et al.</i> 's [51] inner steel tube[46] strain hardening
γ_{so}	Hassanein <i>et al.</i> 's [51] outer steel tube[46] strain hardening
δ	Lateral deflection
$\delta_{u,test}$	Axial displacement of the experimental tests presented in the thesis
ε_f	Ultimate strain
ε_{nom}	Engineering strain
ε_{ln}^{pl}	Logarithmic plastic strain
η	Confined compressive concrete strength reduction factor
η_a	Steel reduction factor
η_c	Concrete enhancement factor
η_{CFDST}	Uenaka <i>et al.</i> 's [54] confinement effect coefficient
θ_c	Concrete compressive angle
θ_{c_ten}	Concrete tensile angle
θ_i	Inner steel tube compressive angle
θ_{i_ten}	Inner steel tube tensile angle
$\theta_{(i-tsi)}$	Hollow cross-section compressive angle
$\theta_{(i-tsi)_ten}$	Hollow cross-section tensile angle
θ_o	Outer steel tube compressive angle
θ_{o_ten}	Outer steel tube tensile angle
$\bar{\lambda}$	Normalized slenderness
N	Poisson coefficient
ν_o	Steel tube Poisson's confinement with the concrete infill
ν_s	Steel tube Poisson's confinement without the concrete infill
ξ	Nominal confinement factor

σ_{nom}	Engineering stress
σ_{true}	True stress
χ	Hollow ratio
ψ	ABAQUS [16] dilatation angle

CONTENTS

INTRODUCTION	26
GENERALITIES	26
1 LITERATURE REVIEW	31
1.1 Generalities	31
1.1.1 Columns and beam-columns: composite members.....	31
1.1.2 Geometric imperfections and residual stresses	32
1.1.3 Stainless steel	33
1.1.4 Confined concrete	34
1.1.5 Recycled aggregate concrete.....	36
1.1.6 CFST columns with RAC under compressive load	37
1.1.7 CFDST columns with NAC under compressive and eccentric load	41
1.1.8 CFDST columns with carbon or high strength steel, stainless steel and NAC under compressive and eccentric load.....	44
2 DESIGN METHODS	52
2.1 Generalities	52
2.2 CFDST under concentric load	52
2.2.1 Uenaka <i>et al.</i> [54].....	52
2.2.2 Han <i>et al.</i> [46]	53
2.2.3 Hassanein <i>et al.</i> [51].....	54
2.2.4 Eurocode 4 (EC4) [18].....	55
2.3 CFDST under eccentric load	57
2.3.1 Uenaka and Kitoh [55].....	57
2.3.2 Han <i>et al.</i> [12]	58
2.3.3 Fouché <i>et al.</i> [56]	60
2.3.4 Eurocode 4 (EC4) [18].....	63
3 EXPERIMENTAL PROGRAMME	66
3.1 Generalities	66
3.2 Concrete	67
3.3 Tubular sections	71
3.4 Imperfections	73

3.5	Test setup and procedure	74
3.6	Results	75
3.7	Experiments to further FE model validation	79
3.7.1	Concentric load - Azevedo [39].....	79
3.7.2	Concentric load - Wang <i>et al.</i> [48].....	85
3.7.3	Concentric load - Han <i>et al.</i> [46].....	87
3.7.4	Eccentric load - Tao <i>et al.</i> [5].....	89
3.7.5	Eccentric load - Li <i>et al.</i> [77].....	91
3.7.6	Eccentric load - Ibañez <i>et al.</i> [87].....	94
3.7.7	Eccentric load - Zhao <i>et al.</i> [88].....	95
3.7.8	Pure bending - Li <i>et al.</i> [77].....	98
4	NUMERICAL MODELLING	100
4.1	Generalities	100
4.2	Finite element model description	100
4.2.1	Geometry, mesh sensitivity and elements.....	100
4.2.2	Boundary conditions, interactions and load application.....	101
4.2.3	Contact and geometric imperfections.....	102
4.3	Material modelling	103
4.3.1	Concrete.....	103
4.3.2	Steel tubes.....	104
4.4	Validation of the numerical model – Concentric load	105
4.4.1	Experimental results.....	106
4.4.2	Tests from Wang <i>et al.</i> [48].....	108
4.4.3	Han <i>et al.</i> [46].....	111
4.5	Validation of the numerical model – Eccentric loads	113
4.5.1	Tests from Tao <i>et al.</i> [5].....	113
4.5.2	Tests from Li <i>et al.</i> [77].....	116
4.5.3	Tests from Ibañez <i>et al.</i> [87].....	118
4.5.4	Zhao <i>et al.</i> [88].....	119
4.6	Validation of the numerical model – Pure bending	122
4.7	Summary of FE ultimate load predictions	124
5	PARAMETRIC STUDY	128
5.1	Generalities	128

5.2	Simulations of members under concentric loads	128
5.3	Simulations of members under eccentric axial compression and pure bending.	130
5.4	Parametric study results and analysis	135
5.4.1	Members under concentric axial compression.....	136
5.4.1.1	<i>Tube diameter</i>	136
5.4.1.2	<i>Hollow ratio χ</i>	138
5.4.1.3	<i>Inner tube slenderness</i>	141
5.4.2	Members under eccentric load	143
5.4.2.1	<i>Outer tube diameter</i>	143
5.4.2.2	<i>Hollow ratio χ</i>	147
5.4.2.3	<i>Outer tube slenderness</i>	151
5.4.2.4	<i>Eccentricity ratio</i>	155
5.4.2.5	<i>Concrete strength (f_c)</i>	156
5.4.3	Results - Summary	160
6	DESIGN RECOMMENDATIONS	162
6.1	Generalities.....	162
6.2	CFDST columns under concentric axial compression	162
6.3	CFDST columns under eccentric axial compression: N-M interaction diagram	164
6.3.1	Proposed design method	174
6.3.2	Proposed design method: confinement effect	179
6.3.3	N-M interaction curve development	188
6.3.4	Reliability analysis.....	200
7	CONCLUSION AND RECOMMENDATIONS FOR FUTURE RESEARCH..	205
7.1	Generalities.....	205
7.2	Main conclusions.....	205
7.3	Future research recommendations	208
	REFERENCES	209

INTRODUCTION

Generalities

A novel model of columns filled with concrete and denominated “double-skin” was first studied in the mid of 1980s by Shakir-Khalil and Illouli [1]. Concrete-filled double-skin tubular (CFDST) columns comprise two steel tubes with different dimensions concentrically positioned inside the other and concrete infill in the space between the sections (Figure 1). This composite column can be formed from different cross-sectional shapes, including square, rectangular, circular or elliptical sections. CFDST members are employed in many types of structural application, such as offshore platforms [2] (Figure 2 and Figure 3), transmission towers [3] (Figure 4), high-rise buildings [4] (Figure 5) and bridge piers [5], which justifies its focus on significant research interest in recent years.

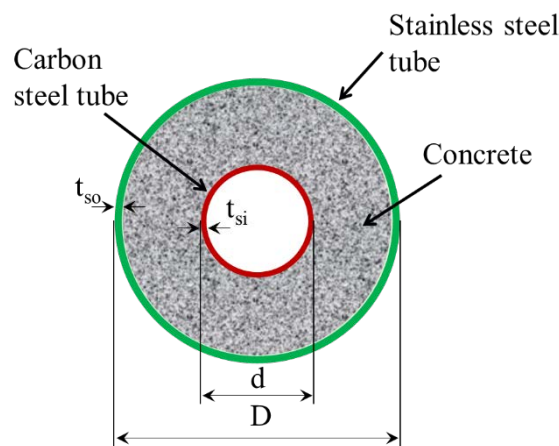


Figure 1 - Cross-section of a CFDST column.

Their advantages are very similar to those of concrete-filled steel tubular (CFST) columns. They include high compressive load-carrying capacity [6], good ductility [6], improved bending stiffness [5] compared to bare steel sections due to the concrete confinement effect, which also provides greater resistance for local buckling [7][5], as well as excellent fire resistance and seismic resistance [8]. In addition, CFDST columns can result in relatively light and efficient structures with lower construction costs than other structural solutions like

concrete-filled steel tubular (CFST) columns due to fewer materials use and a reduction in formwork requirements [5].

Stainless steel is a popular material for structural engineering applications owing to its many favourable attributes compared with carbon steel, including excellent corrosion resistance (especially in offshore construction), high strength and ductility, improved fire resistance, low maintenance requirements and aesthetic appeal [9], [10]. Stainless steel is also fully recyclable, which is an increasingly important factor as construction materials' sustainability is hugely topical. This also applies to concrete, where the use of recycled coarse aggregates (RCA) is currently receiving significant attention from the research community.

International design standards still do not cover the design of CFDST columns. There is a shortage of information available in the literature on CFDST columns made from a combination of stainless steel, carbon steel and recycled aggregate concrete. This thesis investigates the behaviour of concrete-filled double-skin tubular (CFDST) stub columns with a circular stainless steel outer tube, circular carbon steel inner section and recycled aggregate concrete (RAC) for the infill. These were accomplished by using three different types of loading analysis: concentric (columns), eccentric (beam-columns) and pure bending (beams). Accordingly, this research aims to develop a design guideline for CFDST stub columns based on experiments, numerical investigations, statistics and theory. Moreover, it aims to evaluate the use of RAC and stainless steel in CFDST columns by improving the construction field sustainability.



Figure 2 - CFDST columns used in an offshore platform [5].

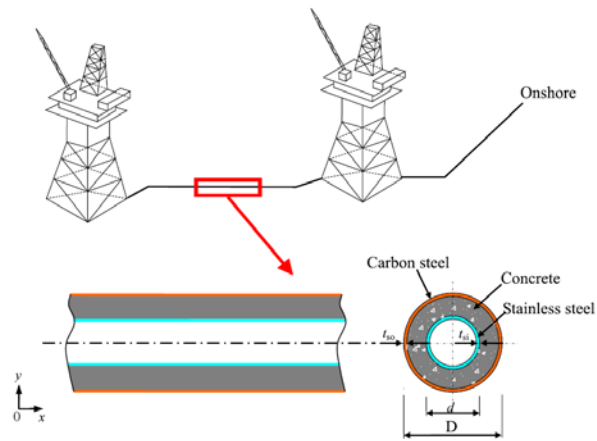


Figure 3 - CFDST cross-section in a submarine pipeline structure [11].



a) Lifting the outer tube; b) Placing the outer tube; c) Pole in service.

Figure 4 - CFDST pole and transmission tower [12].



Figure 5 - CFDST columns in a high-rise building, Office Building Palestra, London [13].

Objectives

The main objectives of this thesis are listed below:

- evaluate the use of RAC in CFDST columns through experimental and finite element (FE) simulations;
- investigate CFDST columns under concentric, eccentric and pure bending throughout a parametric analysis centred in FE simulations;
- develop a design guideline for CFDST beam-columns focusing on the development of N-M interaction diagrams;
- subsequently, compare the results with existing proposed design methods for CFDST columns under concentric and eccentric load;
- finally, statistically assess the developed method using Eurocode 0 (EC0) [14] and AISI [15] based on reliability analyses.

Outline of the thesis

This thesis consists of seven chapters which are summarised below:

The introduction chapter is intended with a brief introduction of the thesis's main focus, illustrating where CFDST columns can be better applied and their advantages. This is followed by their main objectives and the thesis outline.

Chapter 1 presents a literature review on the investigated subject, and it is divided into eight subsections, followed by Chapter 2, which shows the existing design methods for CFDST under concentric and eccentric load.

Chapter 3 focus on a detailed description of the experimental programme centred in the preparation of the recycled coarse aggregate (RCA) used in the CFDST columns with RAC. Moreover, the CFDST columns experimental results in terms of vertical strain and displacement are also reported.

Chapter 4 presents the numerical investigation of CFDST columns under concentric, eccentric and pure bending, which is performed within the ABAQUS finite element software

[16]. The FE simulations were calibrated against present thesis experiments and also from results present in the literature.

Chapter 5 depicts a parametric analysis conducted in ABAQUS [16], comprising approximately 360 different numerical models aiming to provide a higher range of results to represent CFDST columns and beam-columns behaviour accurately. It also describes the current design methods for CFDST columns under concentric and eccentric load

Chapter 6 presents the N-M interaction diagram's proposed design method and a concrete confinement parameter followed by a reliability analysis to assess the validity and efficacy of the proposed design recommendations.

Chapter 7 contains the thesis's main conclusions and proposes future work suggestions for the present thesis's main investigation topics.

1 LITERATURE REVIEW

1.1 Generalities

This chapter presents a literature review of relevant previous research related to concrete-filled double-skin tubular columns under concentric and eccentric loads involving (circular and rectangular) cross-sections and different materials (carbon, high strength and stainless steel and NCA and RCA concrete). Local buckling, infilled confined concrete, geometric imperfections and residual strength; experimental results, finite element modelling and theoretical methods will also be addressed in the present chapter.

1.1.1 Columns and beam-columns: composite members

A column is a structural member subjected to axial compression. A beam-column is a structural member subjected to axial compression together with a bending moment. The failure modes of compression members can occur by the cross-section material yielding failure and instability related collapses. The instability phenomena in tubular members can generally occur by local or global buckling, generally influenced by the columns' slenderness, geometric imperfections and residual stresses. The last two originate from steel tubular manufacturing. The failure mode of a stocky column usually is controlled by the cross-section yielding resistance where the normalized slenderness ($\bar{\lambda}$) has lower values. In contrast, slender columns have higher normalized slenderness, and consequently, their failure mode might occur due to global buckling resistance. However, the local buckling due to geometric imperfections can also affect the stocky columns' behaviour and will be better explored in the next item.

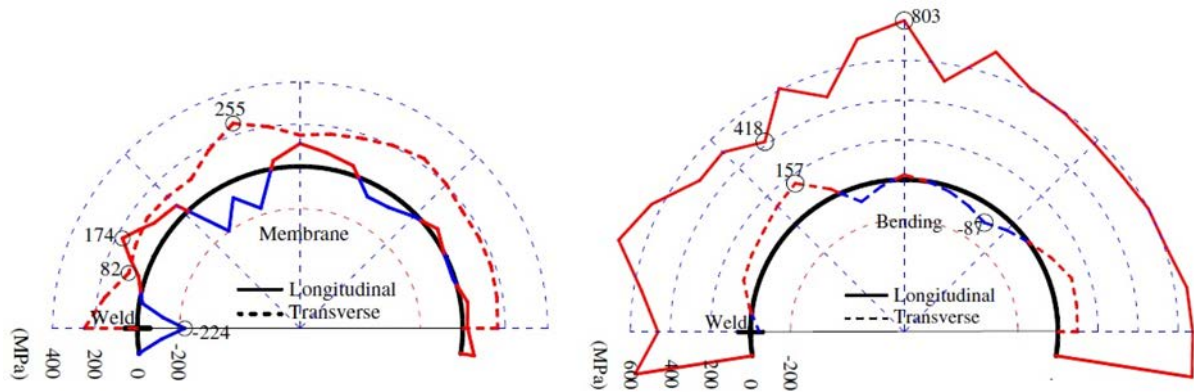
A composite member is usually a structural member with a higher cross-section resistance. Two or more materials are connected and work simultaneously, providing a better capacity response when compared to their individual response [17]. Eurocode 4 (EC4) [18] classifies a composite column in three different types: concrete-encased sections, partially encased sections and concrete-filled rectangular and circular tubes. Simultaneously, the concrete-filled tubular composite column presents the higher cross-section resistance among the three types in terms of axial compressive and bending moment resistance due to the confined

infilled concrete [17]. The concrete-filled double-skin tubular column (CFDST) is a type of composite column that is not yet covered by any design standard. Their cross-section resistance can be obtained by the sum of each material's resistance that compounds it, however, with the additional benefit of the confined infilled concrete and the hollow steel inner tube's low weight.

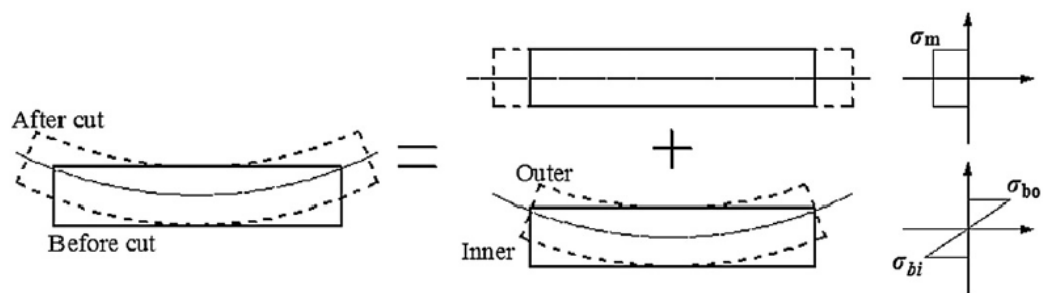
1.1.2 Geometric imperfections and residual stresses

The geometric imperfections and residual stresses occur in the steel tubes during their manufacturing and welding processes, consequently causing a possible local or global buckling failure. Their presence can modify the stress *versus* strain behaviour for both hot-rolled and cold-formed steel tubes and, consequently, reduce the composite columns' compressive resistance. Figure 6 shows the residual stress distribution along the cross-section of a cold-formed circular high strength steel tube. In contrast, the left side figure presents the membrane residual stress, and the right side shows the bending residual stresses. A uniformly residual stress distribution may be observed through the steel tube thickness, where the residual stress is presented in the external surface is in tension while the internal surface is in compression [19].

Li *et al.* [4] investigated the influence of geometric imperfection and residual stress in CFDST columns. It was concluded that the effect of the manufacturing imperfections in the steel tube is minor over the axial compressive capacity of the CFDST columns when the imperfection value is approximately $D/500$ (D is the outer steel tube diameter) for circular tube and $D/100$ for square tubes. The residual stress proved to have a minor influence over the CFDST columns axial compressive capacities for columns with two different stiffnesses (D/t_{so} - D is the outer tube diameter and t_{so} is the outer tube thickness): for circular columns, $D/t_{so} \leq 150(235/f_{sy0})$ and square columns $D/t_{so} \leq 60(235/f_{sy0})$.



a) Residual stress distribution of a cold-formed circular steel tube;



b) Membrane and bending residual stress distribution

Figure 6 - Residual stress distribution [19].

1.1.3 Stainless steel

In addition to the beneficial attributes of the stainless steel before mentioned: low maintenance, corrosion resistance and fully recyclable steel, other different properties than the carbon steel are important to be mentioned. The stress *versus* strain behaviour for stainless and carbon steels are compared in Figure 7. While the carbon steel stress *versus* strain curve has a well-defined plateau at the yield stress followed by strain hardening and plastic deformations, the stainless steel has a nonlinear behaviour with no yield plateau and resistance, ductility and a strain hardening increase trend. A straight line is usually drawn parallel to the elastic range of the stress *versus* strain curve at 0.2% strain to define yield stress ($f_{0.2}$) for the stainless steel [20].

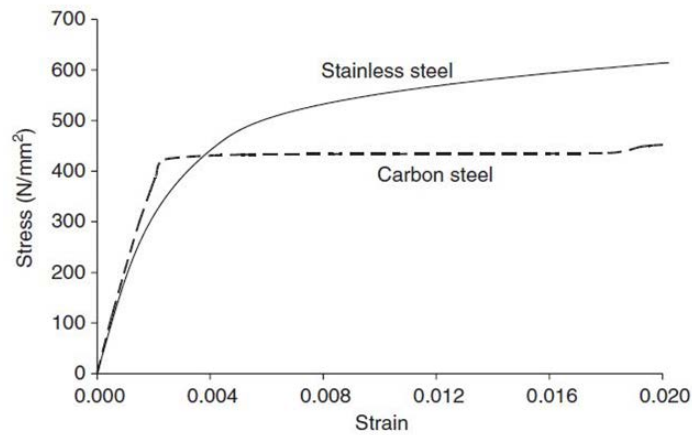


Figure 7 - Stress *versus* strain curve of carbon and stainless steel [20].

There are five different types of stainless steel, divided following their metallurgical structure (chromium, carbon, nickel, magnesium, molybdenum, copper, silicon, sulfur, phosphorus and nitrogen): austenitic, ferritic, duplex, martensitic and hardened by precipitation. Austenitic and duplex stainless steels are the most used in structural applications since both have higher corrosion and ductility resistances, as presented in Figure 8.

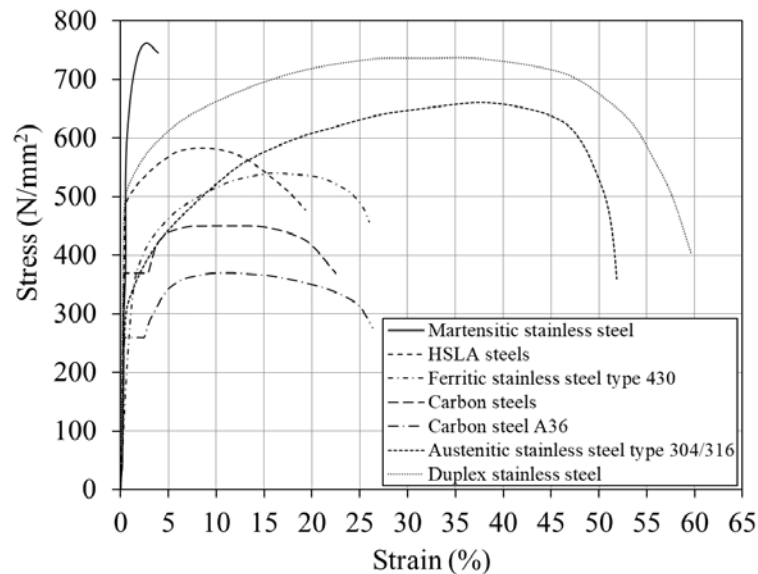


Figure 8 - Stress *versus* strain curves for stainless and carbon steels, adapted from [21].

1.1.4 Confined concrete

The infilled concrete in composite columns provides a beneficial confinement effect. The concrete strength parcel in a composite column presents an additional benefit for increasing

its load-carrying capacity by inhibiting the steel tube local buckling in the inward direction of the column's cross-section.

According to Calado [17], the bond between the steel tube and the infilled concrete in a composite cross-section only occurs if both strains and equivalent yield and compressive strengths become closer. The strain associated with the ultimate concrete compressive strength (3.5‰ - for concrete compressive strength ≤ 50 MPa) is about two times the strain associated with the steel tube yield stress (1.75‰). Therefore, for both steel tube and infilled concrete to work together, deforming simultaneously, the steel tube must be capable of reaching its ultimate and plastic resistance without exhibit any local buckling. This can only occur in Class 1 or 2 sections, as prescribed by Eurocode 3 (EC3) [22].

Moreover, the adherence between the infilled concrete and the steel tube must exist for both materials to develop the composite action. The friction adherence is provided by the roughness of the steel tube's contact surfaces and the infilled concrete, mainly generated by the infilled concrete's transversal pressure present in the steel tube walls during the composite column axial load introduction [23].

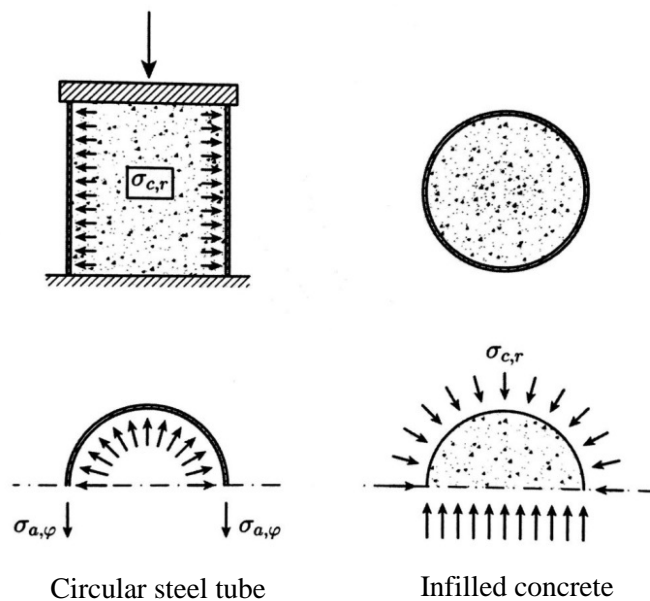


Figure 9 - Radial pressure in the composite column due to the concrete confinement effect [17].

The concrete's adherence to the steel tube also increases the concrete confinement effect. The circular steel tube is the shape that produces the highest concrete confinement effect since it creates triaxial compression stresses in the concrete during axial loading. Following Oliveira and El Debs [24], the effect of concrete confinement is related to the Poisson's coefficient (ν) of both materials (steel = 0.30 and concrete = 0.20). The infilled concrete's longitudinal deformations increase more than the steel tube deformations during higher axial compression

loading stages. This is due to its cracking (above 1‰ of deformation), creating radial pressure between the infilled concrete and steel tube surfaces, Figure 9. Afterwards, as the axial loading increases, the steel tube cannot support the tensile stresses generated by the infilled concrete's radial pressure. Consequently, the concrete confinement effect decreases.

The infilled concrete confinement effect acts differently in CFDST columns (Figure 10), as both steel tubes (inner and outer) are capable of generating triaxial stresses in the confined concrete. During axial compressive loading, the concrete tends to expand laterally. In contrast, the steel tubes inhibit this expansion, causing the radial lateral stresses inwardly and outwardly due to their different Poisson's coefficients. The confinement effect can be higher in CFDST than in CFST columns since the inner steel tube can also produce a radial pressure in the confined concrete [25].

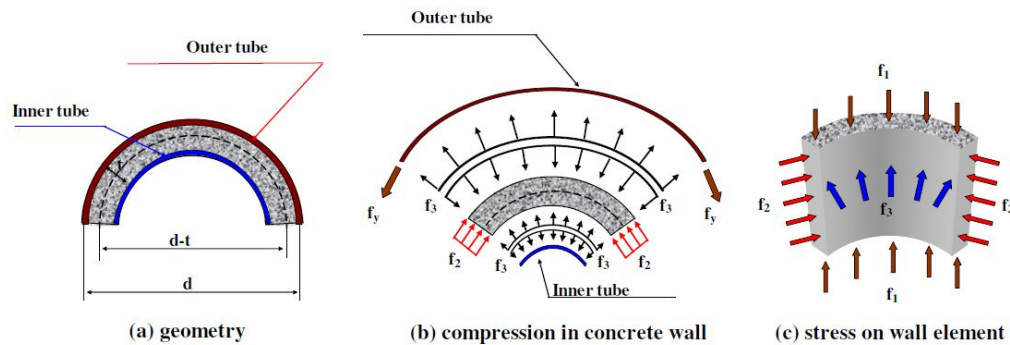


Figure 10 - Triaxial stresses in the infilled concrete of a CFDST column [25].

1.1.5 Recycled aggregate concrete

Among all the investigations currently present in the literature related to CFDST columns, none was found using recycled coarse aggregate concrete (RAC) in double-skin columns. On the other hand, it is common knowledge to reuse materials to reduce construction waste by using recycled aggregates to minimize environmental problems and increase sustainability.

RAC is made from demolished concrete elements which would otherwise be condemned to landfill, thus reducing the requirements for new aggregate materials to be sourced. Figure 11 presents three main types of material used for recycled coarse aggregates (RCA), including crushed concrete, crushed masonry and mixed demolition debris [26]. Recycled coarse aggregates (RCA) should ideally be derived from crushed concrete when employed for structural elements, without any impurities in its composition, such as gypsum and ceramics, to

maintain the envisaged mechanical performance [27]. Like natural coarse aggregates, RCA's mechanical properties are important to RAC structural members' overall performance. Moreover, the cement paste presence attached to recycled aggregate, quality of the original material used in the demolished structure, and aggregates' size and shape following the crushing process can affect the water absorption, density, and concrete porosity. Consequently, these issues affect the concrete mechanical properties [27], [28]. RAC is influenced by the RCA mechanical properties while the concrete mix and recycled aggregates percentage used in the mix (known as the replacement ratio). It has been shown that recycled aggregate concrete has a lower Young's modulus, compressive strength and tensile strength than conventional concrete [29].

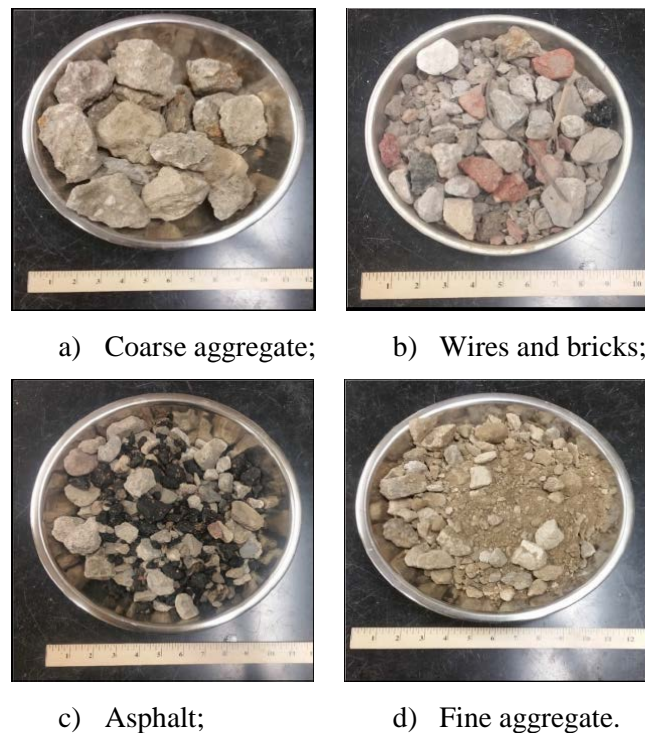


Figure 11 - Recycled coarse aggregates (RCA) from old structural concrete with various deleterious materials and sizes [26].

The recycled aggregate concrete is manufactured by replacing a percentage of the natural coarse or fine aggregate in the concrete's mixture, reducing the production and the consumption of natural aggregates. The aggregate's presence is about 2/3 of the total concrete cast.

1.1.6 CFST columns with RAC under compressive load

Yang and Han [30] carried out tests on 24 concrete-filled steel tubular (CFST) columns composed of RCA concrete and 6 CFST columns with NCA concrete, with cold-formed carbon steel tube and circular and square cross-sections. The CFST columns were subjected to concentric and eccentric load tests. The eccentricity values were determined as the ratio between the load eccentricity and the cross-section radius (e / r_0), which varied between 0 and 0.53. Finally, the obtained results were compared with the existing standards for composite columns, ACI 318-99 [31], AIJ [32], AISC-LRFD [33], BS5400 [34], DBJ1351-2003 [35] and EC4 [18]. The RAC was manufactured in two separately mix, one by replacing 25% of the natural coarse aggregate (NCA) and the second by replacing 50% of the natural coarse aggregate (NCA). The origin of the recycled coarse aggregate (RCA) was concrete debris only, with a compressive strength of $f_c = 50$ MPa. The concrete debris was crushed until the coarse aggregate achieves a dimension of 26.5 mm. The concrete compressive strength of the resulting RAC was $f_c = 40$ MPa. The CFST columns had lengths of 1650 and 1732 mm, with flexural global buckling as the observed failure mode (Figure 12). In general, the CFST columns with NAC showed a higher load capacity than the CFST columns with RAC. Moreover, the standard designs ACI 318-99 [31], AIJ [32], AISC-LRFD [33], BS5400 [34] and DBJ1351-2003 [35] proved to be conservative for circular cross-section and with RAC eccentric loads. However, EC4 [18] attained a maximum load capacity of 5% higher than the tests' load capacity, being against safety. The best standard design response was the AIJ [32], with a mean value of 0.926 and a CoV of 0.036. Finally, it was concluded that the design methods for CFST columns with NAC could be used to provide the load-carrying capacities of RAC CFST columns.

Huang *et al.* [36] studied the confinement generated by the recycled aggregate concrete inside the steel tube columns under axial compression. The proposed method was based on five premises: the concrete core and the steel tube have a perfect connection; the concrete core and the steel tube are under a triaxial stresses state (generated by radial stress of the steel tube); the existence of the concrete core inhibits the steel tube inward local buckling; the steel tube stress *versus* strain curve used in the proposed method considers the elastic range, the yield plateau and the strain hardening phase; the concrete core is under uniform confining pressure, and two hypotheses:

- the confining pressure in the concrete core generated by the steel tube is divided into three phases: approximately linear growth, nonlinear growth and smooth growth, following Zhong [37] and Mei *et al.* [38] (Figure 13 a));
- The stress *versus* strain curve of the recycled confined concrete is characterized by the three phases already mentioned due to the confining pressure (Figure 13 b)).



Figure 12 - Failure mode of the RAC CFST columns [30].

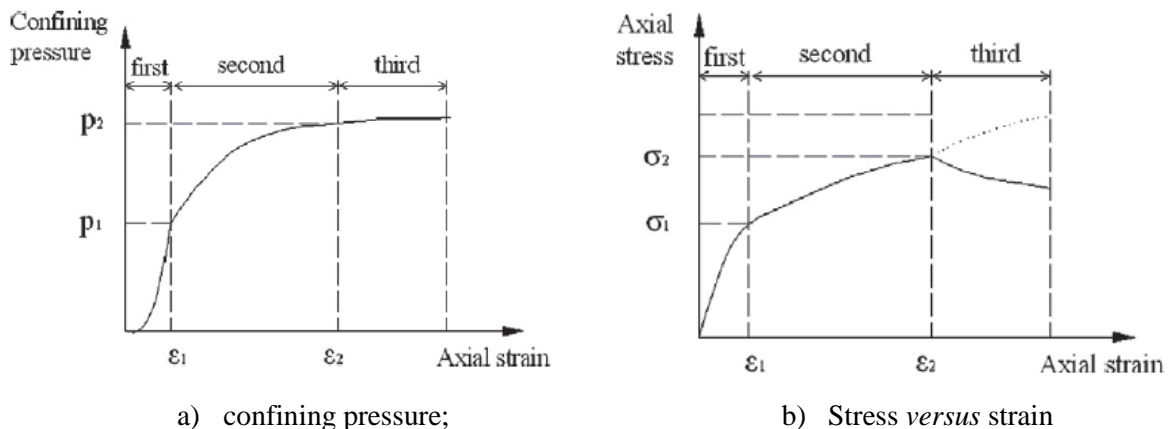


Figure 13 - Behaviour of confined RAC [36].

Based on the analytical method from Huang *et al.* [36] and the test results from Yang and Han [30], it is possible to observe that the steel tube's axial capacity cannot be ignored when assessing the strength of the concrete's portion. The pressure generated by the confined concrete does not remain constant. The development of the steel tube's confinement pressure in the concrete can be considered in three stages, linear growth, nonlinear growth and smooth growth. The percentage of replacement of recycled aggregate in the concrete has a moderate effect on the compressive strength and deformation of the confined concrete. Finally, Huang *et al.* [36] propose equations to simulate a constitutive law for recycled confined concrete in stress versus strain behaviour.

He *et al.* [40] evaluated experimentally and numerically the load-carrying capacity of circular recycled aggregate concrete-filled stainless steel tube (RACFSST) columns. Two circular cross-sections were used CHS 89 x 3 and CHS 101 x 3 (mm) with EN 1.4301 austenitic stainless steel grade and two nominal column's length of 700 mm and 1200 mm. The concrete infilled was a recycled aggregate concrete with different replacement ratios of recycled coarse aggregate (RCA) - 0%, 35% and 70%. A single-sized RCA with a nominal size of 20 mm, a single-sized NCA with a nominal size of 10 mm and a graded NA with a continuous range of nominal sizes from 5 mm to 20 mm was adopted to manufacture the recycled aggregate concrete (RAC) and the natural aggregate concrete (NAC). The grading curves are presented in Figure 14. All the RCA were sun-dried and pre-wetted with additional water to compensate for its high-water absorption before the concrete casting. A total of 12 tests were performed, varying the stainless steel tube diameter, the column's length and the RAC replacement ratio, obtaining different concrete compressive strength values f_c from 52.4 to 67.5 MPa. The proof stress of the stainless steel tubes ($f_{0.2}$) were 303.9 and 271.8 MPa for CHS 89 x 3 and CHS 101 x 3, respectively. The geometric imperfections were also measured.

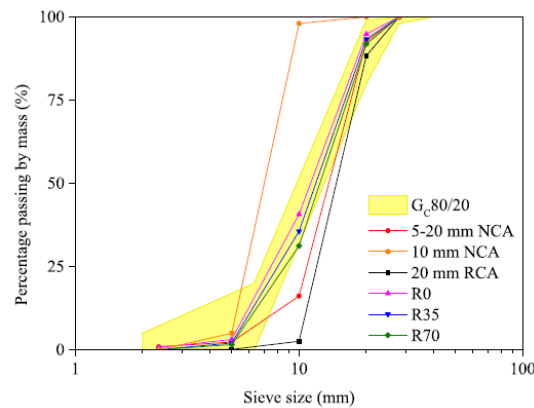


Figure 14 - Grading curves of coarse aggregates [40].

Pin-ended columns tests were conducted, and all twelve columns failed by member flexural buckling (Figure 15). It was also observed that columns with a higher RCA replacement ratio generally exhibited larger mid-height lateral deflections at failure, owing to the lower member flexural stiffness and higher susceptibility to flexural buckling. It was concluded that the reduction factor for flexural buckling resistance is generally insensitive to the RAC replacement ratio.

An FE model was developed in ABAQUS [16] to generate a wide range of cross-section columns in a parametric study. The concrete stress *versus* strain response was calculated by the proposed methods from Han *et al.* [41] to consider the confinement effect and a parameter β (Eq. (1)) proposed by Xiao *et al.* [42] was introduced into the ultimate strain to consider the influence of the RAC replacement ratio. The initial geometric imperfections, measured experimentally, were also included in the FE model through eigenvalue analyses.

$$\beta = 1 + \frac{r}{65.715r^2 - 109.43r + 48.989} \quad (1)$$

where r is the steel tube radius.



Figure 15 - Experimental and numerical deformations of columns with CHS 89 x 3, 1200 of length and RCA replacement ratio of 0%, 35% and 70% [40].

Finally, the experimental and numerical results were compared with international design codes: Eurocode 4 (EC4) [18], Australian/New Zealand standard [43] and AISC 360-10 [33]. The results indicated that the Australian/New Zealand standard [43] led to an unsafe prediction of the flexural buckling resistance. The AISC 360-10 [33] showed a good level of design accuracy but with too conservative results predictions, and Eurocode 4 (EC4) [18] offers the most accurate flexural buckling design prediction but still presents unsafe results for some intermediate columns.

1.1.7 CFDST columns with NAC under compressive and eccentric load

Uenaka [44] performed experiments on 12 CFDST stub columns (450 mm of length), varying the inner and outer tubes to assess their resistance to axial compression, Figure 16. The outer tube remained constant with a circular section of 160 mm in diameter. The inner tube had a square section with three different width values: 27 mm, 53 mm and 80 mm. The steel yield strength (f_y) varied between 199 MPa and 345 MPa, while the concrete compressive strength (f_c) varied between 32.3 MPa and 36.5 MPa.

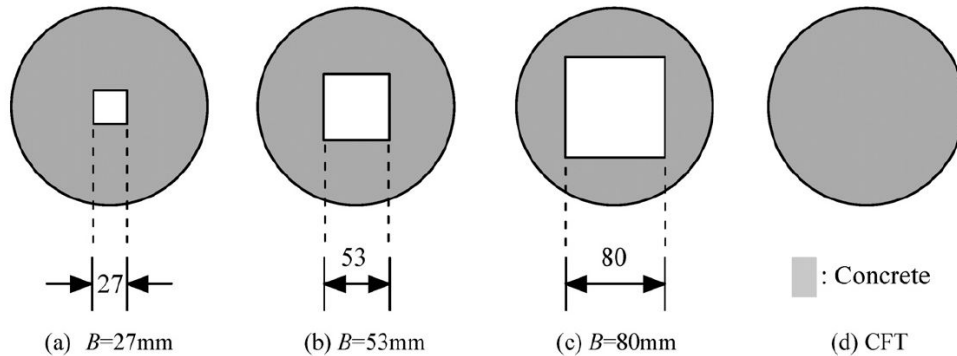


Figure 16 - Cross-section of the CFDST columns [44].

The observed failure modes could be divided into two groups, as shown in Figure 17.

- In the outer tube, local buckling combined with a shear failure of the infilled “sandwich” concrete was observed. This local buckling is usually denominated as “elephant's foot” (only in the thinner outer tubes) without shear failure of the infilled “sandwich” concrete.
- In the inner tube, local buckling in the steel tube, in the inward direction of the tube (into the “hollow” region direction) was verified.

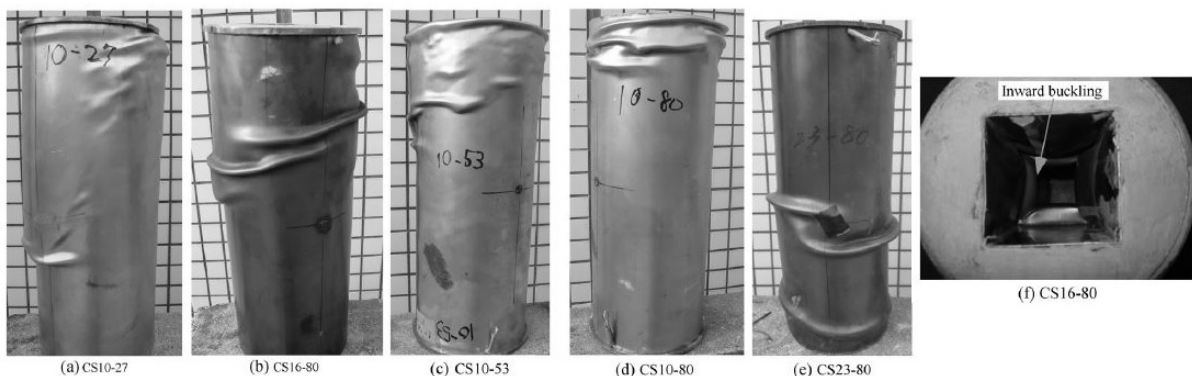


Figure 17 - Failure modes [44].

The experimental results for stub columns under axial compression showed a good agreement regarding the axial capacity calculated through the standard design equations

(compressive strength of both steel tubes plus the compressive strength of the infilled “sandwich” concrete). The mean ratio between experimental and theoretical capacity ($N_{u,test} / N_{u,theoretical}$) was 0.91.

Tao and Han [45] studied columns and beam-columns behaviour, with both outer and inner steel tubes manufactured by cold-formed rectangular carbon steel (Figure 18). An axial compression was applied to three stub columns. Eccentric axial compression was also applied in twenty four beam-columns. Three beams were studied to simulate pure bending using a four-point load test to assess their flexural strength. All the cold-formed rectangular tubes (outer and inner tubes) had the same thickness, $t_{so} = 3.2$ mm, the inner tube = 45 x 75 mm, and the outer tube = 100 x 150 mm. The cold rolling process manufactured the cold-formed tubes. The tensile tests specimens were extracted from the straight region of the tubes. The steel properties were: inner tube $E_{syi} = 194000$ MPa and $f_{syi} = 429$ MPa; outer tube $E_{syo} = 208000$ MPa and $f_{syo} = 380$ MPa. The cubic strength for the stub columns' infilled concrete and beam-columns was 53.6 MPa (f_{cu}), while for the beams was $f_{cu} = 67$ MPa.

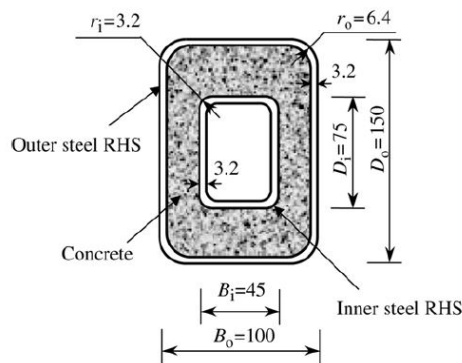


Figure 18 - CFDST columns cross-section [45].

The stub columns' outer tubes' failure mode was flexural buckling in the tube's outward direction. In contrast, the inner tubes presented their curved surfaces in a convex shape (bending in the inward direction of the tube, into the hollow direction) due to the infilled concrete's presence. The outer tube developed a local buckling in the beam tests after reaching the cross-section's ultimate load capacity. The inner tube presented a local buckling in the inward direction of the tube. A global buckling was observed in the beam-column tests, Figure 19. Comparing CFDST columns with composite columns filled with concrete, the behaviour was quite similar in theoretical terms. However, they had higher load-carrying capacities and ductility due to the confined concrete and steel and concrete ratio.



Figure 19 - Failure modes of stub columns, beam-columns and beams [45].

1.1.8 CFDST columns with carbon or high strength steel, stainless steel and NAC under compressive and eccentric load

Han *et al.* [46] performed 80 experiments on double-skin columns subjected to axial compression. All CFDST columns were manufactured with stainless steel on the outer tube, carbon steel on the inner tube and concrete filling the “sandwich” area between the steel tubes. The tested specimens were divided into four different sections: outer and inner circular tube, square outer and circular inner tube, rectangular outer and inner tube with rounded corners, elliptical inner and outer tube (Figure 20). The tests were divided as the column’s configuration for each group, as the load application: straight, inclined and tapered (variable cross-section), as shown in Figure 21.

The studied cross-sections varied in: 220 x 220 x 3.62 mm, 240 x 160 x 3.62 mm, 197 x 197 x 3.62 mm and 215 x 135 x 3.62 mm for the outer tubes and 159 x 159 x 3.72 mm, 106 x 106 x 3.72 mm, 186 x 106 x 3.72 mm, 142 x 62 x 3.72 mm, 136 x 136 x 3.72 mm, 83 x 83 x 3.72, 161 x 81 x 3.72 mm and 117 x 37 x 3.72 mm for the inner tubes. The material properties were varied according to their thickness, where the carbon steel tube, 3.72 mm thick, presented yield stress of $f_y = 380.6$ MPa and $E = 192000$ MPa; the stainless steel tube, 3.62 mm thick,

presented yield stress of $f_y = 319.6$ MPa and $E = 201000$ MPa. The “sandwich” infilled concrete depicted a mean cubic strength of $f_{cu} = 65.6$ MPa. and $E = 33000$ MPa.

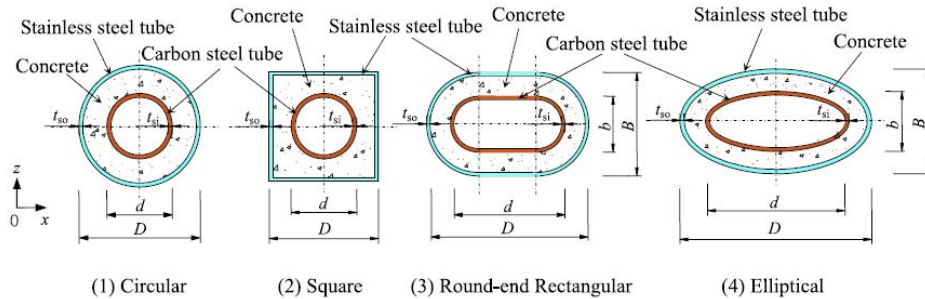


Figure 20 - CFDST columns cross-sections [46].

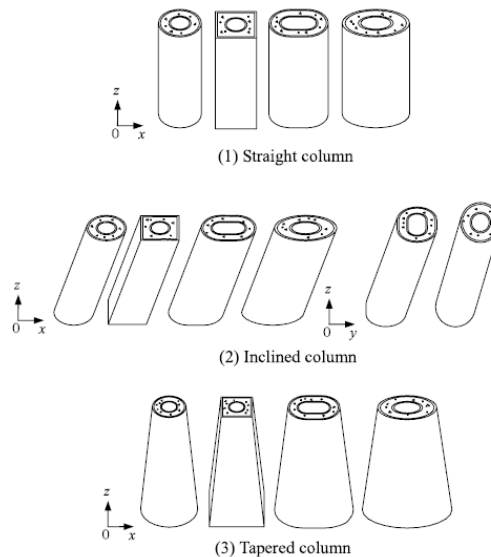


Figure 21 - CFDST columns configurations [46].

The failure mode for straight columns was local buckling in the outward direction of the stainless steel outer tube (Figure 22 a)) close to half of the columns' height and local buckling into the inward direction of the carbon steel inner tube, in almost all the columns. Some CFDST circular columns showed an “elephant's foot” local buckling close to the fixed supports in the outer tubes. For some square, rectangular with rounded corners and elliptical columns, the inner tube presented a "diamond shape" local buckling (Figure 22 b)). The infilled concrete crushed in the same region where the local buckling occurred, i.e. in the outer tubes' outward direction.

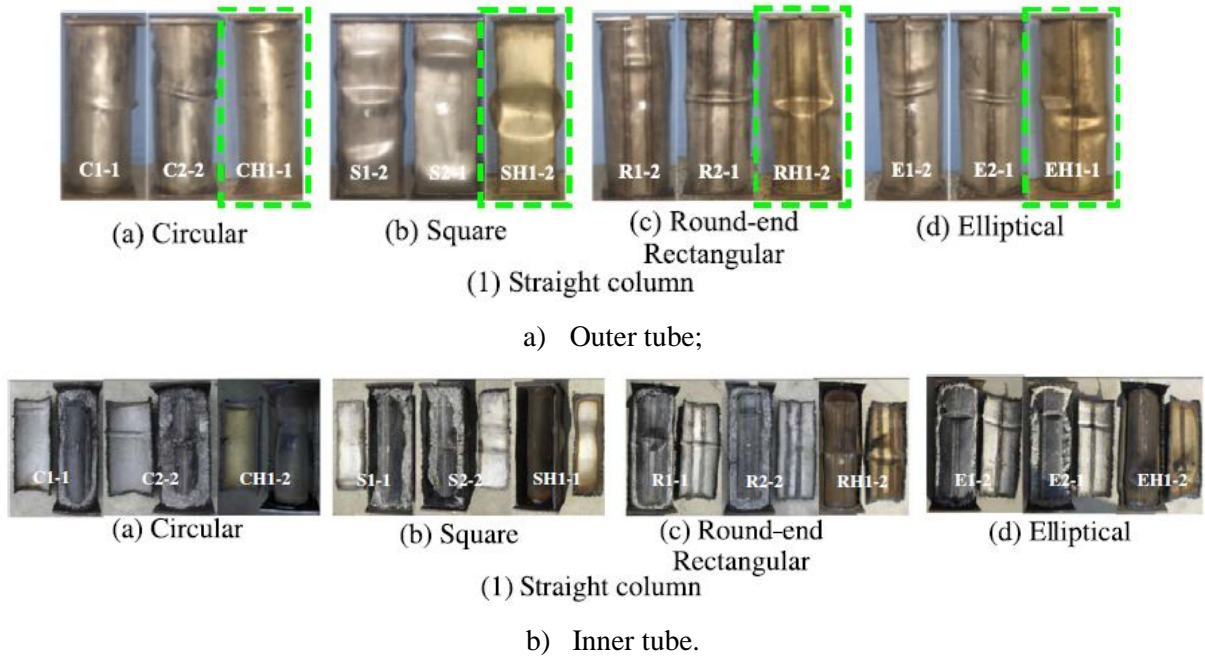


Figure 22 - Typical failure modes for the straight CFDST columns [46].

The presence of stainless steel in CFDST columns improved their ductility. The cross-section load-carrying capacity and stiffness reduced as the ratio between the tube's diameters increase due to the consequent infilled concrete area increase. The square outer tube and the circular inner tube cross-section provided the smallest concrete confinement effect. The composite columns design proved to be conservative, especially for circular sections. Finally, Han *et al.* [46] propose design equations for CFDST columns, which will be discussed in item 2.2.2.

Wang *et al.* [9] also performed experiments on double-skin columns using stainless steel outer tubes. Fourteen stub columns were tested using ferritic stainless steel outer tubes and carbon steel inner tubes. The outer and inner tube cross-sections varied between rectangular and square shapes, as presented in Figure 23. Four different sections were studied: the outer tubes were 120 x 80 x 3 mm and 100 x 80 x 4 mm, while the inner tubes were 20 x 1.5 mm and 20 x 2.5 mm. All the stub columns measured 300 and 250 mm in length. In terms of material properties (tensile tests specimens from straight surfaces), the stainless steel tube was cold-formed and presented yield stress f_y (at 0.2% of strain) and elastic modulus E , ranging from 401 to 439 MPa and 205000 to 214000 MPa, for thicknesses of 3 and 4 mm. The carbon steel tube was also cold-formed and presented yield stress of f_y (0.2%) and elastic modulus E ranging from 357 to 468 MPa and from 204000 to 213000 MPa, for thicknesses of 1.5 and 2.5 mm. The concrete compressive strengths were 40, 80 and 120 MPa.

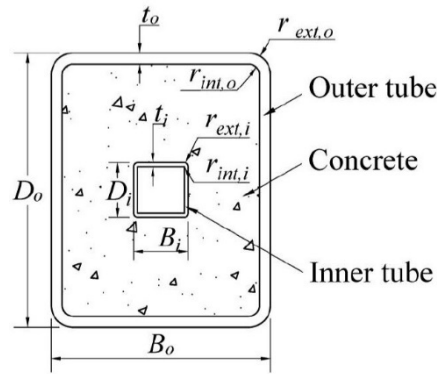


Figure 23 - CFDST column cross-section [9].

The axial compression tests were conducted using displacement control. Simultaneously, a high strength steel ring was placed next to each column's fixed support to avoid a premature “elephant foot” local buckling failure mode. The failure modes were local buckling in the outward direction of the outer tube and local buckling in the inner tube's inward direction due to the concrete's crushing (Figure 24). The axial load *versus* axial strain curve indicated that the columns' ductility was reduced as the concrete compressive strength increase.



Figure 24 - CFDST columns failure modes [9].

A comparison was made between design standards (European standard [18], Australian standard and the American specifications ANSI / AISC [33] and ACI [31]) for tubular columns filled with concrete since no standard explicitly covers CFDST columns with stainless steel in the outer tubes. The results proved to be satisfactory: European and Australian standards presented mean values for the ratio between experimental and theoretical results of 1.07. The American ANSI / AISC [33] specifications revealed higher mean values (more conservative) when compared with ACI [31] 1.17 and 1.15, respectively.

Silva *et al.* [47] performed four compression tests on CFDST stub circular columns (660 mm of height), with austenitic stainless steel (304L) outer tubes (219.08 x 3.6 mm), a concrete compressive strength of $f_c = 60$ MPa and two different inner carbon steel tubes (114.30 x 4.50 mm and 165.10 x 4.25 mm), with $f_y = 357$ MPa and $f_y = 280$ MPa. The varied parameters were the inner carbon steel tube cross-section and the area between both steel tubes with and without the infilled concrete. Figure 25 shows the failure mode of the CFDST column with concrete and without the infilled concrete, respectively. The column's typical failure mode with infilled concrete is the “elephant's foot”, which is the outward local buckling direction of the outer stainless steel tube and the “diamond” failure mode, the inward local buckling direction of the inner carbon steel tube. The failure modes were characterized by the infilled concrete's presence that inhibits the tubes' opposite deformation and the concrete crushing in the regions where the tube's local buckling occurred. For CFDST columns without concrete, both the inner and outer tubes presented the same local buckling failure mode for both columns.



Figure 25 - Failure modes of the CFDST columns [47].

Wang *et al.* [48] investigated experimentally and numerically CFDST stub columns. The double-skin stub columns were manufactured with stainless steel in the outer tube, high strength steel in the inner tube and conventional concrete. The cross-section of both steel tubes of the CFDST stub columns adopted circular sections. Twenty-three tests were made varying the outer and the inner tube diameters and thicknesses. Two different cross-sections for the outer tube, 140 x 3 and 165 x 3 mm were used while five different cross-sections were adopted for the inner tube, 22 x 4, 32 x 6, 38 x 8, 55 x 11 and 89 x 4 mm. All the stub columns had their length equal to 2.5 times the outer tube diameter. In terms of material properties (tensile tests specimens from straight surfaces), the austenitic stainless steel tube EN 1.4301 was cold-formed and presented a yield stress f_y (0.2%) of 300 and 276 MPa and elastic modulus E of 197000 and

200000 MPa. The high strength steel tubes were hot-rolled and depicted a yield stress of f_y (0.2%) and elastic modulus E ranging from 433 to 1029 MPa and from 197000 to 211000 MPa. The concrete compressive strengths were 40, 80 and 120 MPa. A numerical investigation followed with a parametric analysis with 239 simulations using the finite element software ABAQUS [16]. The tests and FE models were compared and used to evaluate the current design provisions for composite columns and incorporated the expressions' concrete compressive strength. Figure 26 presents the failure mode of the CFDST stub columns for experimental and numerical investigations. A high strength steel ring was positioned next to each column's fixed support to avoid the premature “elephant foot” local buckling failure mode during the tests. It is possible to observe an outward local buckling direction of the outer tube and an inward local buckling direction of the inner tube. The authors concluded that current design provisions generally provide a safe prediction. Alternatively, these predictions do not adequately account for strain hardening in the stainless steel outer tubes or the concrete confinement influence over the load-carrying capacity.

Araújo [49] performed a parametric analysis using the finite element software ANSYS [50] on CFDST columns based on the experiments presented by Silva *et al.* [47]. Thirty column models with outer stainless steel tube ($f_y = 324$ MPa), inner carbon steel tube ($f_y = 335$ MPa) and infilled concrete ($f_c = 35$ MPa) were evaluated. The outer stainless steel tube and the inner carbon steel tube cross-sections varied to investigate the hollow ratio parameter (χ) between 0.45 and 0.87. Each group adopted a different cross-section with the same outer tube diameter and thickness and only varied the inner tube cross-section, where: group 1A presented an outer tube diameter of 168.28 mm and an outer tube thickness of 2.77 mm, group 2A 219.08 mm and 3.76 mm, group 3A 273.05 mm and 4.19 mm, group 4A 323.85 mm and 4.57 mm and group 5A 355.6 mm and 4.78 mm, respectively. The hollow ratio parameter (χ), as seen in Figure 27, exhibited some important observations: as the dimension of the inner tube was increased, the columns ultimate load reduced, as the concrete cross-sectional area also decreased; as the hollow ratio parameter (χ) increased, the concrete longitudinal stress decreases (the concrete maximum stress's region moves from the centre to the outside of the cross-section) due to the concrete area reduction; when the hollow ratio parameter (χ) is equal to zero, the maximum concrete stress occurs at the core of the column's cross-section, when the hollow ratio parameter (χ) is equal to 0.25, the maximum concrete stress occurs at the infilled concrete centre, and when the hollow ratio parameter (χ) is equal to 0.5 or 0.75, the maximum concrete stress occurs close to the outer stainless steel tube; the elastic phase's stiffness increases as the hollow ratio parameter (χ) also increases.

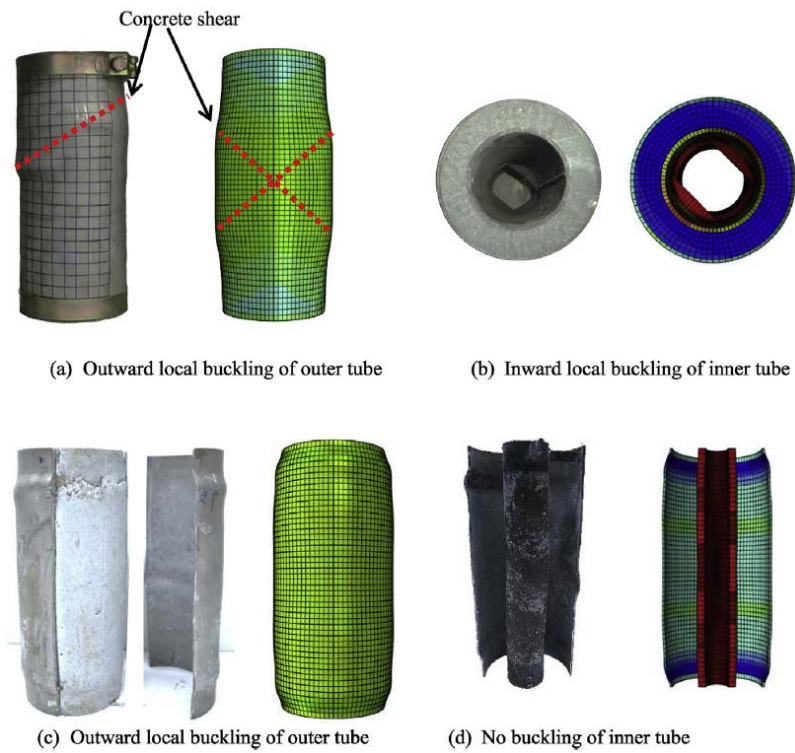


Figure 26 - CFDST stub columns failure modes [48].

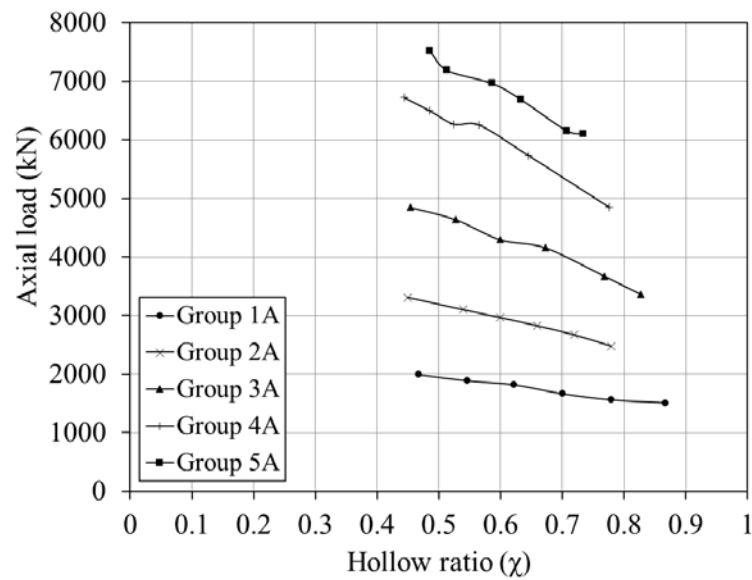


Figure 27 - Axial load *versus* hollow ratio parameter (χ) influence using the same outer tube diameter [49].

Numerous other numerical studies related to CFDST columns with stainless steel in the outer tube and carbon steel in the inner tube can be found in the literature. Hassanein *et al.* [51]

investigated CFDST stub columns and concluded that the ultimate axial load capacity increases by increasing the compressive concrete strength or decreasing the hollow ratio. Hassanein and Kharoob [52] studied CFDST slender columns and concluded that the confinement effect could be ignored for very long columns. On the other hand, the inner tube provides a higher confinement effect than the outer tube for intermediate columns. They also indicated that higher hollow ratio (χ) values proved not to influence the ultimate load strength for intermediate columns but increase their ultimate loads for very long columns. Pagoulatou *et al.* [53] also studied double-skin stub columns through numerical models assessing: diameter-to-thickness ratio, concrete strength, steel yielding, confinement and hollow ratio and proposed an alternative design equation.

2 DESIGN METHODS

2.1 Generalities

The design of concrete-filled double-skin tubular columns and beam-columns is still not included in the international design standards. Nevertheless, reflecting the increasing interest in these members in recent years, different design methods were proposed in the literature. This chapter will first describe these investigations developed by the researchers such as Uenaka *et al.* [54], Han *et al.* [46] and Hassanein *et al.* [51], Uenaka and Kitoh [55], Han *et al.* [12] and Fouché *et al.* [56]. In addition, the concrete-filled tubular columns design method prescribed by Eurocode 4 (EC4) [18] will also be presented, focusing in verify its applicability for CFDST columns.

2.2 CFDST under concentric load

2.2.1 Uenaka et al. [54]

Uenaka et al. [54] proposed a design equation to predict the axial load capacity of CFDST columns based on a modified version of the equation present in the Architectural Institute of Japan-AIJ [57] for CFST columns. Based on Uenaka *et al.* [54] experiments, the outer tube's confinement effect was included in the ultimate strength equation for CFDST columns. The confinement effect is considered in terms of the coefficient η_{CFDST} :

$$N_{uCFDST} = (1 + \eta_{CFDST})A_{so}f_{sy0} + A_c f_c + A_{si}f_{syi} \text{ but } 0.2 < d/D < 0.7 \quad (2)$$

$$\eta_{CFDST} = 1.86 - 2.59 d/D \quad (3)$$

where: A_{so} , A_c and A_{si} , f_{syo} , f_c and f_{syi} , are the cross-section areas, yield stress at 0.2% and the compressive strength for each material. The variable d is the inner tube diameter, while D is the outer tube diameter.

2.2.2 Han *et al.* [46]

Han *et al.* [46] proposed a design equation to predict the load capacity of CFDST columns with an outer stainless steel tube, whereas the confinement effect is only provided by the outer steel tube. The approach is based on the assumption that the ultimate strength of a CFDST stub column $N_{u,Han}$ is equal to the sum of the capacities of the inner tube $N_{i,u}$ and the combined contribution of the outer tube and concrete $N_{osc,u}$, as illustrated in Eq. (4):

$$N_{u,Han} = N_{i,u} + N_{osc,u} \quad (4)$$

These two terms are determined by Eqs. (5) and (6):

$$N_{i,u} = A_{si}f_{syi} \quad (5)$$

$$N_{osc,u} = A_{osc}f_{osc} \quad (6)$$

in which f_{syi} is the yield stress of the inner tube; f_{osc} is a combined strength value for the outer stainless steel tube f_{syo} and the concrete infill f_c , accounting for the confinement effect. A_{si} is the inner tube cross-sectional area whilst A_{osc} is the sum of the cross-sectional areas of the outer stainless steel tube A_{so} and the concrete A_c :

$$A_{osc} = A_{so} + A_c \quad (7)$$

The combined strength value for the outer stainless steel tube and the infill concrete is evaluated with Eq. (8):

$$f_{osc} = C_1 \chi^2 f_{syo} + C_2 (1.14 + 1.02\xi) f_c \quad (8)$$

In this expression, χ is the hollow ratio determined using Eq. (9), whilst C_1 and C_2 can be determined with Eqs. (10) and (11):

$$\chi = d / (D - 2t_{so}) \quad (9)$$

$$C_1 = \alpha / (1 + \alpha) \quad (10)$$

$$C_2 = (1 + \alpha_n) / (1 + \alpha) \quad (11)$$

ξ is the nominal confinement factor, determined by Eq. (12):

$$\xi = A_{so} f_{syo} / A_{ce} f_c \quad (12)$$

In Eqs. (10) and (11), α is the ratio of the outer stainless steel tube area A_{so} to the concrete cross-sectional area A_c and α_n is the ratio of A_{so} to A_{ce} , in which A_{ce} is an equivalent cross-sectional area of the sandwiched concrete, defined as the full area enclosed by the outer tube, given as:

$$A_{ce} = \pi(D - 2t_{so})^2 / 4 \quad (13)$$

2.2.3 Hassanein et al. [51]

Hassanein *et al.* [51] proposed a design model based on a previous CFST columns design prediction made by Liang and Fragomeni [58] combined with the CFDST columns ultimate strength prediction developed by Hassanein *et al.*'s [59] and [60]. The CFDST columns are short columns made of a stainless steel outer tube and a carbon steel inner tube. The strain hardening for both steel tubes was considered in the proposed following equations (γ_{so} and γ_{si}):

$$N_{u,Hassanein} = \gamma_{so} A_{so} f_{syo} + (\gamma_c f_c + 4.1 f_1) A_c + \gamma_{si} A_{si} f_{syi} \quad (14)$$

$$\gamma_{so} = 1.62 \left(\frac{D}{t_{so}} \right)^{-0.1} \quad \text{but } \gamma_{so} \leq 1.2 \quad (15)$$

$$\gamma_{si} = 1.458 \left(\frac{d}{t_{si}} \right)^{-0.1} \quad \text{but } 0.9 \leq \gamma_{si} \leq 1.1 \quad (16)$$

$$\gamma_c = 1.85 D_c^{-0.135} \quad \text{but } 0.85 \leq \gamma_c \leq 1.0 \quad (17)$$

$$D_c = D - 2t_{so} \quad (18)$$

$$f_1 = \begin{cases} 0.7(\nu_o - \nu_s) \frac{2t_{so}}{D - 2t_{so}} f_{syo} & \text{for } D/t_{so} \leq 47 \\ \left((0.006241 - 0.0000357 D/t_{so}) f_{syo} \right) & \text{for } 47 < D/t_{so} \leq 150 \end{cases} \quad (19)$$

$$\begin{aligned} \nu_o = & 0.2312 + 0.3582\nu'_o - 0.1524 \left(\frac{f_c}{f_{syo}} \right) + 4.843\nu'_o \left(\frac{f_c}{f_{syo}} \right) \\ & - 9.169 \left(\frac{f_c}{f_{syo}} \right)^2 \end{aligned} \quad (20)$$

$$\begin{aligned} \nu'_o = & 0.881 \times 10^{-6} \left(\frac{D}{t_{so}} \right)^3 - 2.58 \times 10^{-4} \left(\frac{D}{t_{so}} \right)^2 + 1.953 \times 10^{-2} \left(\frac{D}{t_{so}} \right) \\ & + 0.4011 \end{aligned} \quad (21)$$

in which A_{so} , A_c and A_{si} , f_{syo} , f_c and f_{syi} , are the cross-section areas and the yield stress at 0.2% and the compressive strength for each material, respectively. The variables d , D_c and D are the inner tube diameter, the concrete diameter and the outer tube diameter, respectively. The terms t_{so} and t_{si} are the outer and inner tube thickness. The concrete strength reduction factor γ_c is according to Liang [61], and f_1 is the lateral confining pressure from İpek and Güneyisi [62] ν_o is the Poisson's coefficient of the steel tube with the concrete infill and ν_s is the Poisson's coefficient of the steel tube without the concrete infill and at the maximum strength point, with a value of 0.5, proposed by Tang *et al.* [63].

2.2.4 Eurocode 4 (EC4) [18]

The equation from Eurocode 4 (EC4) [18] to calculate the ultimate strength of CFST columns is the steel tube's sum, the concrete infill, and the reinforcing bar's resistance. However, a first approach may be concerned for CFDST columns changing the reinforcing bar's resistance by the inner steel tube resistance. The ultimate axial resistance considers the increase of the concrete resistance due to the confinement effect and the decrease in steel tube resistance. The approach is introduced in the equation through a reduction factor for the steel resistance η_a and an enhancement factor for the concrete confinement resistance η_c . The relative slenderness calculates these factors $\bar{\lambda}$ and the ratio e/D , where e is the eccentricity and D is the steel outer tube diameter. The equations are presented below:

$$\bar{\lambda} = \sqrt{N_{pl,Rd} / N_{cr}} \quad (22)$$

$$N_{pl,Rd} = A_{so}f_{syo} + \alpha_{cc}A_c f_c + A_{si}f_{syi} \quad (23)$$

$$N_{cr} = \pi^2 (EI)_{eff} / (kL)^2 \quad (24)$$

$$(EI)_{eff} = E_{so}I_{so} + K_e E_c I_c + E_{si}I_{si} \quad (25)$$

$$\eta_{a0} = 0.25(3 + 2\bar{\lambda}) \quad \text{but } \leq 1.0 \quad (26)$$

$$\eta_{c0} = 4.9 - 18.5\bar{\lambda} + 17\bar{\lambda}^2 \quad \text{but } \geq 0.0 \quad (27)$$

$$\eta_a = \eta_{a0} + (1 - \eta_{a0})(10^{e/D}) \quad \text{but } 0 < e/D \leq 1.0 \quad (28)$$

$$\eta_c = \eta_{c0}(1 - 10^{e/D}) \quad \text{but } 0 < e/D \leq 1.0 \quad (29)$$

$$N_{u,EC4} = \eta_a A_{so} f_{syo} + A_c f_c \left[1 + \eta_c \left(\frac{t_{so}}{D} \right) \left(\frac{f_{syo}}{f_c} \right) \right] + A_{si} f_{syi} \quad (30)$$

where α_{cc} is equal to 1.0 when the composite column is concrete-filled, exposing the concrete's total confinement. A_{so} , A_c and A_{si} , f_{syo} , f_c and f_{syi} , E_{so} , E_c and E_{si} , I_{so} , I_c and I_{si} are the cross-section areas, the yield stresses at 0.2% and the compressive strength, Young's modulus and the second moments of area for each material, respectively; t_{so} is the outer tube thickness, and

$(EI)_{\text{eff}}$ is the composite cross-section effective flexural stiffness; K_e is a correction factor with a value of 0.6; $N_{\text{pl,Rd}}$ is the compressive plastic resistance; and $N_{\text{u,EC4}}$ is the ultimate axial strength. The eccentricity e is calculated by $M_{\text{Ed}} / N_{\text{Ed}}$ and when $e/D > 1.0$, while the factors are equal to: $\eta_a = 1.0$ and $\eta_c = 0.0$.

2.3 CFDST under eccentric load

2.3.1 Uenaka and Kitoh [55]

Uenaka and Kitoh [55] proposed equations (Eqs. (31) and (32)) for ultimate axial strength ($N_{\text{u,Uenaka}}$) and bending ($M_{\text{u,Uenaka}}$) for CFDST sections. The approach assumed by the Bernoulli theory and the stress block technique based on the full plastic stress block response, as presented in Figure 28.

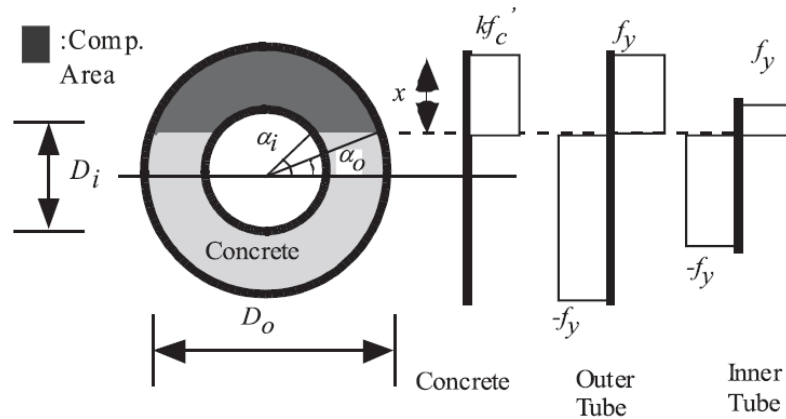


Figure 28 - Stress distributions from Uenaka and Kitoh [55].

$$N_{\text{u,Uenaka}} = \frac{\pi k f_c}{2} \left\{ R^2 \left(1 - \frac{2\alpha_o}{\pi} - \frac{\sin 2\alpha_o}{\pi} \right) - r^2 \left(1 - \frac{2\alpha_i}{\pi} - \frac{\sin 2\alpha_i}{\pi} \right) \right\} - 4f_{syi}(Rt_{so}\alpha_o + rt_{si}\alpha_i) \quad (31)$$

$$M_{\text{u,Uenaka}} = \frac{2k f_c}{3} (R^3 \cos^3 \alpha_o - r^3 \cos^3 \alpha_i) + 4f_{syi}(R^2 t_{so} \cos \alpha_o + r^2 t_{si} \cos \alpha_i) \quad (32)$$

in which R and r , t_{so} and t_{si} , f_{syo} and f_{syi} , are the radius, thicknesses and yield stress at 0.2% of the outer and inner tubes; f_c is the concrete compressive strength, k is the equivalent stress block coefficient equal to 0.85; α_o and α_i are the angles between the horizontal centroid axis and the radial lines across the neutral axis at the outer and inner tube diameters.

2.3.2 Han *et al.* [12]

Han *et al.* [12] developed a design method to obtain the ultimate axial strength ($N_{u,Han}$) and bending ($M_{u,Han}$) for CFDST sections. The method is based on probability theory considering partial factors. Some limits are imposed, such as the outer tube diameter must be larger than 200 mm; the outer tube thickness must be larger than 4 mm; the hollow ratio (χ) must be between 0 and 0.75; the nominal confinement factor (ξ) must be between 0.6 and 4.0. and the ratio between the outer tube diameter and the outer tube thickness must be $D/t_{so} \leq 135 \sqrt{235/f_{syo}}$. The equations are presented below:

$$N_{u,cr} = \varphi N_u \quad (33)$$

$$\varphi = \begin{cases} 1.0 & (\lambda \leq \lambda_o) \\ \alpha_1 \lambda^2 + b_1 \lambda + c_1 & (\lambda_o < \lambda \leq \lambda_p) \\ d_1 (-0.23 \chi^2 + 1) / (\lambda + 35)^2 & (\lambda > \lambda_p) \end{cases} \quad (34)$$

$$a_1 = \frac{1 + (35 + 2\lambda_p - \lambda_o)e_1}{(\lambda_p - \lambda_o)^2} \quad (35)$$

$$b_1 = e_1 - 2\alpha_1 \lambda_p \quad (36)$$

$$c_1 = 1 - \alpha_1 \lambda_o^2 - b_1 \lambda_o \quad (37)$$

$$d_1 = \left[13,000 + 4657 \ln \left(\frac{235}{f_{syo}} \right) \right] \left(\frac{25}{f_c + 5} \right)^{0.3} \left(\frac{\alpha_n}{0.1} \right)^{0.05} \quad (\text{circular sections}) \quad (38)$$

$$e_1 = \frac{-d_1}{(\lambda_p + 35)^3} \quad (39)$$

$$\lambda_p = 1743 / \sqrt{f_{syo}} \quad (\text{circular sections}) \quad (40)$$

$$\lambda_o = \pi / \sqrt{(420\xi + 550)f_{osc}} \quad (\text{circular sections}) \quad (41)$$

$$\begin{cases} \frac{N}{\varphi N_u} + \frac{a_2}{d_2} \left(\frac{M}{M_u} \right) = 1 & \left(N/N_u \geq 2\varphi^3\eta_o \right) \\ -b_2 \left(\frac{N}{N_u} \right)^2 - c_2 \left(\frac{N}{N_u} \right) + \frac{1}{d_2} \left(\frac{M}{M_u} \right) = 1 & \left(N/N_u < 2\varphi^3\eta_o \right) \end{cases} \quad (42)$$

$$a_2 = 1 - 2\varphi^2\eta_o \quad (43)$$

$$b_2 = \frac{1 - \zeta_o}{\varphi^3\eta_o^2} \quad (44)$$

$$c_2 = \frac{2(\zeta_o - 1)}{\eta_o} \quad (45)$$

$$\zeta_o = (0.18 - 0.2\chi^2)\xi^{-1.15} + 1 \quad (\text{circular sections}) \quad (46)$$

$$\eta_o = \begin{cases} (0.5 - 0.245\xi)(-1.8\chi^2 + 0.7\chi + 1) & (\xi \leq 0.4) \\ (0.1 + 0.14\xi^{-0.84})(-1.8\chi^2 + 0.7\chi + 1) & (\xi > 0.4) \end{cases} \quad (\text{circular sections}) \quad (47)$$

$$d_2 = 1 - 0.4 \left(N/N_E \right) \quad (\text{circular sections}) \quad (48)$$

$$N_E = \pi^2 E_{total} A_{total} / \lambda^2 \quad (49)$$

$$E_{total} = \frac{E_{so} I_{so} + E_c I_c + E_{si} I_{si}}{I_{so} + I_c + I_{si}} \quad (50)$$

$$I_{total} = I_{so} + I_c + I_{si} \quad (51)$$

$$A_{total} = A_{so} + A_c + A_{si} \quad (52)$$

$$\lambda = kL / \sqrt{I_{total} / A_{total}} \quad (53)$$

$$M_u = \gamma_{m1} W_{osc} f_{osc} + \gamma_{m2} W_{si} f_{syi} \quad (54)$$

$$\gamma_{m1} = 0.48 \ln(\xi + 0.1) (-0.85\chi^2 + 0.06\chi + 1) + 1.1 \quad (\text{circular sections}) \quad (55)$$

$$\gamma_{m2} = -0.02\chi^{-2.76} \ln \xi + 1.04\chi^{-0.67} \quad (\text{circular sections}) \quad (56)$$

$$W_{osc} = \frac{\pi(D^4 - d^4)}{32D} \quad (\text{circular sections}) \quad (57)$$

$$W_{si} = \frac{\pi(d^4 - (d - 2t_{si})^4)}{32d} \quad (\text{circular sections}) \quad (58)$$

in which A_{so} , A_c and A_{si} , f_{syo} , f_c and f_{syi} , E_{so} , E_c and E_{si} , I_{so} , I_c and I_{si} are the cross-section areas, yield stress at 0.2% compressive strength, elasticity modulus, and second moments of area for each material; λ is the slenderness ratio; N_u is evaluated with the ultimate strength equation developed by Han *et al.* [46], $N_{u,Han}$ (Eq. (4)), as f_{osc} , the hollow ratio χ and the confinement factor ξ can be determined with Eqs. (8), (9) and (12); L is the column length; and k is equal to 1.0 to represent pinned boundary conditions.; M_u is the ultimate bending for CFDST beams; W_{osc} and W_{si} are the flexural modulus of the A_{osc} and the inner steel tube, respectively.

2.3.3 Fouché *et al.* [56]

The interaction curve N-M proposed by Fouché *et al.* [56] assumes that both tubes become fully plastic, and the concrete in compression reaches its crushing strength. The method is similar to the one adopted by Bruneau and Marson [64] for CFST columns. Two criteria are considered in the design equations through the stress distributions when the plastic neutral axis (PNA) is located above or across the inner tube. The equations are presented below:

a) If the neutral axis is located above the inner tube:

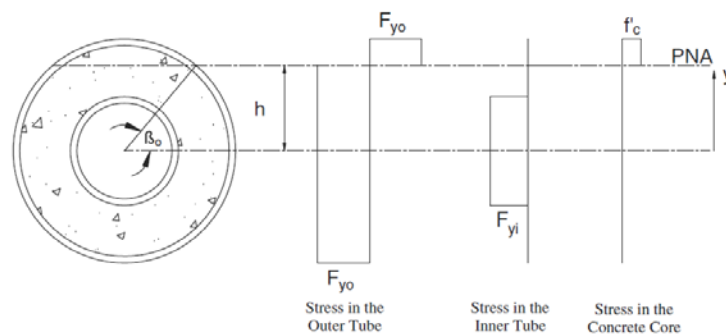


Figure 29 - Stress distributions with neutral axis located above the inner tube, Fouché *et al.* [56].

$$N_{o,c} = (\pi - 2\beta_o)Rt_{so}f_{syo} \quad (\text{outer tube compressive resultant}) \quad (59)$$

$$N_{c,c} = \left[\left(\frac{\pi}{2} - \beta_o \right) R^2 - \frac{1}{2} R^2 \sin 2\beta_o \right] f_c \quad (\text{concrete compressive resultant}) \quad (60)$$

$$N_{i,t} = 2\pi r t_{si} f_{syi} \quad (\text{inner tube tensile force resultant}) \quad (61)$$

$$N_{o,t} = (\pi + 2\beta_o)Rt_{so}f_{syo} \quad (\text{outer tube tensile resultant}) \quad (62)$$

$$y_{o,c} = \frac{2R \cos \beta_o}{(\pi - 2\beta_o)} \quad (\text{outer tube compressive resultant application point}) \quad (63)$$

$$y_{c,c} = \frac{2R}{3} \frac{\cos^3 \beta_o}{\left(\frac{\pi}{2} - \beta_o \right) - \frac{1}{2} \sin 2\beta_o} \quad (\text{concrete compressive resultant application point}) \quad (64)$$

$$y_{i,t} = 0 \quad (\text{inner tube tensile resultant application point}) \quad (65)$$

$$y_{o,t} = \frac{2R \cos \beta_o}{(\pi + 2\beta_o)} \quad (\text{outer tube tensile resultant application point}) \quad (66)$$

$$N_{u,Fouché1} = (N_{o,c} + N_{c,c}) - (N_{i,t} + N_{o,t})$$

$$N_{u,Fouché1} = \left(\frac{\pi}{2} - \beta_o - \frac{1}{2} \sin 2\beta_o \right) R^2 f_c - 4\beta_o R t_{so} f_{syo} - 2\pi r t_{si} f_{syi} \quad (67)$$

$$M_{u,Fouché1} = N_{o,c} y_{o,c} + N_{c,c} y_{c,c} + N_{i,t} y_{i,t} + N_{o,t} y_{o,t}$$

$$M_{u,Fouché1} = \frac{2}{3} R^3 \cos^3 \beta_o f_c - 4R^2 \cos \beta_o t_{so} f_{syo} \quad (68)$$

$$\beta_o = \frac{\pi R^2 f_c - 4\pi r t_{si} f_{syi}}{8R t_{so} f_{syo} + 4R^2 f_c} \quad (69)$$

$$h = R \sin \beta_o \quad (70)$$

b) If the neutral axis is located across the inner tube:

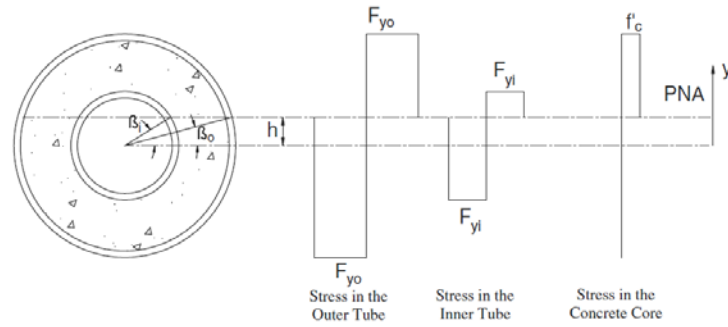


Figure 30 - Stress distributions with the neutral axis located across the inner tube, Fouché *et al.* [56].

$$N_{o,c} = (\pi - 2\beta_o)Rt_{so}f_{syo} \quad (\text{outer tube compressive resultant}) \quad (71)$$

$$N_{i,c} = (\pi - 2\beta_i)rt_{si}f_{syi} \quad (\text{outer tube compressive resultant}) \quad (72)$$

$$N_{c,c} = \left[\left(\frac{\pi}{2} - \beta_o \right) R^2 - \left(\frac{\pi}{2} - \beta_i \right) r^2 - \frac{1}{2} R^2 \sin 2\beta_o + \frac{1}{2} r^2 \sin 2\beta_i \right] f_c \quad (73)$$

(concrete compressive resultant)

$$N_{o,t} = (\pi + 2\beta_o)Rt_{so}f_{syo} \quad (\text{outer tube tensile resultant}) \quad (74)$$

$$N_{i,t} = (\pi + 2\beta_i)rt_{si}f_{syi} \quad (\text{inner tube tensile resultant}) \quad (75)$$

$$y_{o,c} = \frac{2R \cos \beta_o}{(\pi - 2\beta_o)} \quad (\text{outer tube compressive resultant application point}) \quad (76)$$

$$y_{i,c} = \frac{2r \cos \beta_i}{(\pi - 2\beta_i)} \quad (\text{inner tube compressive resultant application point}) \quad (77)$$

$$y_{c,c} = \frac{2}{3} \frac{R^3 \cos^3 \beta_o - r^3 \cos^3 \beta_i}{R^2 \left[\frac{\pi}{2} - \beta_o - \frac{\sin 2\beta_o}{2} \right] - r^2 \left[\frac{\pi}{2} - \beta_i - \frac{\sin 2\beta_i}{2} \right]} \quad (\text{concrete compressive resultant application point}) \quad (78)$$

$$y_{o,t} = \frac{2R \cos \beta_o}{(\pi + 2\beta_o)} \quad (\text{tensile resultant on or above outer tube application point}) \quad (79)$$

$$y_{i,t} = \frac{2r \cos \beta_i}{(\pi + 2\beta_i)} \quad (\text{tensile resultant on or above the inner tube application point}) \quad (80)$$

$$N_{u,Fouché2} = (N_{o,c} + N_{i,c} + N_{c,c}) - (N_{i,t} + N_{o,t}) \quad (81)$$

$$\begin{aligned}
N_{u,Fouché2} &= \left[\left(\frac{\pi}{2} - \beta_o - \frac{1}{2} \sin 2\beta_o \right) R^2 - \left(\frac{\pi}{2} - \beta_i - \frac{1}{2} \sin 2\beta_i \right) r^2 \right] f_c \\
&\quad - 4\beta_o R t_{so} f_{sy_o} - 4\beta_i r t_{si} f_{sy_i} \\
M_{u,Fouché2} &= N_{o,c} y_{o,c} + N_{i,c} y_{i,c} + N_{c,c} y_{c,c} + N_{i,t} y_{i,t} + N_{o,t} y_{o,t} \\
M_{u,Fouché2} &= \frac{2}{3} (R^3 \cos^3 \beta_o - r^3 \cos^3 \beta_i) f_c \\
&\quad + 4(R^2 \cos \beta_o t_{so} f_{sy_o} + r^2 \cos \beta_i t_{si} f_{sy_i})
\end{aligned} \tag{82}$$

$$\beta_o = \frac{\pi(R^2 - r^2)f_c}{4R[2(t_{so}f_{sy_o} + t_{si}f_{sy_i}) + (R - r)f_c]} \tag{83}$$

$$\beta_i = \frac{\pi(R^2 - r^2)f_c}{4r[2(t_{so}f_{sy_o} + t_{si}f_{sy_i}) + (R - r)f_c]} \tag{84}$$

$$h = R \sin \beta_o = r \sin \beta_i \tag{85}$$

where R and r are the outer and inner tube's radius; f_{sy_o} , f_c , and f_{sy_i} the yield stress at 0.2% and compressive strength for each material; β_o and β_i are the angles whose area corresponds to the equivalent stress distribution; and h is the plastic neutral axis location.

2.3.4 Eurocode 4 (EC4) [18]

The equation adopted in Eurocode 4 (EC4) [18] to estimate the CFDST columns ultimate capacity for eccentric loads is the same already presented as Eq. (22). It is interesting to observe that the interaction curve, illustrated in Figure 31, is replaced by a polygonal diagram with points A, B, C and D. In this curve, point A is associated with pure compression, point B to pure bending. Point C represents the force corresponding to $N_{pm,Rd}$ equal to concrete resistance parcel. Finally, point D is associated with the maximum bending capacity. The interaction curve is calculated, assuming a rectangular stress block distribution while neglecting the concrete tensile strength. For concrete fully and partially encased, the $N_{pm,Rd}$ should be taken as $0.85A_c f_c$ and $A_c f_c$ for concrete-filled sections. The equations for concrete-filled sections are presented below:

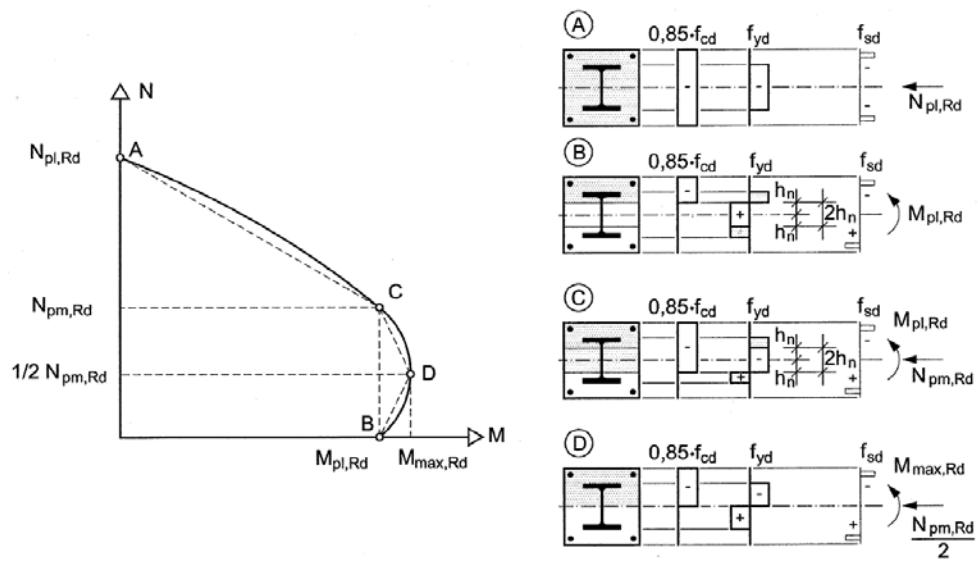


Figure 31 - Eurocode 4 (EC4) [18] CFST columns simplified interaction curve and stress distributions.

a) Point A - Pure compression:

$$N_A = N_{pl,Rd} = A_{so}f_{sy0} + A_c f_c + A_{si}f_{syi} \quad (86)$$

$$M_A = 0 \quad (87)$$

b) Point B - Pure bending:

$$N_B = 0 \quad (88)$$

$$M_B = M_{pl,Rd} \quad (89)$$

c) Point C - flexural resistance in only one plane and compression resistance equal to concrete resistance parcel:

$$N_C = N_{pm,Rd} = A_c \times f_c \quad (90)$$

$$M_C = M_B = M_{pl,Rd} \quad (91)$$

d) Point D - maximum bending capacity and compression resistance equal to half of the concrete resistance parcel:

$$N_D = \frac{1}{2} N_{pm,Rd} = \frac{1}{2} A_c \times f_c \quad (92)$$

$$M_D = W_{so} \times f_{syo} + W_c \times f_c + W_{si} \times f_{syi} \quad (93)$$

where A_{so} , A_c and A_{si} , f_{syo} , f_c and f_{syi} , W_{so} , W_c and W_{si} are the cross-section areas, yield stress at 0.2% compressive strength and the flexural modulus of the outer steel tube, concrete and inner steel tube, respectively.

3 EXPERIMENTAL PROGRAMME

3.1 Generalities

The experimental investigation in RAC CFDST stub columns subjected to concentric load and the descriptions from the literature used to calibrate the developed numerical model are presented in this chapter. The experimental programme comprised four tests on circular CFDST stub columns and was conducted at the Civil Engineering Laboratory of the State University of Rio de Janeiro (UERJ). The tests' main objectives were to examine the cross-section plastic resistance behaviour and assess the influence of RAC rather than conventional concrete for the infill. The columns comprise an outer tube made from grade 1.4307 austenitic stainless steel and an inner tube in grade VMB300 hot-rolled carbon steel. The cross-sections dimensions are presented in Table 1, including the diameters of the outer (D) and inner (d) tubular sections, their respective thicknesses, t_{so} and t_{si} , and the overall length L . Furthermore, four tests on natural aggregate concrete (NAC) circular CFDST stub columns from a previous experimental investigation [65] are also presented in this section of the thesis (NAC1-NAC4), aiming to compare the NAC CFDST stub columns with the four samples (RAC1-RAC4) with recycled aggregate concrete (RAC). By varying the inner tube's diameter, two hollow ratios χ equal to either 0.55 or 0.67 were considered, where χ is determined from Eq. (9).

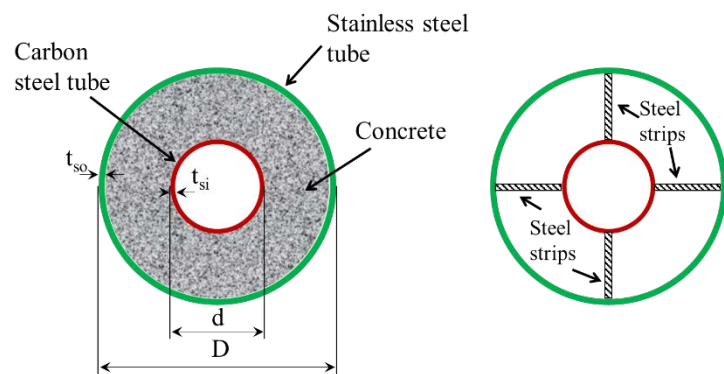
This expression was introduced by Han *et al.* [46], where its scope was established for CFDST circular stub column hollow ratios ranging between 0.5 and 0.7. The stub column lengths were approximately equal to three times the outer tube diameter. This recommendation is in line with Han *et al.* [46], to prevent global buckling failures. A cross-section view is illustrated in Figure 32 a). Small steel strips with a diameter of 5.5 mm were welded to the inner steel tube as shown in Figure 32 b) to maintain concentricity during concrete casting, as recommended by Wang *et al.* [9].

Table 1 - Stub column specimens' geometry and results.

Specimen	L (mm)	D (mm)	t_{so} (mm)	d (mm)	t_{si} (mm)	$N_{u,test}$ (kN)	$\delta_{u,test}$ (mm)
NAC1	550.0	168.3	2.8	88.9	5.5	1941	16
NAC2						1865	20
NAC3				108.4	4.5	1649	16
NAC4						1612	15
RAC1	500.0			88.9	5.5	2087	21
RAC2						2075	21
RAC3				108.4	4.5	1685	12
RAC4						1693	12



a) Top view;



b) Schematic view.

Figure 32 - CFDST cross-sections before casting.

3.2 Concrete

The RAC specimens were designed to be class 30/37, with a minimum compressive strength f_c of 30 MPa. The NAC specimens of the preview experimental investigation and the RAC specimens were cast in two series using the same concrete mix proportions, which is presented in Table 2. The first series contained natural coarse aggregate (NCA) [65]. Alternatively, the second series had 50% of the NCA replaced with the same amount of recycled coarse aggregate (RCA). A superplasticiser was included in both series to improve the concrete

more workability. The quantity was selected as 0.15% of the cement weight. The NAC and RAC reached mean compressive cylinder strengths f_c of 30 and 33 MPa, respectively. These were determined by conducting compressive tests on at least eight cylindrical samples (Table 3) from each batch of concrete on the same day that the corresponding columns were tested. The concrete compressive test was performed 40 days after casting for the NAC columns and 30 days after casting for the RAC specimens.

Table 2 - Concrete mix proportion details.

Mix proportions (to the weight of cement)	NAC	RAC
Cement	1.00	
Sand	2.29	
NA	1.58	0.79
RA	0	0.79
Water/cement ratio	0.43	0.46
Superplasticizer	0.0015	

Table 3 - Concrete compressive strength (after 28 days).

Specimens	Compressive strength (MPa)	
	NAC	RAC
1	30	29
2	28	35
3	30	36
4	28	30
5	29	-
6	31	-
7	31	-
8	32	-
Mean	30	33

Standard Deviation	1.458	3.368
CoV	0.049	0.103

The recycled coarse aggregate (RCA) was manufactured through the crushing of concrete elements from a previous experimental campaign [66], as shown in Figure 33, which had a mean compressive cylinder strength of 41 MPa. The characteristic properties and the granulometry analysis of the concrete's aggregates were determined before casting following the relevant Brazilian standards [67], [68], [69] and [70], Table 4 to Table 7. It is noteworthy that the recycled coarse aggregates (RCA) had a significantly greater water absorption capacity when compared with the natural coarse aggregates, as expected. Following the recommendations of other researchers who have worked with RAC [71], the recycled coarse aggregates (RCA) were treated before casting by first sieving to ensure that the particles were the same size as the natural coarse aggregates (NCA). Afterwards, water was added just before casting in the saturated condition to compensate for the higher water absorption properties. The compressive strength of the RAC was higher than for the NAC, most likely due to this treatment. It was also possible that the original material's quality also positively affected the compressive strength of the RAC [71].

Table 4 - Fine aggregate grain composition.

Sieve (mm)	Retained material (%)		Gathered retained (%)
	specimen 1	specimen 2	mean
9.52	0.0	0.0	0.0
6.30	0.2	0.2	0.2
4.75	0.3	0.4	0.6
2.36	4.6	5.5	5.6
1.18	17.1	20.7	24.5
0.60	35.7	36.1	60.4
0.30	28.8	26.1	87.9
0.15	10.2	8.9	97.4
Bottom	2.8	2.2	99.8
Fineness modulus			2.8
Maximum dimension			6.3 mm

Table 5 - Natural coarse aggregate (NCA) grain composition.

Sieve (mm)	Retained material (%)		Gathered retained (%)
	specimen 1	specimen 2	mean
12.5	0.0	0.0	0.0
9.52	11.4	11.5	11.5
6.30	41.1	39.4	51.7
4.75	21.6	22.5	73.7
2.36	15.7	14.7	89.0
1.18	2.7	3.0	91.8
0.60	2.7	3.2	94.8
0.30	2.00	2.7	97.1
0.15	1.1	1.4	98.4
Bottom	1.4	1.6	99.9
Fineness modulus			5.6
Maximum dimension			9.5 mm

Table 6 - Recycled coarse aggregate (RCA) grain composition.

Sieve (mm)	Retained material (%)		Gathered retained (%)
	specimen 1	specimen 2	mean
12.5	0.0	0.0	0.0
9.52	11.4	11.5	11.5
6.30	41.1	39.4	51.7
4.75	21.6	22.5	73.7
2.36	15.7	14.7	89.0
1.18	2.7	3.0	91.8
0.60	2.7	3.2	94.8
0.30	2.0	2.7	97.1
0.15	1.1	1.4	98.4
Bottom	1.4	1.6	99.9
Fineness modulus			5.6
Maximum dimension			9.5 mm

Table 7 - Characteristics of the coarse aggregates.

Property	NCA	RCA
Fineness modulus (%)	5.6	
Maximum diameter (mm)	9.5	
Bulk density (kg/m ³)	1370	1090
Pore volume (%)	49.6	59.6
Specific gravity (kg/m ³)	2710	2700
Water absorption (%)	1.4	11.9



Figure 33 - View of the crushed concrete to make the RCA.

3.3 Tubular sections

The steelwork industry measured the mechanical properties of the carbon steel inner tubes. The steel was found to have Young's modulus E of 200000 MPa, yield stress f_y of 375 MPa, ultimate stress f_u of 474 MPa and ultimate strain ϵ_u of 34%. The austenitic stainless steel outer tubes' mechanical properties were obtained through tensile coupon testing at the State University of Rio de Janeiro (UERJ). A total of four repeat tests were conducted (Figure 34), following EN 10002-1 [72] and the testing procedure for curved coupons given by Huang and

Young [73]. The results are depicted in Figure 35 and Table 8, in which $f_{0.2}$ is the 0.2% proof stress of the stainless steel, and ϵ_f is the fracture strain measured over a gauge length of 50 mm.

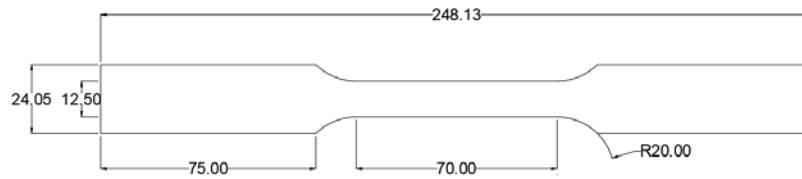


Figure 34 - Steel coupons geometry (mm).

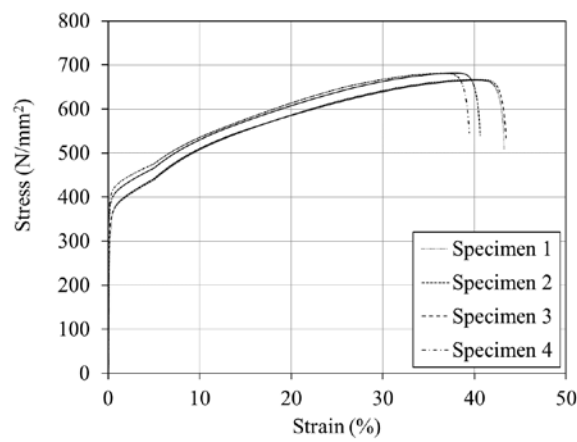


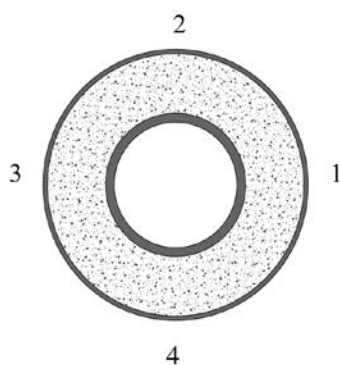
Figure 35 - Stress *versus* strain of the four tensile specimens for the outer stainless steel tube.

Table 8 - Mechanical properties of the grade 1.4307 stainless steel.

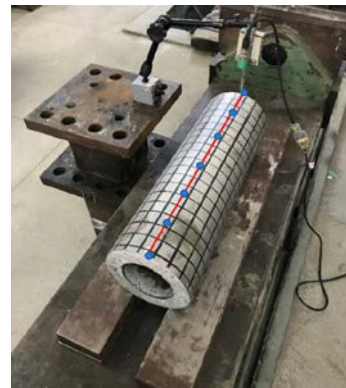
Specimen	E (MPa)	$f_{0.2}$ (MPa)	f_u (MPa)	ϵ_f (%)
1	171000	405	666	58
2	152000	428	682	60
3	165000	401	667	58
4	187000	443	681	61
Mean	167000	419	674	59
Standard Deviation	14.35	19.73	8.79	1.49
CoV	0.085	0.047	0.013	0.025

3.4 Imperfections

Geometric imperfections are typically introduced into metallic sections during the manufacturing process and can reduce the members' capacity. It has been recommended that geometric imperfections account for analytical studies as a function of the steel tube thickness, with a typical suggested value of thickness divided by 10 (i.e. $t_{so}/10$) [74]. In the current test programme, the stainless steel tubes geometric imperfections were measured using a displacement transducer according to the procedure outlined by Luquin [75]. The circular cross-sections were divided into four quadrants, as shown in Figure 36 a). Seven points along the column's length in each quadrant were measured as indicated in Figure 36 b); the results are finally presented in Figure 37. In all cases, the measured imperfections were less than the tube's thickness divided by 10 ($t_{so}/10 = 0.28$ mm), values usually adopted in cold-formed thin-walled stub columns numerical models.

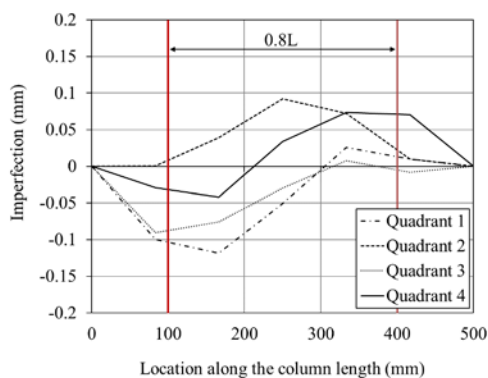


a) Quadrant locations;

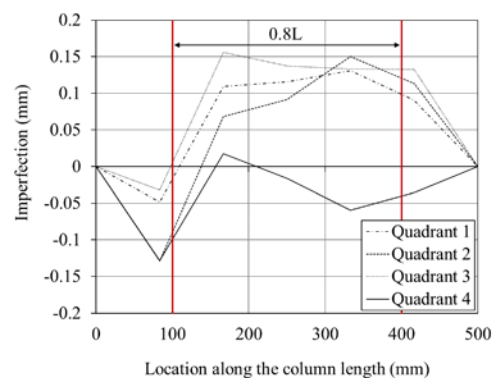


b) Measurement's locations along the column length.

Figure 36 - Geometric imperfection measurement.



a) 108.4×4.5 mm tube - RAC1 and RAC2;

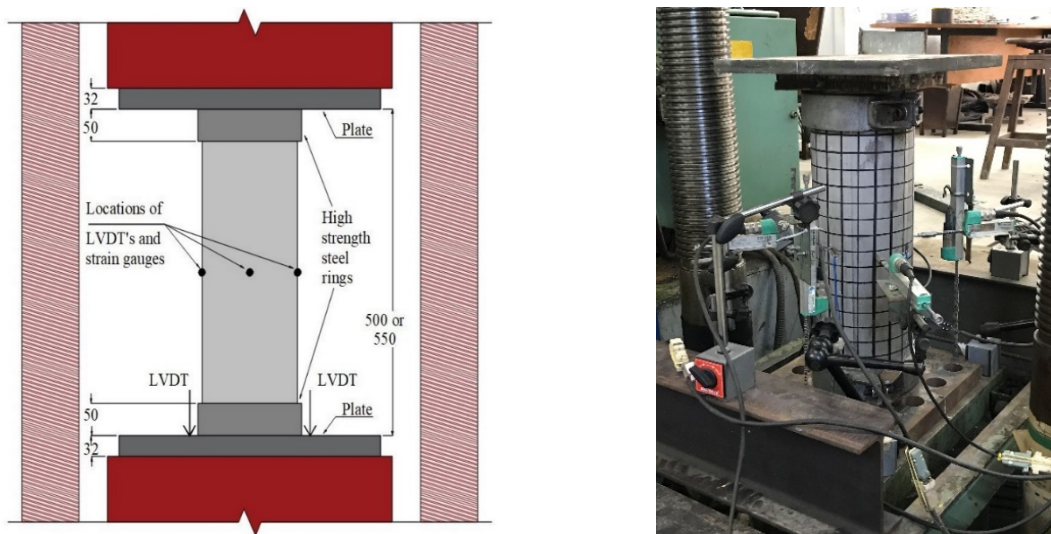


b) 88.9×5.5 mm tube - RAC3 and RAC4.

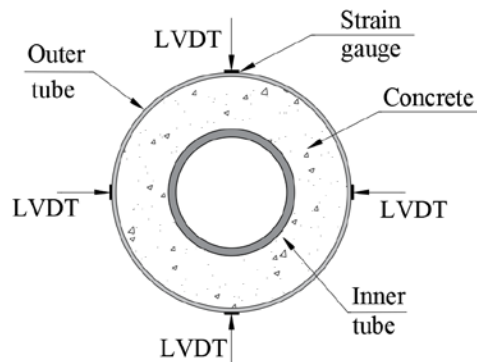
Figure 37 - Measured geometric imperfections along the stainless steel tubular column length.

3.5 Test setup and procedure

The tests were conducted using a 3000 kN displacement-controlled universal testing machine. The columns were carefully positioned to avoid eccentricities, and after that, an axial load was then applied in terms of an equivalent displacement at a rate of 0.003 mm/s. Two plates with a thickness of 32 mm were positioned at the column ends. The bottom end of the columns had fixed boundary conditions. The top-end had a ball seating that locked upon the load application, also providing fixed support. A circular ring made from high strength steel was placed close to the column ends to avoid the “elephant foot” buckling mode recommended by previous investigations [9]. The tests instrumentation included four displacement transducers (LVDTs) and four axial strain gauges at the columns mid-height to acquire the lateral displacements and strains. Two additional LVDTs were utilized at the bottom plate to monitor the longitudinal displacement, as shown in Figure 38.



a) Test geometry (all dimensions are in mm);



b) Cross-section instrumentation.

Figure 38 - Test layout and instrumentation.

3.6 Results

The CFDST stub columns compressive response was observed during the tests. The ultimate loads ($N_{u,test}$) are presented in Table 1, together with their corresponding axial displacement $\delta_{u,test}$ at $N_{u,test}$. It is clear that the columns with the smaller inner tubes and therefore larger volumes of concrete infill (i.e. NAC1, NAC2, RAC1 and RAC2) presented, as expected, higher ultimate load-carrying capacities compared with the columns with larger inner tubes and smaller concrete volumes (i.e. NAC3, NAC4, RAC3 and RAC4).

In terms of the aggregate type, the columns with RAC generally achieved higher loads than the equivalent members with NAC, reflecting the higher strength of the RAC. Figure 39 presents the CFDST stub columns' deformed configurations after testing, showing the outward-only local buckling of the outer tubes, typically near the middle of the columns' length and then propagating towards the column ends. This was accompanied by a visible concrete shear failure. In Figure 40, an inward-only local buckling of the inner tube for specimen RAC1 was observed. The presence of the infill concrete prevented the steel tubes from buckling locally in both directions. Similar failure modes were observed in all eight specimens.



NAC4 NAC2 NAC3 NAC1 RAC2 RAC1 RAC4 RAC3

a) NAC infill;

b) RAC infill.

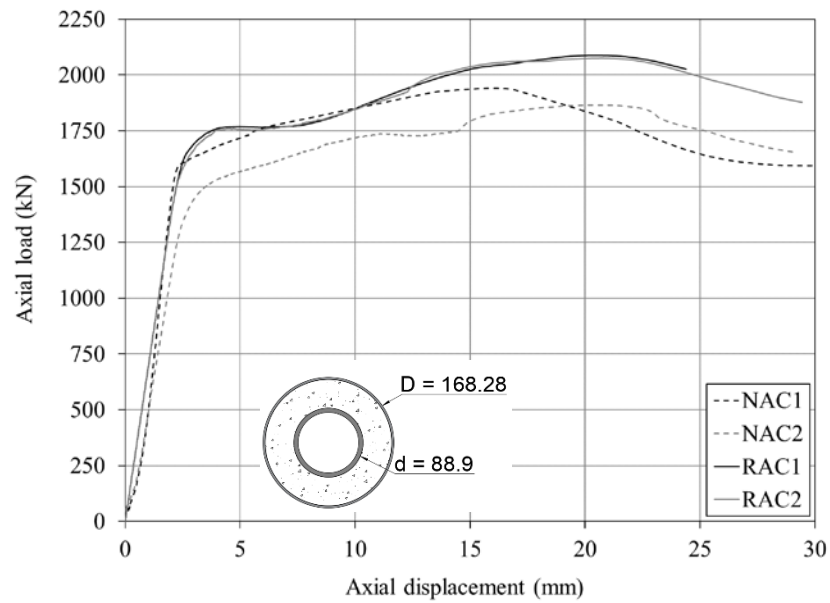
Figure 39 - Deformed specimens after testing showing outward-only local buckling of the outer stainless steel tube.



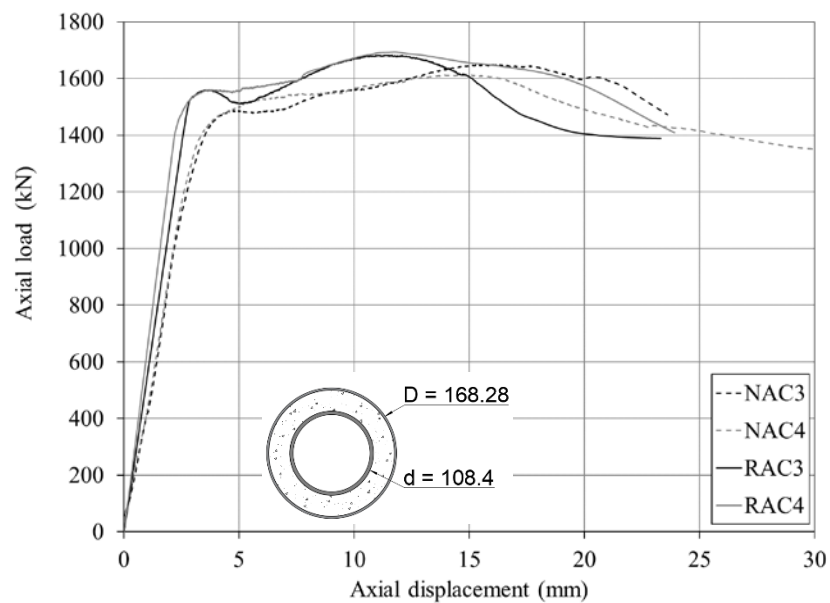
Figure 40 - Specimen RAC1 after testing showing an inward-only local buckling of the carbon steel inner tube.

Figure 41 presents the experimental results in terms of axial load *versus* axial displacement curves for all CFDST stub column tests. The axial displacements were monitored with two LVDTs positioned at the bottom plate, as previously mentioned, but only the mean value is here presented. The data from specimens NAC1, NAC2, RAC1 and RAC2 (i.e. those with the smaller inner steel tubes) are shown in Figure 41 a), while the remaining columns' results are depicted in Figure 41 b). Key observations from these figures, as well as the ultimate load ($N_{u,test}$) and deflection $\delta_{u,test}$ data presented in Table 1, can be summarised as follows:

- irrespective of the concrete type, the specimens behaved similarly, with very comparable load-displacement responses;
- for all specimens, the load-displacement behaviour was linear until reaching the first load peak. The RAC columns had a slightly stiffer response in the elastic range in all cases; it is noteworthy that the RAC compressive strength was stronger than their NAC counterparts;
- following the attainment of the peak load, the RAC columns exhibited a slight reduction in load-carrying capacity, which was not evident for the NAC columns, most likely due to a change in the effective Young's modulus induced by the concrete crushing;
- all columns, irrespective of the concrete type, displayed reasonable ductility with some increase in the load-carrying capacity in the plastic range before the failure;
- in general, the CFDST columns with larger volumes of concrete (Figure 41 a)) had higher load-carrying capacities, as expected, as well as presented more ductility, when compared with those with less concrete, as indicated by the $\delta_{u,test}$ values in Table 1.



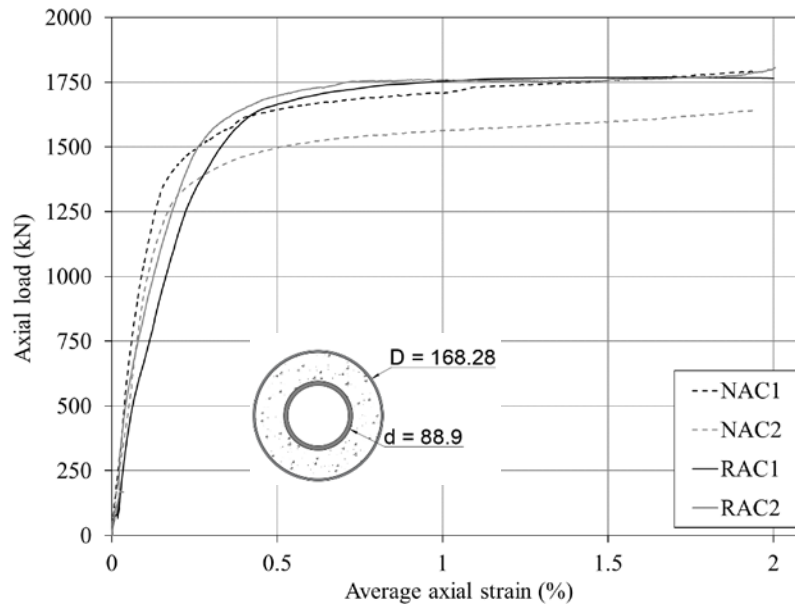
a) Inner tube 88.9 mm diameter;



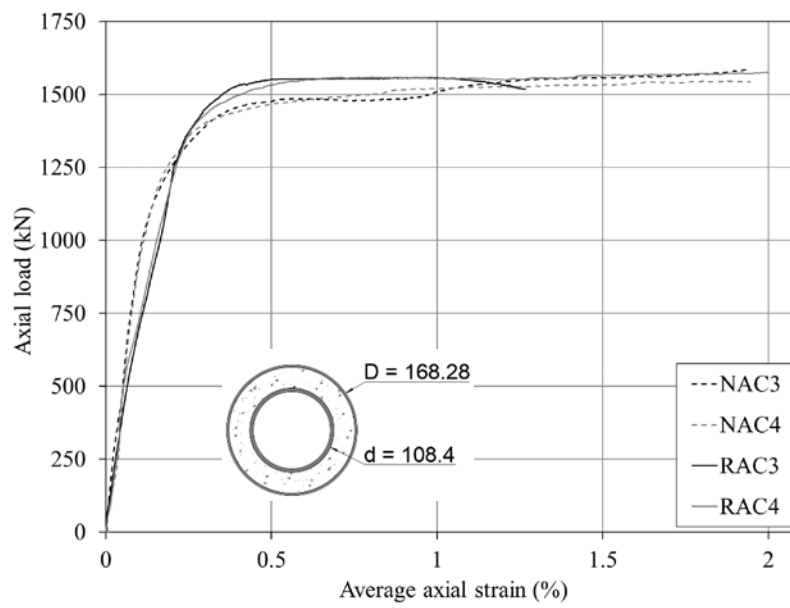
b) Inner tube 108.4 mm diameter.

Figure 41 - Axial load *versus* axial displacement curves for the CFDST columns.

Figure 42 presents the strain data in terms of axial load *versus* axial strain curves for a) the specimens with smaller inner tubes and therefore greater concrete volume and b) those with larger inner tubes. As previously explained, four strain gauges were affixed to each column (one in each of the four quadrants) at the mid-height. The mean longitudinal strains from the four measured values are presented in Figure 42. Strains were measured up to about 2% strain.



a) Inner tube 88.9 mm diameter;



b) Inner tube 108.4 mm diameter.

Figure 42 - CFDST columns axial load *versus* mean axial strain curves.

3.7 Experiments to further FE model validation

The following experiments from the literature review and the previous experiments developed in this thesis are used to validate the FE models in Chapter 4. They are also used to evaluate the existing design methods and to develop the guideline in Chapter 6. CFST RAC columns experiments from Azevedo [39] were not used in the FE validation and are detailed in this chapter only to emphasize the use of RAC in structural elements.

The experiments adopted from the literature to validate the FE model with concentric load were Wang *et al.* [48] and Han *et al.* [46]. The experiments adopted from the literature to validate the FE model with eccentric load were Tao *et al.* [5], Li *et al.* [77], Ibañez *et al.* [87] and Zhao *et al.* [88]. Li *et al.* [77] was the only experiment found in the literature to validate the FE model with a pure bending response.

3.7.1 Concentric load - Azevedo [39]

Azevedo [39] studied the behaviour of concrete-filled circular stub columns with cold-formed carbon steel tubes and recycled coarse aggregate concrete. A total of 27 tests were performed, 4 with only carbon steel columns and 23 with composite columns. The varied parameters in the experimental analysis were: concrete compressive strength ($f_c = 30$ MPa and 40 MPa); three different values of percentage replacement of recycled coarse aggregate (RCA) in the recycled concrete (0%, 30% and 50%); carbon steel tube diameter (153.0 x 6.56 and 178.0 x 6.56 mm); and carbon steel tube slenderness (D/t_{so}).

The cold-formed carbon steel tubes' mechanical properties were obtained through tensile coupon testing. The results are presented for both diameters in Table 9 and Table 10. The recycled coarse aggregate (RCA) was manufactured through the crushing of concrete elements from the same previous experimental campaign [66] already cited in this chapter, with a mean compressive cylinder strength of 41 MPa. Before casting, the RA was treated by first sieving to keep it the same size as the natural coarse aggregates (NCA). Next, water was added to the RCA before casting. The specimens and the concrete mix details are summarized in Table 11.

Figure 43 presents the typical failure mode for CFST stub columns, with a cross-section plastic resistance followed by local buckling (“elephant's foot”) close to the supports and the

column's mid-length. Similar behaviour was observed during loading until the columns reached their ultimate loads. From this point on, the infilled concrete begins to control the composite column's behaviour and the deformation direction, redistributing the steel and concrete materials' internal forces. In terms of comparison between NAC and RAC, it was possible to observe that the CFST columns with RAC presented higher and/or equal load capacity than those CFST columns with NAC. However, they presented less ductility, probably due to the RAC's larger cracking distribution (Figure 44). The columns' ultimate load was not considerably changed regarding the replacement percentage of RCA (30% and 50%). The load capacity of the CFST columns for RAC and NAC are presented in Table 12.

A longitudinal cut of the CFST columns with RAC is presented in Figure 45. The cut presents the outer tube of carbon steel deformation, following the deformation of the recycled concrete. The concrete is retained in the steel tube where local buckling occurred due partially to the adhesion between both materials. The presence of the weld along the cold-formed carbon steel tubes could also be observed to remain intact during the test, ratifying that it did not compromise the load-carrying capacities of the CFST stub columns.

Table 9 - Mechanical properties of the carbon steel with diameter of 153 mm [39].

D (mm)	E (MPa)	f_y (MPa)	f_u (MPa)	ϵ_y (mm/mm)	ϵ_u (mm/mm)
153,	209330	382	461	0.003	0.174
		515	556	0.002	0.114
		380	464	0.003	0.176
Mean		426	494	0.003	0.155
Standard Deviation		77.37	54.00	0.001	0.035
CoV		0.182	0.109	0.217	0.228

Table 10 - Mechanical properties of the carbon steel with diameter of 178 mm [39].

D (mm)	E (MPa)	f_y (MPa)	f_u (MPa)	ϵ_y (mm/mm)	ϵ_u (mm/mm)
178	209560	512	570	0.002	0.119
		403	471	0.003	0.184
		405	473	0.003	0.188
Mean		440	505	0.003	0.164
Standard Deviation		62.36	56.59	0.001	0.039
CoV		0.142	0.112	0.217	0.237

Figure 43 presents the typical failure mode for CFST stub columns, with a cross-section plastic resistance followed by local buckling (“elephant's foot”) close to the supports and the column’s mid-length. Similar behaviour was observed during loading until the columns reached their ultimate loads. From this point on, the infilled concrete begins to control the composite column’s behaviour and the deformation direction, redistributing the steel and concrete materials' internal forces. In terms of comparison between NAC and RAC, it was possible to observe that the CFST columns with RAC presented higher and/or equal load capacity than those CFST columns with NAC. However, they presented less ductility, probably due to the RAC's larger cracking distribution (Figure 44). The columns' ultimate load was not considerably changed regarding the replacement percentage of RCA (30% and 50%). The load capacity of the CFST columns for RAC and NAC are presented in Table 12.

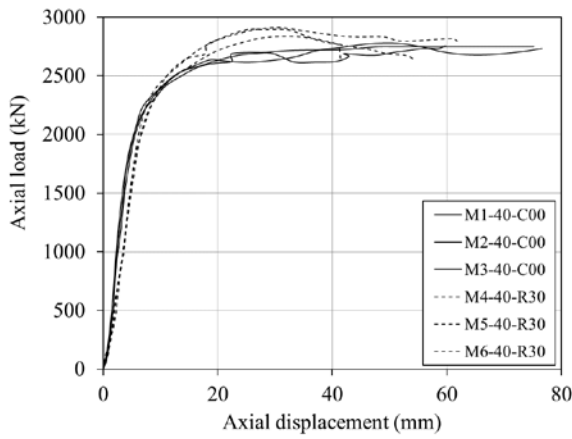
A longitudinal cut of the CFST columns with RAC is presented in Figure 45. The cut presents the outer tube of carbon steel deformation, following the deformation of the recycled concrete. The concrete is retained in the steel tube where local buckling occurred due partially to the adhesion between both materials. The presence of the weld along the cold-formed carbon steel tubes could also be observed to remain intact during the test, ratifying that it did not compromise the load-carrying capacities of the CFST stub columns.

Table 11 - Concrete mix proportion details [39].

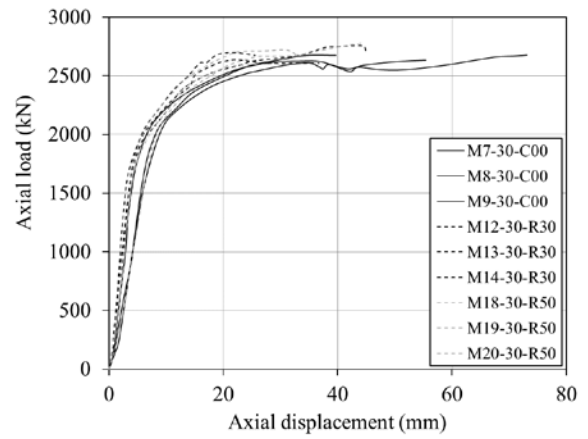
Specimen	D (mm)	Cement (kg)	Sand (kg)	NCA (kg)	RCA (kg)	Water (kg)	Water/cement ratio	Superplasticizer
M1-40-C00	0.057	22.0	49.5	54.0	0.0	10.6	0.48	0.279
M2-40-C00								
M3-40-C00								
M4-40-R30	0.057	22.0	49.5	37.8	16.2	10.6	0.54	0.279
M5-40-R30								
M6-40-R30								
M7-30-C00	0.071	24.5	63.5	66.5	0.0	13.3	0.54	0.314
M8-30-C00								
M9-30-C00								
M10-30-C00								
M11-30-C00								
M12-30-R30	0.079	27.0	70.0	51.3	22.0	14.6	0.54	0.346
M13-30-R30								
M14-30-R30								
M15-30-R30								
M16-30-R30								
M17-30-R30								
M18-30-R50	0.079	27.0	70.0	36.6	36.6	14.6	0.54	0.346
M19-30-R50								
M20-30-R50								
M21-30-R50								
M22-30-R50								
M23-30-R50								



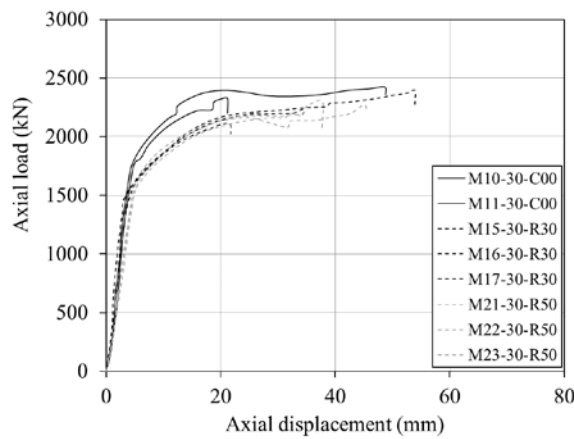
Figure 43 - Typical failure modes of CFST columns with RAC [39].



a) $D = 178 \text{ mm}$ and $f_c = 40 \text{ MPa}$;



b) $D = 178 \text{ mm}$ and $f_c = 30 \text{ MPa}$;



c) $D = 153 \text{ mm}$ and $f_c = 30 \text{ MPa}$.

Figure 44 - Axial load *versus* axial displacement curves [39].

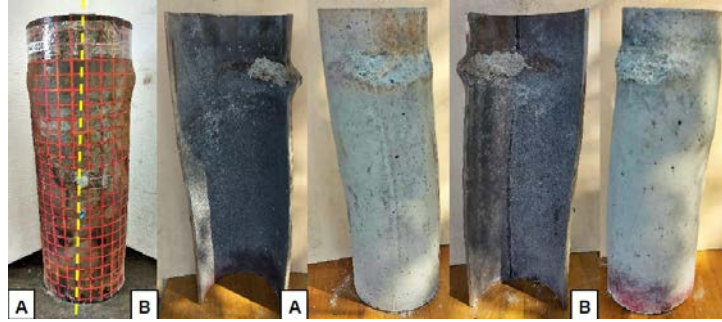


Figure 45 - Longitudinal cut of the CFST stub columns with RAC [39].

Table 12 - CFST column specimens' results [39].

Specimen	D (mm)	f_c (MPa)	RCA replacement (%)	$N_{u,test}$ (kN)	
M1-40-C00	178	40.0	0.0	2003	
M2-40-C00				2051	
M3-40-C00				2600	
M4-40-R30			30.0	2227	
M5-40-R30				2153	
M6-40-R30				2100	
M7-30-C00	153	30.0	0.0	1952	
M8-30-C00				2140	
M9-30-C00				1921	
M10-30-C00			1823		
M11-30-C00			1881		
M12-30-R30			178	30.0	30.0
M13-30-R30	1851				
M14-30-R30	1871				
M15-30-R30	153	50.0	50.0		1650
M16-30-R30					1561
M17-30-R30					1578
M18-30-R50	178		50.0	50.0	1991
M19-30-R50					1952
M20-30-R50					1822
M21-30-R50	153	50.0		50.0	1507
M22-30-R50					1532
M23-30-R50					1543

3.7.2 Concentric load - Wang *et al.* [48]

As aforementioned, the tests from Wang *et al.* [48] were performed on CFDST stub columns with a stainless steel outer tube, high strength carbon steel inner tube and conventional concrete with a compressive strength at 28 days f_c 40 MPa for the infill. The high strength carbon steel inner tubes' material properties were obtained through standard tensile coupon tests are presented in Table 13 and Figure 46. The stainless steel outer tubes material properties were also obtained through standard tensile coupon tests. They were: (a) 140 x 3 mm: Young's modulus E_{syo} 197000 MPa, the yield stress was taken as 0.2%, with a value of f_{syo} 300 MPa, the ultimate stress f_{suo} 705 MPa and the elongation δ_o 62%; (b) 165 x 3 mm: Young's modulus E_{syo} 200000 MPa, the yield stress was taken as 0.2%, with a value of f_{syo} 276 MPa, the ultimate stress f_{suo} 753 MPa and the elongation δ_o 68%. The steel tubes dimensions, material properties of the inner steel tubes and the experimental results $N_{u,test}$ are presented in Table 13.

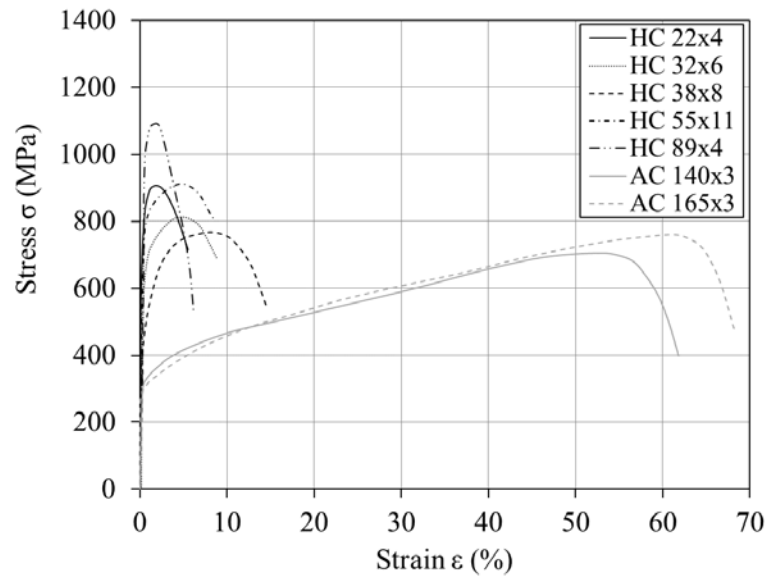


Figure 46 - Stress *versus* strain curves from tensile tests [48].

Figure 47 presents the deformed shape and failure modes for a general view of a CFDST column after the test. Figure 47 a) presents the outer steel tube outward local buckling due to the presence of the infilled concrete, which avoid its inward local buckling. Figure 47 b) and c) shows the failure mode of two different inner tubes dimensions, HC 55x11 and HC 89x4, respectively, where the thicker inner steel tube did not exhibit local buckling. The different

failure modes behaviour occurs due to the inner steel tubes slenderness. Concrete crushing was found in the same region where local buckling occurred in the outer steel tube. Probably, the concrete crushing initiated the CFDST column's failure, followed by the steel tube's local buckling.

Table 13 - Geometric details and experimental ultimate loads [48].

CFDST column	D (mm)	t_{so} (mm)	d (mm)	t_{si} (mm)	L (mm)	f_{syi} (MPa)	f_{syui} (MPa)	E_{syi} (GPa)	δ_i (%)	$N_{u, test}$ (kN)
AC140×3-HC22×4	140	3	22	4	350	794	901	197	5	1410
AC140×3-HC32×6	140	3	32	6	350	619	811	208	9	1423
AC140×3-HC38×8	140	3	38	8	350	433	765	197	15	1626
AC140×3-HC55×11	140	3	55	11	350	739	941	211	9	2543
AC140×3-HC89×4	140	3	89	4	350	1029	1093	209	6	2025
AC165×3-HC22×4	165	3	22	4	413	794	901	197	5	1750
AC165×3-HC32×6	165	3	32	6	413	619	811	208	9	1943
AC165×3-HC89×4	165	3	89	4	413	1029	1093	209	6	2375

Figure 48 presents the axial load *versus* mean axial strain (axial displacement divided by the total length) of the column responses obtained experimentally. It is noteworthy that for some CFDST columns, the peak load could not be found even for higher loads and plastic strains values. In these situations, the ultimate load was determined as the load at which the slope of the load *versus* axial displacement response reaches 1% of its initial stiffness, as proposed by dos Santos *et al.* [84].

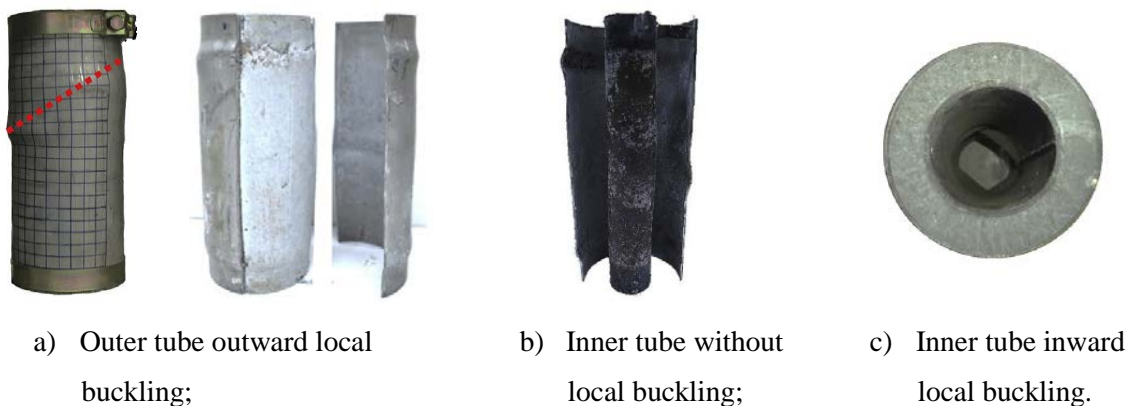
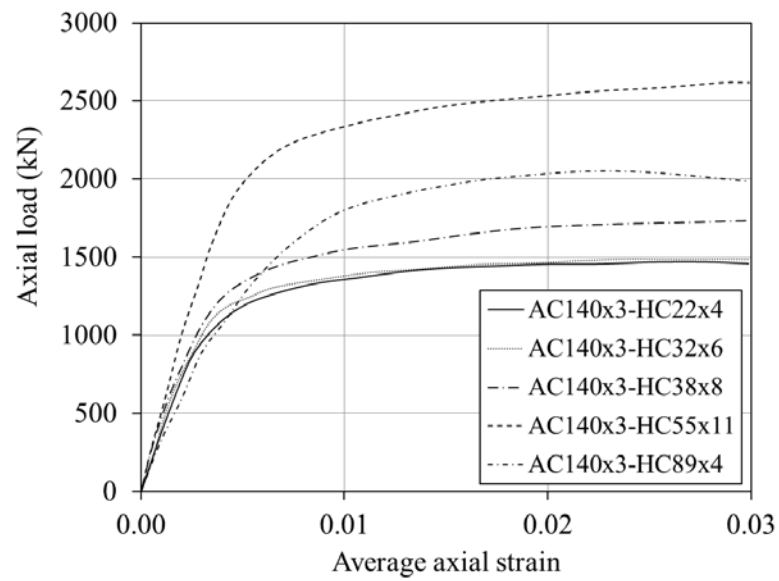
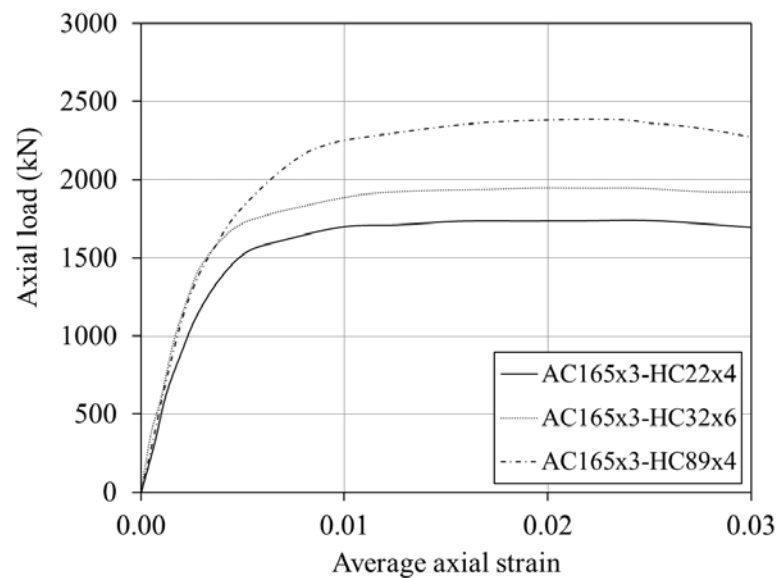


Figure 47 - Failure modes [48].



a) Outer diameter $D = 140$ mm;



b) Outer diameter $D = 165$ mm.

Figure 48 - Axial load *versus* mean axial strain for the CF DST columns [48].

3.7.3 Concentric load - Han *et al.* [46]

As previously discussed, the tests from Han *et al.* [46] adopted a stainless steel outer tube, carbon steel inner tube and conventional concrete with a compressive strength at the time of the test of f_c 52 MPa for the infill. The Young's modulus E_c of the conventional concrete was informed on the reference, with an experimental value of 33000 MPa. All the CF DST columns

had a length of 660 mm. The material properties of both steel tubes were obtained through standard tensile coupon tests. The inner carbon steel tube properties were: Young's modulus $E_{s_{yi}}$ 192000 MPa, the yield stress was taken as 0.2%, with a value of $f_{s_{yi}}$ 381 MPa, the ultimate stress $f_{s_{ui}}$ 519 MPa and the elongation δ_i 28%. The outer stainless steel tube properties were: Young's modulus of the stainless steel was $E_{s_{yo}}$ 201000 MPa, and the yield stress was taken as 0.2%, with $f_{s_{yo}}$ 320 MPa, the ultimate stress of $f_{s_{uo}}$ 627 MPa and the elongation of δ_o 29%. The steel tubes dimensions and the ultimate loads $N_{u, test}$ are presented in Table 14.

Table 14 - Geometric details and ultimate experimental loads [46].

CFDST column	D (mm)	t_{so} (mm)	d (mm)	t_{si} (mm)	$N_{u, test}$ (kN)
C1-1_220×3.62-159×3.72	220	3.62	159	3.72	2537
C1-2_220×3.62-159×3.72	220	3.62	159	3.72	2566
C2-1_220×3.62-106×3.72	220	3.62	106	3.72	3436
C2-2_220×3.62-106×3.72	220	3.62	106	3.72	3506

Figure 49 presents the failure mode of the CFDST columns. The outward buckling of the outer steel tube was observed close to the middle height and the supports of the CFDST cross-section. The “elephant-foot” shape local buckling was close to the supports on the outer steel tube and the “distorted diamond” failure mode on the inner steel tubes in the inward direction. The concrete crushing was found in the same region where the outward buckling occurred in the outer steel tube. The axial load *versus* axial displacement responses is shown in Figure 50. As the hollow ratio (γ) increase and concrete infilled cross-section decreases, the ultimate load and the stiffness of the CFDST columns decrease. Both cross-sections present a proportional vertical load to vertical displacement during the elastic stage, rising until an accentuated peak load and followed by the curve's fall.

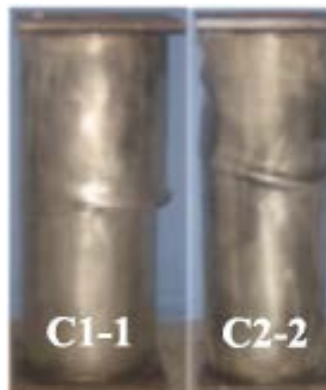
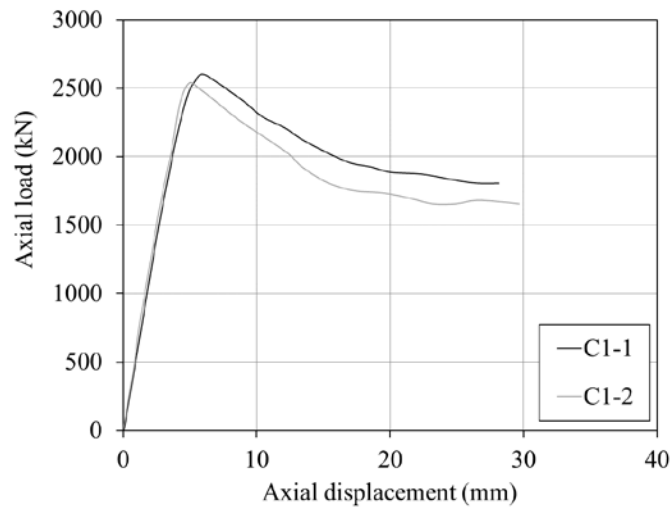
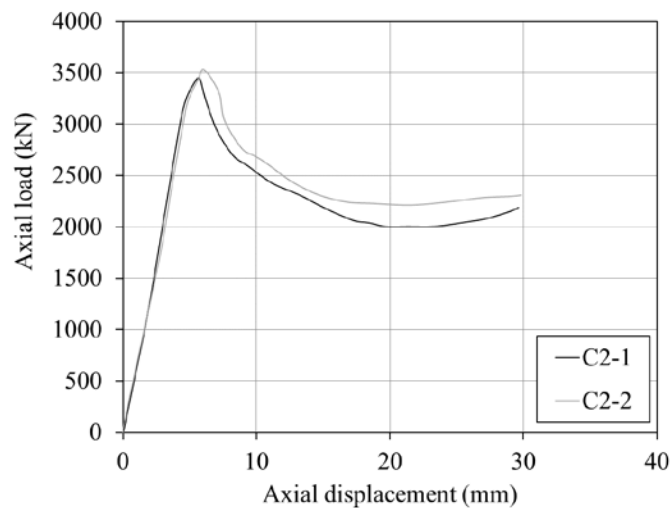


Figure 49 - Failure mode [46].



a) Inner tube diameter $d = 159$ mm ($\chi = 0.75$);



b) Inner tube diameter $d = 106$ mm ($\chi = 0.5$).

Figure 50 - Axial load *versus* axial displacement [46].

3.7.4 Eccentric load - Tao *et al.* [5]

The tests from Tao *et al.* [5] were conducted on CFDST stub columns with cold-formed circular carbon steel in the outer and inner tubes and conventional concrete with a compressive strength at 28 days of f_c 37 MPa for the infill. The Young's modulus E_c of the conventional concrete was 33300 MPa. For the cold-formed circular steel tubes, standard tensile coupon tests were conducted to provide the material properties. The Young's modulus of the steel tubes was considered equal to 200000 MPa, and the yield stress was taken as 0.2%, with f_{syo} of 294.5 MPa for the outer tube and f_{syi} of 374.5 MPa for the inner tube. The steel tubes dimensions,

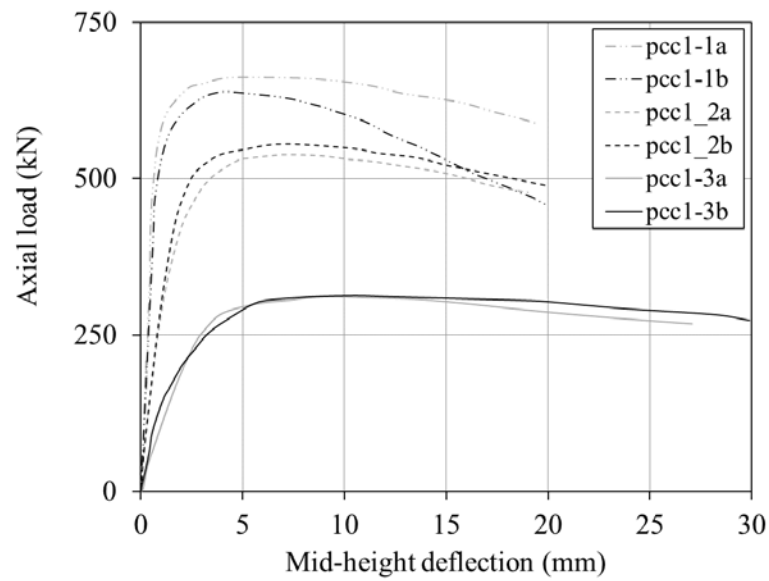
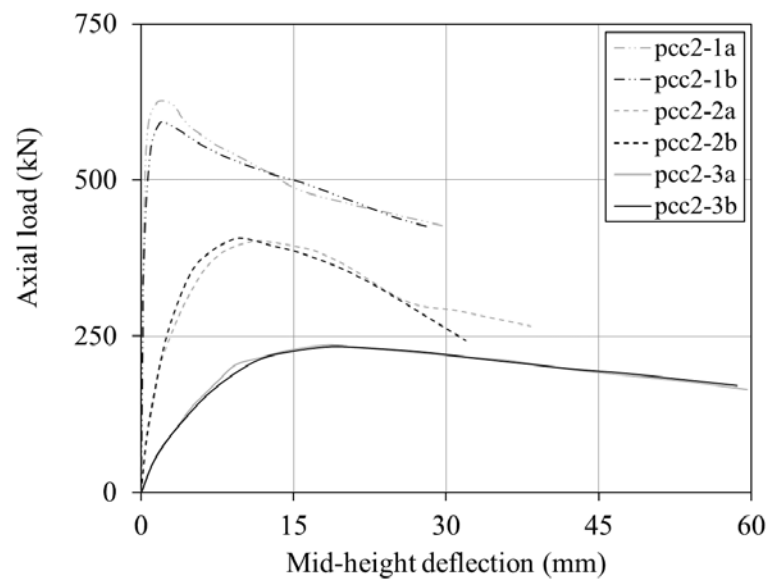
eccentricity and ultimate load $N_{u,test}$ are presented in Table 15. The beam-columns were tested with pin-ended supports and with welded plates with a thickness of 30 mm in the supports. Global buckling was the typical CFDST beam-column failure mode, as showed in Figure 51. Figure 52 presents the axial load *versus* deflection at the column mid-height: a) $L = 887$ mm and b) $L = 1770$ mm, respectively. The ultimate load and flexural stiffness decreased as the slenderness ratio and/or the eccentricity value increased. No local buckling was observed in the beam-columns compression region, and higher eccentricity values showed more ductility. The composite action due to the concrete confinement and the steel tubes provided an overall structural enhancement.

Table 15 - Specimen label, dimensions, eccentricity and ultimate capacities [5].

Specimen	D (mm)	t_{so} (mm)	d (mm)	t_{si} (mm)	L (mm)	e (mm)	$N_{u,test}$ (kN)
pcc1-1a	114	3	58	3	887	4	664
pcc1-1b	114	3	58	3	887	4	638
pcc1-2a	114	3	58	3	887	14	536
pcc1-2b	114	3	58	3	887	14	549
pcc1-3a	114	3	58	3	887	45	312
pcc1-3b	114	3	58	3	887	45	312
pcc2-1a	114	3	58	3	1770	0	620
pcc2-1b	114	3	58	3	1770	0	595
pcc2-2a	114	3	58	3	1770	15.5	400
pcc2-2b	114	3	58	3	1770	15.5	394
pcc2-3a	114	3	58	3	1770	45	228
pcc2-3b	114	3	58	3	1770	45	227



Figure 51 - Failure mode [5].

a) $L = 887$ mm;b) $L = 1770$ mm.Figure 52 - Axial load *versus* mid-span deflection [5].

3.7.5 Eccentric load - Li *et al.* [77]

The tests from Li *et al.* [77] were conducted on CFDST stub columns with cold-formed circular carbon steel in the outer and inner tubes and infilled with grout of a compressive strength f_c measured during the tests equal to 41 MPa. The Young's modulus E_c of the grout was provided in the paper, i.e., 22800 MPa. For the cold-formed circular steel tubes, standard

tensile coupon tests were conducted to provide the material properties. The Young's modulus of the outer tube was E_{yso} 196000 MPa, the yield stress was f_{syo} 307 MPa, the ultimate stress was f_{sou} 407 MPa, and the elongation δ_o 39.4%. The Young's modulus of the inner tube was E_{ysi} 187000 MPa, the yield stress was f_{ysi} 321 MPa, the ultimate stress was f_{siu} 396 MPa, and the elongation δ_i 27.5%. The steel tubes dimensions, eccentricity and ultimate load $N_{u,test}$ are presented in Table 16. The beam-columns were tested through a compressive machine with axial load applied eccentrically. Both beam-columns ends had a thick plate welded on them with hinged ends allowing free rotation at both supports. Figure 53 shows the deformed shape and failure mode of a general view of beam-column after the test. The failure mode of overall global buckling was observed for both beam-columns with different eccentricity values. An outward buckling occurred in the outer steel tube in the compressive region at the middle of the beam-columns. The grout crushed in the same region where the outer tube had outward buckling, followed by a transverse and longitudinal crack of the grout in the tensile region of the beam-columns. An inward buckling was also found in the inner steel tube.

Table 16 - Specimen label, dimensions, eccentricity and ultimate capacities [77].

Specimen	D (mm)	t_{so} (mm)	d (mm)	t_{si} (mm)	L (mm)	e (mm)	$N_{u,test}$ (kN)
GBC1-1	140	2.5	114	2	1000	20	479
GBC1-2	140	2.5	114	2	1000	20	494
GBC2-1	140	2.5	114	2	1000	70	284
GBC2-2	140	2.5	114	2	1000	70	276

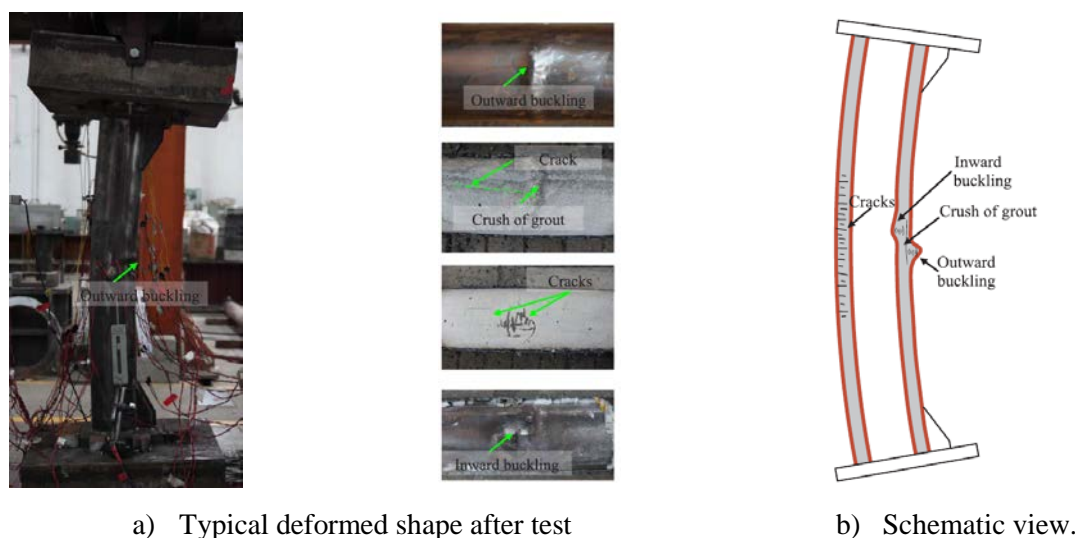


Figure 53 - Failure mode [77].

Figure 54 and Figure 55 presents the axial load *versus* axial displacement and the axial load *versus* deflection at the mid-height curves of the beam column's, respectively, with an eccentricity of (a) $e = 20$ mm and (b) $e = 70$ mm. The curves presented three distinctive stages: first, a linear elastic, followed by an elastic-plastic ending with a descending stage. The beam-columns stiffness and load capacity were significantly affected by the applied eccentricity value, decreasing as the eccentricity value increased.

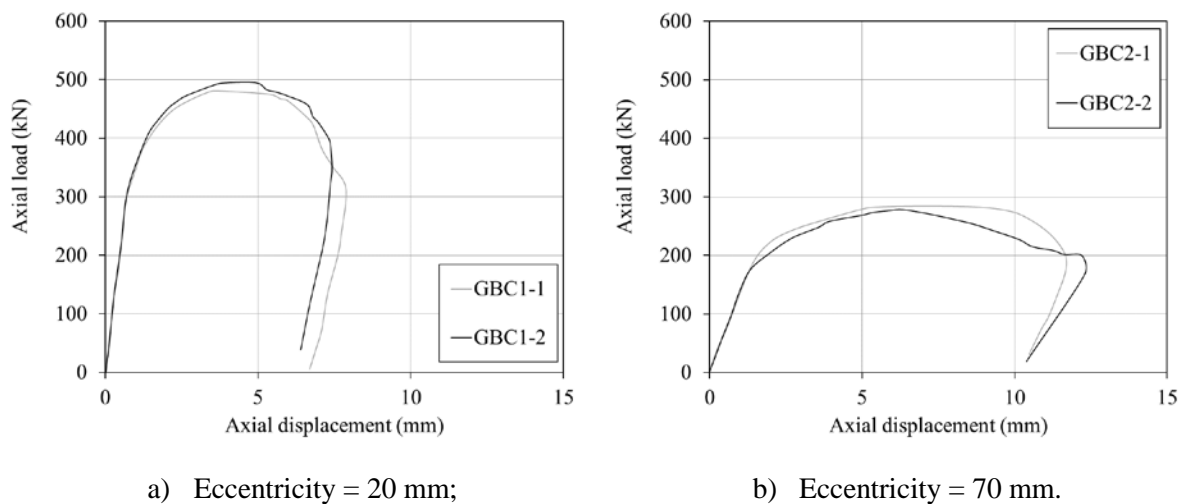


Figure 54 - Axial load *versus* axial displacement [77].

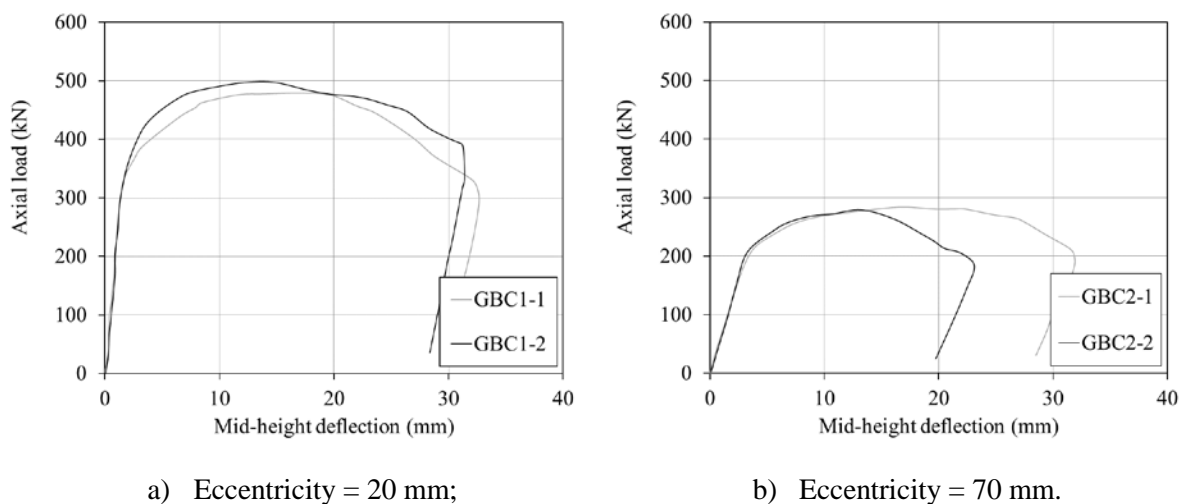


Figure 55 - Axial load *versus* mid-span deflection [77].

3.7.6 Eccentric load - Ibañez *et al.* [87]

The tests from Ibañez *et al.* [87] were conducted on CFDST stub columns with cold-formed circular carbon steel in the outer and inner tubes and conventional concrete with two different values of compressive strength for the infill: f_c of 30 MPa and 90 MPa. The nominal yield stress of all the cold-formed circular steel tubes was f_y 275 MPa, except for the section of 108 x 2, which had a f_{ysi} 355 MPa. The same Young's modulus for all tubes with a value of E_y 210000 MPa was considered. The steel tubes dimensions, eccentricity and ultimate load $N_{u,test}$ are presented in Table 17.

Table 17 - Specimen label, dimensions, eccentricity and ultimate capacities [87].

Specimen	D (mm)	t_{so} (mm)	d (mm)	t_{si} (mm)	L (mm)	Concrete (MPa)	e (mm)	$N_{u,test}$ (kN)
C-C-a-30-00	219.1	3	108	2	300	C30	0	1966
C-C-a-30-05	219.1	3	108	2	300	C30	5	1853
C-C-a-30-10	219.1	3	108	2	300	C30	10	1790
C-C-a-30-20	219.1	3	108	2	300	C30	20	1733
C-C-a-30-25	219.1	3	108	2	300	C30	25	1920
C-C-a-30-50	219.1	3	108	2	300	C30	50	1736
C-C-a-90-00	219.1	3	108	2	300	C90	0	2876
C-C-a-90-05	219.1	3	108	2	300	C90	5	2792
C-C-a-90-10	219.1	3	108	2	300	C90	10	2611
C-C-a-90-20	219.1	3	108	2	300	C90	20	2185
C-C-a-90-25	219.1	3	108	2	300	C90	25	2185
C-C-a-90-50	219.1	3	108	2	300	C90	50	1747
C-C-b-30-00	219.1	3	101.6	2	300	C30	0	1995
C-C-b-30-05	219.1	3	101.6	2	300	C30	5	2085
C-C-b-30-10	219.1	3	101.6	2	300	C30	10	1987
C-C-b-30-20	219.1	3	101.6	2	300	C30	20	2012
C-C-b-30-25	219.1	3	101.6	2	300	C30	25	2016
C-C-b-30-50	219.1	3	101.6	2	300	C30	50	1623
C-C-b-90-00	219.1	3	101.6	2	300	C90	0	2988
C-C-b-90-05	219.1	3	101.6	2	300	C90	5	3151
C-C-b-90-10	219.1	3	101.6	2	300	C90	10	3109
C-C-b-90-20	219.1	3	101.6	2	300	C90	20	2504
C-C-b-90-25	219.1	3	101.6	2	300	C90	25	2627
C-C-b-90-50	219.1	3	101.6	2	300	C90	50	1430

The CFDST columns and beam-columns were tested in a horizontal frame with an axial compression load, as presented in Figure 56. Two thick plates with a dimension of 300 x 300 x 15 mm were welded at both column's ends. Both supports were pinned, and the eccentricity

value was applied at both ends. From Table 17 may be observed that, as expected, when a higher concrete compressive strength of 90 MPa is used, an increase in the CFDST columns and beam-columns ultimate load was achieved. On the other hand, as the applied eccentricity value increases, the ultimate load capacity decreases. However, this trend is not observed from the eccentricity value from 20 mm to 50 mm, which the load capacity starts to increase again. Probably, this might occur due to the experimental setup where a tensile strength could have been added to the compressive strength.



Figure 56 - Test set-up [87].

3.7.7 Eccentric load - Zhao *et al.* [88]

Zhao *et al.* [88] conducted tests on CFDST stub columns with circular stainless steel in the outer tube and cold-formed circular carbon steel inner tube and a conventional concrete with a compressive strength f_c , on the day of the tests, equal to 48 MPa for the infill. The Young's modulus E_c of the conventional concrete was experimentally measured, i.e., 31000 MPa. The steel tubes material properties were obtained through standard tensile coupon tests. The Young's modulus of the carbon steel with a thickness of t_{si} 2.01 mm was E_{syi} 208000 MPa, and the yield stress was taken as 0.2%, with $f_{syi} = 275$ MPa, the ultimate stress $f_{siu} = 351$ MPa and the elongation $\delta_i = 22\%$. The carbon steel Young's modulus for a thickness of t_{si} 2.52 mm was E_{syi} 205000 MPa, and the yield stress was taken as 0.2%, with $f_{syi} = 276$ MPa, the ultimate stress $f_{siu} = 384$ MPa and the elongation $\delta_i = 25\%$. The stainless steel Young's modulus was E_{syo} 191000 MPa, and the yield stress was taken as 0.2%, with $f_{syo} = 322$ MPa, the ultimate stress of

$f_{s\text{ou}} = 708$ MPa and the elongation $\delta_o = 46\%$. The steel tubes dimensions, eccentricity and ultimate load capacity $N_{u,\text{test}}$ are presented in Table 18.

Table 18 - Specimen label, dimensions, eccentricity and ultimate capacities [88].

Specimen	D (mm)	t_{so} (mm)	d (mm)	t_{si} (mm)	L (mm)	e (mm)	$N_{u,\text{test}}$ (kN)
C1-0.44-4-a	114	1.88	48	2.52	800	4	597
C1-0.44-4-b	114	1.88	48	2.52	800	4	690
C1-0.69-a	114	1.88	76	2.01	800	14	429
C1-0.69-b	114	1.88	76	2.01	800	14	430
C2-0.44-4-a	114	1.88	48	2.52	1300	4	536
C2-0.44-4-b	114	1.88	48	2.52	1300	4	556
C2-0.69-14-a	114	1.88	76	2.01	1300	14	360
C2-0.69-14-b	114	1.88	76	2.01	1300	14	384
C3-0.44-4-a	114	1.88	48	2.52	1800	4	415
C3-0.44-4-b	114	1.88	48	2.52	1800	4	489
C3-0.69-14-a	114	1.88	76	2.01	1800	14	307
C3-0.69-14-b	114	1.88	76	2.01	1800	14	272

The beam-columns were tested under compression load with knife-edge positioned at both ends to provide pinned supports, which allowed rotation in the axis where the eccentricity was applied. High steel strength plates with 6 mm of thickness were welded in both beam-columns ends. Figure 57 presents the failure mode of the beam-columns for different eccentricity values applied and length, as represented in each image. A typical global buckling occurred, without obvious local buckling in the middle of the beam-columns except for specimen C1-0.69-14. The local buckling is related to the higher stresses at the compression side caused by the large applied eccentricity value.



Figure 57 - Failure mode [88].

Figure 58 shows the axial load *versus* deflection at the beam-columns mid-height. The graphs are distributed as: (a) eccentricity of 4 mm and length of 800 mm, (b) eccentricity of 14 mm and length of 800 mm, (c) eccentricity of 4 mm and length of 1300 mm, (d) eccentricity of 14 mm and length of 1300 mm, (e) eccentricity of 4 mm and length of 1800 mm and (f) eccentricity of 14 mm and length of 1800 mm, respectively. The typical three phases were observed for all the beam-columns: elastic stage, elastic-plastic stage with the stiffness decrease and post-failure stage. The global buckling with a lateral deflection at the middle of the beam-columns was only observed after the maximum load was achieved. The beam-column load capacity decreased as the slenderness ratio and eccentricity value increased.

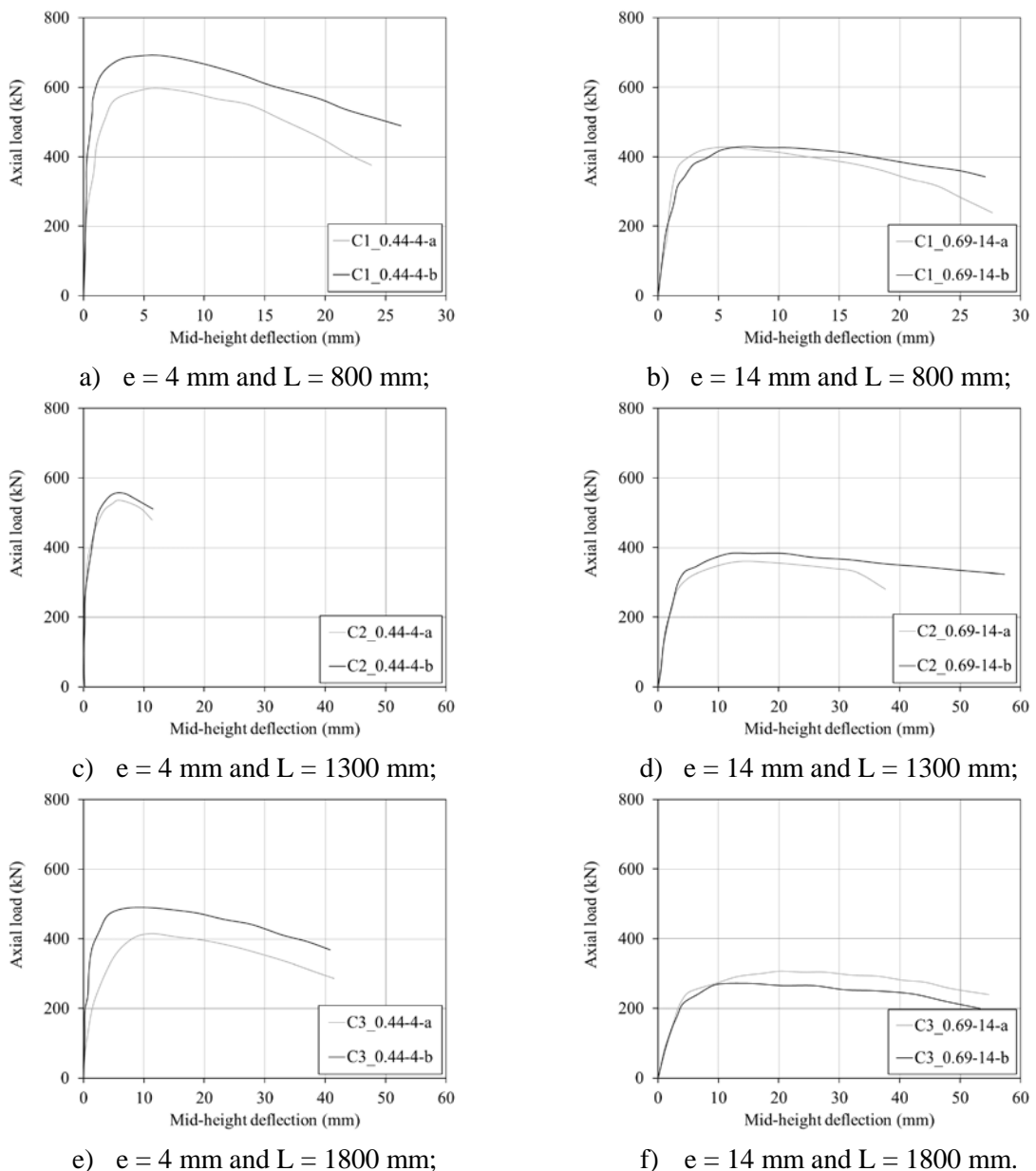


Figure 58 - Axial load *versus* mid-span deflection [88].

3.7.8 Pure bending - Li *et al.* [77]

Li *et al.* [77] also conducted experiments in CFDST beams to study their flexural behaviour under pure bending. The same material properties cited in item 3.7.5 were used. A two-point bending test was conducted through a rigid spread beam to apply the load, with a distance between both point loads of 500 mm. The beam presented hinged support on one side and rolling support on the other side, with the distance between the supports of $L = 1080$ mm. The outer steel tube dimension was 140×2.5 mm, and the inner tube dimension was 114×2 mm. Figure 59 and Figure 60 presents the CFDST beam typical failure mode. An overall flexural deformation was observed in the middle length of the beam. An outward buckling and an inward buckling occurred in the middle length of the beam outer steel tube and inner steel tube, respectively. The grout was crushed and presented cracks in the same region where the local buckling was found.

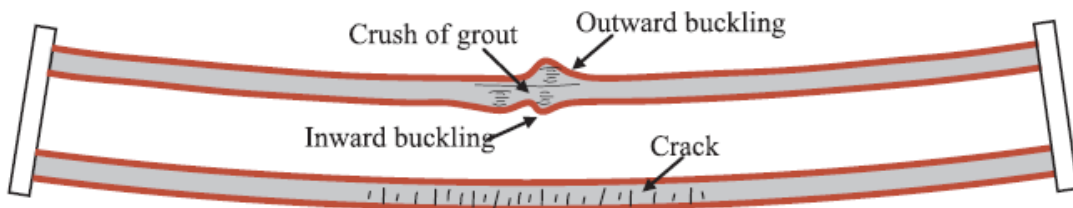
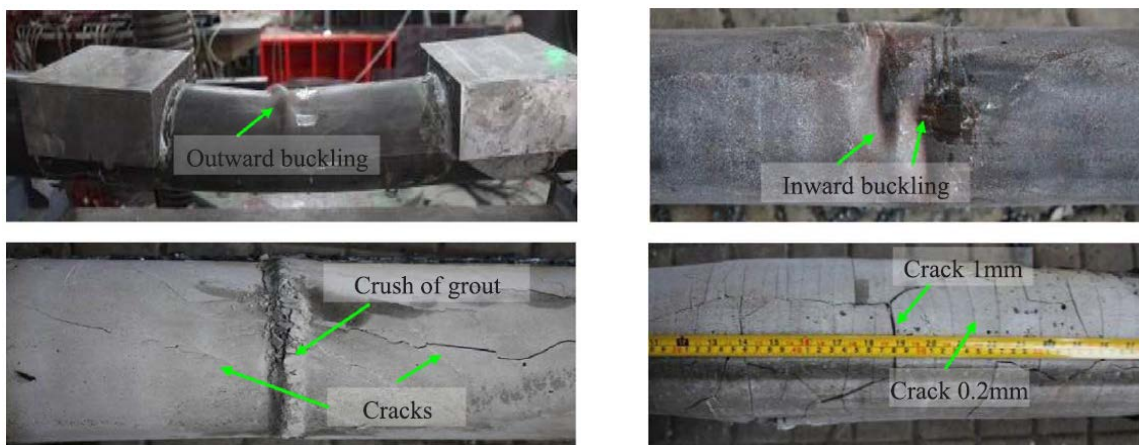


Figure 59 - Typical failure mode of a CFDST beam [77].



a) Inner steel tube;

b) Outer steel tube.

Figure 60 - Failure mode [77].

Figure 61 presents the moment *versus* deflection at the mid-span of the beams under pure bending. The beams' ultimate flexural strength was: GB-1 $M_{u, \text{test}}$ 28.5 kNm and GB-2 $M_{u, \text{test}}$ 30.8 kNm. The moment *versus* mid-span deflection curves behaves with two distinctive stages, initial elastic and elastic-plastic, followed by the beam's failure and moment decreases.

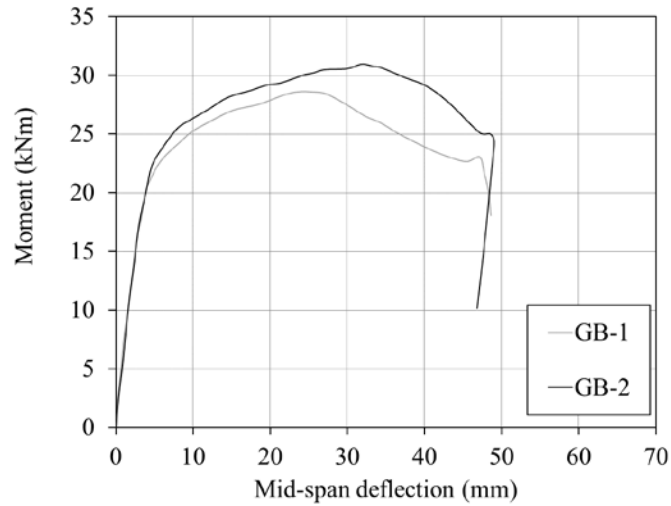


Figure 61 - Moment *versus* mid-span deflection of the CFDST beam under pure bending [77].

4 NUMERICAL MODELLING

4.1 Generalities

A numerical investigation into the behaviour of concrete-filled double-skin tubular stub columns (CFDST) will be presented in this chapter. The finite element software ABAQUS [16] was adopted to evaluate the CFDST stub columns under concentric (stub column), eccentric (beam-column) axial compression and pure bending (beam). The finite element modelling process will be described during the chapter, as well as the constitutive model used to implement the stress *versus* strain of each material. This will be followed by the FE model validation against the experiments available in the literature for beam-columns and beams and the tests performed in this study for columns.

4.2 Finite element model description

The three-dimensional finite element modelling was developed using three different load strategies. A comprehensive description of their development will be divided into the following subitems: geometry, mesh sensitivity and elements; boundary conditions, interactions and load application; contact and geometric imperfections; constitutive material models; and results.

4.2.1 Geometry, mesh sensitivity and elements

The column's cross-section geometry was fully considered to accurately model the FE columns under concentric and eccentric axial compression without the need for any simplification. A second FE model under pure bending was developed considering half of the beam's cross-section, using double symmetry in length aiming to enhance computational efficiency. Both FE models presented different boundary conditions; equal geometry, as can be observed in Figure 62. The 4-node doubly curved reduced integration shell element was used

to model both steel tubes and the circular steel ring (S4R). An 8-node linear brick reduced integration solid element was utilised to model the concrete (C3D8R).

The mesh size was selected based on a sensitivity analysis to improve convergence problems conducted by Tao *et al.* [76] and assessed in Wang *et al.* [48]. A uniform mesh size of approximately 8 mm for longitudinal and circumferential directions and 10 mm for radial directions (concrete core) was adopted.

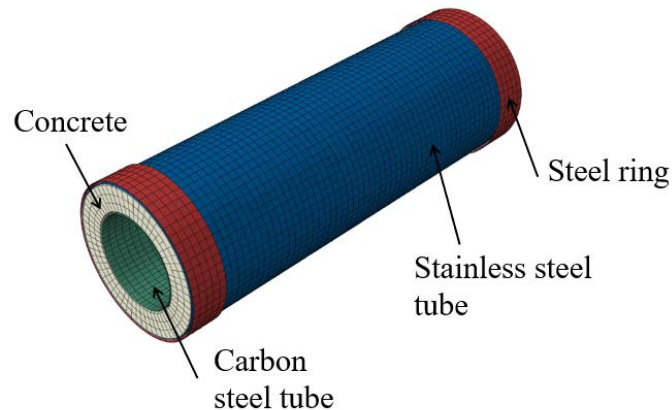


Figure 62 - Geometry of the FE model in ABAQUS [16].

4.2.2 Boundary conditions, interactions and load application

In order to simulate the fixed ends employed in the tests with concentric load, the top surface of the modelled stub columns was coupled to a reference point through a rigid body constraint, where all degrees of freedom were restrained except for the longitudinal translation. The columns under eccentric load had the top and the bottom surfaces of the modelled stub beam-columns coupled to reference points through a rigid body constraint. Both surfaces were kept fixed in all degrees of freedom except for the rotation in the load direction application axis that was free. The compressive and eccentric load were applied through a reference point at the column's bottom end while employing displacement control. The longitudinal displacement was kept free to displace, as it is possible to be observed in Figure 63 a).

The second FE model was developed to simulate a beam under pure bending and followed the analysis procedures for pure bending experiments presented in Li *et al.* [77]. The half model boundary conditions were simply supported at the end of the beam, while symmetry conditions in the middle of the beam were adopted. A concentric compression load was applied as prescribed displacement on the beam top to simulate de envisaged pure bending, as shown

in Figure 63 b). The distance from the beam end to the load application point and the distance from the load application point to the symmetry surface was equal. All the four regions of the beam were equal and were calculated as two times the column length divided by four to obtain a pure bending condition with a constant maximum moment in the middle of the beam. The simply supported condition at the end of the beam and the load application point was applied in reference points. The reference points were connected to the beam end surface and a region above the beam, respectively, through a coupling constraint. These constraints connected the surfaces of the beam to the considered reference points.

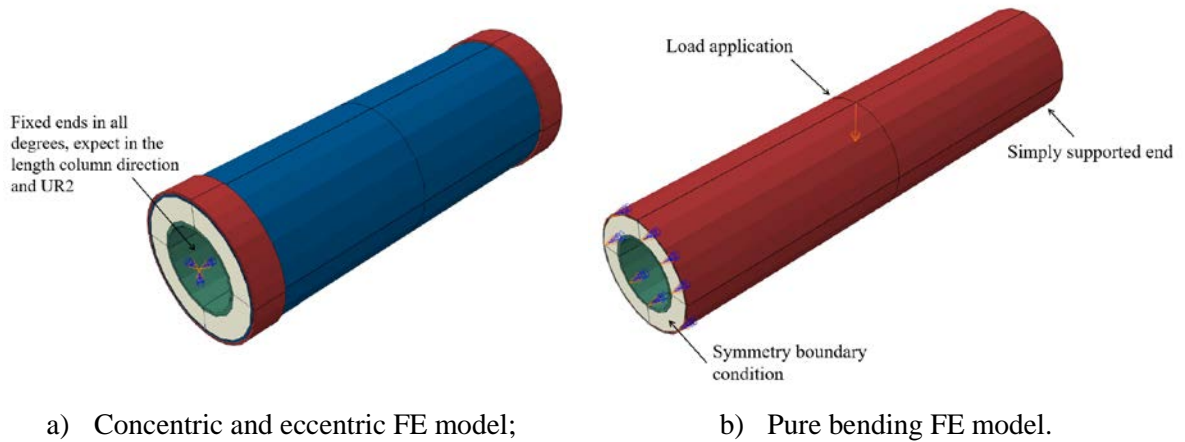


Figure 63 - Boundary conditions.

4.2.3 Contact and geometric imperfections

A surface-to-surface contact simulates the contact between the steel tubes and the concrete sandwich and between the outer steel tube and the circular steel ring. As suggested by Tao et al. [74], hard contact was specified in the normal direction. A Coulomb friction model was used in the tangential behaviour, with a 0.25 friction coefficient, as recommend by Han *et al.* [46]. A shear stress limit (f_{mean}) was also specified at the contact between the concrete and the steel sections, based on the guidance for circular tubes proposed by Roeder *et al.* [78], i.e.:

$$f_{mean} = 2.314 - 0.0195 \left(\frac{D}{t_{so}} \right) \quad (94)$$

The initial geometric imperfections were measured in the stainless steel tubular test specimens. These values were included in the numerical analysis through the deformed shape and amplitude obtained from an eigenvalue analysis [79]. The amplitude of the buckling mode shape was included as a fraction of the steel tube thickness and, following a sensitivity study, a value of $0.2t_{so}$ (≈ 0.5 mm) was employed.

4.3 Material modelling

4.3.1 Concrete

The concrete infill was simulated using the concrete damage plasticity (CDP) model available in ABAQUS [16]. The compressive strength was taken from the concrete material tests conducted in the experimental programme previously described. The Young's modulus E_{c_NAC} for NAC was determined with the recommended equation adopted by ACI [31] and presented below. The E_{c_RAC} for RAC was determined by the method proposed by Gholampour *et al.* [80] given by:

$$E_{c_NAC} = 4700\sqrt{f_c} \quad (95)$$

$$E_{c_RAC} = 0.016 \times (6.1 - 0.015RAC\%) \times (5.3 - 1.7w_{eff}/c)^{3.9} \quad (96)$$

in which f_c is the concrete compressive strength in MPa, $RAC\%$ is the recycled aggregate replacement, and w_{eff}/c is the effective water-to-cement ratio. The stress *versus* strain model for confined concrete in compression proposed by Tao *et al.* [76] was employed to simulate the infill material, as presented in Figure 64. In this approach, the ascending and descending branches can be determined from Eqs. (97) and (98), respectively:

$$\sigma = f_c \times \frac{A \times X + B \times X^2}{1 + (A - 2) \times X + (B + 1) \times X^2} \quad 0 < \varepsilon \leq \varepsilon_{c0} \quad (97)$$

$$\sigma = f_r + (f_c - f_r) \times \exp\left[-\left(\frac{\varepsilon - \varepsilon_{cc}}{\alpha}\right)^\beta\right] \quad \varepsilon \geq \varepsilon_{cc} \quad (98)$$

In these expressions, f_c is the longitudinal compressive concrete stress determined from the material tests; A and B are the peak stress values corresponding to ε_{c0} and ε_{cc} , respectively, as shown in Figure 64; ε_{c0} and ε_{cc} are the strains corresponding to the stresses at A and B; X is a parameter calculated as $X = \frac{\varepsilon}{\varepsilon_{c0}}$; f_r is the residual stress at the end of the softening branch; and α and β are parameters used to determine the softening branch curve shape.

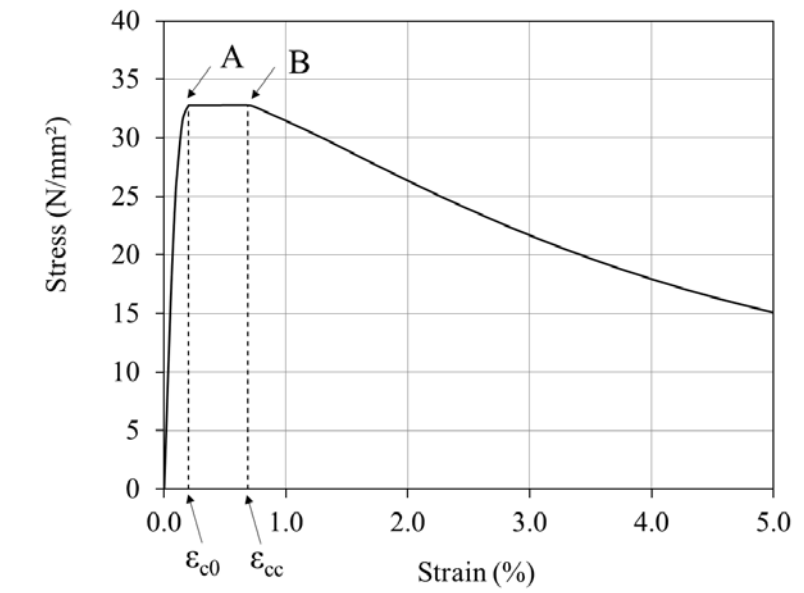


Figure 64 - Stress *versus* strain relationship for confined concrete in compression [76].

In addition to the stress *versus* strain response, some additional parameters are required for the CDP model, including the dilatation angle (ψ), eccentricity (e_f), the ratio of the compressive strengths under biaxial and uniaxial loading (f_{b0}/f_c) and the stress invariant on the tensile meridian to the compressive meridian (K_c). The assigned values were 36° , 0.1 and 1.16 for ψ , e_f , and f_{b0}/f_c , respectively, based on the ABAQUS manual's guidance [16] and $2/3$ for K_c , following Li *et al.* [81] recommendations.

For the concrete tensile properties required in the CDP model, the approach recommended by the Comité Euro-International du Béton (CEB-FIP Model Code) [82] was adopted whereby the energy fraction (G_f) is determined for the confined concrete behaviour as:

$$G_f = (0.0469d_{max}^2 - 0.5d_{max} + 26) \left(\frac{f_c}{10} \right)^{0.7} \quad (99)$$

In this expression, d_{max} is the maximum coarse aggregate size.

4.3.2 Steel tubes

The measured carbon and stainless steel tubes material properties were incorporated into the respective FE simulations for validation purposes. For the carbon steel inner tubes, the constitutive relationship proposed by Yun and Gardner [83] was employed to represent the behaviour, using the key property values earlier presented in this thesis. The measured stress

versus strain curve was used for stainless steel. For both steel sections, the measured and proposed engineering stress *versus* strain curves were converted into true stress *versus* true plastic strain curves using the expressions present in Eqs. (100) and (101) and were inputted into ABAQUS [16] as true stress *versus* logarithmic plastic strain:

$$\sigma_{true} = \sigma_{nom}(1 + \varepsilon_{nom}) \quad (100)$$

$$\varepsilon_{ln}^{pl} = \ln(1 + \varepsilon_{nom}) - \frac{\sigma_{nom}}{E} \quad (101)$$

In these expressions, σ_{true} is the true stress, σ_{nom} is the engineering stress, ε_{ln}^{pl} is the logarithmic plastic strain, ε_{nom} is the engineering strain, and E is the material Young's modulus.

4.4 Validation of the numerical model – Concentric load

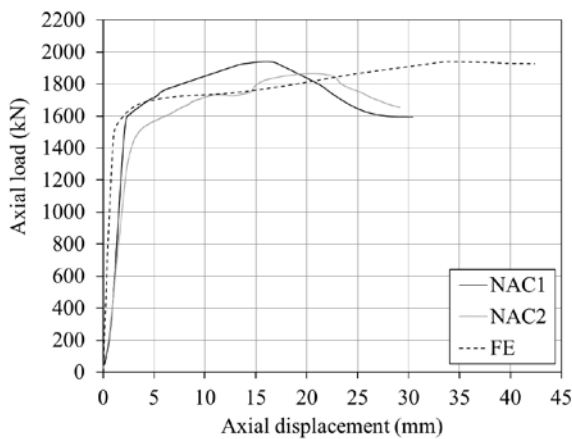
The FE model's accuracy for a concentric axial compression load was evaluated by comparing the full load-deformation responses, ultimate loads, deformed shapes and failure modes of the experiments previously presented in this thesis and with experiments from the literature against those obtained from the numerical simulations. The experiments adopted from the literature were Wang *et al.* [48] and Han *et al.* [46], summarized in Table 19. The stress *versus* strain model for confined conventional concrete in compression of all the validated FE models utilised the values proposed by Tao *et al.* [76].

Table 19 - Summarized references used in the FE's validation for CFDST columns.

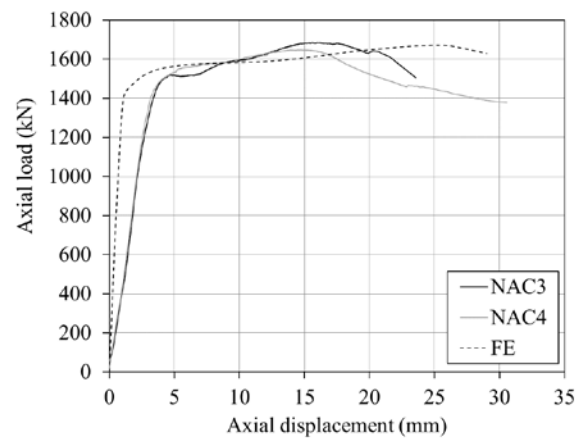
Autor	Structural member	Concrete	Number of tests
Wang <i>et al.</i> [48]	Column	NAC	8
Han <i>et al.</i> [46]		NAC	4
Rodrigues [65]		NAC	4
Tested specimens		RAC	4

4.4.1 Experimental results

Figure 65 and Figure 66 presents the axial load *versus* axial displacement responses obtained experimentally and numerically for (a) NAC1/NAC2 and (b) NAC3/NAC4 and (a) RAC1/RAC2 and (b) RAC3/RAC4, respectively. Figure 67 and Figure 68 depicts the corresponding axial load *versus* axial strain responses obtained experimentally and numerically. The ultimate loads from the tests ($N_{u,test}$) and the FE model's corresponding values ($N_{u,FE}$) are presented in Table 20, together with the $N_{u,FE}/N_{u,test}$ ratio. Figure 69 compares the deformed shape for RAC1 and RAC2 from (a) the experiments and (b) the FE model.

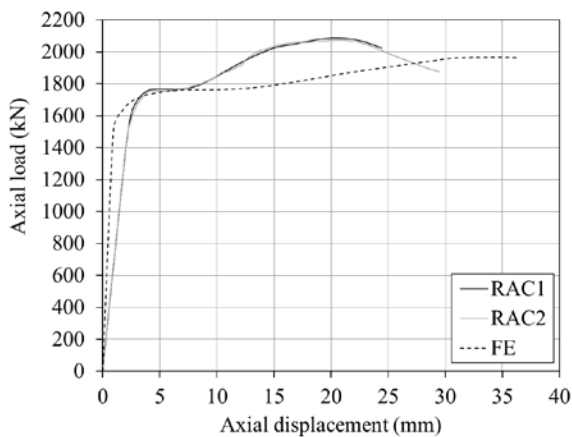


a) Inner tube 88.9 x 5.5 mm;

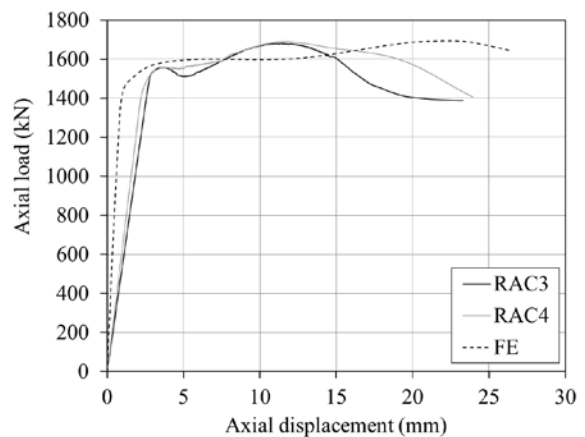


b) Inner tube 108.4 x 4.5 mm.

Figure 65 - Axial load *versus* axial displacement for the NAC CFDST columns.

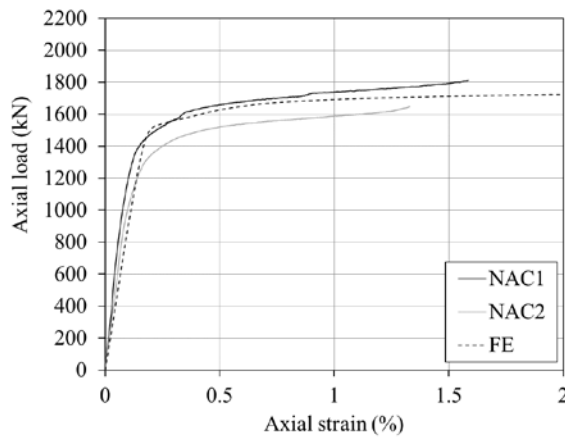


a) Inner tube 88.9 x 5.5 mm;

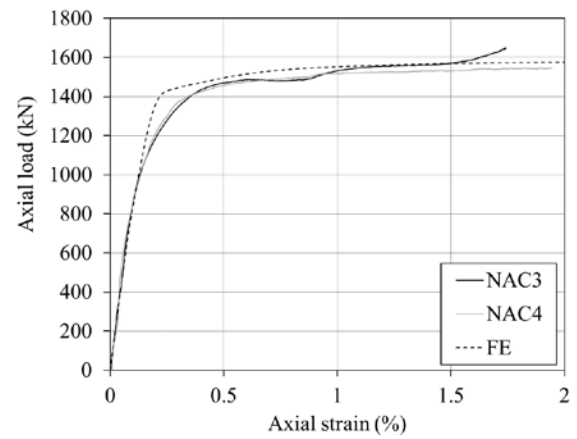


b) Inner tube 108.4 x 4.5 mm.

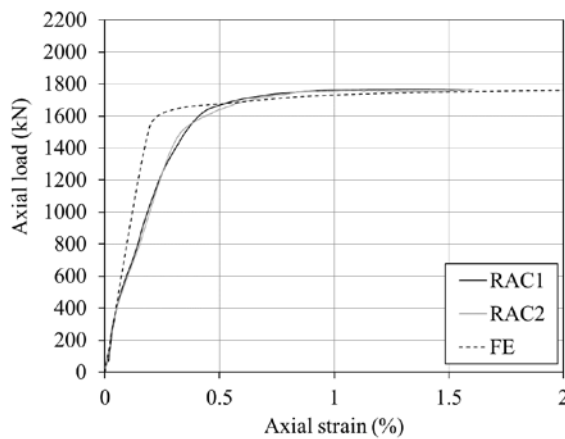
Figure 66 - Axial load *versus* axial displacement for the RAC CFDST columns.



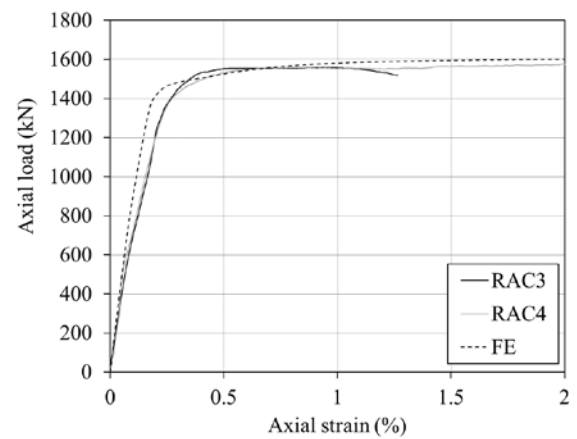
a) Inner tube 88.9 x 5.5 mm;



b) Inner tube 108.4 x 4.5 mm.

Figure 67 - Axial load *versus* axial strain for the NAC CFDST columns.

a) Inner tube 88.9 x 5.5 mm;



b) Inner tube 108.4 x 4.5 mm.

Figure 68 - Axial load *versus* axial strain for the RAC CFDST columns.

Table 20 - Comparison of the ultimate loads from the experimental and the FE model.

CFDST column	$N_{u,test}$ (kN)	$N_{u,FE}$ (kN)	$N_{u,FE}/N_{u,test}$
NAC1	1941	1940	1.00
NAC2	1865		1.04
NAC3	1649	1670	1.01
NAC4	1612		1.04
RAC1	2087	1966	0.94
RAC2	2075		0.95
RAC3	1685	1695	1.01
RAC4	1693		1.00
Mean			0.998
CoV			0.036

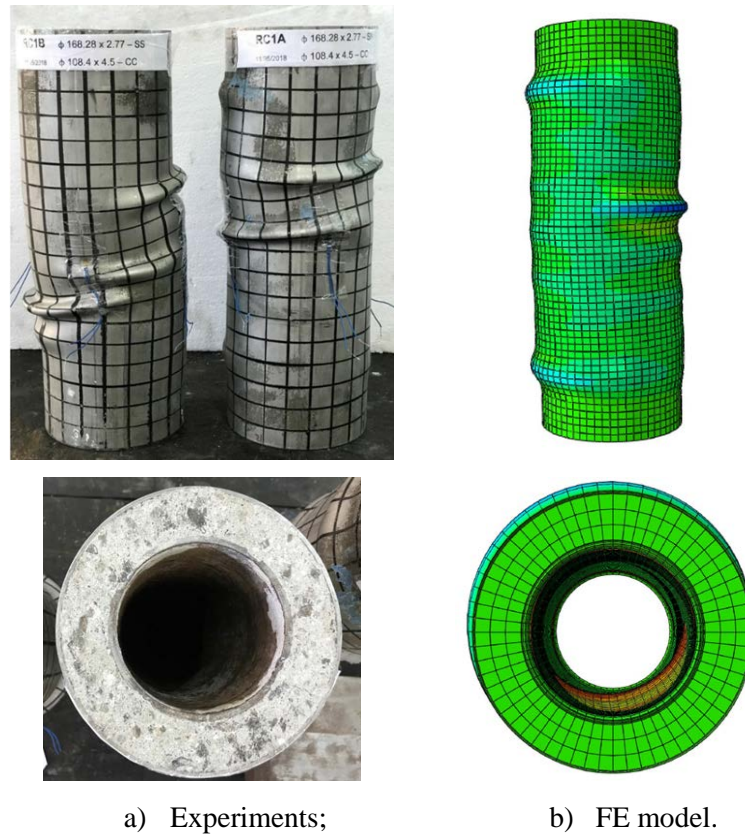


Figure 69 - Comparison of failure mode.

As shown in Table 20, the FE model provides good predictions of the ultimate loads, with the mean value of $N_{u,FE}/N_{u,test}$ equal to 0.998 and the coefficient of variation (CoV) of 0.036. The experimental and numerical axial load *versus* axial displacement and axial load *versus* axial strain curves also show that the FE model accurately represents the experiments. The failure modes and deformed shape of experimental and numerical results are almost identical: both exhibited local buckling in the middle of the column and close to the supports with an outward buckling in the outer steel tube and an inward buckling inner steel tube.

4.4.2 Tests from Wang *et al.* [48]

As aforementioned, the tests from Wang *et al.* [48] were performed on CFDST stub columns with a stainless steel outer tube, high strength carbon steel inner tube and conventional concrete and are described in 3.7.2. The Young's modulus E_c of the conventional concrete was calculated as suggested by Tao *et al.* [76], as 29910 MPa. All the steel tubes' constitutive relationship was obtained through the paper's curves together with the true stress-logarithmic

plastic strain in ABAQUS [16]. The CFDST stub columns experimental and numerical ultimate loads $N_{u, \text{test}}$ and $N_{u, \text{FE}}$ are presented in Table 21. It is noteworthy that the ultimate load from the FE model was determined as the load at which the slope of the load *versus* axial displacement response reaches 1% of its initial stiffness, as proposed by dos Santos *et al.* [84].

Table 21 - Comparison of the ultimate loads from the experimental from Wang *et al.* [48] and the FE model.

CFDST column	$N_{u, \text{test}}$ (kN)	$N_{u, \text{FE}}$ (kN)	$N_{u, \text{FE}}/N_{u, \text{test}}$
AC140×3-HC22×4	1410	1548	1.10
AC140×3-HC32×6	1423	1662	1.17
AC140×3-HC38×8	1626	1698	1.04
AC140×3-HC55×11	2543	2539	1.00
AC140×3-HC89×4	2025	1975	0.98
AC165×3-HC22×4	1750	1747	1.00
AC165×3-HC32×6	1943	1865	0.96
AC165×3-HC89×4	2375	2279	0.96
Mean			1.025
CoV			0.072

Figure 70 presents a comparison of the deformed shape for (a) a general view of a CFDST column after the test and (b) the FE model. Figure 71 presents the axial load *versus* mean axial strain (axial displacement divided by the total length) of the column responses obtained experimentally and numerically.

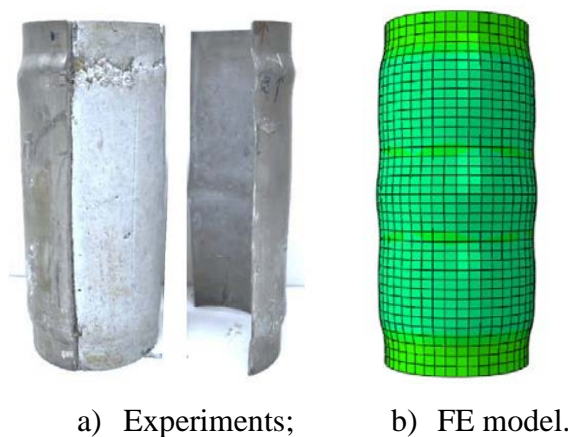


Figure 70 - Comparison of failure mode [48].

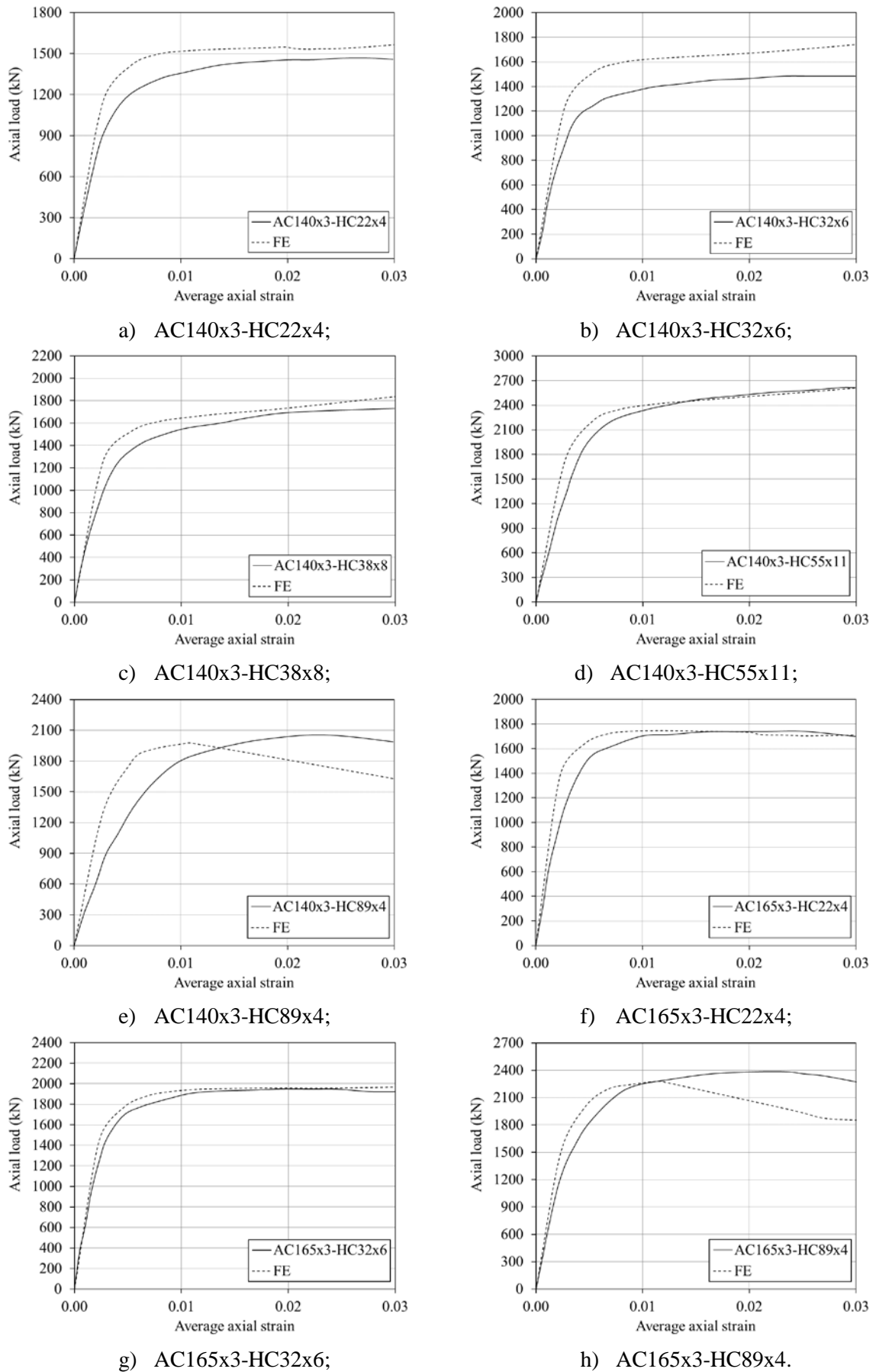


Figure 71 - Axial load *versus* mean axial strain for the CF DST columns from Wang *et al.* [48].

As shown in Table 21, the FE model provides good predictions of the ultimate loads, with the mean value of $N_{u,FE}/N_{u,test}$ equal to 1.025 and the coefficient of variation (CoV) of 0.072. The experimental and numerical axial load *versus* axial strain curves also show that the FE model accurately represents the experiments. The failure modes and deformed shape of experimental and numerical results are almost identical: both exhibited local buckling in the middle of the column and close to the supports with an outward buckling in the outer steel tube and an inward buckling inner steel tube.

4.4.3 Han et al. [46]

As previously discussed, the tests from Han *et al.* [46] adopted a stainless steel outer tube, carbon steel inner tube and conventional concrete and are described in 3.7.3. The constitutive relationship proposed by Gardner and Yun [85], together with the true stress-logarithmic plastic strain in ABAQUS [16], was employed to represent the behaviour of the cold-formed carbon steel inner tube. The constitutive relationship proposed by Rasmussen [86] was adopted on the cold-formed stainless steel outer tube. The CFDST stub columns experimental and numerical ultimate loads $N_{u,test}$ and $N_{u,FE}$ are presented in Table 22.

Table 22 - Comparison of the ultimate experimental loads from Han *et al.* [46] and the FE model.

CFDST column	$N_{u,test}$ (kN)	$N_{u,FE}$ (kN)	$N_{u,FE}/N_{u,test}$
C1-1_220×3.62-159×3.72	2537	2439	0.96
C1-2_220×3.62-159×3.72	2566		0.95
C2-1_220×3.62-106×3.72	3436	2942	0.86
C2-2_220×3.62-106×3.72	3506		0.84
Mean			0.902
CoV			0.070

Figure 72 presents the axial load *versus* axial displacement of the column responses obtained experimentally and numerically. Figure 73 compares the deformed shape for (a) a general view of a CFDST column after the test and (b) the FE model.

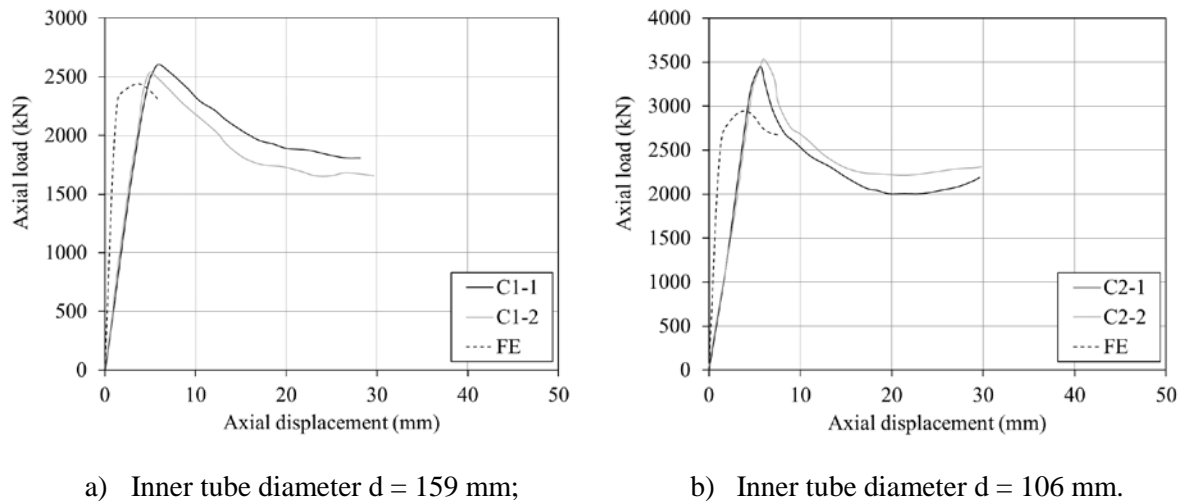


Figure 72 - Axial load *versus* axial displacement for the CFDST columns from Han *et al.* [46].

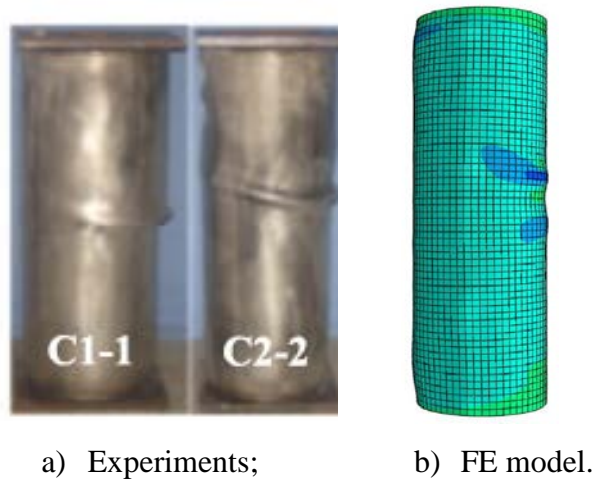


Figure 73 - Comparison of failure mode [46].

As shown in Table 22, the FE model provides good predictions of the ultimate loads, with the mean value of $N_{u,FE}/N_{u,test}$ equal to 0.902 and the coefficient of variation (CoV) of 0.070. The experimental and numerical axial load *versus* axial displacement curves also show that the FE model accurately represents the experiments. The failure modes and deformed shape of experimental and numerical results are almost identical: both exhibited local buckling in the middle of the column and close to the supports with an outward buckling in the outer steel tube and an inward buckling inner steel tube.

4.5 Validation of the numerical model – Eccentric loads

The accuracy of the FE model for an eccentric load was evaluated against comparisons based on full load-deformation responses, ultimate loads, deformed shapes and failure modes related to experiments present in literature: Tao *et al.* [5], Li *et al.* [77], Ibañez *et al.* [87] and Zhao *et al.* [88], are summarized in Table 23. The stress *versus* strain model for confined conventional concrete in compression of all the validated FE models was proposed by Tao *et al.* [76]. Gardner and Yun [83] proposed the constitutive relationship in terms of true stress *versus* logarithmic plastic strain in ABAQUS [16]. This strategy was used to represent all the cold-formed carbon steel tubes' behaviour in the FE model validation.

Table 23 - Summarized references used in the CFDST beam-columns FE's validation.

Autor	Structural member	Concrete	Number of tests
Tao <i>et al.</i> [5]	Columns and beam-columns	NAC	12
Li <i>et al.</i> [77]	Beam-columns	NAC	4
Ibañez <i>et al.</i> [87]	Columns and beam-columns	NAC	24
Zhao <i>et al.</i> [88]	Beam-columns	NAC	12

4.5.1 Tests from Tao *et al.* [5]

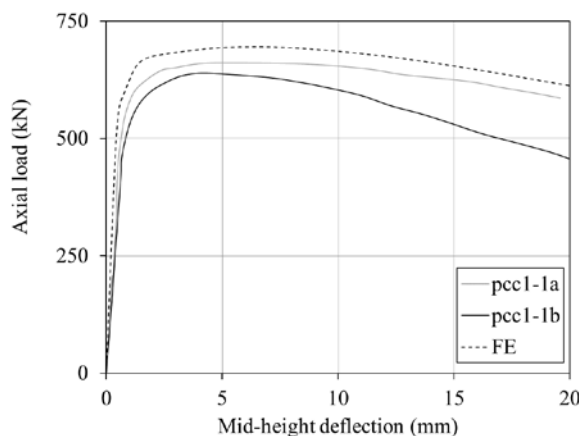
The tests from Tao *et al.* [5] were conducted on CFDST stub columns with cold-formed circular carbon steel in the outer and inner tubes and conventional concrete and are described in 3.7.4. The Young's modulus E_c of the conventional concrete was calculated following Tao *et al.* [76] recommendation, with a 28604 MPa. The CFDST beam-columns eccentricity applied and experimental and numerical ultimate loads $N_{u,test}$ and $N_{u,FE}$ are presented in Table 24.

Table 24 - Specimen label, eccentricity and ultimate capacities from Tao *et al.* [5].

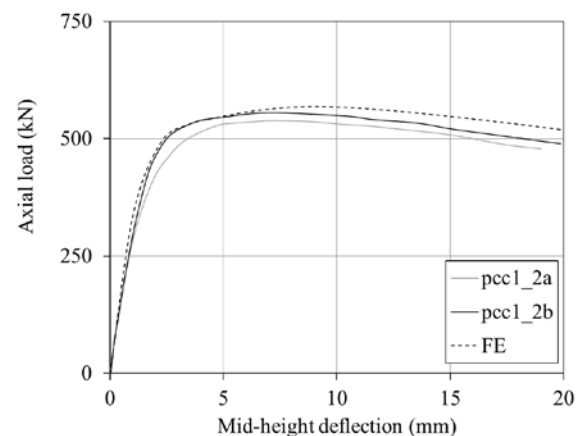
Specimen	e (mm)	$N_{u,test}$ (kN)	$N_{u,FE}$ (kN)	$N_{u,FE}/N_{u,test}$
pcc1-1a	4	664	696	1.05

pcc1-1b	4	638		1.09
pcc1-2a	14	536	568	1.06
pcc1-2b	14	549		1.03
pcc1-3a	45	312	325	1.04
pcc1-3b	45	312		1.04
pcc2-1a	0	620	622	1.00
pcc2-1b	0	595		1.05
pcc2-2a	15.5	400	412	1.03
pcc2-2b	15.5	394		1.05
pcc2-3a	45	228	248	1.09
pcc2-3b	45	227		1.09
Mean				1.052
CoV				0.026

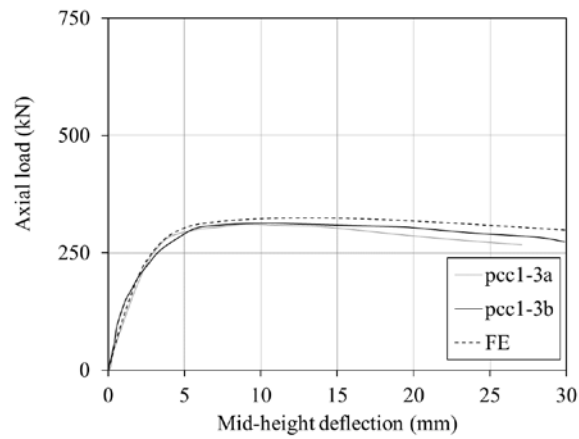
Figure 74 and Figure 75 presents the axial load *versus* deflection at the column mid-height obtained experimentally and numerically. Figure 74 presents columns with $L = 887$ mm: (a) eccentricity of 4 mm, (b) eccentricity of 14 mm and (c) eccentricity of 45 mm, respectively. Figure 75 presents columns with $L = 1770$ mm: (a) eccentricity of 0 mm, (b) eccentricity of 15.5 mm and (c) eccentricity of 45 mm, respectively. Figure 76 compares the deformed shape for (a) a general view of beam-column after test and (b) the FE model.



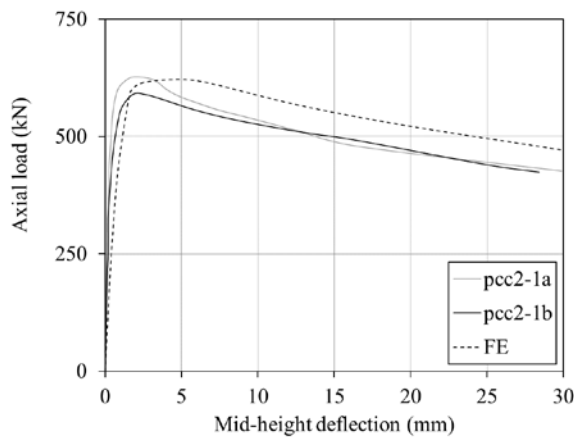
a) Eccentricity = 4 mm;



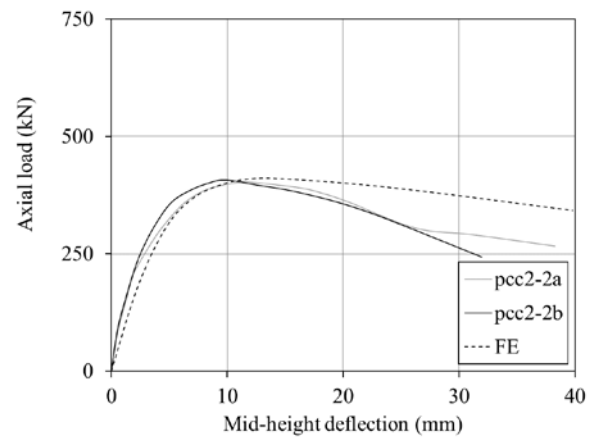
b) Eccentricity = 14 mm;



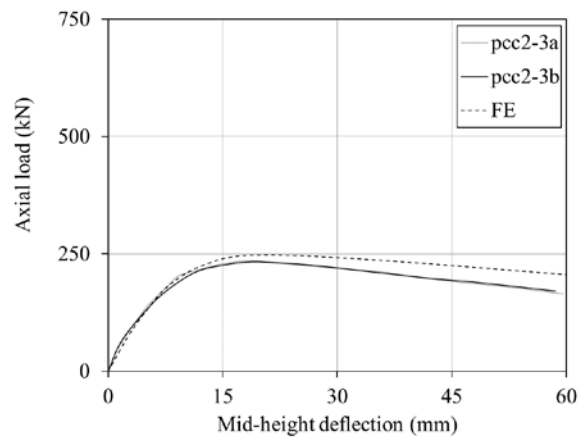
c) Eccentricity = 45 mm.

Figure 74 - Axial load *versus* mid-height deflection for CFDST columns with $L = 887$ mm.

a) Eccentricity = 0 mm;



b) Eccentricity = 15.5 mm;



c) Eccentricity = 45 mm.

Figure 75 - Axial load *versus* mid-height deflection for CFDST columns with $L = 1770$ mm.

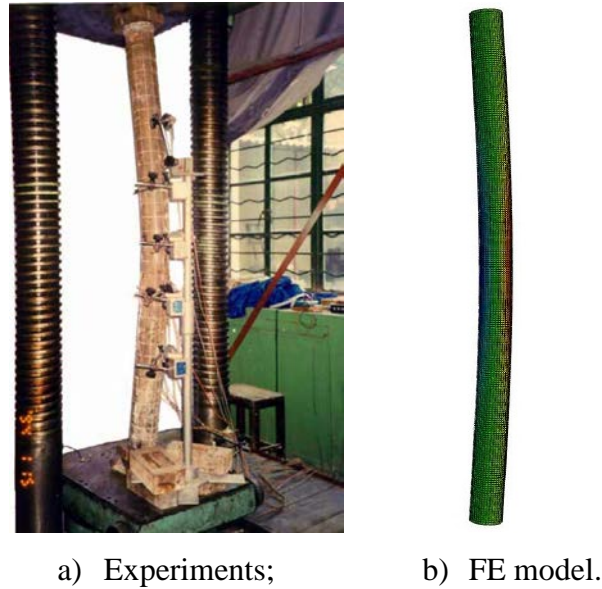


Figure 76 - Comparison of failure mode [76].

As shown in Table 24, the FE model provides good predictions of the ultimate loads, with the mean value of $N_{u,FE}/N_{u,test}$ equal to 1.052 and the coefficient of variation (CoV) of 0.026. The experimental and numerical axial load *versus* middle-height deflection curves also show that the FE model accurately represents the experiments, where all the curves had three distinctive stages: linear elastic, elastic-plastic, and descending stage. The failure modes and deformed shape of experimental and numerical results are almost identical: both exhibited overall global buckling in the middle of the beam-columns.

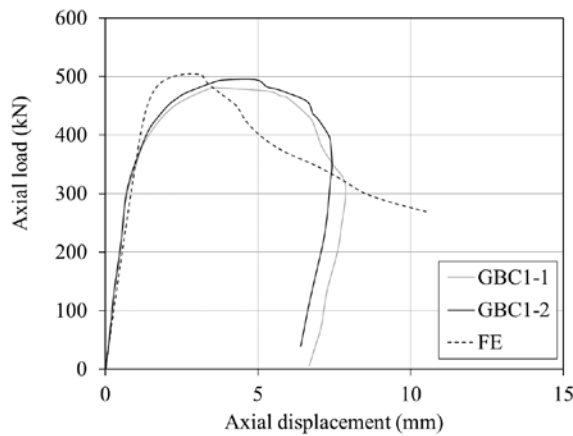
4.5.2 Tests from Li *et al.* [77]

The tests from Li *et al.* [77] were conducted on CFDST stub columns with cold-formed circular carbon steel in the outer and inner tubes and infilled with grout and are described in 3.7.5. The CFDST beam-columns eccentricity applied and experimental and numerical ultimate loads $N_{u,test}$ and $N_{u,FE}$ are presented in Table 25.

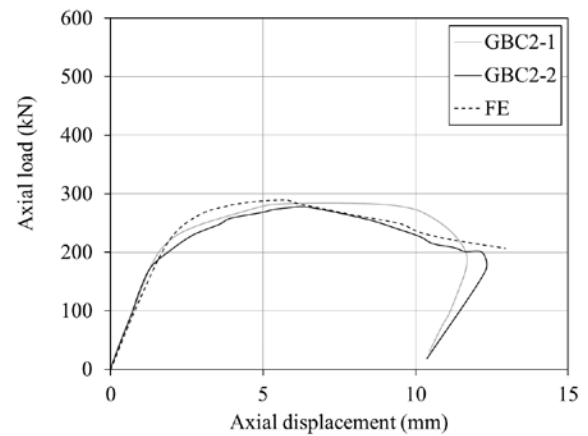
Figure 77 presents axial load *versus* axial displacement curves of the column's responses obtained experimentally and numerically with an eccentricity of (a) $e = 20$ mm and (b) $e = 70$ mm. Figure 78 presents the axial load *versus* deflection at the mid-height of the columns responses obtained experimentally and numerically, respectively, with an eccentricity of (a) $e = 20$ mm and (b) $e = 70$ mm. Figure 79 compares the deformed shape for (a) a general view of beam-column after test and (b) the FE model.

Table 25 - Specimen label, eccentricity and ultimate capacities from Li *et al.* [77].

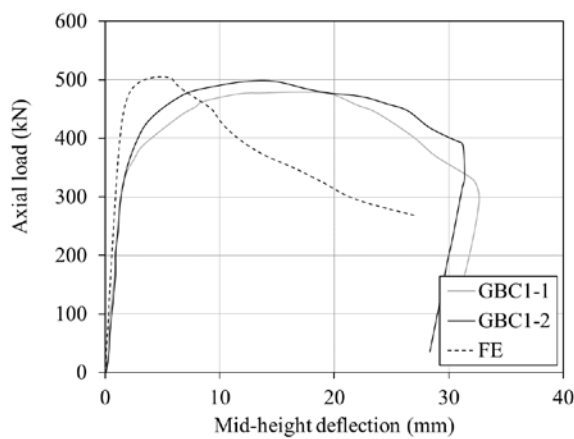
Specimen	e (mm)	$N_{u,test}$ (kN)	$N_{u,FE}$ (kN)	$N_{u,FE}/N_{u,test}$
GBC1-1	20	479	505	1.05
GBC1-2	20	494		1.02
GBC2-1	70	284	289	1.02
GBC2-2	70	276		1.05
Mean				1.035
CoV				0.017



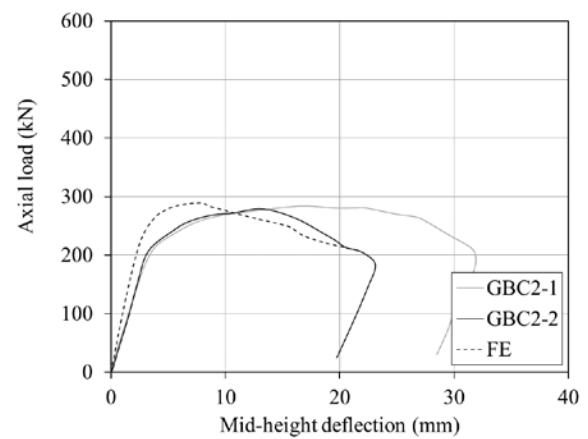
a) Eccentricity = 20 mm;



b) Eccentricity = 70 mm.

Figure 77 - Axial load *versus* axial displacement for CFDST beam-columns.

a) Eccentricity = 20 mm;



b) Eccentricity = 70 mm.

Figure 78 - Axial load *versus* mid-height deflection for CFDST beam-columns.

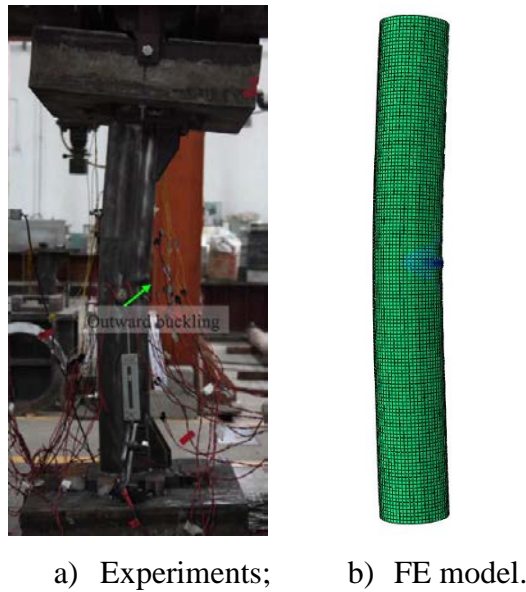


Figure 79 - Comparison of failure mode [77].

As shown in Table 25, the FE model provides good predictions of the ultimate loads, with the mean value of $N_{u,FE}/N_{u,test}$ equal to 1.035 and the coefficient of variation (CoV) of 0.017. The experimental and numerical axial load *versus* axial displacement and axial load *versus* middle-height deflection curves also show that the FE model accurately represents the experiments, where all the curves had three distinctive stages: linear elastic elastic-plastic and descending stage. The failure modes and deformed shape of experimental and numerical results are almost identical: both exhibited overall global buckling in the middle of the beam-columns, followed by an outward buckling in the middle of the column in the outer steel tube and an inward buckling in the middle of the column in the inner steel tube.

4.5.3 Tests from Ibañez *et al.* [87]

The tests from Ibañez *et al.* [87] were conducted on CFDST stub columns with cold-formed circular carbon steel in the outer and inner tubes and conventional concrete and are described in 3.7.6. The Young's modulus E_c of the conventional concrete was calculated as Tao *et al.* [76] recommendation, with a value of 25743 MPa and 44588 MPa. The CFDST beam-columns eccentricity applied, the concrete compressive strength and experimental and numerical ultimate loads $N_{u,test}$ and $N_{u,FE}$ are presented in Table 26. As shown in Table 26, the FE model provides good predictions of the ultimate loads, with the mean value of $N_{u,FE}/N_{u,test}$

equal to 0.967 and the coefficient of variation (CoV) of 0.173. The $N_{u,FE}/N_{u,test}$ values did not present an accurate prediction when the eccentricity value applied was greater than 10 mm due to unexpected higher load capacity in the experiments.

Table 26 - Specimen label, concrete compressive strength, eccentricity and ultimate capacities from Ibañez *et al.* [87].

Specimen	Concrete (MPa)	e (mm)	$N_{u,test}$ (kN)	$N_{u,FE}$ (kN)	$N_{u,FE}/N_{u,test}$
C-C-a-30-00	C30	0	1966	1940	0.99
C-C-a-30-05	C30	5	1853	1809	0.98
C-C-a-30-10	C30	10	1790	1717	0.96
C-C-a-30-20	C30	20	1733	1552	0.90
C-C-a-30-25	C30	25	1920	1478	0.77
C-C-a-30-50	C30	50	1736	1157	0.67
C-C-a-90-00	C90	0	2876	3369	1.17
C-C-a-90-05	C90	5	2792	3041	1.09
C-C-a-90-10	C90	10	2611	2922	1.12
C-C-a-90-20	C90	20	2185	2581	1.18
C-C-a-90-25	C90	25	2185	2440	1.12
C-C-a-90-50	C90	50	1747	1889	1.08
C-C-b-30-00	C30	0	1995	1902	0.95
C-C-b-30-05	C30	5	2085	1792	0.86
C-C-b-30-10	C30	10	1987	1702	0.86
C-C-b-30-20	C30	20	2012	1533	0.76
C-C-b-30-25	C30	25	2016	1459	0.72
C-C-b-30-50	C30	50	1623	1143	0.70
C-C-b-90-00	C90	0	2988	3242	1.09
C-C-b-90-05	C90	5	3151	3086	0.98
C-C-b-90-10	C90	10	3109	2961	0.95
C-C-b-90-20	C90	20	2504	2615	1.04
C-C-b-90-25	C90	25	2627	2473	0.94
C-C-b-90-50	C90	50	1430	1909	1.33
Mean					0.967
CoV					0.173

4.5.4 Zhao *et al.* [88]

Zhao *et al.* [88] conducted tests on CFDST stub columns with circular stainless steel in the outer tube and cold-formed circular carbon steel inner tube and a conventional concrete and

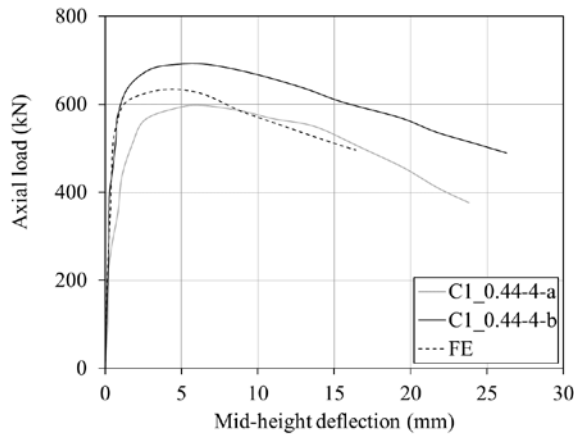
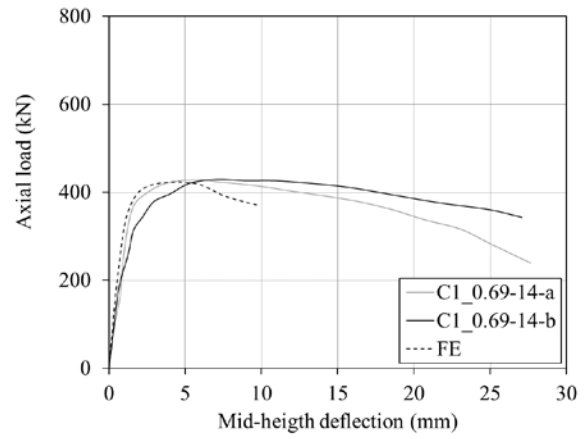
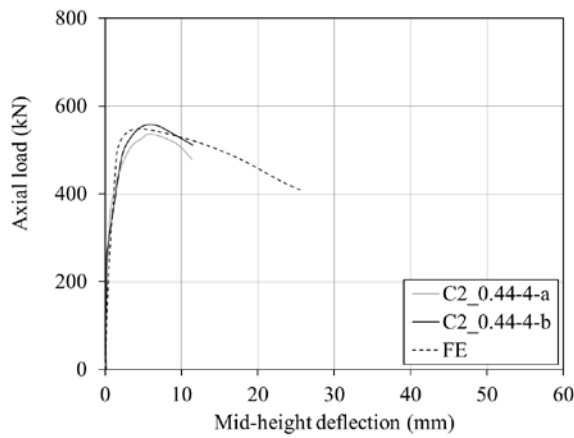
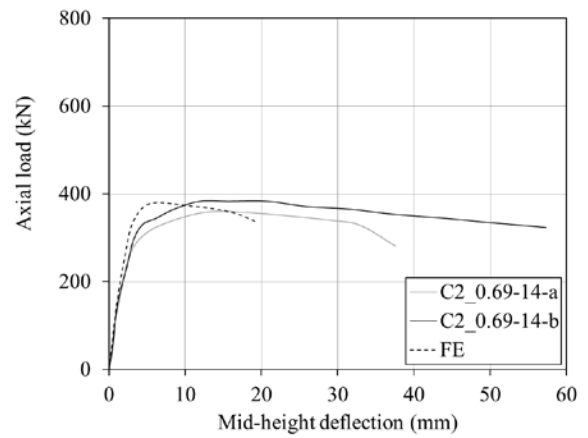
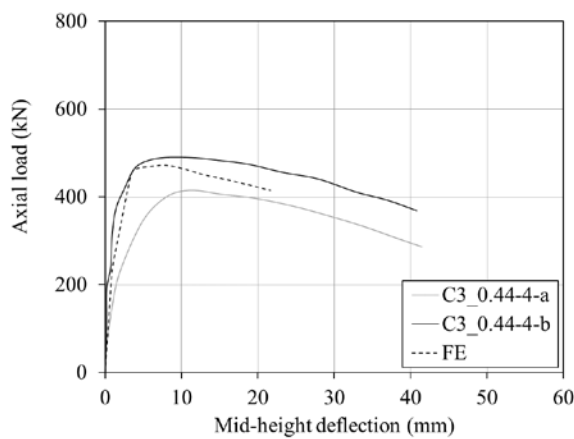
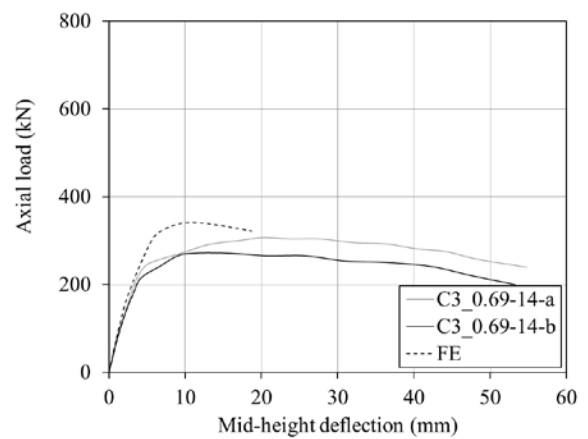
are described in 3.7.7. Rasmussen [86] proposed a constitutive relationship based on a true stress-logarithmic plastic strain. This was used in ABAQUS [16] to represent all the stainless steel outer tube behaviour. The CFDST beam-columns eccentricity applied and experimental and numerical ultimate loads $N_{u,test}$ and $N_{u,FE}$ are presented in Table 27.

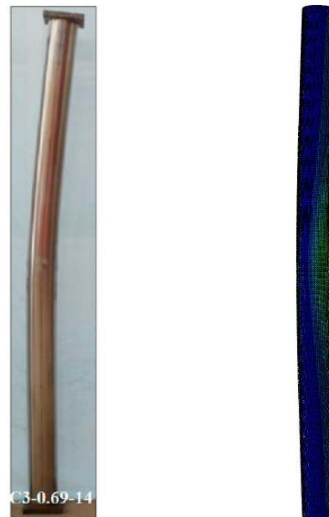
Table 27 - Specimen label, eccentricity and ultimate capacities from Zao *et al.* [88].

Specimen	e (mm)	$N_{u,test}$ (kN)	$N_{u,FE}$ (kN)	$N_{u,FE}/N_{u,test}$
C1-0.44-4-a	4	597	634	1.06
C1-0.44-4-b	4	690		0.92
C1-0.69-a	14	429	424	0.99
C1-0.69-b	14	430		0.99
C2-0.44-4-a	4	536	548	1.02
C2-0.44-4-b	4	556		0.99
C2-0.69-14-a	14	360	381	1.06
C2-0.69-14-b	14	384		0.99
C3-0.44-4-a	4	415	473	1.14
C3-0.44-4-b	4	489		0.97
C3-0.69-14-a	14	307	341	1.11
C3-0.69-14-b	14	272		1.25
Mean				1.040
CoV				0.088

Figure 80 presents the axial load *versus* deflection at the column mid-height responses obtained experimentally and numerically. The graphs are distributed as: (a) eccentricity of 4 mm and length of 800 mm, (b) eccentricity of 14 mm and length of 800 mm, (c) eccentricity of 4 mm and length of 1300 mm, (d) eccentricity of 14 mm and length of 1300 mm, (e) eccentricity of 4 mm and length of 1800 mm and (f) eccentricity of 14 mm and length of 1800 mm, respectively. Figure 81 compares the deformed shape for (a) a general view of beam-column after test and (b) the FE model.

As shown in Table 27, the FE model provides good predictions of the ultimate loads, with the mean value of $N_{u,FE}/N_{u,test}$ equal to 1.040 and the coefficient of variation (CoV) of 0.088. The experimental and numerical axial load *versus* middle-height deflection curves also show that the FE model accurately represents the experiments, where all the curves had three distinctive stages: linear elastic, elastic-plastic, and descending stage. The failure modes and deformed shape of experimental and numerical results are almost identical: both exhibited overall global buckling in the middle of the beam-columns.

a) $e = 4$ mm and $L = 800$ mm;b) $e = 14$ mm and $L = 800$ mm;c) $e = 4$ mm and $L = 1300$ mm;d) $e = 14$ mm and $L = 1300$ mm;e) $e = 4$ mm and $L = 1800$ mm;f) $e = 14$ mm and $L = 1800$ mm.Figure 80 - Axial load *versus* mid-height deflection for CFDST beam-columns.



a) Experiments; b) FE model.

Figure 81 - Comparison of failure mode [88].

4.6 Validation of the numerical model – Pure bending

The FE model's accuracy for pure bending was evaluated by comparing the full load-deformation responses, ultimate loads, deformed shapes and failure modes with those obtained from Li *et al.* [77] experiments. The stress *versus* strain model for confined conventional concrete in compression of all the validated FE models was proposed by Tao *et al.* [76]. Gardner and Yun [83] proposed the constitutive relationship. The true stress-logarithmic plastic strain in ABAQUS [16] was employed to represent all the cold-formed carbon behaviour steel tubes in the FE model's validation.

The FE model for beams was only designed to demonstrate the flexural behaviour under pure bending. The tests from Li *et al.* [77] were conducted on the CFDST beam and were described in 3.7.8. The moment *versus* deflection at the mid-span of the beam responses obtained experimentally and numerically are shown in Figure 82. The experimental beams' ultimate flexural strength was: GB-1 $M_{u,test}$ 28.5 kNm and GB-2 $M_{u,test}$ 30.8 kNm. The ultimate flexural strength of the numerical beam was $M_{u,FE}$ 26.85 kNm, summarized in Table 28. Figure 83 compares the deformed shape for (a) a beam after a pure bending test and (b) the FE model.

Table 28 - Specimen label and bending capacities from Li *et al.* [77].

Specimen	$M_{u,test}$ (kNm)	$M_{u,FE}$ (kN)	$M_{u,FE}/M_{u,test}$
GB-1	28.5	26.85	0.94
GB-2	30.8		0.87
Mean			0.905
CoV			0.055

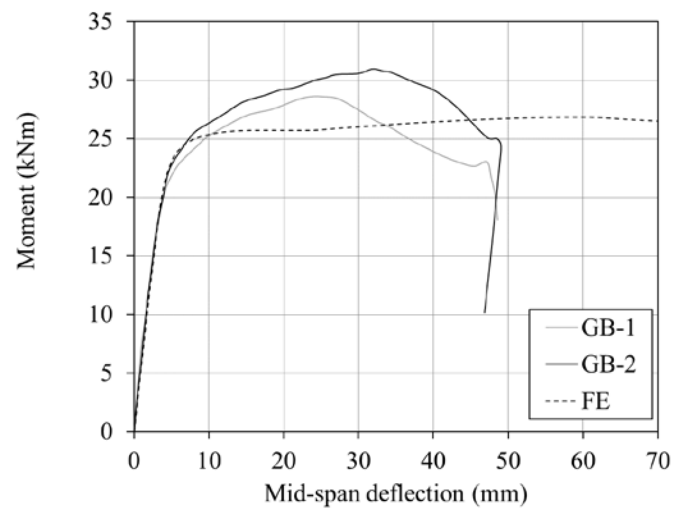
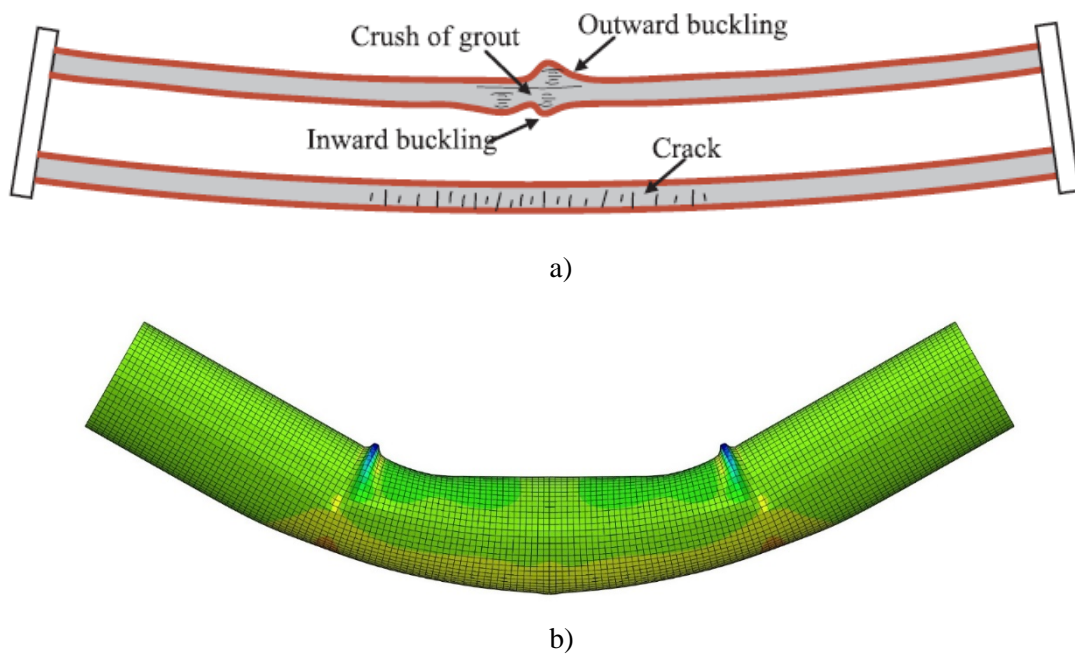
Figure 82 - Moment *versus* mid-span deflection for the CFDST beam under pure bending.

Figure 83 - Comparison of failure mode [77].

As shown in Table 28, the FE model provides good predictions of the ultimate flexural strength, with the mean value of $M_{u,FE}/M_{u,test}$ equal to 0.905 and the coefficient of variation (CoV) of 0.055. The experimental and numerical moment *versus* mid-span deflection curves also shows that the FE model accurately represents the experiments. All the curves had two distinctive stages, initial elastic and elastic-plastic, followed by the failure. The failure modes and deformed shape of experimental and numerical results are very similar: both exhibited overall flexural deformation at the middle length of the beam, with an outward buckling in the outer steel tube and an inward buckling in the inner steel tube.

4.7 Summary of FE ultimate load predictions

It is clear from the data presented from the items above that the FE model provides a good depiction of load-displacement, load-axial strain and moment-displacement response. The responses' overall shape is very similar, and the FE model reasonably well depicts the key behavioural aspects such as initial stiffness, yielding, and capacity. Concerning the data in Table 29, it is again shown that the FE model provides an accurate and reliable prediction of the columns' ultimate capacity, with a mean $N_{u,FE}/N_{u,test}$ value of 1.00 and a coefficient of variation (CoV) of 0.11. These values include all the data presented above, including the tests with CFDST columns from this thesis and the literature data for columns, beam-columns and beams. All the deformed shape images presented in the previous items indicated the failure modes, which show the outward-only local buckling of the outer steel tube and the inner steel tube inward-only local buckling. Overall, it can be concluded that the FE model is capable of realistically depicting the overall and ultimate behaviour of CFDST stub columns, beam-columns and beams and thus is suitable for further parametric and design studies.

Table 29 - Experimental and FE model ultimate load comparison.

	Failure modes	Specimen	$N_{u,test}$ (kN) or $M_{u,test}$ (kNm)	$N_{u,FE}$ (kN) or $M_{u,FE}$ (kNm)	$N_{u,FE}/N_{u,test}$ OR $M_{u,FE}/M_{u,test}$
Columns	Local buckling: outward buckling of the outer steel tube and inward buckling of the inner	NAC1	1941	1940	1.00
		NAC2	1865		1.04
		NAC3	1649	1670	1.01
		NAC4	1612		1.04
		RAC1	2087	1966	0.94
		RAC2	2075		0.95
		RAC3	1685		1.01

steel tube followed by the concrete crushing in the region of the outward buckling.	RAC4	1693		1.00	
	AC140×3-HC22×4	1410	1548	1.10	
	AC140×3-HC32×6	1423	1662	1.17	
	AC140×3-HC38×8	1626	1698	1.04	
	AC140×3-HC55×11	2543	2539	1.00	
	AC140×3-HC89×4	2025	1975	0.98	
	AC165×3-HC22×4	1750	1747	1.00	
	AC165×3-HC32×6	1943	1865	0.96	
	AC165×3-HC89×4	2375	2279	0.96	
	C1-1_220×3.62-159×3.72	2537	2439	0.96	
	C1-2_220×3.62-159×3.72	2566		0.95	
	C2-1_220×3.62-106×3.72	3436	2942	0.86	
	C2-2_220×3.62-106×3.72	3506		0.84	
	Beam-columns	Global buckling in the middle of the beam-column.	pcc1-1a	664	696
pcc1-1b			638	1.09	
pcc1-2a			536	568	1.06
pcc1-2b			549		1.03
pcc1-3a			312	325	1.04
pcc1-3b			312		1.04
pcc2-1a			620	622	1.00
pcc2-1b			595		1.05
pcc2-2a			400	412	1.03
pcc2-2b			394		1.05
pcc2-3a			228	248	1.09
pcc2-3b			227		1.09
GBC1-1			479	505	1.05
GBC1-2			494		1.02
GBC2-1			284	289	1.02
GBC2-2			276		1.05
C-C-a-30-00			1966	1940	0.99
C-C-a-30-05			1853	1809	0.98
C-C-a-30-10			1790	1717	0.96
C-C-a-30-20			1733	1552	0.90
C-C-a-30-25			1920	1478	0.77
C-C-a-30-50			1736	1157	0.67
C-C-a-90-00			2876	3369	1.17
C-C-a-90-05			2792	3041	1.09
C-C-a-90-10			2611	2922	1.12
C-C-a-90-20			2185	2581	1.18
C-C-a-90-25			2185	2440	1.12
C-C-a-90-50			1747	1889	1.08
C-C-b-30-00			1995	1902	0.95
C-C-b-30-05			2085	1792	0.86
C-C-b-30-10			1987	1702	0.86
C-C-b-30-20			2012	1533	0.76

		C-C-b-30-25	2016	1459	0.72
		C-C-b-30-50	1623	1143	0.70
		C-C-b-90-00	2988	3242	1.09
		C-C-b-90-05	3151	3086	0.98
		C-C-b-90-10	3109	2961	0.95
		C-C-b-90-20	2504	2615	1.04
		C-C-b-90-25	2627	2473	0.94
		C-C-b-90-50	1430	1909	1.33
		C1-0.44-4-a	597	634	1.06
		C1-0.44-4-b	690		0.92
		C1-0.69-a	429	424	0.99
		C1-0.69-b	430		0.99
		C2-0.44-4-a	536	548	1.02
		C2-0.44-4-b	556		0.99
		C2-0.69-14-a	360	381	1.06
		C2-0.69-14-b	384		0.99
		C3-0.44-4-a	415	473	1.14
		C3-0.44-4-b	489		0.97
		C3-0.69-14-a	307	341	1.11
		C3-0.69-14-b	272		1.25
Beams	Global flexural buckling in the middle of the beam.	GB-1	28	26.85	0.96
		GB-2	30.8		0.87
Mean	1.00				
Standard deviation	0.11				
CoV	0.11				

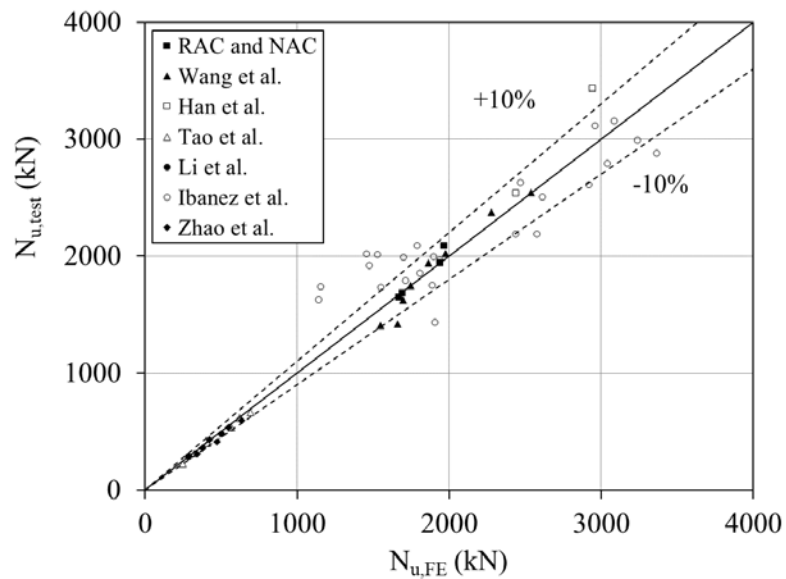


Figure 84 - Tests axial compression load *versus* FE axial compression load.

The experiments and the finite element model results for axial compression load from Table 29 are presented in Figure 84. The results close to the diagonal line represents the perfect situation where the experiment result is equal to the FE result. The dashed lines represent limits +10% above and -10% below for $N_{u,test}$ to be equal to $N_{u,FE}$. The marked results are the experiments studied in this thesis and the experiments from the literature used to validate the FE model. All the studied experiments are very close to the FE results (i.e., close to the diagonal line), where only Ibañez *et al.* [87] presented values distant from +10% and -10%, due to probably problems during the tests. This comparison enables evaluating the accuracy of the finite element model.

5 PARAMETRIC STUDY

5.1 Generalities

The validated numerical model is employed in the current chapter to develop a parametric study to generate a higher range of results and investigate CFDST stub columns' overall behaviour under concentric and eccentric axial loads, flexural response focusing on determining the influence of the most relevant parameters. Throughout the parametric study, it was assumed that the columns were made of austenitic stainless steel in the outer tube, carbon steel in the inner tube and RCA in the concrete infill. The material properties of the steel tubes and the RAC were previously described in section 3. Therefore, the inner carbon steel tube has 375 MPa yield stress. The corresponding value for the stainless steel outer tube $f_{0.2}$ is 419 MPa. The concrete contains RAC with a replacement ratio of 50%, with 33 MPa and 80 MPa concrete compressive strengths.

Two groups of parametric studies were conducted in this thesis. Firstly, CFDST stub columns subjected to concentric load. This was followed by CFDST stub beam-columns subjected to eccentric loads and CFDST beams under a pure bending moment.

5.2 Simulations of members under concentric loads

The variables investigated in the parametric study of CFDST stubs columns under concentric axial compression were: the hollow ratio (γ), the outer tube diameter (D), the inner tube diameter (d) and the inner tube thickness (t_{si}). These variables were chosen, aiming to determine their influence in the concrete confinement improvement. As greater outer tube diameter (D) and smaller inner steel tube diameter (d) provides greater concrete area and consequently greater load capacity, thicker inner steel tubes also increase the load capacity. All the columns had the same experimental value for the total length $L = 500$ mm and outer tube thickness of $t_{so} = 2.8$ mm, totalizing 36 numerical models. The variables investigated range is presented in Table 30.

Table 30 - Cross-sections geometrical properties - CFDST columns.

Specimens	Hollow ratio χ	Outer tube diameter D (mm)	Inner tube diameter d (mm)	t_{st} (mm)
C141.3 x 2.8_60.3 x 4.5	0.44	141.3	60.3	4.5
C141.3 x 2.8_76.2 x 4.5	0.56	141.3	76.2	4.5
C141.3 x 2.8_88.9 x 4.5	0.65	141.3	88.9	4.5
C141.3 x 2.8_108.4 x 4.5	0.80	141.3	108.4	4.5
C141.3 x 2.8_114.3 x 4.5	0.84	141.3	114.3	4.5
C141.3 x 2.8_60.3 x 5.5	0.44	141.3	60.3	5.5
C141.3 x 2.8_76.2 x 5.5	0.56	141.3	76.2	5.5
C141.3 x 2.8_88.9 x 5.5	0.65	141.3	88.9	5.5
C141.3 x 2.8_108.4 x 5.5	0.80	141.3	108.4	5.5
C141.3 x 2.8_114.3 x 5.5	0.84	141.3	114.3	5.5
C168.3 x 2.8_60.3 x 4.5	0.37	168.3	60.3	4.5
C168.3 x 2.8_76.2 x 4.5	0.47	168.3	76.2	4.5
C168.3 x 2.8_88.9 x 4.5	0.55	168.3	88.9	4.5
C168.3 x 2.8_108.4 x 4.5	0.67	168.3	108.4	4.5
C168.3 x 2.8_114.3 x 4.5	0.70	168.3	114.3	4.5
C168.3 x 2.8_141.3 x 4.5	0.87	168.3	141.3	4.5
C168.3 x 2.8_60.3 x 5.5	0.37	168.3	60.3	5.5
C168.3 x 2.8_76.2 x 5.5	0.47	168.3	76.2	5.5
C168.3 x 2.8_88.9 x 5.5	0.55	168.3	88.9	5.5
C168.3 x 2.8_108.4 x 5.5	0.67	168.3	108.4	5.5
C168.3 x 2.8_114.3 x 5.5	0.70	168.3	114.3	5.5
C168.3 x 2.8_141.3 x 5.5	0.87	168.3	141.3	5.5
C219.1 x 2.8_60.3 x 4.5	0.28	219.1	60.3	4.5
C219.1 x 2.8_76.2 x 4.5	0.36	219.1	76.2	4.5
C219.1 x 2.8_88.9 x 4.5	0.42	219.1	88.9	4.5
C219.1 x 2.8_108.4 x 4.5	0.51	219.1	108.4	4.5
C219.1 x 2.8_114.3 x 4.5	0.54	219.1	114.3	4.5
C219.1 x 2.8_141.3 x 4.5	0.66	219.1	141.3	4.5
C219.1 x 2.8_168.3 x 4.5	0.79	219.1	168.3	4.5
C219.1 x 2.8_60.3 x 5.5	0.28	219.1	60.3	5.5
C219.1 x 2.8_76.2 x 5.5	0.36	219.1	76.2	5.5
C219.1 x 2.8_88.9 x 5.5	0.42	219.1	88.9	5.5
C219.1 x 2.8_108.4 x 5.5	0.51	219.1	108.4	5.5
C219.1 x 2.8_114.3 x 5.5	0.54	219.1	114.3	5.5
C219.1 x 2.8_141.3 x 5.5	0.66	219.1	141.3	5.5
C219.1 x 2.8_168.3 x 5.5	0.79	219.1	168.3	5.5

5.3 Simulations of members under eccentric axial compression and pure bending

The parametric cross-sections of CFDST stub beam-columns under eccentric compression load and pure bending moment were selected according to their outer tube slenderness limits (D/t_{so}) in AISC 360 [89], aiming to cover a high range of cross-sections variation. The slenderness limits for circular elements subjected to compression and flexural are:

$$\lambda_p = 0.07 \left(\frac{E}{f_y} \right) \quad (102)$$

$$\lambda_r = 0.31 \left(\frac{E}{f_y} \right) \quad (103)$$

$$\begin{aligned} \frac{D}{t_{so}} \leq \lambda_p &\rightarrow \text{compact} \\ \lambda_p < \frac{D}{t_{so}} < \lambda_r &\rightarrow \text{noncompact} \\ \frac{D}{t_{so}} \geq \lambda_r &\rightarrow \text{slender} \end{aligned} \quad (104)$$

In addition to the slenderness limit and through the CFDST stub columns under concentric axial loads observed in the last item of the thesis, the assessed parameters were: the hollow ratio (γ), the outer tube diameter (D) and the outer tube thickness (t_{so}). It was found from the previous concentric load parametric study that the parameters which most influences the CFDST load capacity are the outer tube diameter (D) and thickness (t_{so}). Moreover, the hollow ratio (γ) was chosen to investigate the prerogative from Han *et al.* [46], where the load capacity and the stiffness of the CFDST columns decrease as the hollow ratio (γ) decreases. The D/d ratio and inner tube thickness (t_{si}) equal to 5 mm were kept constant in the parametric study. The beam-column length (L) was calculated as proposed by Han *et al.* [46], i.e., 2.5 times the outer tube diameter (D).

The pure bending model considered the beams length (L) as two times the beam-column lengths. The material properties were equal to the ones adopted in the CFDST stub columns under concentric axial compression parametric study except for the concrete compressive strength, which was considered two values: $f_c = 33$ MPa as in the experiments and $f_c = 80$ MPa, aiming to evaluate the CFDST beam-columns response to a higher concrete compressive strength.

The eccentricity values were selected to cover multiple points in the M-N interaction curve encompassing a percentage of the outer tube diameter. The beam-columns and beams will be presented as BC and B, respectively. The beams were only studied under pure bending (PB). A total of 360 models were simulated in these parametric studies, with cross-sections illustrated in Table 31 and Figure 85.

Table 31 - Cross-sections geometrical properties - CFDST beam-columns and beams.

Specimens	D/t_{so}	D/t_{si}	$e_{-}\%D$ (mm)	Hollow ratio χ	Outer tube diameter D (mm)	t_{so} (mm)	Inner tube diameter d (mm)	L (mm)
BC200 x 1_100 x 5 – e0%D	200	20	0	0.51	200	1	100	500
BC200 x 1_100 x 5 – e2.5%D	200	20	5	0.51	200	1	100	500
BC200 x 1_100 x 5 – e7.5%D	200	20	15	0.51	200	1	100	500
BC200 x 1_100 x 5 – e15%D	200	20	30	0.51	200	1	100	500
BC200 x 1_100 x 5 – e30%D	200	20	60	0.51	200	1	100	500
BC200 x 1_100 x 5 – e50%D	200	20	100	0.51	200	1	100	500
BC200 x 1_100 x 5 – e85%D	200	20	170	0.51	200	1	100	500
BC200 x 1_100 x 5 – e200%D	200	20	400	0.51	200	1	100	500
B200 x 1_100 x 5 – PB	200	20	-	0.51	200	1	100	1000
BC200 x 5_100 x 5 – e0%D	40	20	0	0.53	200	5	100	500
BC200 x 5_100 x 5 – e2.5%D	40	20	5	0.53	200	5	100	500
BC200 x 5_100 x 5 – e7.5%D	40	20	15	0.53	200	5	100	500
BC200 x 5_100 x 5 – e15%D	40	20	30	0.53	200	5	100	500
BC200 x 5_100 x 5 – e30%D	40	20	60	0.53	200	5	100	500
BC200 x 5_100 x 5 – e50%D	40	20	100	0.53	200	5	100	500
BC200 x 5_100 x 5 – e85%D	40	20	170	0.53	200	5	100	500
BC200 x 5_100 x 5 – e200%D	40	20	400	0.53	200	5	100	500
B200 x 5_100 x 5 – PB	40	20	-	0.53	200	5	100	1000
BC200 x 10_100 x 5 – e0%D	20	20	0	0.56	200	10	100	500
BC200 x 10_100 x 5 – e2.5%D	20	20	5	0.56	200	10	100	500
BC200 x 10_100 x 5 – e7.5%D	20	20	15	0.56	200	10	100	500
BC200 x 10_100 x 5 – e15%D	20	20	30	0.56	200	10	100	500
BC200 x 10_100 x 5 – e30%D	20	20	60	0.56	200	10	100	500
BC200 x 10_100 x 5 – e50%D	20	20	100	0.56	200	10	100	500
BC200 x 10_100 x 5 – e85%D	20	20	170	0.56	200	10	100	500
BC200 x 10_100 x 5 – e200%D	20	20	400	0.56	200	10	100	500
B200 x 10_100 x 5 – PB	20	20	-	0.56	200	10	100	1000
BC300 x 1_150 x 5 – e0%D	300	30	0	0.50	300	1	150	750
BC300 x 1_150 x 5 – e2.5%D	300	30	7.5	0.50	300	1	150	750
BC300 x 1_150 x 5 – e7.5%D	300	30	22.5	0.50	300	1	150	750
BC300 x 1_150 x 5 – e15%D	300	30	45	0.50	300	1	150	750
BC300 x 1_150 x 5 – e30%D	300	30	90	0.50	300	1	150	750
BC300 x 1_150 x 5 – e50%D	300	30	150	0.50	300	1	150	750

BC300 x 1_150 x 5 – e85%D	300	30	255	0.50	300	1	150	750
BC300 x 1_150 x 5 – e200%D	300	30	600	0.50	300	1	150	750
B300 x 1_150 x 5 – PB	300	30	-	0.50	300	1	150	1500
BC300 x 5_150 x 5 – e0%D	60	30	0	0.52	300	5	150	750
BC300 x 5_150 x 5 – e2.5%D	60	30	7.5	0.52	300	5	150	750
BC300 x 5_150 x 5 – e7.5%D	60	30	22.5	0.52	300	5	150	750
BC300 x 5_150 x 5 – e15%D	60	30	45	0.52	300	5	150	750
BC300 x 5_150 x 5 – e30%D	60	30	90	0.52	300	5	150	750
BC300 x 5_150 x 5 – e50%D	60	30	150	0.52	300	5	150	750
BC300 x 5_150 x 5 – e85%D	60	30	255	0.52	300	5	150	750
BC300 x 5_150 x 5 – e200%D	60	30	600	0.52	300	5	150	750
B300 x 5_150 x 5 – PB	60	30	-	0.52	300	5	150	1500
BC300 x 10_150 x 5 – e0%D	30	30	0	0.54	300	10	150	750
BC300 x 10_150 x 5 – e2.5%D	30	30	7.5	0.54	300	10	150	750
BC300 x 10_150 x 5 – e7.5%D	30	30	22.5	0.54	300	10	150	750
BC300 x 10_150 x 5 – e15%D	30	30	45	0.54	300	10	150	750
BC300 x 10_150 x 5 – e30%D	30	30	90	0.54	300	10	150	750
BC300 x 10_150 x 5 – e50%D	30	30	150	0.54	300	10	150	750
BC300 x 10_150 x 5 – e85%D	30	30	255	0.54	300	10	150	750
BC300 x 10_150 x 5 – e200%D	30	30	600	0.54	300	10	150	750
B300 x 10_150 x 5 – PB	30	30	-	0.54	300	10	150	1500
BC300 x 20_150 x 5 – e0%D	15	30	0	0.58	300	20	150	750
BC300 x 20_150 x 5 – e2.5%D	15	30	7.5	0.58	300	20	150	750
BC300 x 20_150 x 5 – e7.5%D	15	30	22.5	0.58	300	20	150	750
BC300 x 20_150 x 5 – e15%D	15	30	45	0.58	300	20	150	750
BC300 x 20_150 x 5 – e30%D	15	30	90	0.58	300	20	150	750
BC300 x 20_150 x 5 – e50%D	15	30	150	0.58	300	20	150	750
BC300 x 20_150 x 5 – e85%D	15	30	255	0.58	300	20	150	750
BC300 x 20_150 x 5 – e200%D	15	30	600	0.58	300	20	150	750
B300 x 20_150 x 5 – PB	15	30	-	0.58	300	20	150	1500
BC400 x 1_200 x 5 – e0%D	400	40	0	0.50	400	1	200	1000
BC400 x 1_200 x 5 – e2.5%D	400	40	10	0.50	400	1	200	1000
BC400 x 1_200 x 5 – e7.5%D	400	40	30	0.50	400	1	200	1000
BC400 x 1_200 x 5 – e15%D	400	40	60	0.50	400	1	200	1000
BC400 x 1_200 x 5 – e30%D	400	40	120	0.50	400	1	200	1000
BC400 x 1_200 x 5 – e50%D	400	40	200	0.50	400	1	200	1000
BC400 x 1_200 x 5 – e85%D	400	40	340	0.50	400	1	200	1000
BC400 x 1_200 x 5 – e200%D	400	40	800	0.50	400	1	200	1000
B400 x 1_200 x 5 – PB	400	40	-	0.50	400	1	200	2000
BC400 x 5_200 x 5 – e0%D	80	40	0	0.51	400	5	200	1000
BC400 x 5_200 x 5 – e2.5%D	80	40	10	0.51	400	5	200	1000
BC400 x 5_200 x 5 – e7.5%D	80	40	30	0.51	400	5	200	1000
BC400 x 5_200 x 5 – e15%D	80	40	60	0.51	400	5	200	1000
BC400 x 5_200 x 5 – e30%D	80	40	120	0.51	400	5	200	1000
BC400 x 5_200 x 5 – e50%D	80	40	200	0.51	400	5	200	1000
BC400 x 5_200 x 5 – e85%D	80	40	340	0.51	400	5	200	1000

BC400 x 5_200 x 5 – e200%D	80	40	800	0.51	400	5	200	1000
B400 x 5_200 x 5 – PB	80	40	-	0.51	400	5	200	2000
BC400 x 10_200 x 5 – e0%D	40	40	0	0.53	400	10	200	1000
BC400 x 10_200 x 5 – e2.5%D	40	40	10	0.53	400	10	200	1000
BC400 x 10_200 x 5 – e7.5%D	40	40	30	0.53	400	10	200	1000
BC400 x 10_200 x 5 – e15%D	40	40	60	0.53	400	10	200	1000
BC400 x 10_200 x 5 – e30%D	40	40	120	0.53	400	10	200	1000
BC400 x 10_200 x 5 – e50%D	40	40	200	0.53	400	10	200	1000
BC400 x 10_200 x 5 – e85%D	40	40	340	0.53	400	10	200	1000
BC400 x 10_200 x 5 – e200%D	40	40	800	0.53	400	10	200	1000
B400 x 10_200 x 5 – PB	40	40	-	0.53	400	10	200	2000
BC400 x 20_200 x 5 – e0%D	20	40	0	0.56	400	20	200	1000
BC400 x 20_200 x 5 – e2.5%D	20	40	10	0.56	400	20	200	1000
BC400 x 20_200 x 5 – e7.5%D	20	40	30	0.56	400	20	200	1000
BC400 x 20_200 x 5 – e15%D	20	40	60	0.56	400	20	200	1000
BC400 x 20_200 x 5 – e30%D	20	40	120	0.56	400	20	200	1000
BC400 x 20_200 x 5 – e50%D	20	40	200	0.56	400	20	200	1000
BC400 x 20_200 x 5 – e85%D	20	40	340	0.56	400	20	200	1000
BC400 x 20_200 x 5 – e200%D	20	40	800	0.56	400	20	200	1000
B400 x 20_200 x 5 – PB	20	40	-	0.56	400	20	200	2000
BC500 x 1_250 x 5 – e0%D	500	50	0	0.50	500	1	250	1250
BC500 x 1_250 x 5 – e2.5%D	500	50	12.5	0.50	500	1	250	1250
BC500 x 1_250 x 5 – e7.5%D	500	50	37.5	0.50	500	1	250	1250
BC500 x 1_250 x 5 – e15%D	500	50	75	0.50	500	1	250	1250
BC500 x 1_250 x 5 – e30%D	500	50	150	0.50	500	1	250	1250
BC500 x 1_250 x 5 – e50%D	500	50	250	0.50	500	1	250	1250
BC500 x 1_250 x 5 – e85%D	500	50	425	0.50	500	1	250	1250
BC500 x 1_250 x 5 – e200%D	500	50	1000	0.50	500	1	250	1250
B500 x 1_250 x 5 – PB	500	50	-	0.50	500	1	250	2500
BC500 x 5_250 x 5 – e0%D	100	50	0	0.51	500	5	250	1250
BC500 x 5_250 x 5 – e2.5%D	100	50	12.5	0.51	500	5	250	1250
BC500 x 5_250 x 5 – e7.5%D	100	50	37.5	0.51	500	5	250	1250
BC500 x 5_250 x 5 – e15%D	100	50	75	0.51	500	5	250	1250
BC500 x 5_250 x 5 – e30%D	100	50	150	0.51	500	5	250	1250
BC500 x 5_250 x 5 – e50%D	100	50	250	0.51	500	5	250	1250
BC500 x 5_250 x 5 – e85%D	100	50	425	0.51	500	5	250	1250
BC500 x 5_250 x 5 – e200%D	100	50	1000	0.51	500	5	250	1250
B500 x 5_250 x 5 – PB	100	50	-	0.51	500	5	250	2500
BC500 x 10_250 x 5 – e0%D	50	50	0	0.52	500	10	250	1250
BC500 x 10_250 x 5 – e2.5%D	50	50	12.5	0.52	500	10	250	1250
BC500 x 10_250 x 5 – e7.5%D	50	50	37.5	0.52	500	10	250	1250
BC500 x 10_250 x 5 – e15%D	50	50	75	0.52	500	10	250	1250
BC500 x 10_250 x 5 – e30%D	50	50	150	0.52	500	10	250	1250
BC500 x 10_250 x 5 – e50%D	50	50	250	0.52	500	10	250	1250
BC500 x 10_250 x 5 – e85%D	50	50	425	0.52	500	10	250	1250
BC500 x 10_250 x 5 – e200%D	50	50	1000	0.52	500	10	250	1250

B500 x 10_250 x 5 – PB	50	50	-	0.52	500	10	250	2500
BC500 x 20_250 x 5 – e0%D	25	50	0	0.54	500	20	250	1250
BC500 x 20_250 x 5 – e2.5%D	25	50	12.5	0.54	500	20	250	1250
BC500 x 20_250 x 5 – e7.5%D	25	50	37.5	0.54	500	20	250	1250
BC500 x 20_250 x 5 – e15%D	25	50	75	0.54	500	20	250	1250
BC500 x 20_250 x 5 – e30%D	25	50	150	0.54	500	20	250	1250
BC500 x 20_250 x 5 – e50%D	25	50	250	0.54	500	20	250	1250
BC500 x 20_250 x 5 – e85%D	25	50	425	0.54	500	20	250	1250
BC500 x 20_250 x 5 – e200%D	25	50	1000	0.54	500	20	250	1250
B500 x 20_250 x 5 – PB	25	50	-	0.54	500	20	250	2500
BC600 x 1_300 x 5 – e0%D	600	60	0	0.50	600	1	300	1500
BC600 x 1_300 x 5 – e2.5%D	600	60	15	0.50	600	1	300	1500
BC600 x 1_300 x 5 – e7.5%D	600	60	45	0.50	600	1	300	1500
BC600 x 1_300 x 5 – e15%D	600	60	90	0.50	600	1	300	1500
BC600 x 1_300 x 5 – e30%D	600	60	180	0.50	600	1	300	1500
BC600 x 1_300 x 5 – e50%D	600	60	300	0.50	600	1	300	1500
BC600 x 1_300 x 5 – e85%D	600	60	510	0.50	600	1	300	1500
BC600 x 1_300 x 5 – e200%D	600	60	1200	0.50	600	1	300	1500
B600 x 1_300 x 5 – PB	600	60	-	0.50	600	1	300	3000
BC600 x 5_300 x 5 – e0%D	120	60	0	0.51	600	5	300	1500
BC600 x 5_300 x 5 – e2.5%D	120	60	15	0.51	600	5	300	1500
BC600 x 5_300 x 5 – e7.5%D	120	60	45	0.51	600	5	300	1500
BC600 x 5_300 x 5 – e15%D	120	60	90	0.51	600	5	300	1500
BC600 x 5_300 x 5 – e30%D	120	60	180	0.51	600	5	300	1500
BC600 x 5_300 x 5 – e50%D	120	60	300	0.51	600	5	300	1500
BC600 x 5_300 x 5 – e85%D	120	60	510	0.51	600	5	300	1500
BC600 x 5_300 x 5 – e200%D	120	60	1200	0.51	600	5	300	1500
B600 x 5_300 x 5 – PB	120	60	-	0.51	600	5	300	3000
BC600 x 10_300 x 5 – e0%D	60	60	0	0.52	600	10	300	1500
BC600 x 10_300 x 5 – e2.5%D	60	60	15	0.52	600	10	300	1500
BC600 x 10_300 x 5 – e7.5%D	60	60	45	0.52	600	10	300	1500
BC600 x 10_300 x 5 – e15%D	60	60	90	0.52	600	10	300	1500
BC600 x 10_300 x 5 – e30%D	60	60	180	0.52	600	10	300	1500
BC600 x 10_300 x 5 – e50%D	60	60	300	0.52	600	10	300	1500
BC600 x 10_300 x 5 – e85%D	60	60	510	0.52	600	10	300	1500
BC600 x 10_300 x 5 – e200%D	60	60	1200	0.52	600	10	300	1500
B600 x 10_300 x 5 – PB	60	60	-	0.52	600	10	300	3000
BC600 x 20_300 x 5 – e0%D	30	60	0	0.54	600	20	300	1500
BC600 x 20_300 x 5 – e2.5%D	30	60	15	0.54	600	20	300	1500
BC600 x 20_300 x 5 – e7.5%D	30	60	45	0.54	600	20	300	1500
BC600 x 20_300 x 5 – e15%D	30	60	90	0.54	600	20	300	1500
BC600 x 20_300 x 5 – e30%D	30	60	180	0.54	600	20	300	1500
BC600 x 20_300 x 5 – e50%D	30	60	300	0.54	600	20	300	1500
BC600 x 20_300 x 5 – e85%D	30	60	510	0.54	600	20	300	1500
BC600 x 20_300 x 5 – e200%D	30	60	1200	0.54	600	20	300	1500
B600 x 20_300 x 5 – PB	30	60	-	0.54	600	20	300	3000

BC600 x 30_300 x 5 – e0%D	20	60	0	0.56	600	30	300	1500
BC600 x 30_300 x 5 – e2.5%D	20	60	15	0.56	600	30	300	1500
BC600 x 30_300 x 5 – e7.5%D	20	60	45	0.56	600	30	300	1500
BC600 x 30_300 x 5 – e15%D	20	60	90	0.56	600	30	300	1500
BC600 x 30_300 x 5 – e30%D	20	60	180	0.56	600	30	300	1500
BC600 x 30_300 x 5 – e50%D	20	60	300	0.56	600	30	300	1500
BC600 x 30_300 x 5 – e85%D	20	60	510	0.56	600	30	300	1500
BC600 x 30_300 x 5 – e200%D	20	60	1200	0.56	600	30	300	1500
B600 x 30_300 x 5 – PB	20	60	-	0.56	600	30	300	3000

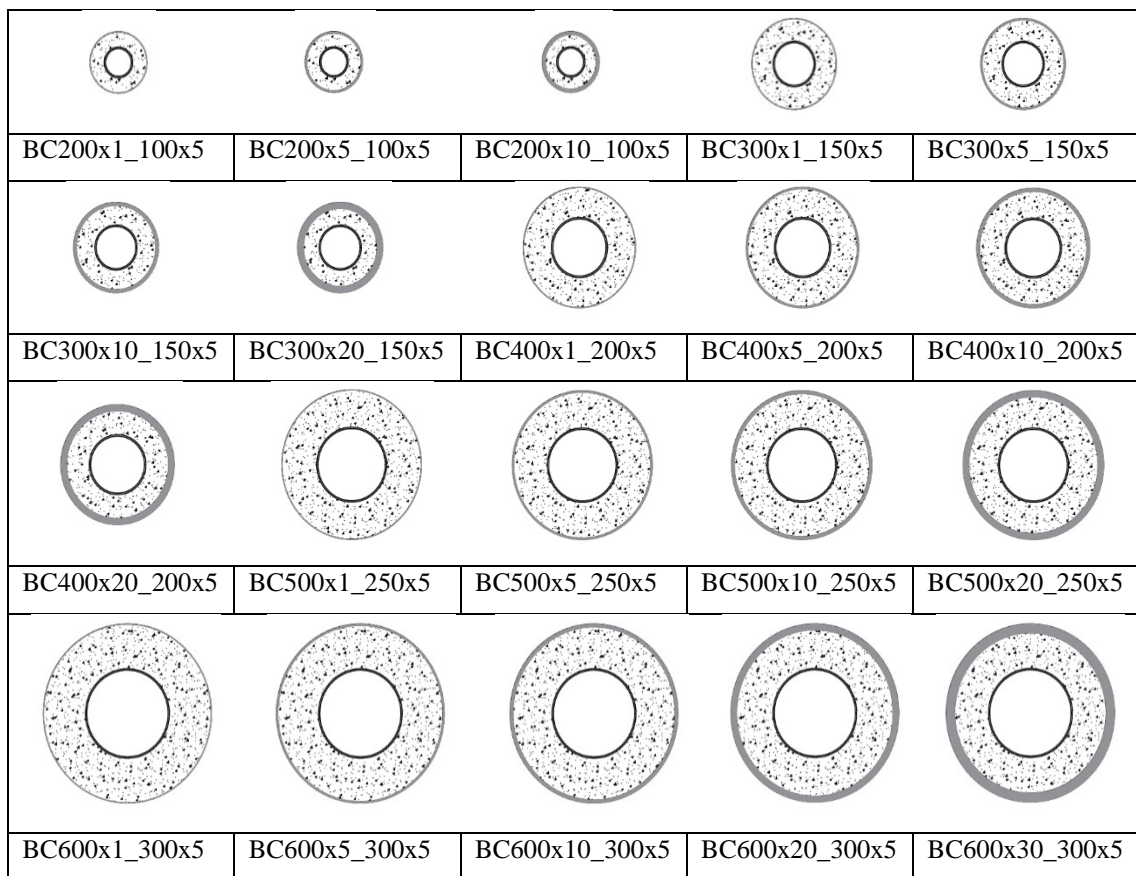


Figure 85 - Cross-sections: CFDST beam-columns and beams CFDST stub columns.

5.4 Parametric study results and analysis

In this section, the results from the parametric studies are presented. The results will be described in two groups: 1- CFDST stub columns under concentric axial compression; 2- CFDST stub columns under eccentric axial compression and pure bending. The load-carrying capacities predicted by the FE model under concentric axial compression were normalized

using the design values proposed by Han *et al.* [46] for CFDST columns ($N_{u,Han}$), which were described in item 2.2.2.

5.4.1 Members under concentric axial compression

The CFDST stub columns parametric study results under concentric axial compression will be presented in sub items that focused on the influences of tube diameter, hollow ratio (χ) and inner tube slenderness.

5.4.1.1 Tube diameter

CFDST stub columns with three different outer tube diameters D were assessed in this analysis, equal to 141.3, 168.3 and 219.1 mm, respectively. For each diameter D , six different inner tube diameters d were evaluated, ranging from 60.3 to 141.3 mm. The inner and outer tube thicknesses remained equal to the experimental values ($t_{si} = 5.5$ mm and $t_{so} = 2.8$ mm). Clearly, as the tube diameters varied, the concrete infill volume also changed. The CFDST stub columns axial load *versus* axial displacement responses for various inner tube diameters are depicted in Figure 86. All columns had an identical behaviour in the elastic range. After that, the responses' overall shape is quite similar, with strain hardening in the steel tubes acting together with the concrete confinement effect to increase their load-carrying capacities as the displacement increased. This trend is most evident for columns with a relatively small inner tube diameter (i.e., $d = 60.3$ and 70.6 mm) and a large concrete infill volume. On the other hand, for the CFDST stub column with a comparatively large inner tube diameter of 141.3 mm, only a small contribution of the strain hardening was observed. The concrete confinement effect was also drastically reduced.

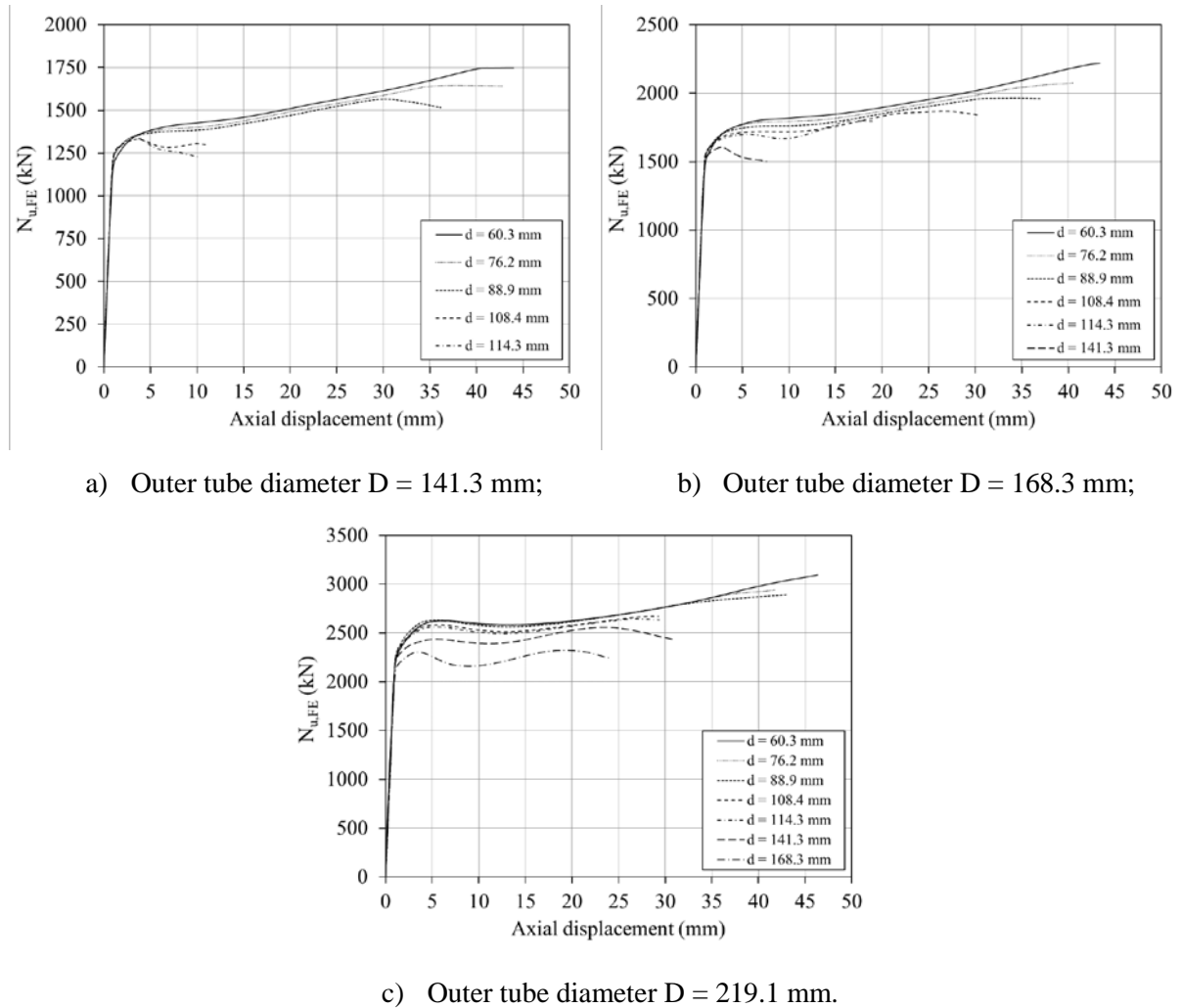


Figure 86 - CF DST stub columns axial load *versus* axial displacement response varying the inner tube diameter.

Figure 87 presents the axial load predicted by the FE model for each specimen, normalised by the corresponding design load $N_{u,Han}$ (Eq. (4)) *versus* concrete cross-sectional area normalised by the overall cross-sectional area (i.e. A_c/A_{total} , where $A_{total}=A_{si}+A_{so}+A_c$). The analysis included three different outer tube diameters D and five inner tube diameters d . As aforementioned, the inner and outer tube thicknesses remain equal to the experimental values ($t_{so} = 2.8$ mm, a) $t_{si} = 4.5$ mm, and b) 5.5 mm) in this analysis. Also, as stated before, when the FE model's ultimate load capacity is not evident, it was determined as the load at which the slope of the load-axial displacement curve was equal to 1% of its initial value following the procedure adopted [84].

The columns load-carrying capacity tended to increase for members with a relatively large outer tube diameter. Besides, the design expression accuracy proposed by Han *et al.* [46]

proved to be dependent on the cross-sectional geometry. The predicted load capacity was on the safe side for columns with a relatively large concrete volume ($A_c/A_{total} > 0.75$). On the other hand, when the concrete cross-sectional area was reduced (i.e., $A_c/A_{total} < 0.75$), the design expression provided an unconservative prediction (i.e., $N_{u,FE}/N_{u,Han} < 1$). Overall, it could be observed that for any value of A_c/A_{total} , the design expression is most conservative for columns with relatively small inner tube diameters and, consequently, larger volumes of concrete infill.

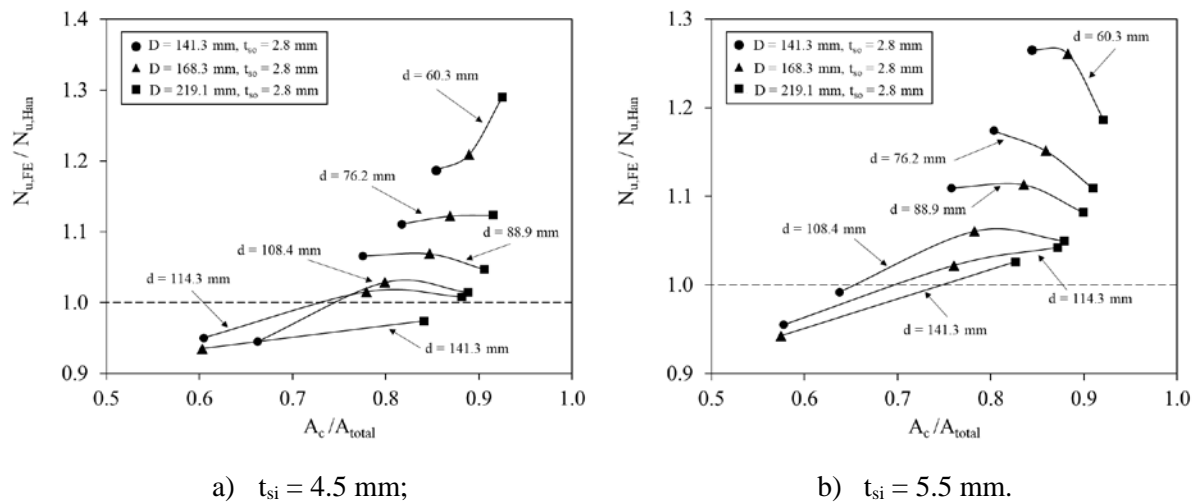


Figure 87 - Influence of tube diameter on the normalized axial load *versus* normalized concrete cross-sectional area response.

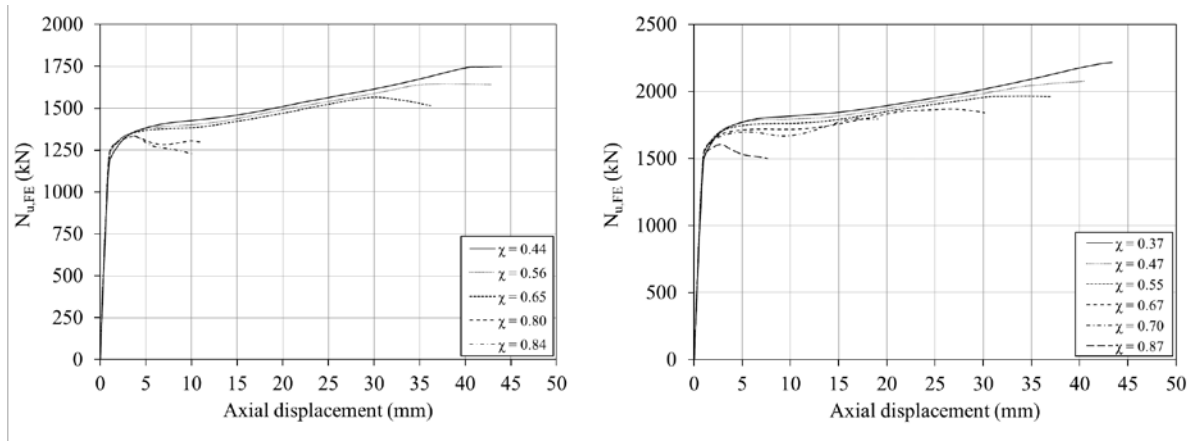
5.4.1.2 Hollow ratio χ

Two different hollow ratios χ were considered in the experimental programme, equal to either 0.55 or 0.67. In this section, the inner tube geometries varied to explore a wider range of χ from 0.28 up to 0.87. Concerning the definition of the hollow ratio provided by Eq. (9), it is noteworthy that a relatively small value of χ , i.e., close to zero, corresponds to an almost fully solid column and their behaviour is expected to be similar to that of a concrete-filled tube (CFST). Meanwhile, when χ is relatively large, i.e., close to unity, their response resembles a hollow steel-only section.

Figure 88 presents the axial load $N_{u,FE}$ *versus* axial displacement for columns with different hollow ratios; all columns had an outer tube diameter D of a) 141.3, b) 168.3, and c) 219.1 mm and thickness t_{so} 2.8 mm, respectively. The inner tube diameter d varied to generate a range of χ values, while the thickness t_{si} remains constant at 5.5 mm. This analysis has been

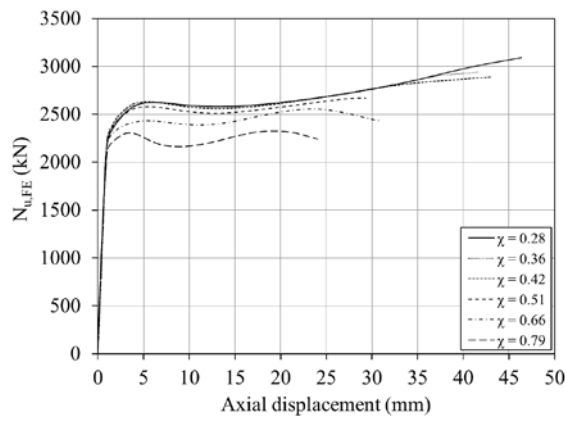
completed for all of the outer tube diameters examined in the previous section. It could be observed that for the range of χ examined, the response was, one more time, identical in the elastic range. The first peak load is slightly higher for CFDST columns with a relatively low χ value. As the axial displacement increases, the load-carrying capacity of these members continues to increase. The member's behaviour proved to be quite similar to a stocky CFST. Therefore, as the axial displacement increases, the column's cross-sectional area also increases, thus improving their associated load-carrying capacity. On the other hand, for the members with a relatively high χ (i.e., $\chi > 0.67$), the load remained almost constant and did not increase. In addition, the CFDST columns ductility with low χ values, i.e., those that are similar to CFST columns, is larger than for those with relatively high hollow ratios. This trend is most likely due to the positive influence of the concrete's confinement effect over the columns' strength and stability, as shown in Figure 89. The curve presents the FE result for the lateral confining pressure between the concrete and the outer steel tube for two different load stages and two opposite values of hollow ratios: yielding point a) and failure b), $\chi = 0.37$ and $\chi = 0.87$ c), respectively. Therefore, it confirmed the conclusion that the lower hollow ratio provided a higher confining pressure.

Figure 90 shows the normalized peak axial load ($N_{u,FE}/N_{u,Han}$) versus hollow ratio χ for a range of columns with different inner and outer diameters; the inner tube thickness was a) 4.5 and b) 5.5 mm. The two dotted lines in the y-direction represent the χ for the test specimens, i.e., 0.55 and 0.67. Again, it can be confirmed that the load-carrying capacity predicted using Han *et al.* [46] method is most conservative for CFDST columns with relatively low hollow ratios. This method turned to be unconservative for the range of parameters examined in this study, i.e., for χ values greater than 0.67.



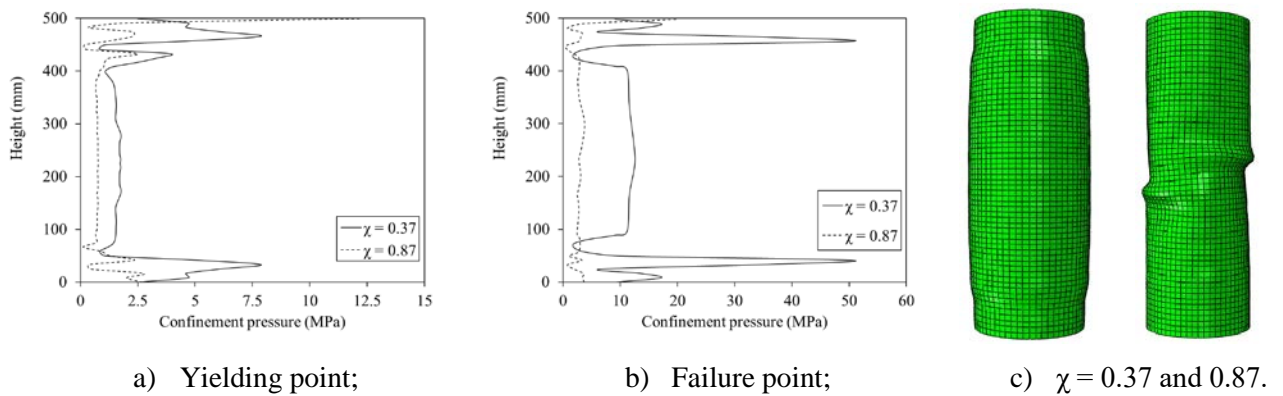
a) Outer tube diameter $D = 141.3$ mm;

b) Outer tube diameter $D = 168.3$ mm;



c) Outer tube diameter $D = 219.1$ mm.

Figure 88 - Influence of hollow ratio on the axial load *versus* axial displacement response for CFDST columns with an outer diameter of 168.3 mm.



a) Yielding point;

b) Failure point;

c) $\chi = 0.37$ and 0.87 .

Figure 89 - Lateral confining pressure along with the columns' height, measured through ABAQUS [16].

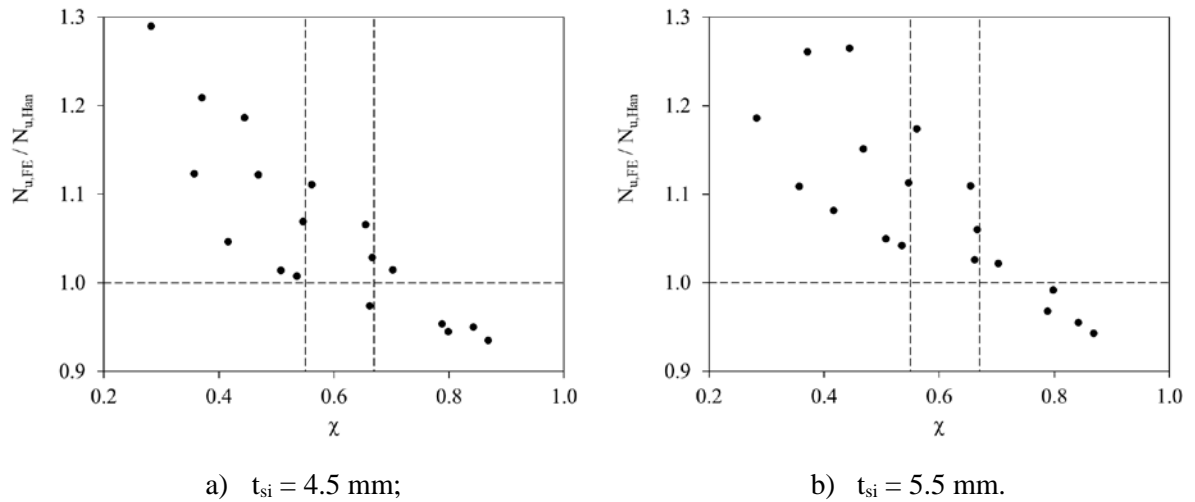


Figure 90 - Normalized axial capacity *versus* hollow ratio.

5.4.1.3 Inner tube slenderness

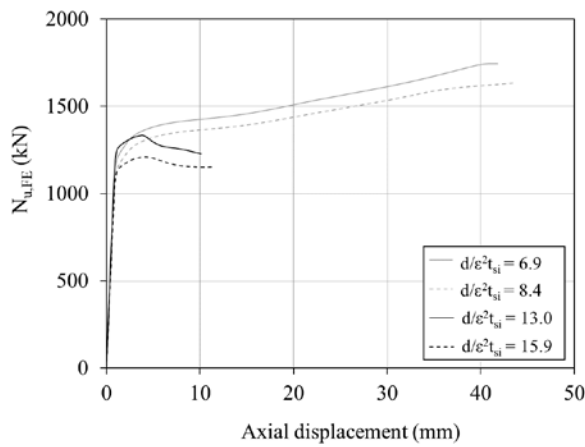
In this section, the influence of the inner steel tubes' slenderness was assessed by varying the $d/\varepsilon^2 t_{si}$ ratio, as the slenderness limit calculated from Eurocode 4 (EC4) [18] (Eq. 105). CFDST stub columns axial load *versus* axial displacement curves are presented in Figure 91 for CFDST stub columns with varying inner tube slendernesses from 6.9 (i.e., $d = 60.3$ mm and $t_{si} = 5.5$ mm) up to 23.4 (i.e., $d = 168.3$ mm and $t_{si} = 4.5$ mm). In this analysis, the outer tube thickness was kept constant at $t_{so} = 2.8$ mm and the outer tube diameter were varied as a) 141.3, b) 168.3 and c) 219.1 mm, respectively. The load-carrying capacity was relatively similar for the slenderness's range examined, with the members with stockier inner tubes reaching higher capacities. The ductility was much higher for the members with smaller inner tubes, i.e., those behaving more similarly to a CFST.

The slenderness limit for concrete-filled columns was equal to the slenderness limit for unfilled columns, i.e., class 3, as:

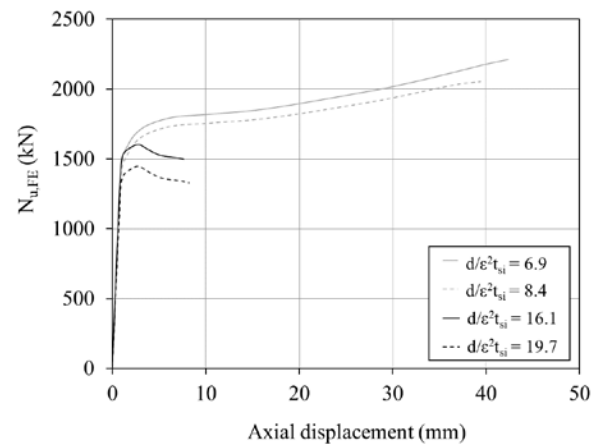
$$d/t_{si} \leq 90 \left(\frac{235}{f_{syi}} \right) \quad (105)$$

To further assess the influence of the inner tube slenderness over the load-carrying capacity, Figure 92 presents the normalised axial capacity ($N_{u,FE}/N_{u,Han}$) plotted against $d/\varepsilon^2 t_{si}$. It can be observed that the specimens with compact inner tubes exhibited higher values of

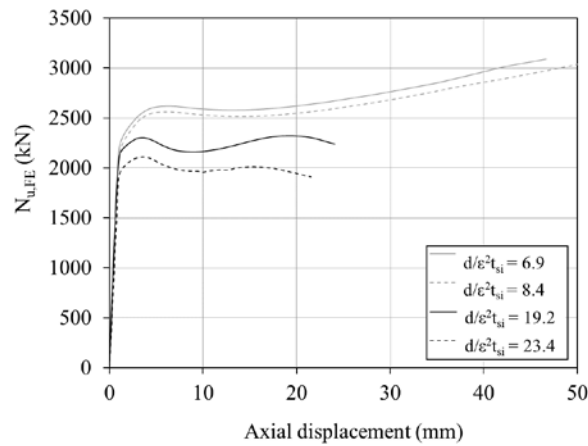
$N_{u,FE}/N_{u,Han}$. This trend can be attributed to the greater volume of concrete as well as the improved confinement afforded to the concrete infill.



a) Outer tube diameter $D = 141.3$ mm;



b) Outer tube diameter $D = 168.3$ mm;



c) Outer tube diameter $D = 219.1$ mm.

Figure 91 - Influence of tube slenderness over the axial load *versus* axial displacement response for CFDST columns with different inner tube geometries.

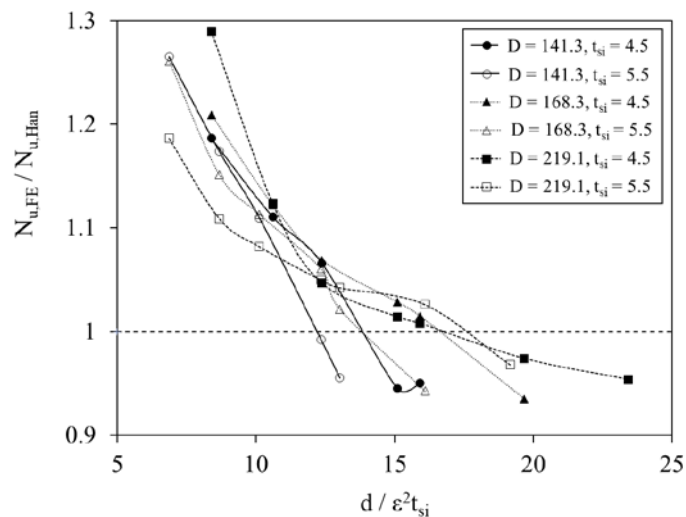


Figure 92 - Influence of the local slenderness of the inner steel tube over the normalized ultimate axial load, for in a constant value of $t_{so} = 2.8$ mm (all values in the legend are in mm).

5.4.2 Members under eccentric load

The CFDST stub beam-columns parametric study results for eccentric axial compression and pure bending will be presented in the next sub items focusing on the influence of outer tube diameter (D), hollow ratio (χ), outer tube slenderness (D/t_{so}), eccentricity ratio (e/D) and the concrete compressive strength (f_c).

5.4.2.1 Outer tube diameter

CFDST stub columns and beam-columns with five different outer tube diameters D were examined in this analysis, equal to 200, 300, 400, 500 and 600 mm, respectively. For each outer diameter D , six different inner tube diameters d were also assessed, ranging from 100 to 300 mm. The outer to inner diameter ratio (D/d) was kept constant and equal to 2. The inner tube thickness was kept constant as $t_{si} = 5$ mm. The outer tube thickness (t_{so}) assumed five different values as 1, 5, 10, 20 and 30 mm. Figure 93 presents the axial load *versus* axial displacement curves for each eccentricity applied to the beam-columns.

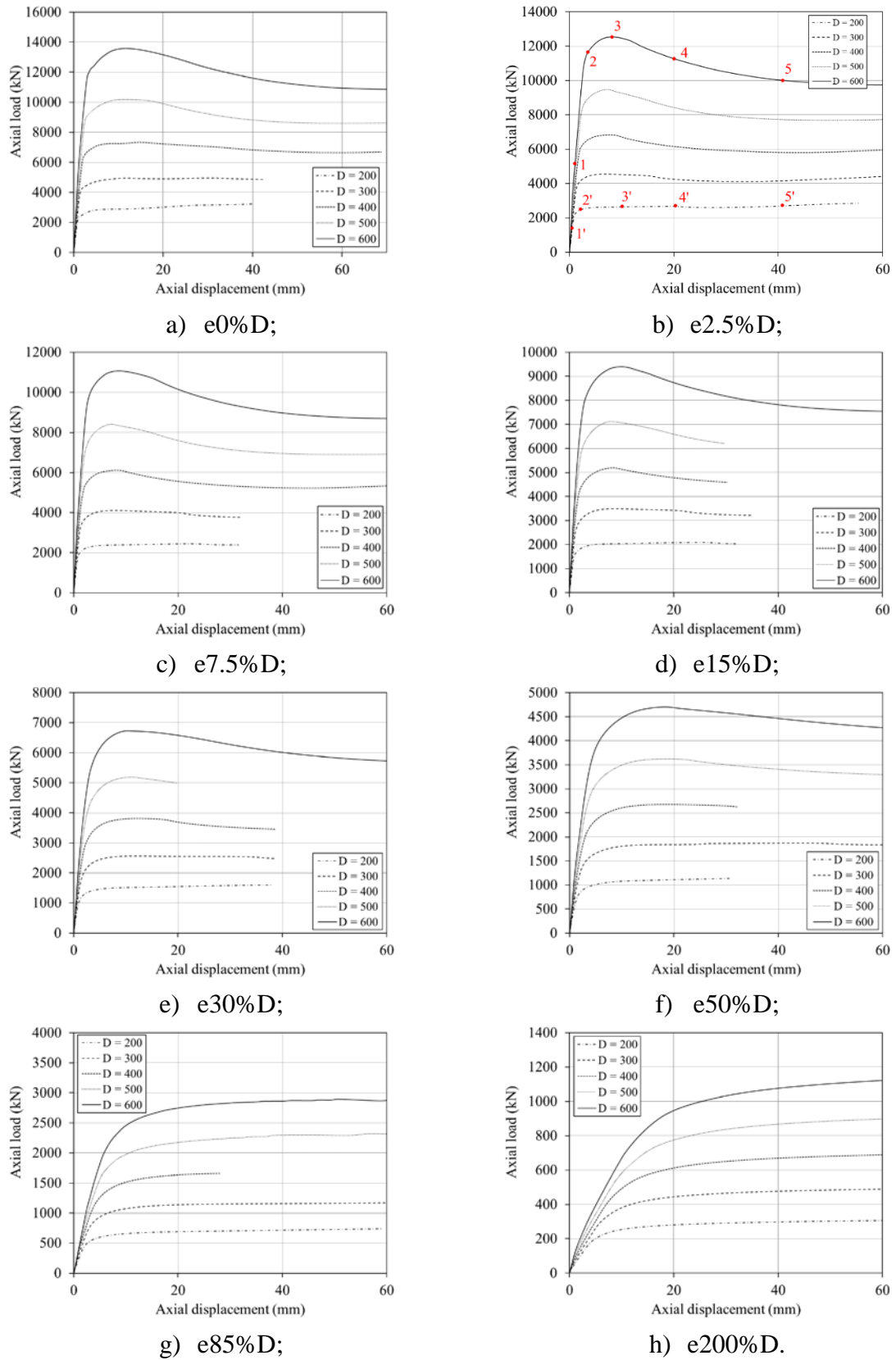


Figure 93 - Axial load *versus* axial displacement response for CFDST columns with the outer and inner tube thicknesses of 5 mm and variable outer diameters.

The CFDST with outer and inner tube 5 mm thicknesses will be used to illustrate the general behaviour of all the analysed cross-sections. As observed in the concentric axial compression analysis, as the tube diameters varied, the concrete infill volume also changed. All of the columns had identical responses in the elastic range. After that, the overall response is quite different between the investigated diameters. Concentric columns (eccentricity 0% of D), the smallest outer tube diameters ($D = 200$ mm, $D = 300$ mm and $D = 400$ mm) presented two load peaks where the second and ultimate load was higher. The ductility increases with steel tube strain hardening that acted together to enhance the concrete confinement effect. On the other hand, for larger outer tube diameters ($D = 500$ mm and $D = 600$ mm), only one peak load was observed with very little strain hardening and ductility.

In columns under eccentric axial compression, as the eccentricity increases, the columns with the smallest diameters ($D = 200$ mm, $D = 300$ mm and $D = 400$ mm) altered their two peak loads response, where the second peak load started to become smaller than the first. When the eccentricity exceeded 50% of the outer tube diameter, all the beam-column sections modified their behaviour, becoming more similar to a flexural element, with a higher ductility and strain hardening response and a smaller load capacity.

Figure 94 presents the CFDST beam-columns outer steel tube longitudinal stress distribution and the deformed shape for key points identified in Figure 93 b). Figure 94 a) represents a CFDST beam-column with $D = 600$ mm, $t_{so} = 5$ mm, $d = 300$ mm, $t_{si} = 5$ mm and $e = 2.5\%D$ while Figure 94 b) is associated to a CFDST beam-column with $D = 200$ mm, $t_{so} = 5$ mm, $d = 100$ mm, $t_{si} = 5$ mm and $e = 2.5\%D$. The adopted key point represented: 1 the linear range; 2, 3 (first peak load), 4 and 5 the yielding range; 1' the linear range; 2' and 3' the yielding stage; 4' first peak load; 5' second peak load and failure. The yielding stage proved to be higher for CFDST columns and beam-columns, where the outer tube diameter and the concrete confinement effect are significant.

Figure 95 was produced to illustrate beam-columns behaviour as the concrete area was varied (A_c). It presents the FE peak load model results for each specimen *versus* the concrete cross-sectional area normalised by the overall cross-sectional area (i.e., A_c/A_{total} , where $A_{total} = A_{si} + A_{so} + A_c$). Since Han *et al.* [46] proposed design load was only developed for CFDST columns under concentric axial compression, the vertical axis was not normalised by it as in item 5.4.1. The figures are divided into the outer tube thicknesses (t_{so}), where each marker represents an outer tube diameter (D), and each line depicts a different eccentricity. The outer tube thickness $t_{so} = 30$ mm was only evaluated in the CFDST cross-section with the larger outer tube diameter $D = 600$ mm, and consequently was not presented in the figure. The same

situation occurred for the smaller outer tube diameter $D = 200$ mm in Figure 95 d), where the outer tube thickness $t_{so} = 20$ mm was not studied with this outer tube diameter value.

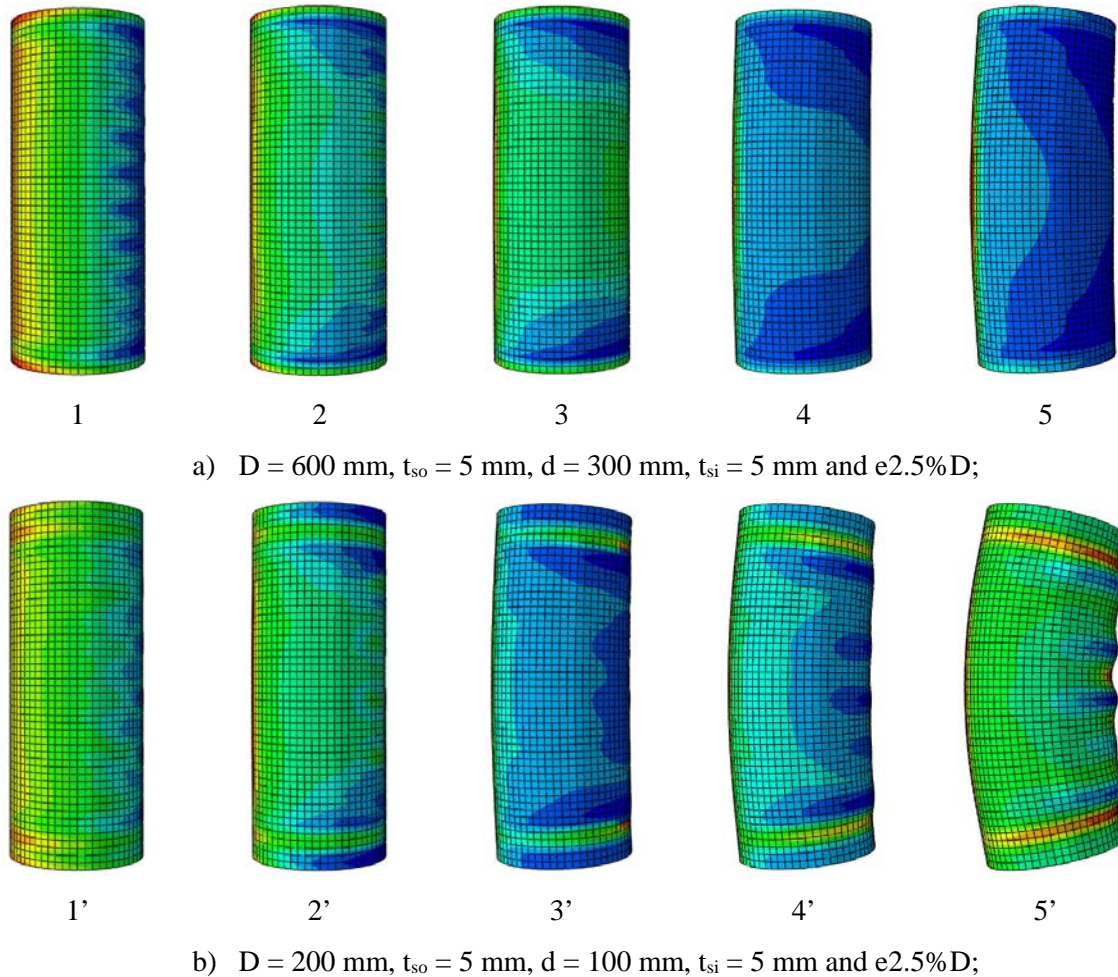


Figure 94 - Longitudinal stress and deformed shape of CFDST beam-columns for the selected key points defined in Figure 93 b).

The columns' capacity increased for members with a relatively large outer tube diameter and smaller eccentricity, independent of the outer tube thickness (t_{so}). Simultaneously, it could be observed that this increase is more accentuated for lower outer steel tube thickness (t_{so}). Moreover, as the A_c/A_{total} increases, the load capacity also increases, emphasising the significance of the concrete infill confinement.

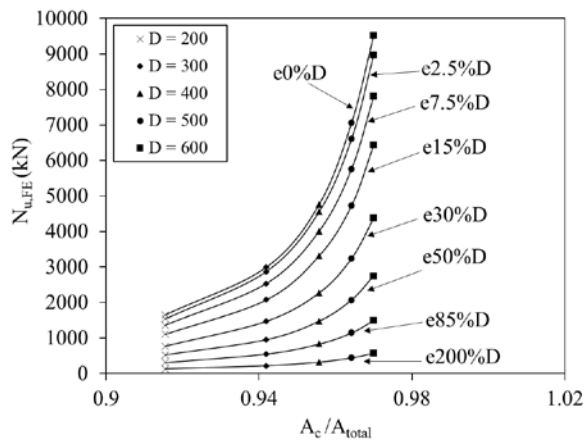
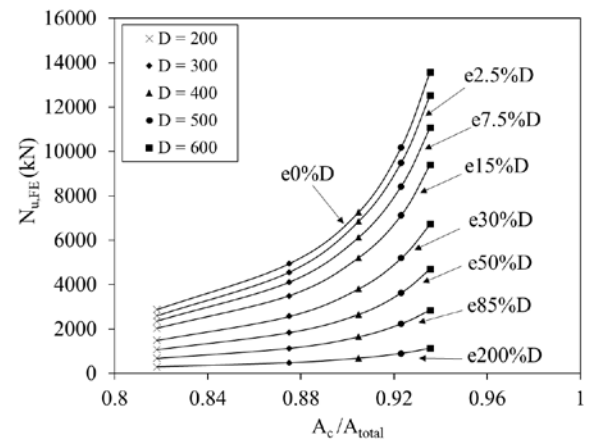
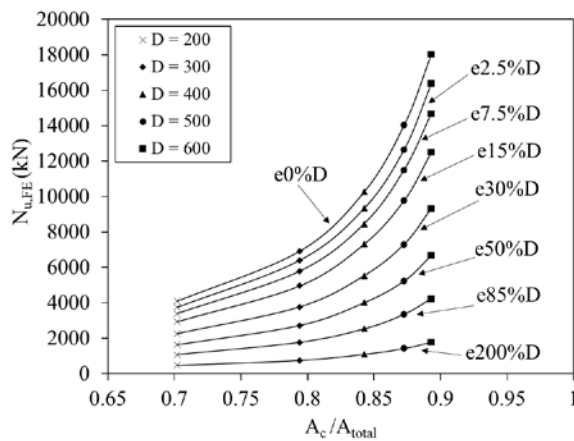
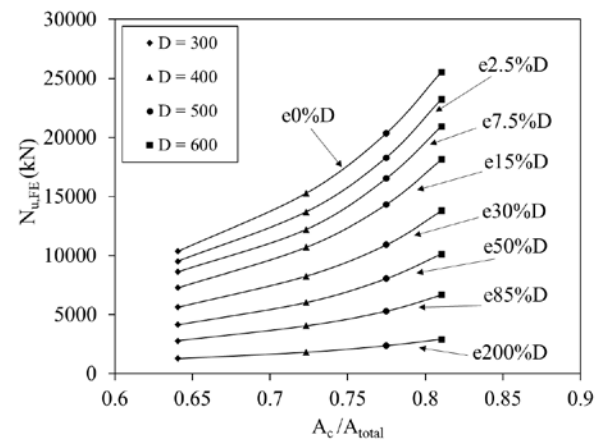
a) $t_{so} = 1 \text{ mm}$;b) $t_{so} = 5 \text{ mm}$;c) $t_{so} = 10 \text{ mm}$;d) $t_{so} = 20 \text{ mm}$.

Figure 95 - Influence of the outer tube diameter over the axial load *versus* normalized concrete cross-sectional area response.

5.4.2.2 Hollow ratio χ

Different hollow ratios χ were considered for beam-columns, ranging from 0.50 to 0.58 and were selected according to the CFDST optimized cross-section, defined by Han *et al.* [46]. This criterion was also applied to select a $2 D/d$ ratio. The inner tube diameter (d) and the outer tube slenderness (t_{so}) were varied to examine the hollow ratio significance. The definition (2.2.2) of the hollow ratio for columns subjected to concentric axial compression is the same for columns subjected to eccentric axial compression, where a small value of χ , i.e., close to

zero, corresponds to an almost fully solid column and when χ is relatively large, i.e., close to the unity, the section behaves almost like a hollow steel-only section.

Figure 96 presented the axial load $N_{u,FE}$ *versus* axial displacement for beam-columns with a range of different hollow ratios and associated eccentricity values. All the assessed five outer tube diameter D are depicted. The outer tube thickness t_{so} was kept as 5 mm to illustrate their response while representing the investigated outer tube thicknesses. The curves response is similar to the ones presented in item 5.4.2.1. However, the curves are now plotted as hollow ratio (χ) label instead of outer steel tube diameter (D). It could be observed that for the χ investigated range, the response was again identical in the elastic range. The axial displacement is higher for CFDST beam-columns with a relatively low χ value, as expected since low χ values express a larger concrete area. In addition, the CFDST beam-columns ductility with low χ values proved to be greater than for those with relatively high hollow ratios. These response trends were observed for all the studied eccentricities.

Figure 97 shows the FE model predicted ultimate loads *versus* hollow ratio χ for columns with different inner and outer diameters, outer tube thickness, eccentricities. All these models had a constant 5 mm inner tube thickness. This figure illustrates the hollow ratio influence over the load-carrying capacity. A unique response was observed for all outer tube diameter (D), whereas the load capacity increase was proportional to their hollow ratio (χ). However, the hollow ratio behaviour is inverse when the different outer tube diameters are evaluated, where larger outer tube diameters lead to smaller hollow ratios.

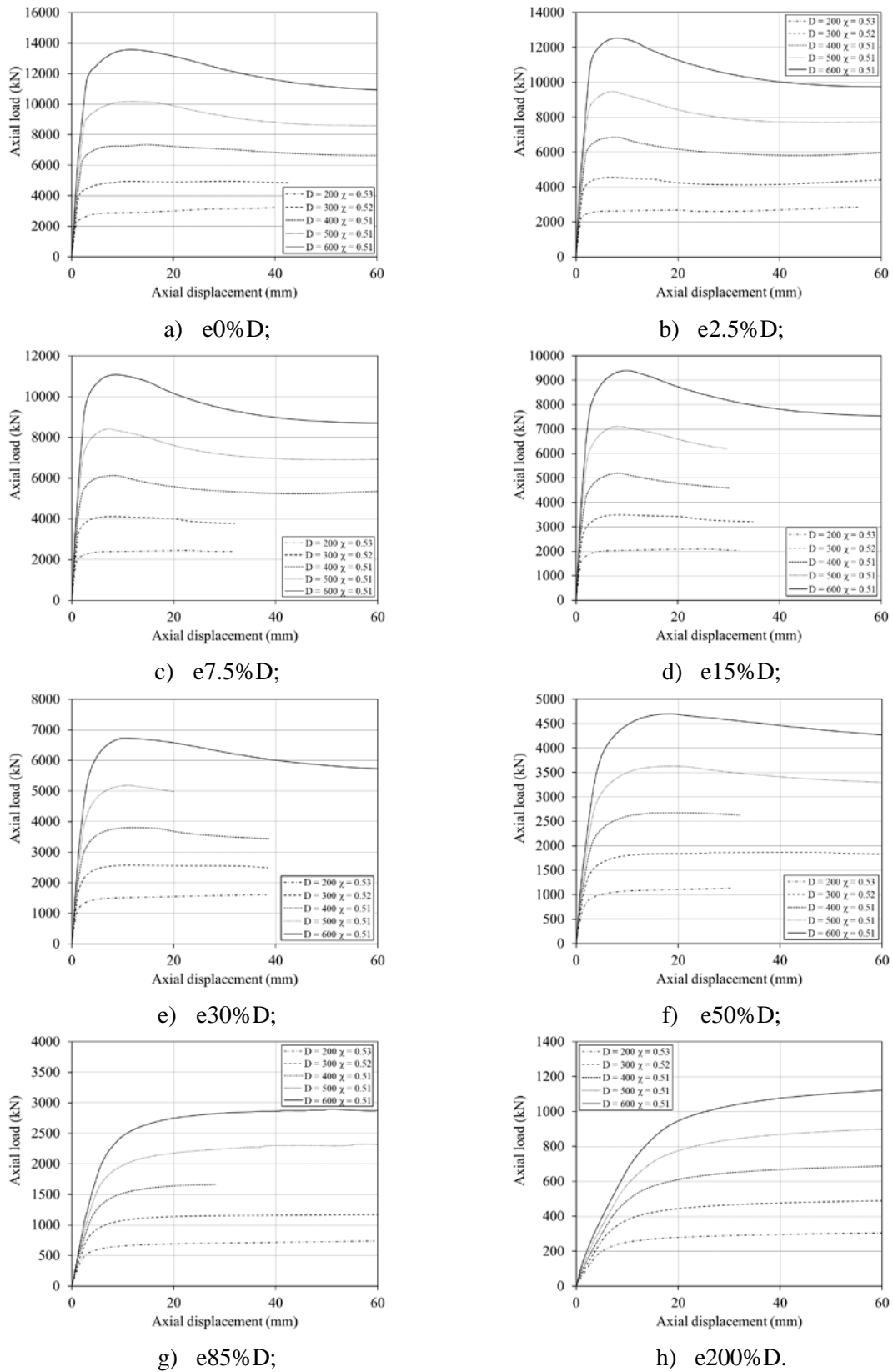
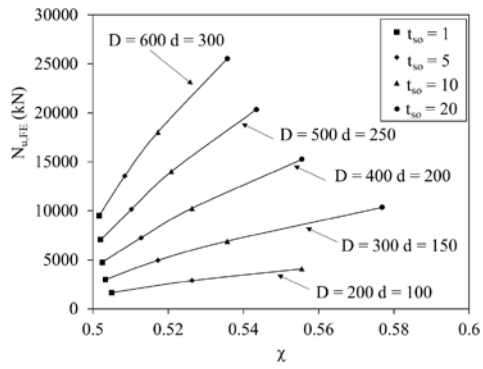
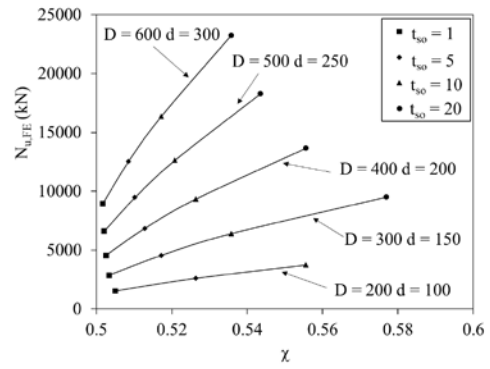


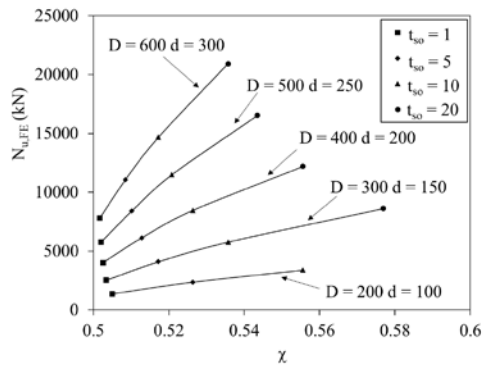
Figure 96 - Axial load *versus* axial displacement response for CF DST columns with outer and inner tube thicknesses of 5 mm and different hollow ratio.



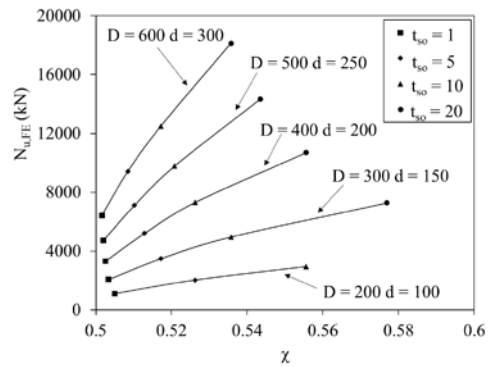
a) e0%D;



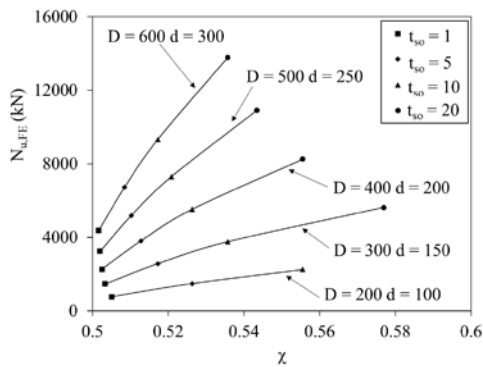
b) e2.5%D;



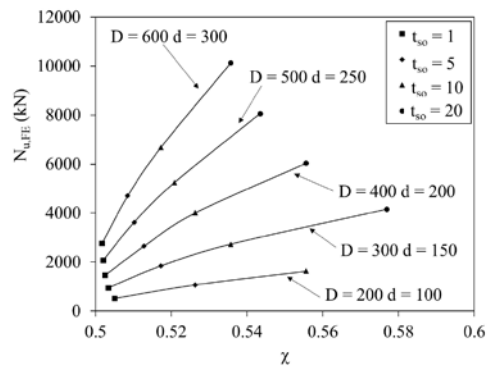
c) e7.5%D;



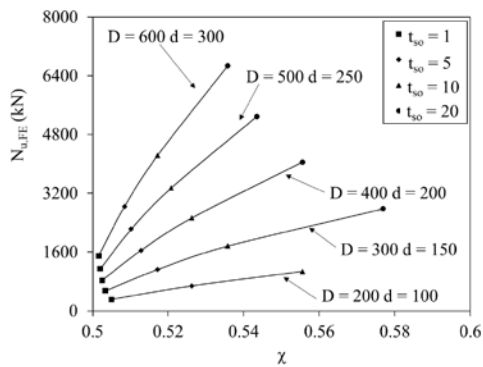
d) e15%D;



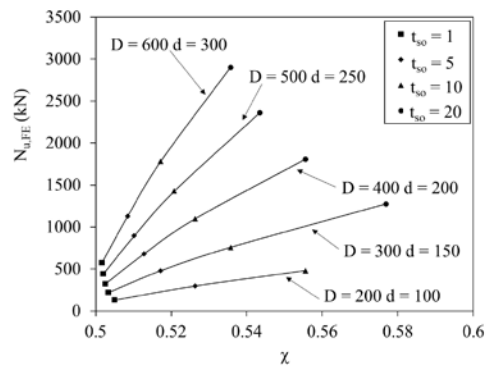
e) e30%D;



f) e50%D;



g) e85%D;



h) e200%D.

Figure 97 - Axial load versus normalized hollow ratio.

5.4.2.3 Outer tube slenderness

In this section, the influence of the outer steel tubes' slenderness over the ultimate capacity was assessed by varying the D/t_{so} ratio. The axial load *versus* axial displacement curves are presented in Figure 98 for CFDST beam-columns varying the outer tube slendernesses ($D/\varepsilon^2 t_{so}$) from 22.4 (i.e. $D = 200$ mm and $t_{so} = 5$ mm) to 67.3 (i.e. $D = 600$ mm and $t_{so} = 5$ mm). In this figure, both tube thicknesses were kept constant as 5 mm to illustrate the axial load *versus* axial displacement behaviour for all studied thicknesses. Irrespective of the eccentricity applied, the load capacity was enhanced as the $D/\varepsilon^2 t_{so}$ ratio increased. This can be easily explained since the outer tube diameter (D), and the concrete area also increased in these cases.

As previously presented (item 5.4.2.1), for each eccentricity depicted in Figure 98, it was possible to observe that the peak loads reduce their intensity, and the failure became less abrupt. This behaviour is notorious since as the eccentricity applied increased, the load capacity was reduced. The axial load *versus* axial displacement curve started to change from a column's to a beam's response.

Figure 99 presents the FE model ultimate load *versus* the outer tube slenderness ratio ($D/\varepsilon^2 t_{so}$) for cases with outer tube thickness (t_{so}) equal to 1, 5, 10 and 20 mm. In these cases, smaller $D/\varepsilon^2 t_{so}$ values represent thicker outer tubes. For all eccentricities, smaller $D/\varepsilon^2 t_{so}$ ratios led to higher load-carrying capacities. This behaviour expresses the relevance of the outer tube thickness (t_{so}) in the load-carrying capacity of CFDST columns and beam-columns. For the CFDST columns (Figure 99 a)), the load capacity gain when comparing $t_{so} = 1$ mm and $t_{so} = 20$ mm separately for each outer tube diameter (D) is: $D = 300$ mm is three times higher; $D = 400$ mm is 3.2 times higher; $D = 500$ mm is 2.9 times higher and $D = 600$ mm is 2.7 times higher, respectively. For the CFDST beam-columns (Figure 99 b) to h)), the gain is even higher for larger eccentricities (such as $e200\%D$): $D = 300$ mm, 400 mm, 500 mm and 600 mm, the load capacity is six, 5.6, 5.3 and 5.0 times higher, respectively.

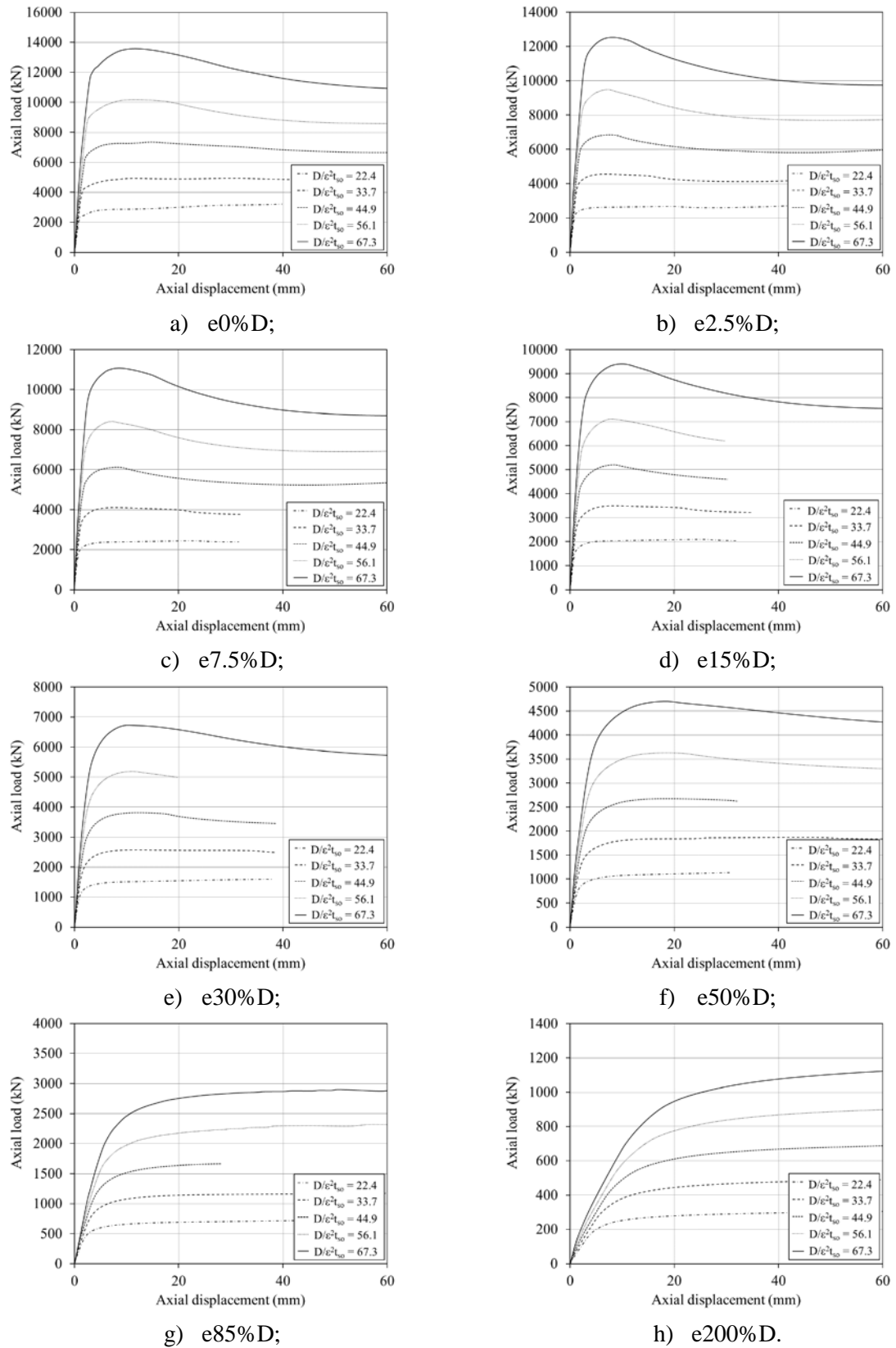


Figure 98 - Axial load *versus* axial displacement response for CFDST columns with outer and inner tube thicknesses of 5 mm and various inner tube geometries.

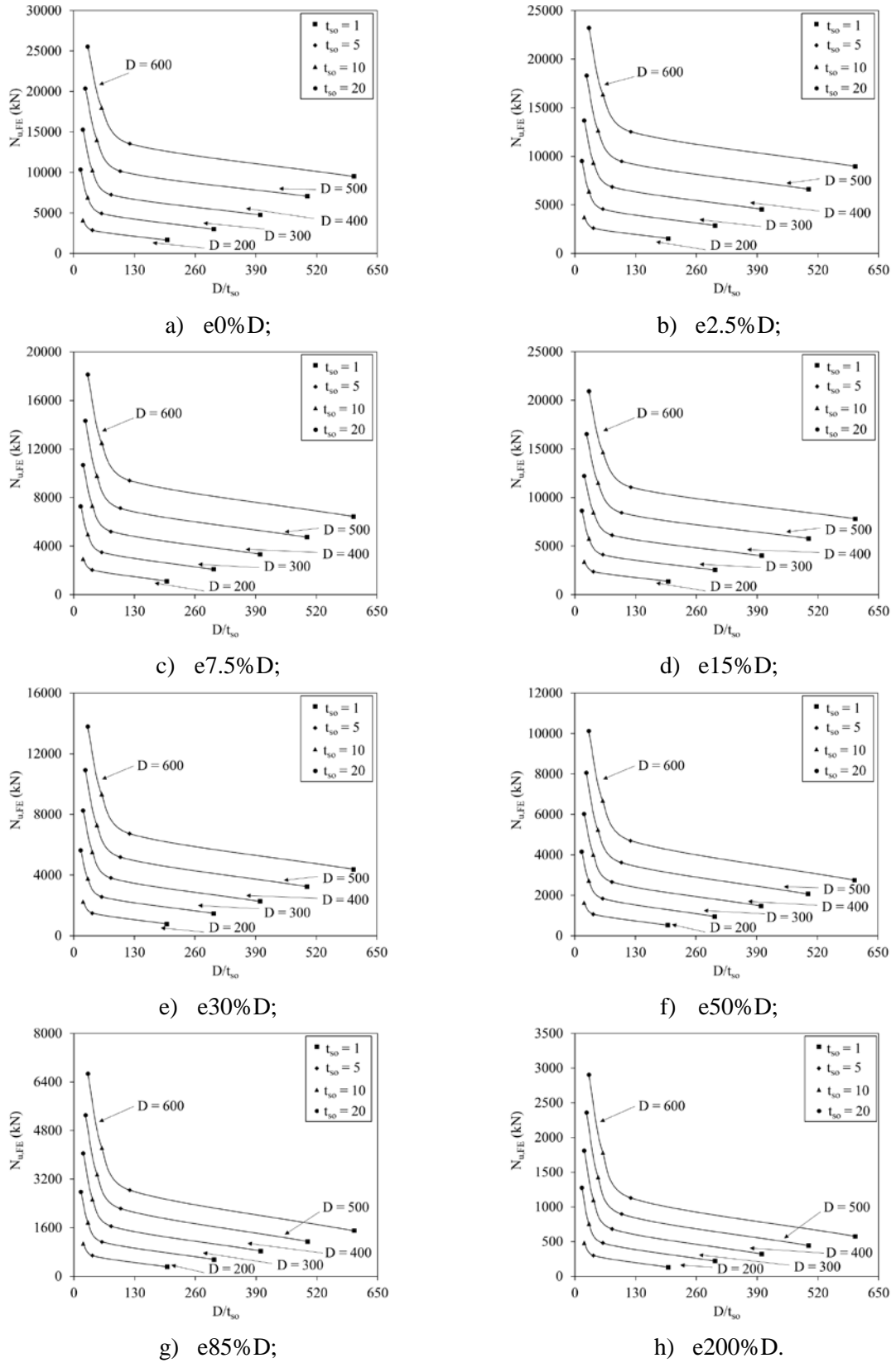


Figure 99 - Influence of the outer steel tube's local slenderness over the normalized ultimate axial load (all values in mm).

The outer tube slenderness limit and the compressive design resistance for concrete-filled columns calculated from Eurocode 4 (EC4) [18] were compared with the FE model axial load prediction in Figure 100 and Figure 101. These figures are related to cases with a compressive strength f_c of 33 and 80 MPa. The compressive design resistance equations were previously presented in section 2.2.4. They were adapted to represent stainless steels by considering their yield stress as 0.2% proof stress and the inner carbon steel tube. The last cited item was added by replacing the reinforcing bars' resistance part, while the effective length factor k was assumed as equal to 1.0 to reflect the pinned-ended conditions. The slenderness limit for concrete-filled columns was equal to the slenderness limit for unfilled columns, i.e., class 3, as:

$$D/t_{so} \leq 90 \left(235/f_{syo} \right) \quad (106)$$

Figure 100 and Figure 101 show that all the N_{FE}/N_{EC4} ratios were less than 1, leading to an unconservative prediction and unsafe design resistance for CFDST beam-columns with N_{EC4} . However, for CFDST columns, the N_{EC4} predictions were not too conservative and provided safe design results. Moreover, the ratio between the beam-columns numerical and predicted strengths in terms of the outer tube slenderness tends to be a constant line for all the analysed eccentricity values.

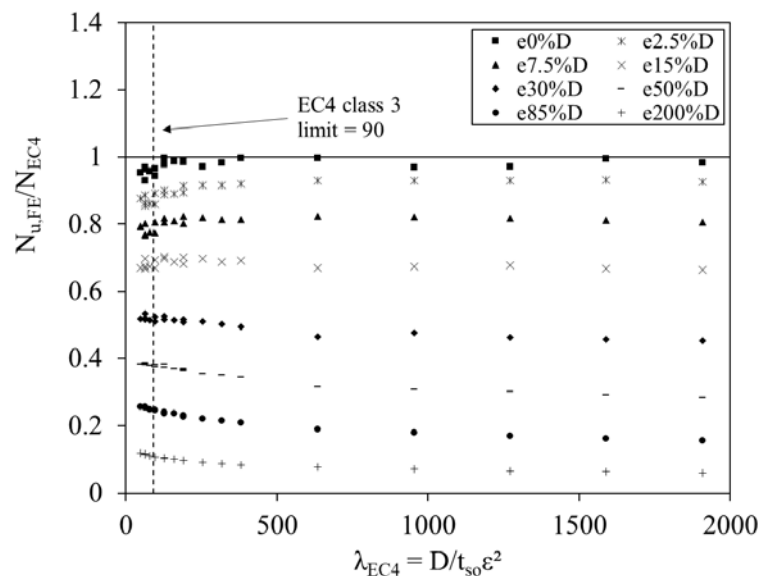


Figure 100 - Normalized axial load *versus* outer tube slenderness for a 33 MPa f_c concrete compressive strength.

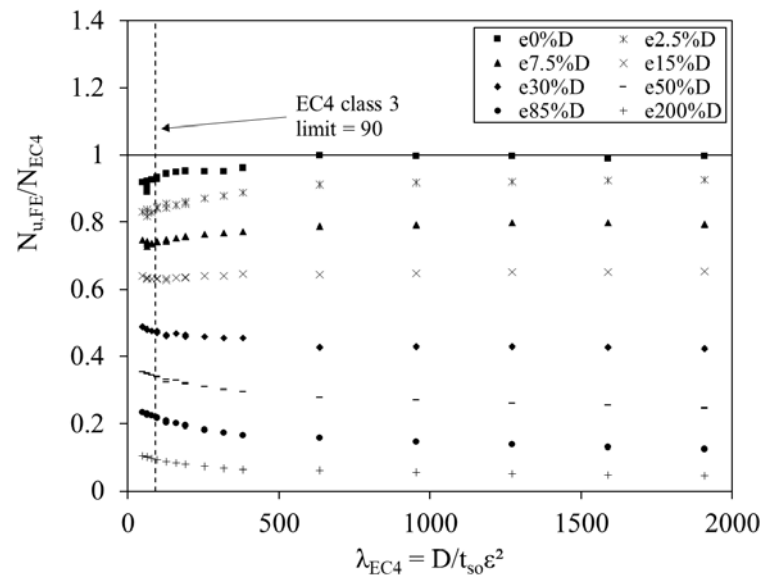


Figure 101 - Normalized axial load *versus* outer tube slenderness for an 80 MPa f_c concrete compressive strength.

5.4.2.4 Eccentricity ratio

In this thesis item, the eccentricity used in the beam-columns divided by the outer tube diameter will be analysed. The CFDST stub column and beam-column studied in the parametric analysis were plotted in Figure 102 as axial load *versus* eccentricity ratio. The CFDST columns and beam-columns were represented by the outer tube slenderness D/t_{so} . The graph shows a trend where all the cross-section studied load-carrying capacities decreased with an increase in the load eccentricity ratio. The curve is more accentuated for columns with a large outer diameter (D) and outer thickness (t_{so}). On the other hand, the curve becomes almost linear when the outer tube diameter and outer thickness were smaller (for instance, $D/t_{so} = 200$: $D = 200$ and $t_{so} = 1$ mm).

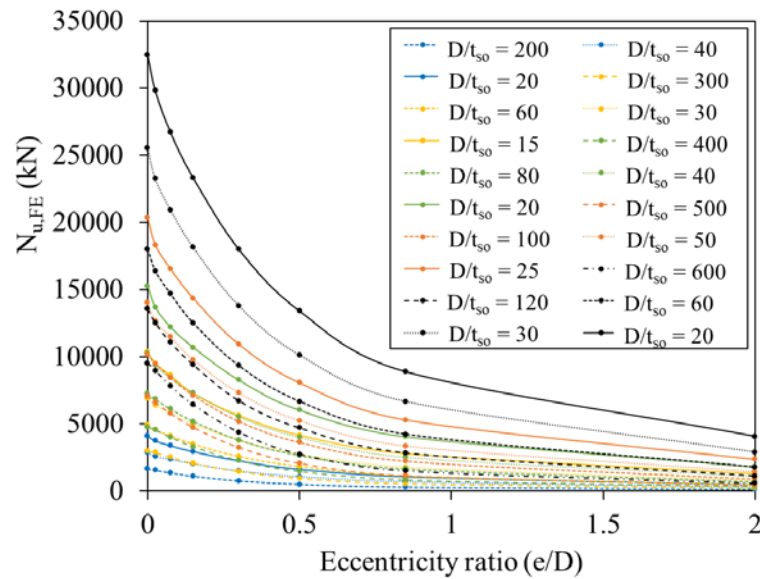


Figure 102 - Axial load *versus* eccentricity ratio (e/D).

5.4.2.5 Concrete strength (f_c)

Figure 103 illustrates the influence of the concrete compressive strength (f_c) over the CFDST beam-columns behaviour in terms of their associated axial load *versus* the concrete compressive strength curves. The load capacity of the beam-columns was enhanced as the concrete compressive strength increased. A constant trend could also be observed for columns with thinner outer tubes ($t_{so} = 1$ mm) and larger slenderness ratio, where the difference of load capacity between columns with $f_c = 33$ MPa and with $f_c = 80$ MPa is almost twice. Whereas, there is almost no difference between the columns load capacity for thicker outer tubes ($t_{so} = 20$ mm) and smaller slenderness ratio. Table 32 shows the slenderness ratio analysed. This difference is less significant when the outer tube thickness (t_{so}) is thinner and the slenderness ratio is larger due to a premature outer steel tube failure. It may be better explained by comparing the same displacement values after the peak load for each cross-section in terms of longitudinal stress of the outer steel tube, as presented in Table 33 and Figure 104.

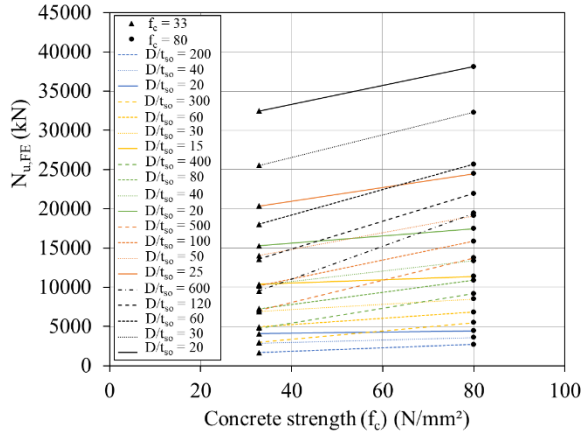
Table 32 - Analysed slenderness ratio.

D (mm)	t _{so} (mm)	d (mm)	t _{si} (mm)	D/t _{so}
200	1	100	5	200
200	5	100	5	40
200	10	100	5	20
300	1	150	5	300
300	5	150	5	60
300	10	150	5	30
300	20	150	5	15
400	1	200	5	400
400	5	200	5	80
400	10	200	5	40
400	20	200	5	20
500	1	250	5	500
500	5	250	5	100
500	10	250	5	50
500	20	250	5	25
600	1	300	5	600
600	5	300	5	120
600	10	300	5	60
600	20	300	5	30
600	30	300	5	20

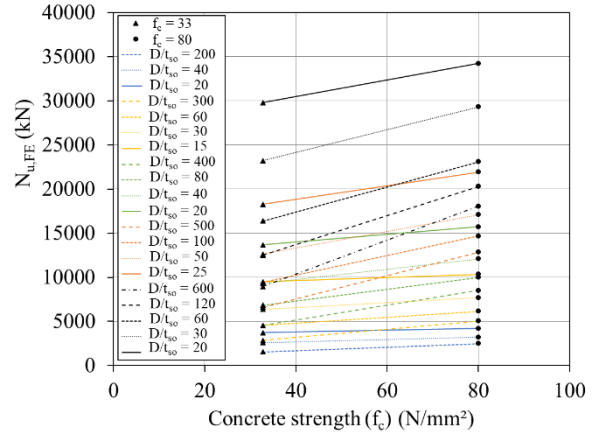
Table 33 - Longitudinal stress deformation.

Figures	D (mm)	t _{so} (mm)	d (mm)	t _{si} (mm)	D/t _{so}	e (D%)	f _c (N/mm ²)	Deformation response
Figure 104 a)	200	1	100	5	1	0	33	Achieved failure – f _u – post peak load stage
Figure 104 b)	600	30	300	5	20	0	33	Achieved yielding – f _y – elastic-plastic stage

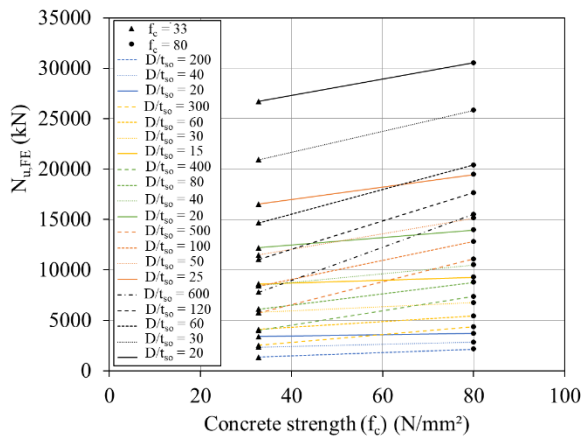
Figure 104 c)	200	1	100	5	1	0	80	Achieved failure – f_u – post peak load stage
Figure 104 d)	600	30	300	5	20	0	80	Achieved yielding – f_y – elastic-plastic stage



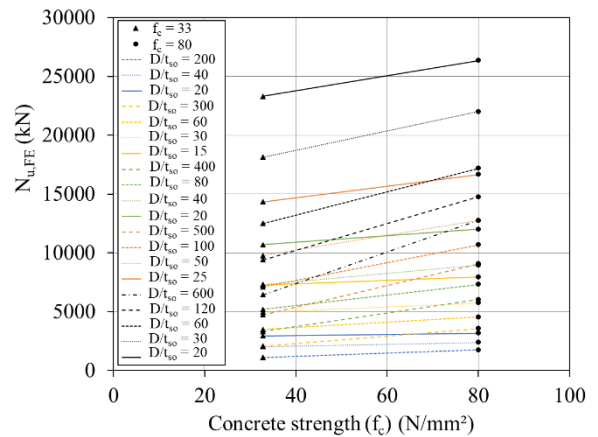
a) e0%D;



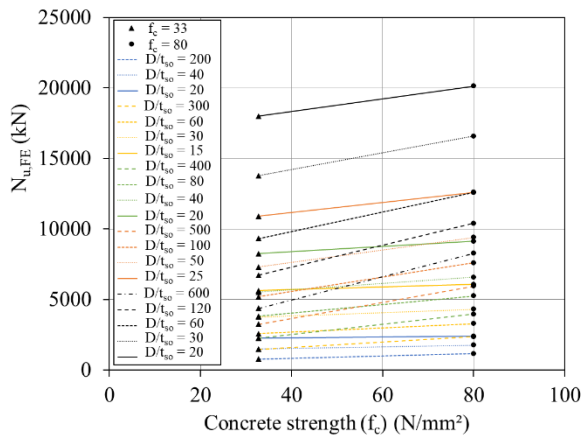
b) e2.5%D;



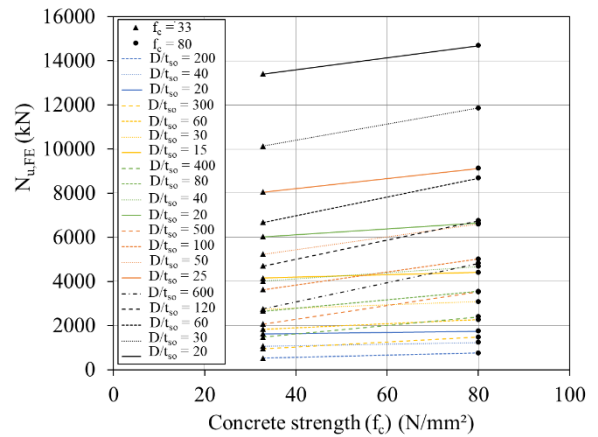
c) e7.5%D;



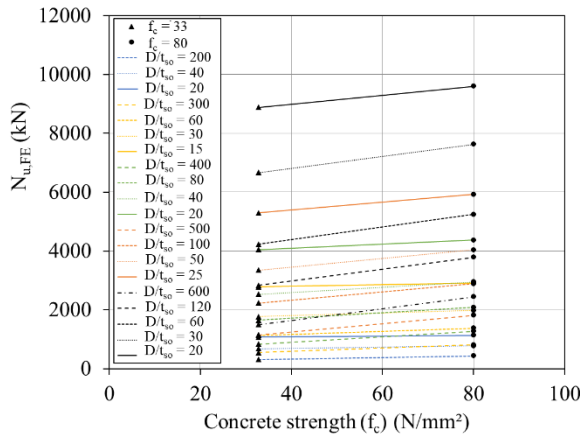
d) e15%D;



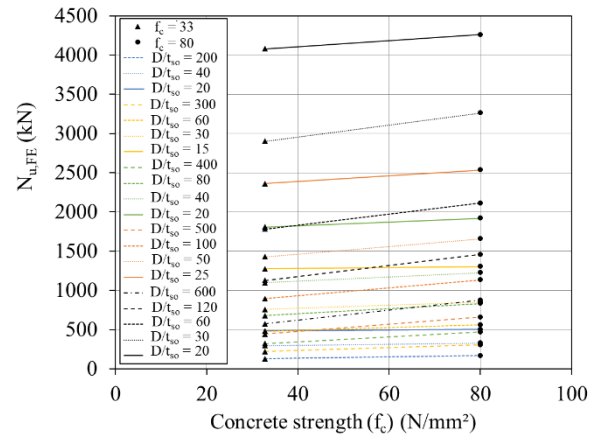
e) e30%D;



f) e50%D;

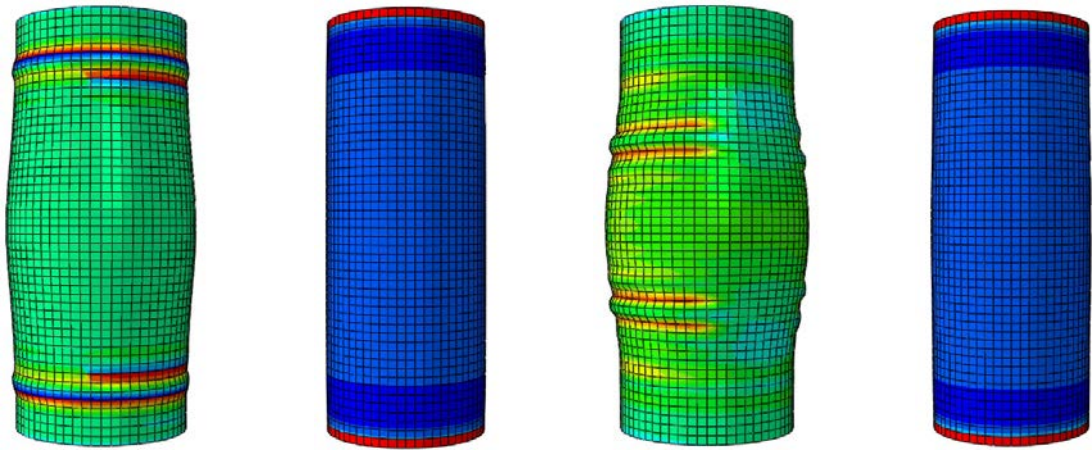


g) e85%D;



h) e200%D.

Figure 103 - Axial load *versus* concrete strength (f_c) (MPa).



d = 100 mm, t_{si} = 5 mm, e0%D and f_c = 33 MPa;

d = 100 mm, t_{si} = 5 mm, e0%D and f_c = 80 MPa;

a) D = 200 mm and t_{so} = 1 mm;

b) D = 600 mm and t_{so} = 30 mm;

c) D = 200 mm and t_{so} = 1 mm;

d) D = 600 mm and t_{so} = 30 mm.

Figure 104 - Longitudinal stress and deformation of the outer steel tube.

5.4.3 Results - Summary

The principal conclusions observed in this chapter are summarized in the key points below:

1. Under concentric axial compression:
 - all columns had an axial load *versus* axial displacement similar behaviour, with strain hardening in the steel tubes together with the concrete confinement effect increasing their load-carrying and displacement capacities, especially for CFDST columns with the greater concrete area and outer tube diameter (D);
 - Han *et al.* [46] design expression is most conservative for columns with relatively small inner tube diameters and consequently larger volumes of concrete infill;
 - CFDST columns with a relatively low hollow ratio (χ) value presented similar behaviour of a stocky CFST column while CFDST columns with a relatively high χ value presented similar behaviour of a hollow steel tubular column;
 - the load-carrying capacity and ductility of CFDST columns increases as the χ value decreases due to the higher concrete confining pressure;
 - Han *et al.* [46] design expression is most conservative for columns with relatively low hollow ratios and unconservative for χ values greater than 0.67;
 - smaller inner steel tube slenderness resulted in higher load-carrying capacity and ductility;
 - the concrete compressive strength increase enhanced the load capacity of the columns.

2. Under eccentric axial compression:
 - all the beam-columns had an axial load *versus* axial displacement identical behaviour during the elastic phase and different response after that, which depending on the outer tube diameter value;
 - CFDST beam-columns with D = 200 mm, D = 300 mm and D = 400 mm presented two load peaks where the second and ultimate load was higher than the first, while D = 500 mm and D = 600 mm had only one peak load with very little strain hardening and ductility;

- the second peak load of CFDST beam-columns with $D = 200$ mm, $D = 300$ mm and $D = 400$ mm started to become smaller than the first as the eccentricity applied was increased;
- as the eccentricity exceeded 50% of the outer tube diameter, all the beam-column become more similar to a flexural element, with a higher ductility and strain hardening response and a smaller load capacity;
- the yielding stage proved to be higher for CFSDT columns and beam-columns, where the outer tube diameter and the concrete confinement effect are significantly larger;
- the beam-columns capacity increased for members with a relatively large outer tube diameter;
- as the A_c/A_{total} increases, the load capacity also increases due to the concrete infill confinement;
- the load-carrying capacity and ductility of CFDST beam-columns increases as the χ value decreases due to the higher concrete confining pressure. This behaviour was observed for all the studied eccentricities;
- smaller $D/\varepsilon^2 t_{so}$ values represent thicker outer steel tubes when their thickness (t_{so}) is larger. For all eccentricities, smaller $D/\varepsilon^2 t_{so}$ ratios led to higher load-carrying capacities. The load capacity gain can be three times when comparing the outer steel tubes thickness (t_{so}) of 1 mm and 20 mm, for only a CFDST column. The load capacity gain can be 5.6 times when comparing the outer steel tubes thickness (t_{so}) of 1 mm and 20 mm, for CFDST beam-columns for larger eccentricities (such as $e \geq 200\%D$);
- the Eurocode 4 (EC4) [18] (N_{EC4}) predictions provided safe design results for CFDST columns while N_{EC4} predictions were unconservative and provided unsafe design results for CFDST beam-columns;
- the CFDST beam-columns load-carrying capacities decreased as the load eccentricity ratio increased. This decrease is more accentuated for beam-columns with a large outer tube diameter (D) and outer tube thickness (t_{so});
- the concrete compressive strength increase enhanced the load capacity of the beam-columns. This enhancement is higher when the beam-columns have thicker outer tubes.

6 DESIGN RECOMMENDATIONS

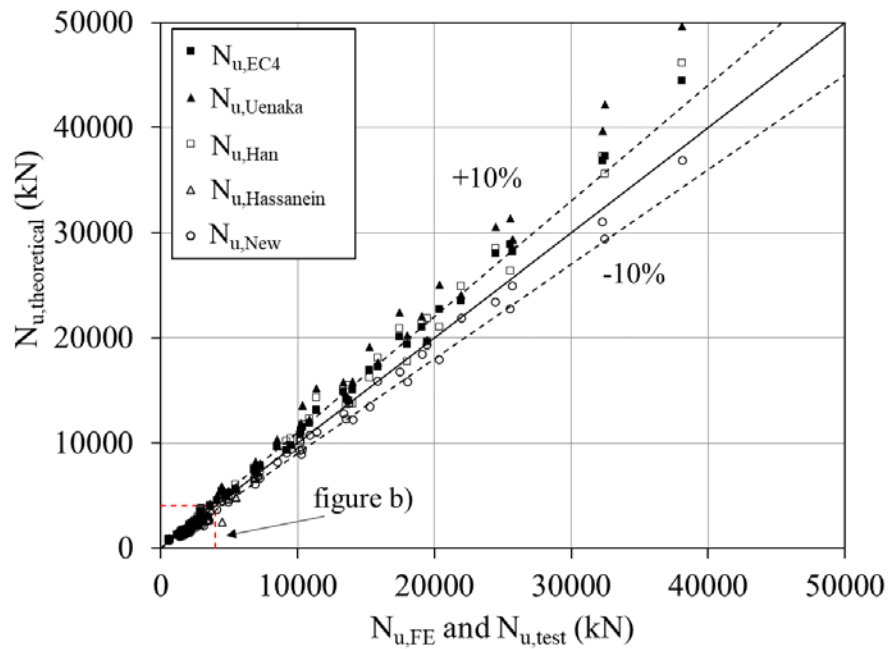
6.1 Generalities

This chapter will evaluate the experimental and numerical results with a set of design methods for CFDST columns under concentric and eccentric axial compression, previously discussed in items 2.2 and 2.3. The evaluated methods for elements under concentric axial compression were the Eurocode 4 (EC4) [18] design standard for CFST columns adapted for CFDST columns and the methods proposed by Uenaka *et al.* [54], Han *et al.* [46] and Hassanein *et al.* [51]. This assessment will be followed by a detailed description of the process to derive N-M interaction diagrams made of CFDST cross-section. This procedure was developed within the MATLAB [90] software framework to assess the CFDST columns load-carrying capacities when subjected to eccentric axial compression. The beam-columns load-carrying capacity can be readily predicted using the intersection of the applied load value and the N-M interaction curve. Moreover, the N-M interaction diagram will also be compared with the methods described in 2.3, i.e., Eurocode 4 (EC4) [18], Uenaka and Kitoh [55], Han *et al.* [12] and Fouché *et al.* [56]. Finally, a reliability analysis of the evaluated design method will be presented.

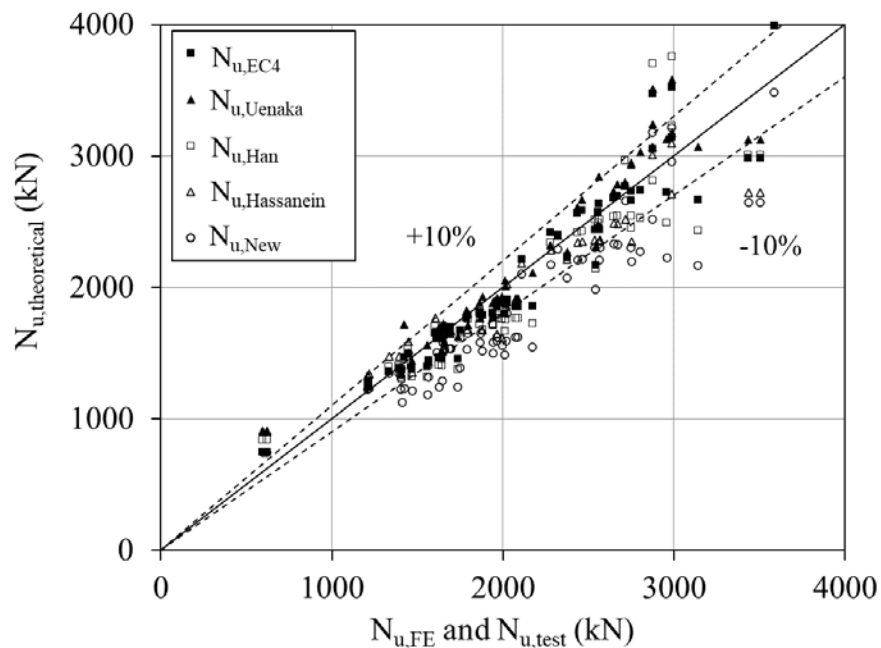
6.2 CFDST columns under concentric axial compression

Figure 105 depicts a comparison of the experimental ($N_{u,test}$) and FE ($N_{u,FE}$) ultimate loads, previously presented (4.4 and 5.2), and their corresponding design predictions ($N_{u,EC4}$, $N_{u,Uenaka}$, $N_{u,Han}$, $N_{u,Hassanein}$ and $N_{u,new}$). This comparison enables assessing the accuracy of these design expressions commonly adopted to forecast the ultimate load of CFDST columns. Besides the design methods previously presented, the load capacity obtained from MATLAB [90] N-M interaction curve is also plotted, while its full description and use will be explained in item 6.3. It is noteworthy that any point below the diagonal line is considered a safe prediction, whereas any prediction above the line is unsafe. The dashed lines represent limits +10% above and -10% below for $N_{u,theoretical}$ to be equal to $N_{u,FE}$ and/or $N_{u,test}$. The first graph a)

represents all the CFDST columns studied in this thesis, while the second contains a similar version limited in the horizontal and vertical axes to 4000 kN.



a) CFDST cross-sections studied - total results: plotted until 50000 kN;



b) CFDST cross-sections studied - partial results: plotted until 4000 kN.

Figure 105 - Existing design formula accuracy assessment.

It is clear from the data presented in Figure 105 that a significant number of the design predictions, particularly the $N_{u,EC4}$, $N_{u,Uenaka}$ and $N_{u,Han}$ values, failed into the unsafe side.

Alternatively, Figure 105 b) shows that the experimental and FE results are very close to the proposed equation values (i.e., close to the diagonal line). These conclusions imply that for higher load capacities (Figure 105 a)), the design methods prove to be unsafe. This observation might have happened due to a limitation of scope for these design predictions related to higher concrete compressive strength (f_c) and/or outer tube slenderness ($\lambda_{EC4} = D/t_{so}\varepsilon^2$).

It is important to observe that the adopted Eurocode 4 (EC4) [18] equation was the same proposed for CFST columns with NAC. However, the reinforced steel capacity was replaced by the inner steel tube capacity. Uenaka *et al.*'s [54] equation was only proposed for carbon steel tube, NAC for cross-sections with the d/D ratio limited to a $0.2 < d/D < 0.7$ range. Han *et al.*'s [46] method was developed for carbon steel inner tubes, stainless steel outer tubes, NAC, and a hollow ratio (χ) varying from 0.5 to 0.75. Hassanein *et al.*'s [51] design proposal was developed for carbon steel inner tube, stainless steel outer tube, NAC, an outer steel tube slenderness of $D/t_{so} < 59$, a concrete compressive strength f_c varying from 40 to 120 MPa and limits of strain hardening effects for both steel tubes, i.e., 1.2 for the stainless steel tube and between 0.9 and 1.1 for the carbon steel tube.

All the methods were only developed for NAC, while the concrete confinement effect was only due to the outer steel tube. The coefficient of variation (CoV) for the experimental and FE results divided by the predicted capacity were: 0.088 for Eurocode 4 (EC4) [18], 0.110 for Uenaka *et al.* [54], 0.118 for Han *et al.* [46], 0.153 for Hassanein *et al.* [51] and 0.109 when using the MATLAB [90] N-M interaction diagram. It is noteworthy that the proposed equations have some limitations about the CFDST cross-section (described above) and were not considered in Figure 105. However, the proposed new model from MATLAB [90] considers all the cross-sections and the NAC infilled, resulting in a CoV in good agreement for experimental and FE results.

6.3 CFDST columns under eccentric axial compression: N-M interaction diagram

The N-M interaction diagram was developed using the MATLAB software [90] since each cross-section area's angles depended on the neutral axis position (h). An interactive routine was developed to plot each axial load and bending moment capacities for each arbitrary neutral axis (h). The N-M diagram was compared to the results of the literature's experiments and the parametric analysis (5.4.2) obtained from ABAQUS [16]. The FE results for members under

combined axial compression and bending moment considered second-order effects that account for the lateral deflection of the element, i.e.:

$$M_{u,FE} = N_{u,FE}(e + \delta) \quad (107)$$

where $N_{u,FE}$ is the axial load and δ is the lateral deflection at the column mid-height from ABAQUS [16] results; e is the applied eccentricity value assessed as a percentage of the outer tube diameter (D).

The parametric FE results ($N_{u,FE}$) for beam-columns and the N-M interaction diagram developed in MATLAB [90] (best explored in item 6.3.1) are compared with the proposed design methods in the literature, from Han *et al.* [12], Uenaka and Kitoh [55] and Fouché *et al.* [56]. The angles and neutral axis (h) were calculated through the equation from Fouché *et al.* [56] to obtain the Uenaka and Kitoh [55] N-M diagram. The final equations for N_u and M_u are the same from Fouché *et al.* [56] and Uenaka and Kitoh [55]. However, Uenaka and Kitoh [55] consider the equivalent concrete stress block coefficient $k = 0.85$.

Figure 106 ($f_c = 33$ MPa) shows the proposed N-M interaction diagram represented in a dashed black line. In contrast, Han *et al.*'s [12] method are in the solid green line, Uenaka and Kitoh's [55] approach is in solid red line and Fouché *et al.*'s [56] proposed design is in the solid blue line. All the proposed methods were developed for NAC. The proposed N-M interaction diagram is on the safe side in all images in Figure 106, while Han *et al.* [12] approach agrees with the FE parametric results only for cross-sections with an outer steel tube thickness of $t_{so} = 5$ mm and 10 mm. This trend occurs due to a limitation in the method where: $D \geq 200$ mm, $t_{so} \geq 4$ mm, $D/t_{so} \leq 135 \times 235/f_{syo}$, $0.0 \leq \chi \leq 0.75$ and $0.6 \leq \xi \leq 4.0$. Table 34 shows the parametric cross-sections studied, where the black dashed rectangles are the cross-sections elements that are not suitable for the use of Han *et al.*'s [12] method. It was also observed from the graphs that Han *et al.*'s [12] method seems to have no limitation for cross-sections with greater outer tube thicknesses ($t_{so} = 20$ and 30 mm). Therefore, Han *et al.*'s [12] method should specify other limitation for greater outer tube thicknesses, whereas it should not exceed at least the value of 20 mm ($t_{so} \leq 20$ mm). Figure 107 presents the same evaluated curves with a different concrete compressive strength of $f_c = 80$ MPa. The same considerations are observed in these cross-sections. However, none of the FE results evaluated is in good agreement with Han *et al.*'s [12] method, probably due to the higher concrete compressive strength value. Also, there is no specification in Han *et al.*'s [12] proposed design about its applicability in concrete

with higher compressive strengths. Finally, Han *et al.*'s [12] method should present a second limitation where the concrete compressive strength (f_c) should not exceed at least the value of 33 MPa ($f_c \leq 33$ MPa).

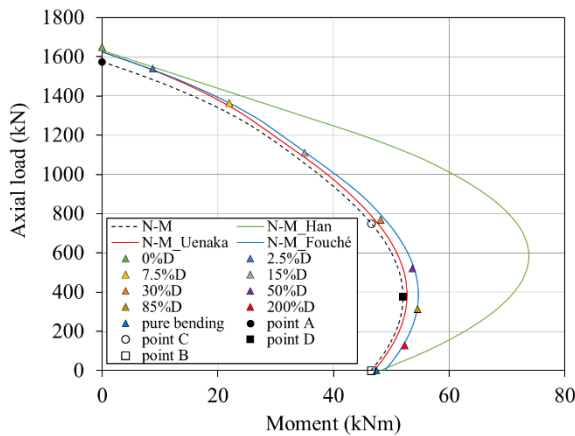
In Figure 106, Uenaka and Kitoh's [55] approach is in good agreement with almost all the FE parametric results. However, Uenaka and Kitoh's [55] diagram is on the unsafe side, e.g. Figure 106 c), when the outer tube thickness (t_{so}) is greater than 10 mm ($t_{so} \geq 10$ mm), and it is very conservative, e.g. Figure 106 d) when the outer tube thickness (t_{so}) is smaller than 1 mm ($t_{so} \leq 1$ mm). It happened because Uenaka and Kitoh's [55] method uses an approximation with only the outer angle β_o and the inner angle β_i to calculate the areas, the outer and inner tube thicknesses are not considered when calculating the cross-section angles. Therefore, for greater outer tube thickness values, this method is not applicable. Figure 107 presents the same evaluated curves with a different concrete compressive strength, of $f_c = 80$ MPa. Almost all the FE results evaluated are on the unsafe side (e.g. Figure 107 b)) for Uenaka and Kitoh's [55] method. At the same time, they are only in good agreement (e.g. Figure 107 a)) for this approach when the outer tube thickness (t_{so}) is equal to or smaller than 1 mm ($t_{so} \leq 1$ mm) due to the higher concrete compressive strength value. This method should also have a second limitation, whereas the concrete compressive strength (f_c) should not exceed at least the value of 33 MPa ($f_c \leq 33$ MPa).

In Figure 106, Fouché *et al.*'s [56] proposed design is in good agreement with almost all the FE parametric results, except when the outer tube thickness (t_{so}) is greater than 10 mm ($t_{so} \geq 10$ mm) where the method is on the unsafe side (e.g. Figure 106 g)). The same approximation of Uenaka and Kitoh's [55] method is used, where the outer tube thickness is not considered when calculating the cross-section angles. Fouché *et al.*'s [56] method proved not to apply to thicker outer tubes with these results. Figure 107 presents Fouché *et al.*'s [56] proposed design performance where all the FE results were on the design unsafe side. This response probably occurred due to the adopted 80 MPa higher concrete compressive strength.

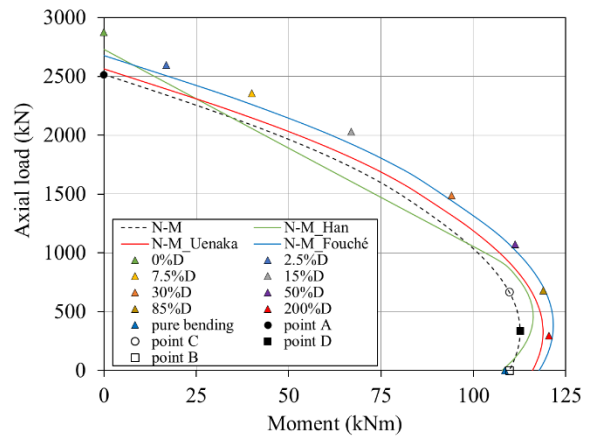
Table 34 - Han *et al.*'s [12] method limitations.

Cross-section	Outer tube diameter $D \geq 200$ mm	$t_{so} \geq 4$ mm	$D/t_{so} \leq 76$ mm	Hollow ratio (χ) $0.0 \leq \chi \leq 0.75$	Confinement factor (ξ) $0.6 \leq \xi \leq 4.0$.
200 x 1_100 x 5	200	1	200	0.51	0.26
200 x 5_100 x 5	200	5	40	0.53	1.38
200 x 10_100 x 5	200	10	20	0.56	3.00
300 x 1_150 x 5	300	1	300	0.50	0.17
300 x 5_150 x 5	300	5	60	0.52	0.90

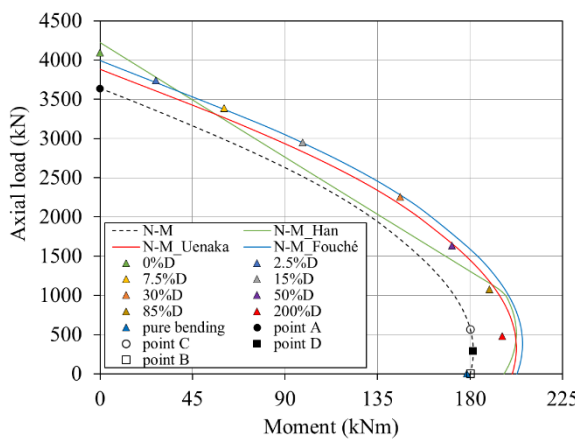
300 x 10_150 x 5	300	10	30	0.54	1.89
300 x 20_150 x 5	300	20	15	0.58	4.23
400 x 1_200 x 5	400	1	400	0.50	0.13
400 x 5_200 x 5	400	5	80	0.51	0.66
400 x 10_200 x 5	400	10	40	0.53	1.38
400 x 20_200 x 5	500	20	20	0.56	3.00
500 x 1_250 x 5	500	1	500	0.50	0.10
500 x 5_250 x 5	500	5	100	0.51	0.53
500 x 10_250 x 5	500	10	50	0.52	1.09
500 x 20_250 x 5	600	20	25	0.54	2.32
600 x 1_300 x 5	600	1	600	0.50	0.09
600 x 5_300 x 5	600	5	120	0.51	0.44
600 x 10_300 x 5	600	10	60	0.52	0.90
600 x 20_300 x 5	200	20	30	0.54	1.89
600 x 30_300 x 5	200	30	20	0.56	3.00



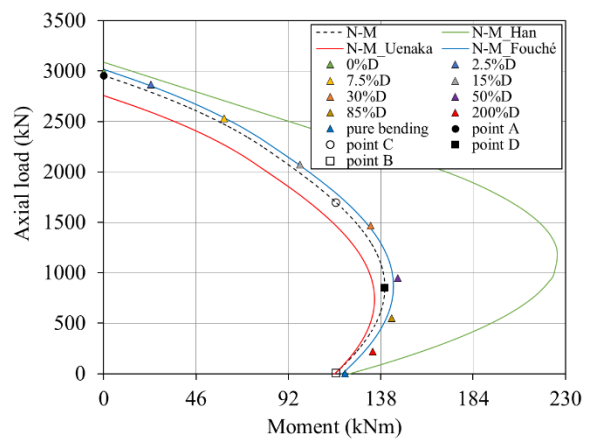
a) 200x1_100x5;



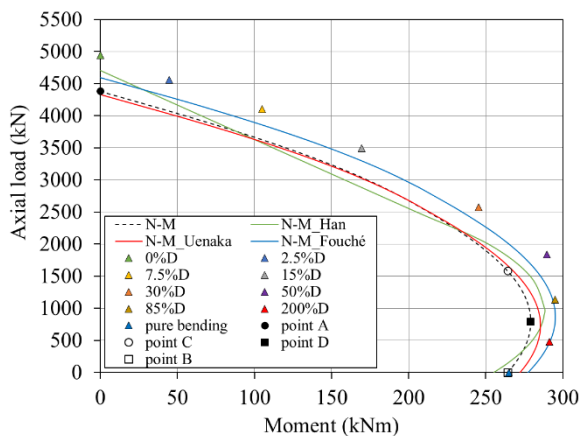
b) 200x5_100x5;



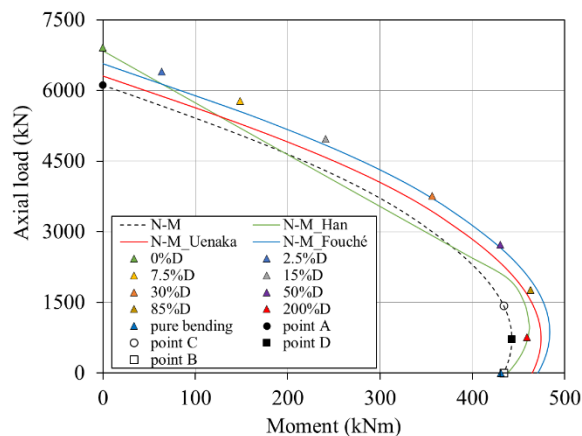
c) 200x10_100x5;



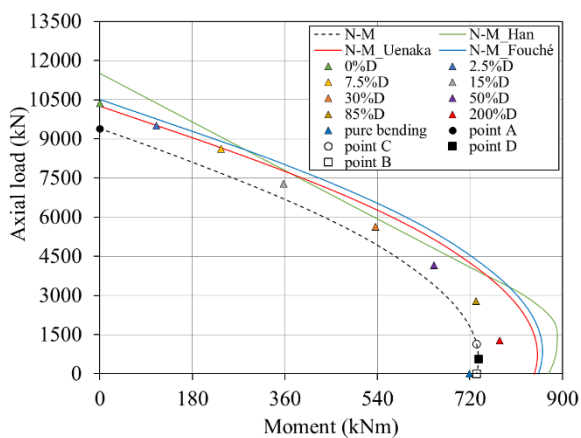
d) 300x1_150x5;



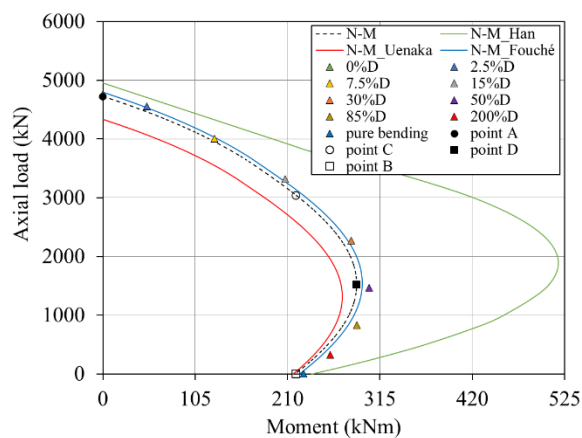
e) 300x5_150x5;



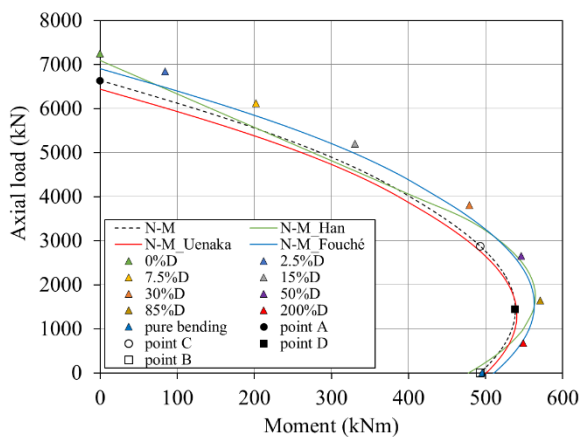
f) 300x10_150x5;



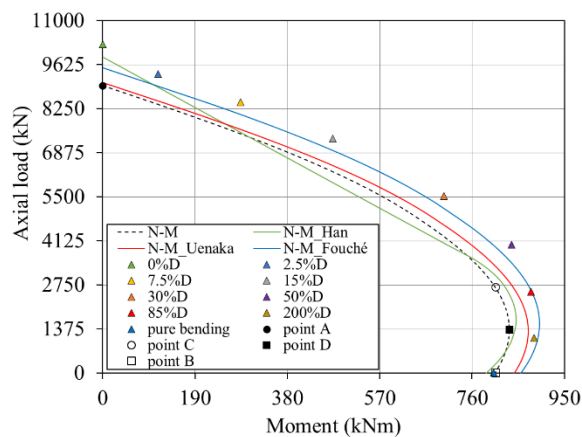
g) 300x20_150x5;



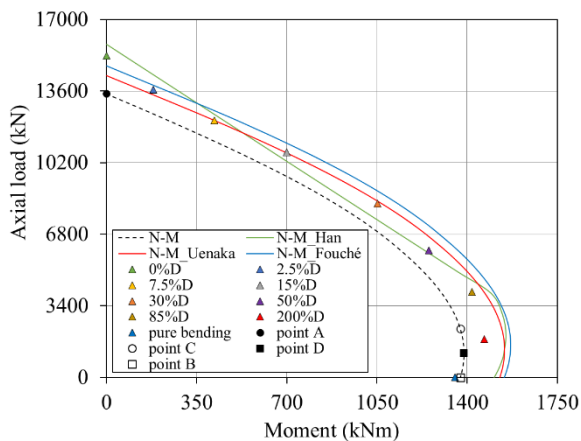
h) 400x1_200x5;



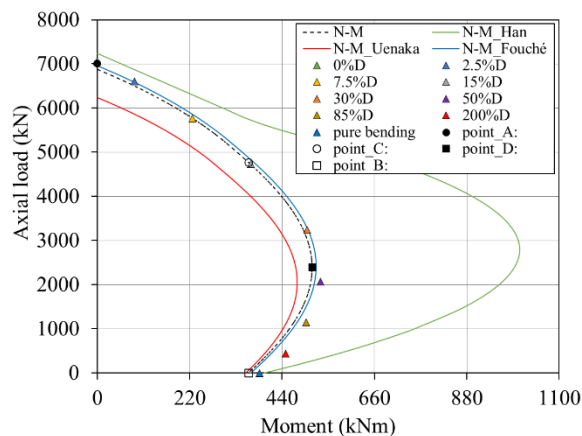
i) 400x5_200x5;



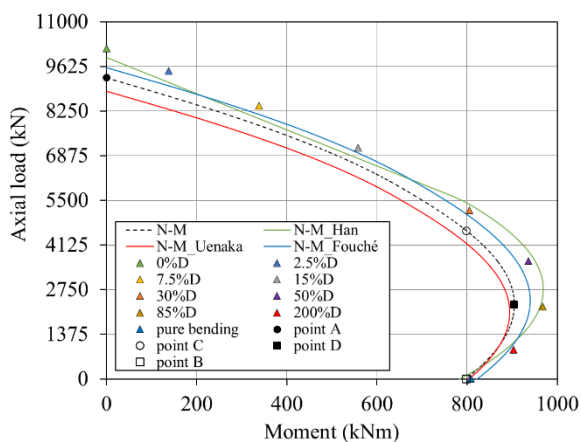
j) 400x10_200x5;



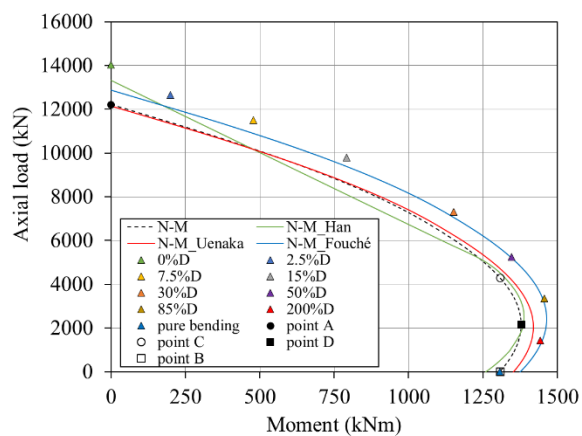
k) 400x20_200x5;



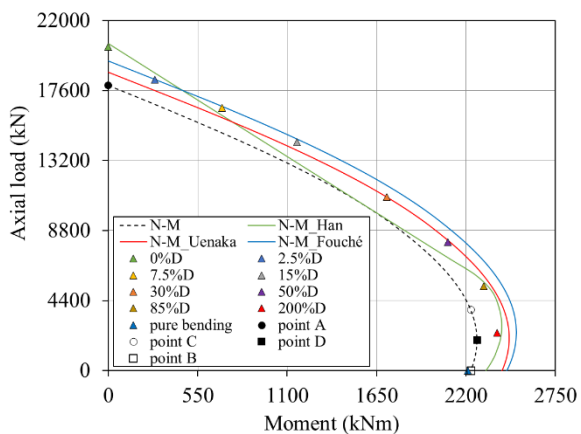
l) 500x1_250x5;



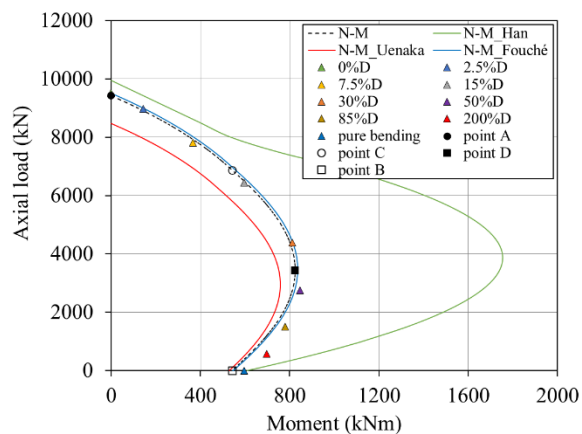
m) 500x5_250x5;



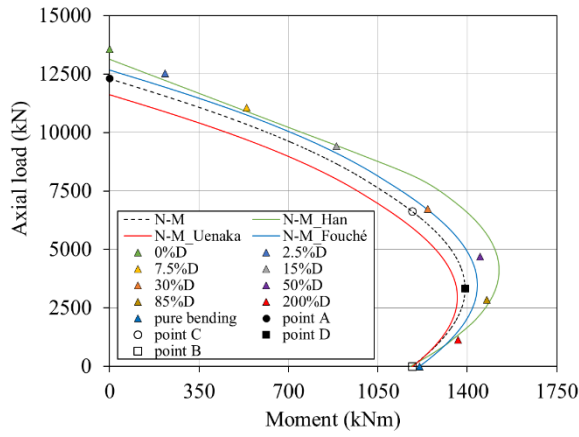
n) 500x10_250x5;



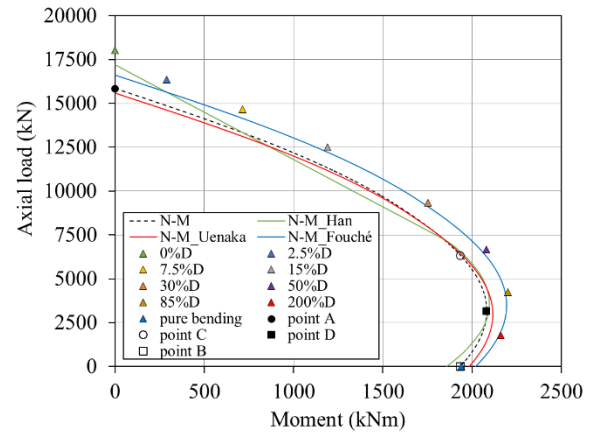
o) 500x20_250x5;



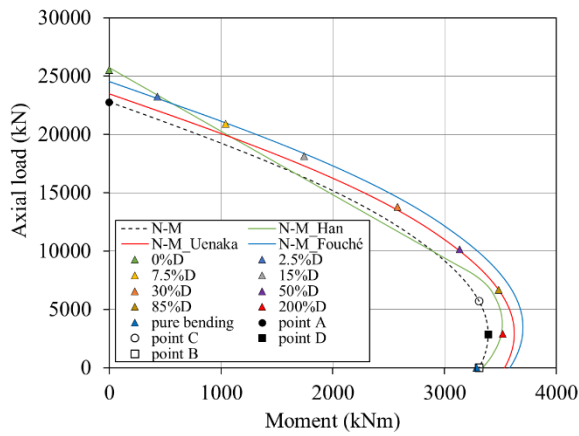
p) 600x1_300x5;



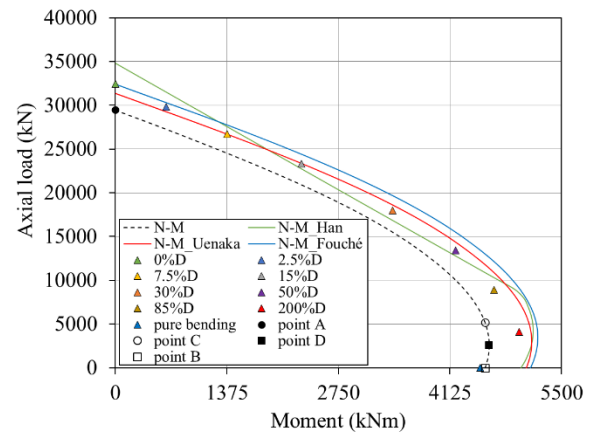
q) 600x5_300x5;



r) 600x10_300x5;

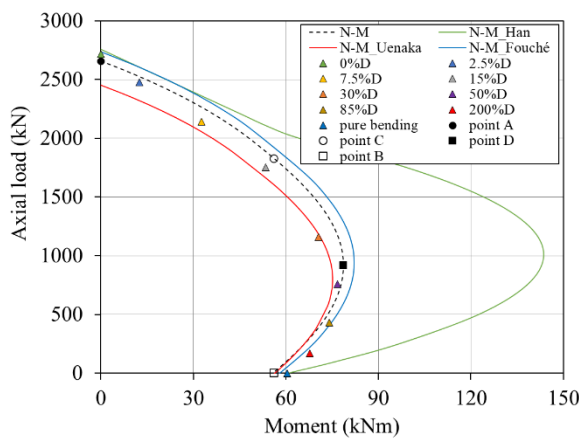


s) 600x20_300x5;

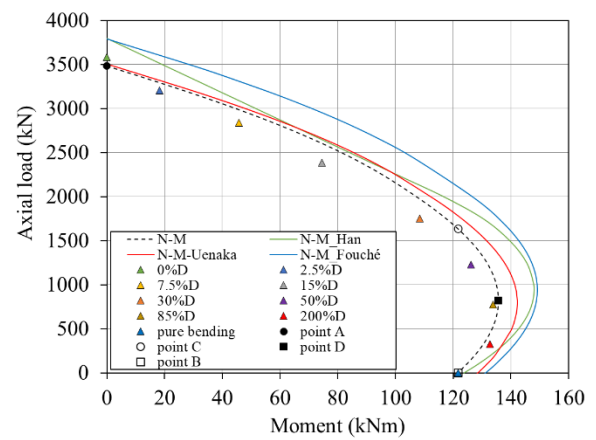


t) 600x30_300x5.

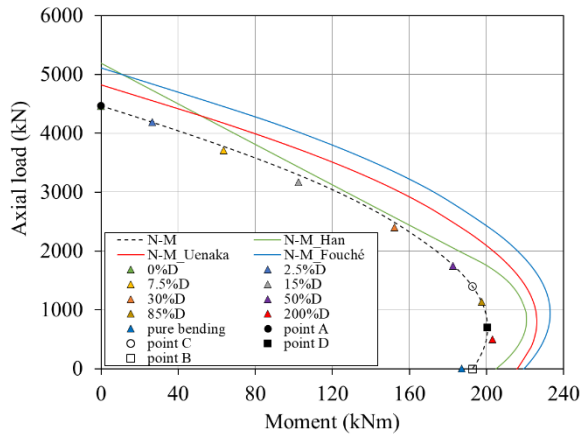
Figure 106 - Proposed N-M interaction curve and current design methods (Han *et al.* [12], Uenaka and Kitoh [55] and Fouché *et al.* [56]), for concrete strength (f_c) of 30 MPa.



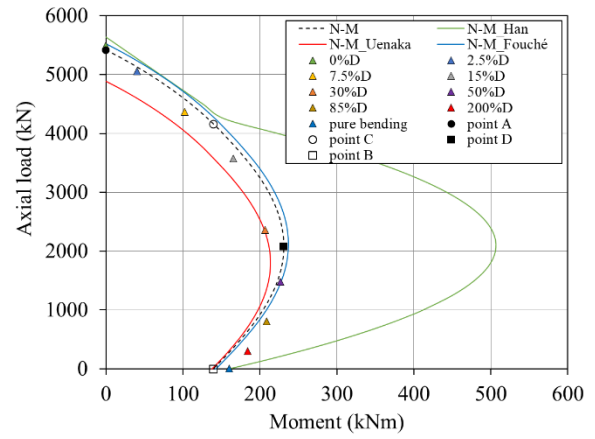
a) 200x1_100x5;



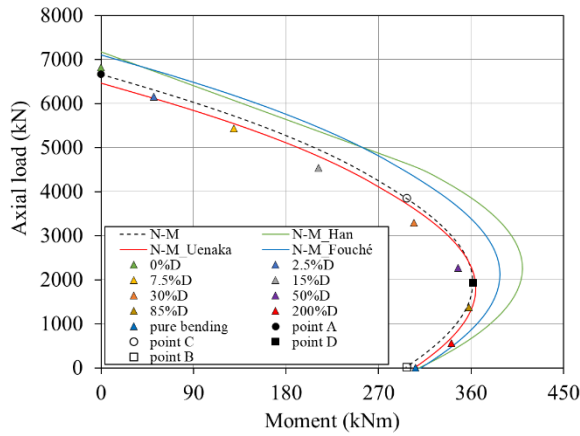
b) 200x5_100x5;



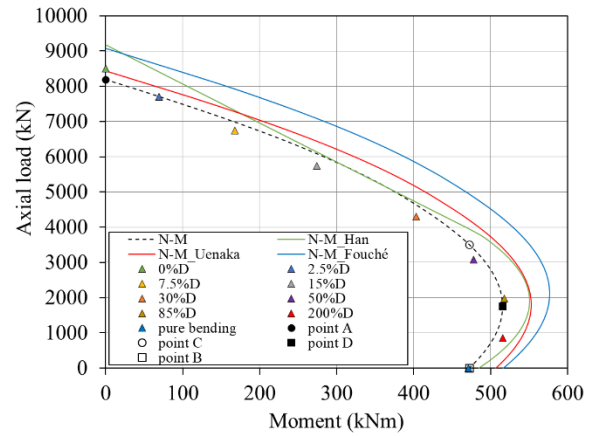
c) 200x10_100x5;



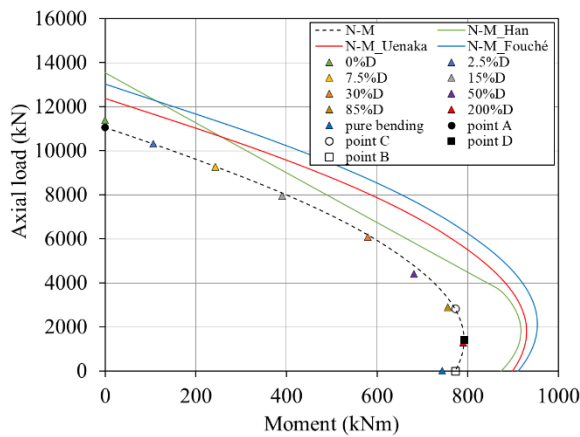
d) 300x1_150x5;



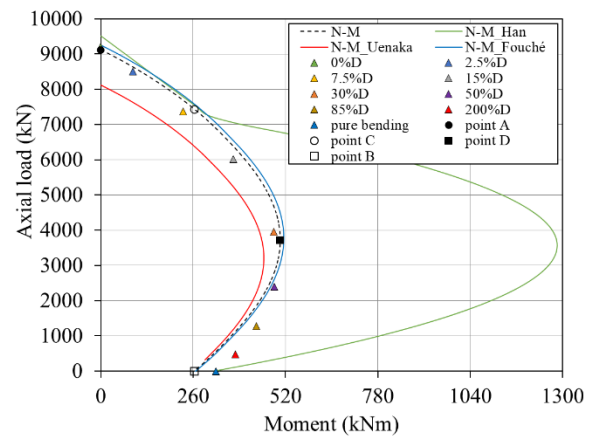
e) 300x5_150x5;



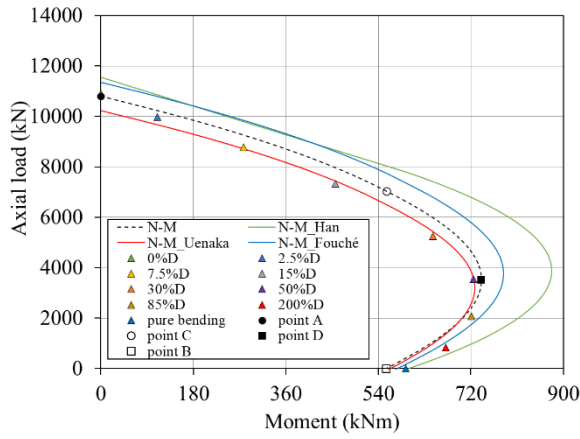
f) 300x10_150x5;



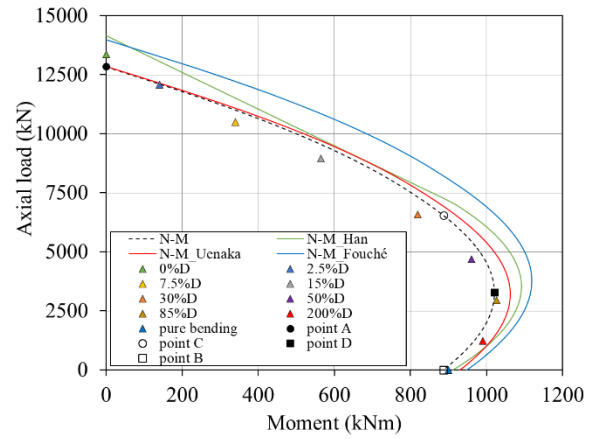
g) 300x20_150x5;



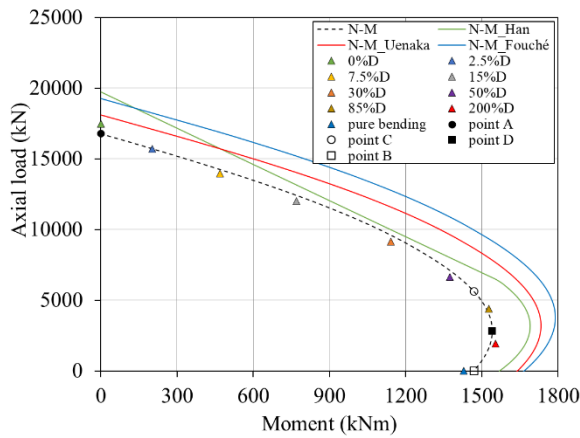
h) 400x1_200x5;



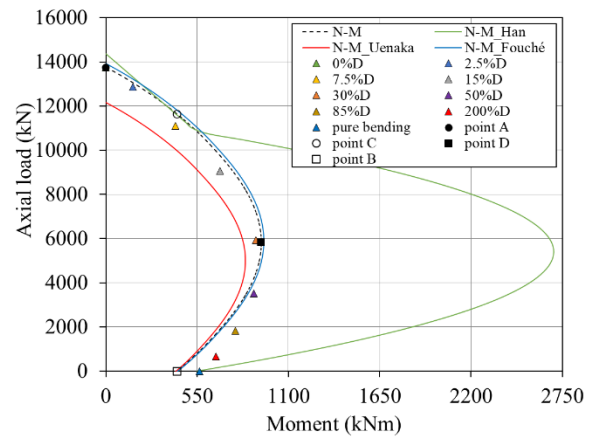
i) 400x5_200x5;



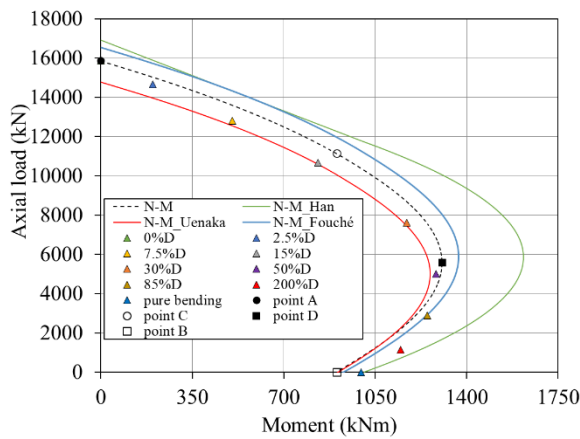
j) 400x10_200x5;



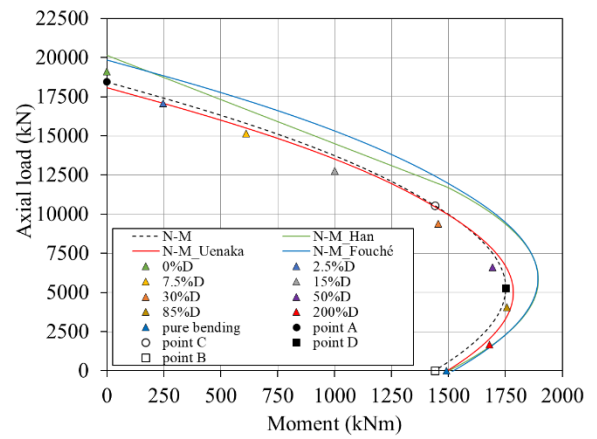
k) 400x20_200x5;



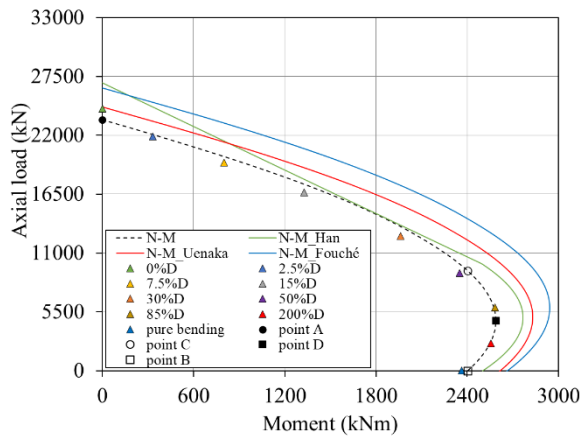
l) 500x1_250x5;



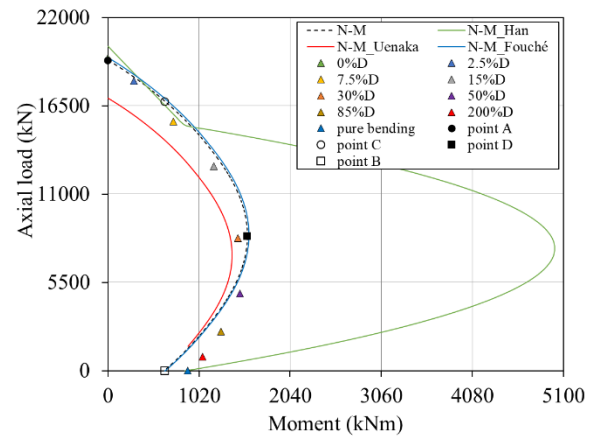
m) 500x5_250x5;



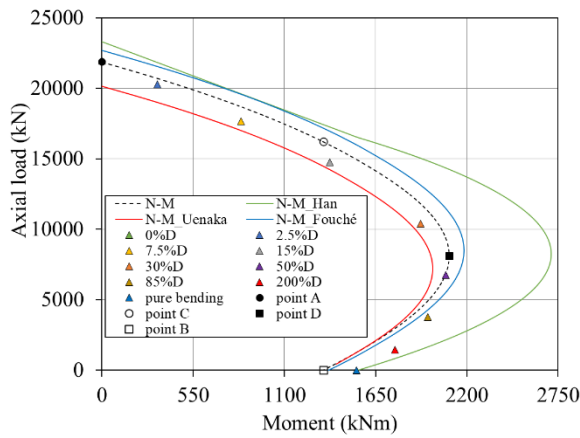
n) 500x10_250x5;



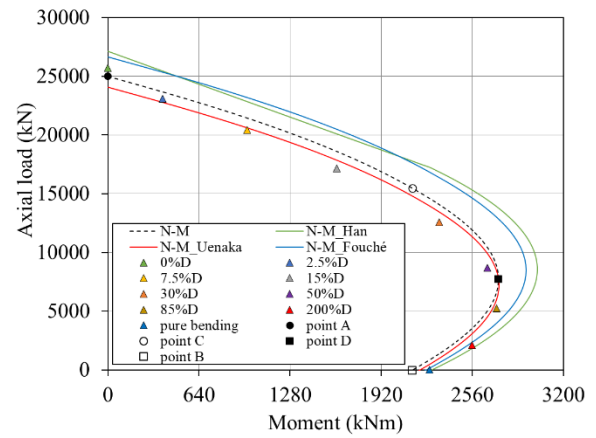
o) 500x20_250x5;



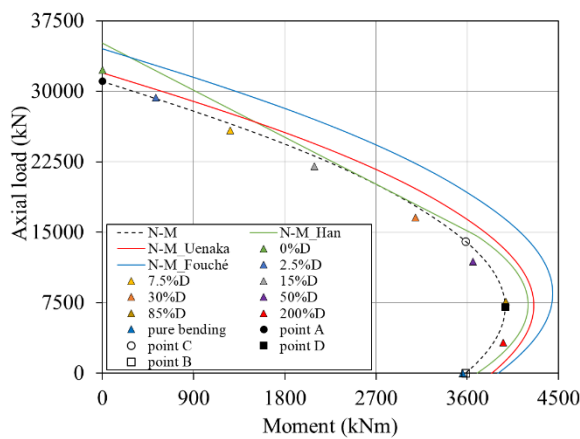
p) 600x1_300x5;



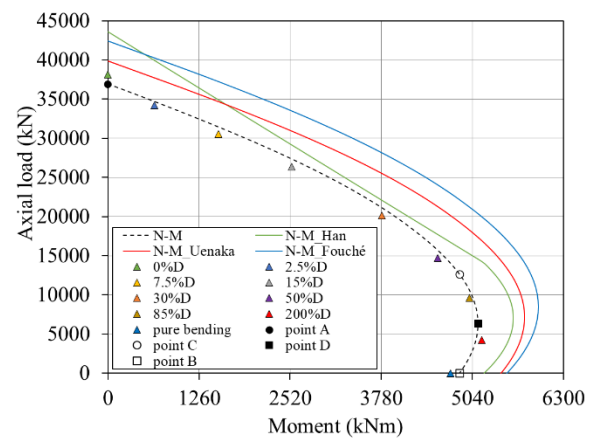
q) 600x5_300x5;



r) 600x10_300x5;



s) 600x20_300x5;



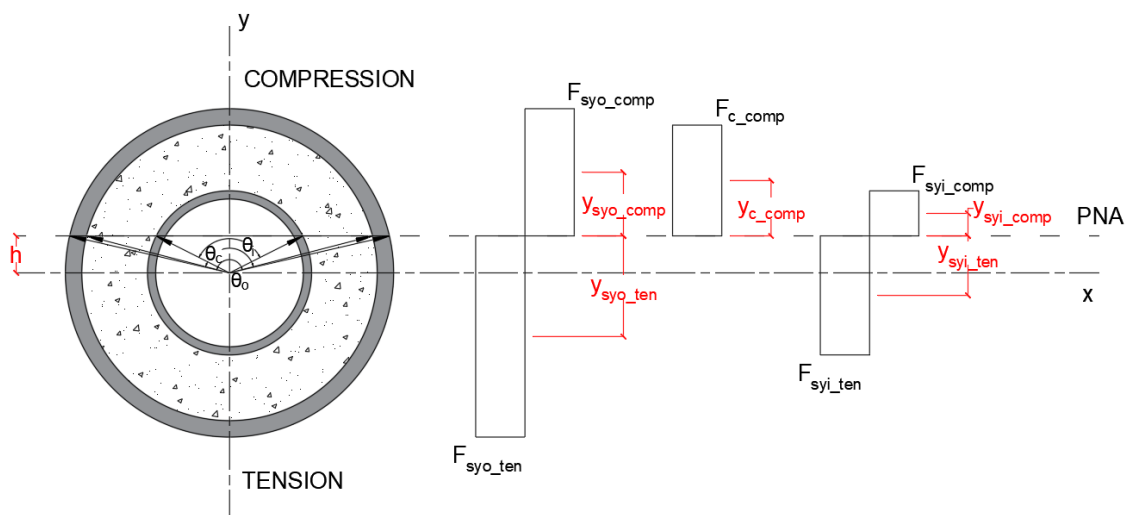
t) 600x30_300x5.

Figure 107 - Proposed N-M interaction curve and current design methods (Han *et al.* [12], Uenaka and Kitoh [55] and Fouché *et al.* [56]), for concrete strength (f_c) of 80 MPa.

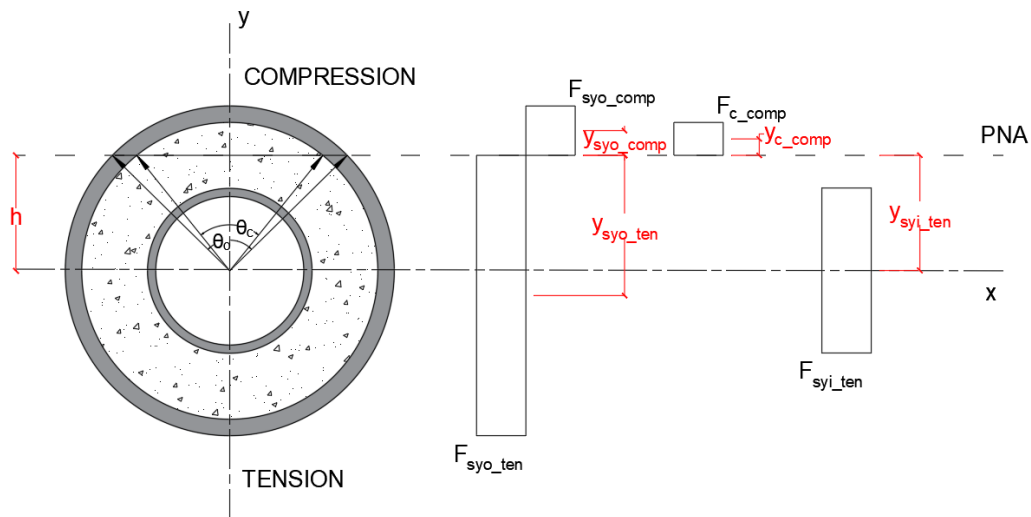
6.3.1 Proposed design method

An N-M interaction diagram for CFDST sections was developed through MATLAB software [90], and was based on a rigid-plastic material analysis assuming a rectangular stress block distribution. The steel stresses were limited, either in compression or tension, to the 0.2% yield stress for the outer stainless steel tube (f_{yso}) or the yield stress for the inner carbon steel tube (f_{ysi}). The concrete compressive strength (f_c) was used as the compression concrete strength, while the concrete strength under tension was considered equal to zero.

The stress distribution procedure for producing the N-M interaction diagram for the CFDST cross-section can be divided into two steps. Firstly, an arbitrary position for the cross-section's neutral axis inside the inner steel tube's hollow is assumed. The second step assumes that a point outside the inner tube, as shown in Figure 108. After this step, the three materials' stress block distribution (stainless steel, concrete and carbon steel) are calculated considering the rigid plastic material assumption. This step follows with an evaluation of the acting axial load and the bending moment. These values can be obtained considering the areas above each arbitrary position of the neutral axis (h). All these steps were performed by changing the neutral axis's position until it accounts for the entire outer tube diameter of the CFDST cross-section. Finally, the simplified equations proposed below (Eqs. (107) to (124)) can be easily applied in the Excel software by varying the neutral axis values (h).



a) PNA inside the inner steel tube;



b) PNA outside the inner steel tube.

Figure 108 - CF DST sections stress distributions under combined axial load and bending moment.

In Figure 108, F_{syo} , F_c and F_{syi} represent the resistance parcels for the outer steel tube, infilled concrete and inner steel tube, respectively. In these figures, regions above the neutral axis (h) are in compression, and below this are in tension. The axial load N_i and the bending moment M_i for a cross-section with a neutral axis position I can be evaluated with the equations below. In these equations, M_{syo} , M_c and M_{syi} are the bending moments for the outer steel tube, infilled concrete and inner steel tube, respectively:

$$N_i = F_{syo} + F_c + F_{syi} \quad (108)$$

$$M_i = M_{syo} + M_c + M_{syi} \quad (109)$$

When the PNA is located across the inner steel tube, a resistance parcel related to this element also needs to be accounted. This parcel is also in compression and must be considered in evaluating the axial load and bending moment (N_u and M_u) capacities. Alternatively, when the PNA is located above the inner steel tube, there is no compressive resistance parcel for this element. The equations below are applicable for both situations, just by considering the compressive inner steel tube parcel as zero when the PNA is located above this element. The resistance parcel of all the elements in compression was also taken as positive. The axial load $N_{u,pred}$ and the bending moment capacities $M_{u,pred}$ can be evaluated with the following equations:

$$N_{u,pred} = F_{syo_comp} + F_{c_comp} + F_{syi_comp} - F_{syo_ten} - F_{syi_ten} \quad (110)$$

$$M_{u,pred} = F_{syo_comp}y_{syo_comp} + F_{c_comp}y_{c_comp} + F_{syi_comp}y_{syi_comp} \\ + F_{syo_ten}y_{syo_ten} + F_{syi_ten}y_{syi_ten} \quad (111)$$

where F_{syo_comp} , F_{c_comp} and F_{syi_comp} are the resistance parcels of the outer steel tube, infilled concrete and inner steel tube under compression; F_{syo_ten} and F_{syi_ten} are the resistance parcels of the outer steel tube and inner steel tube under tension; y_{syo_comp} , y_{c_comp} , and y_{syi_comp} are the application points of the resultant compressive force acting in the outer steel tube, the infilled concrete and the inner steel tube; y_{syo_ten} and y_{syi_ten} are the application points of the resultant tensile force acting in the outer steel tube and the inner steel tube.

The resultant compressive force, the resultant tensile force and their centroids, which maintaining the cross-sections in equilibrium, can be determined with:

$$F_{syo_comp} = f_{syo} \left[\frac{R^2}{2} (\theta_o - \sin \theta_o) - \frac{R_c^2}{2} (\theta_c - \sin \theta_c) \right] \quad (112)$$

$$R_c = \frac{D - 2t_{so}}{2} \quad (113)$$

$$F_{c_comp} = f_c \left[\frac{R_c^2}{2} (\theta_c - \sin \theta_c) - \frac{r^2}{2} (\theta_i - \sin \theta_i) \right] \quad (114)$$

$$F_{syi_comp} = f_{syi} \left[\frac{r^2}{2} (\theta_i - \sin \theta_i) - \frac{(r - t_{si})^2}{2} (\theta_{(i-t_{si})} - \sin \theta_{(i-t_{si})}) \right] \quad (115)$$

$$F_{syo_ten} = f_{syo} \left\{ \pi(R^2 - R_c^2) - \left[\frac{R^2}{2} (\theta_o - \sin \theta_o) - \frac{R_c^2}{2} (\theta_c - \sin \theta_c) \right] \right\} \quad (116)$$

$$F_{syi_ten} = f_{syi} \left\{ \pi[r^2 - (r - t_{si})^2] \right. \\ \left. - \left[\frac{r^2}{2} (\theta_i - \sin \theta_i) - \frac{(r - t_{si})^2}{2} (\theta_{(i-t_{si})} - \sin \theta_{(i-t_{si})}) \right] \right\} \quad (117)$$

$$y_{syo_comp} = \frac{4}{3} \left[\frac{R^3 \sin^3(\theta_o/2) - R_c^3 \sin^3(\theta_c/2)}{R^2(\theta_o - \sin \theta_o) - R_c^2(\theta_c - \sin \theta_c)} \right] \quad (118)$$

$$y_{c_comp} = \frac{4}{3} \left[\frac{R_c^3 \sin^3(\theta_c/2) - r^3 \sin^3(\theta_i/2)}{R_c^2(\theta_c - \sin \theta_c) - r^2(\theta_i - \sin \theta_i)} \right] \quad (119)$$

$$y_{s_{yi_comp}} = \frac{4}{3} \left[\frac{r^3 \sin^3 \left(\frac{\theta_i}{2} \right) - (r - t_{si})^3 \sin^3 \left(\frac{\theta_{(i-t_{si})}}{2} \right)}{r^2 (\theta_i - \sin \theta_i) - (r - t_{si})^2 (\theta_{(i-t_{si})} - \sin \theta_{(i-t_{si})})} \right] \quad (120)$$

$$y_{s_{yo_ten}} = \frac{4}{3} \left[\frac{R^3 \sin^3 \left(\frac{\theta_{o_ten}}{2} \right) - R_c^3 \sin^3 \left(\frac{\theta_{c_ten}}{2} \right)}{R^2 (\theta_{o_ten} - \sin \theta_{o_ten}) - R_c^2 (\theta_{c_ten} - \sin \theta_{c_ten})} \right] \quad (121)$$

$$y_{s_{yi_ten}} = \frac{4}{3} \left[\frac{r^3 \sin^3 \left(\frac{\theta_{i_ten}}{2} \right) - (r - t_{si})^3 \sin^3 \left(\frac{\theta_{(i-t_{si})_ten}}{2} \right)}{r^2 (\theta_{i_ten} - \sin \theta_{i_ten}) - (r - t_{si})^2 (\theta_{(i-t_{si})_ten} - \sin \theta_{(i-t_{si})_ten})} \right] \quad (122)$$

$$\theta_o + 2\beta_o = \pi$$

$$\theta_c + 2\beta_c = \pi$$

$$\theta_i + 2\beta_i = \pi$$

(123)

$$\theta_{(i-t_{si})} + 2\beta_{(i-t_{si})} = \pi$$

$$h = R \sin \beta_o$$

$$h = R_c \sin \beta_c$$

$$h = r \sin \beta_i$$

(124)

$$h = (r - t_{si}) \sin \beta_{(i-t_{si})}$$

$$\theta_o + \theta_{o_ten} = 2\pi$$

$$\theta_c + \theta_{c_ten} = 2\pi$$

$$\theta_i + \theta_{i_ten} = 2\pi$$

(125)

$$\theta_{(i-t_{si})} + \theta_{(i-t_{si})_ten} = 2\pi$$

where R , R_c and r are the radius of the outer steel tube, the infilled concrete and the inner steel tube under compression; D and t_{so} are the diameter and the thickness of the outer steel tube; θ_o , θ_c , θ_i and $\theta_{(i-t_{si})}$ are the angles for each resistance parcel in compression and θ_{o_ten} , θ_{c_ten} , θ_{i_ten} and $\theta_{(i-t_{si})_ten}$ are the angles for each resistance parcel in tension, which are attributed to an arbitrary neutral axis value. The angles represent the outer steel tube, the infilled concrete, the inner steel tube, and the inner steel tube's hollow section, respectively. The variables β_o , β_c , β_i and $\beta_{(i-t_{si})}$ are the same β angles adopted by Fouché *et al.* [56] and previously described in item 2.3.3. These variables can be calculated based on the cross-section geometry, while $f_{s_{yo}}$, $f_{s_{yi}}$ and f_c represent the steels' stresses and the concrete compressive strength. The procedure presented above can be simplified for compression load N and bending M as described below:

$$\begin{aligned}
N_{u,pred} = & f_{syi}(r - t_{si})^2 \sin(2\beta_{(i-t_{si})}) \\
& - \frac{R_c^2}{2}(f_c - 2f_{sy0}) \sin(2\beta_c) + \frac{r^2}{2}(f_c - 2f_{syi}) \sin(2\beta_i) \\
& - f_{sy0}R^2 \sin(2\beta_o) + [2(\beta_{(i-t_{si})} - \beta_i)f_{syi} + (\beta_i - \pi/2)f_c]r^2 \\
& - 4f_{syi}rt_{si}\beta_{(i-t_{si})} + 2f_{syi}t_{si}^2\beta_{(i-t_{si})} + \frac{R_c^2}{2}(\pi - 2\beta_c)f_c \\
& - 2f_{sy0}(R^2\beta_o - R_c^2\beta_c)
\end{aligned} \tag{126}$$

$$\begin{aligned}
M_{u,pred} = & \frac{1}{3}[-4f_{syi}(r - t_{si})^3 \cos \beta_{(i-t_{si})}^3 + 2R_c^3(f_c - 2f_{sy0}) \cos \beta_c^3 \\
& - 2r^3(f_c - 2f_{syi}) \cos \beta_i^3 + 4f_{sy0}R^3 \cos \beta_o^3]
\end{aligned} \tag{127}$$

Alternatively, the required four points (as described in Eurocode 4 [18]) to draw a conservative N-M diagram can be obtained through the equations below:

- Point A – pure compression: The compression load N is calculated through the total cross-section area of each element, and all angles β are equal to 90° . The bending M is equal to zero:

$$N_A = f_{sy0}\pi(R^2 - R_c^2) + f_c\pi(R_c^2 - r^2) + f_{syi}\pi(r^2 - r_{(i-t_{si})}^2) \tag{128}$$

$$M_A = 0 \tag{129}$$

- Point B – pure bending: The compression load N is equal to zero. The bending M is calculated as the conservative approximation proposed by Fouché *et al.* [56] where $\sin(\beta) = \beta$ and $\cos(\beta) = 1$:

$$N_B = 0 \tag{130}$$

$$\begin{aligned}
M_B = & \frac{1}{3} \left[-4f_{syi}(r - t_{si})^3 \cos \left(\frac{h}{r - t_{si}} \right)^3 + 2R_c^3(f_c - 2f_{sy0}) \cos \left(\frac{h}{R_c} \right)^3 \right. \\
& \left. - 2r^3(f_c - 2f_{syi}) \cos \left(\frac{h}{r} \right)^3 + 4f_{sy0}R^3 \cos \left(\frac{h}{R} \right)^3 \right]
\end{aligned} \tag{131}$$

$$h_B = \frac{1}{4} \frac{\pi f_c (r^2 - R_c^2)}{[f_c(r - R_c) + 2f_{sy0}(R_c - R) - 2f_{syi}t_{si}]} \tag{132}$$

- Point C: The compression load N is equal to the resistance parcel of the total cross-section area of the “sandwich” concrete, and the moment M is the same value obtained to pure bending point:

$$N_c = 2N_D = f_c \pi (R_c^2 - r^2) \quad (133)$$

$$M_c = M_B = \frac{1}{3} \left[-4f_{syi}(r - t_{si})^3 \cos\left(\frac{h}{r - t_{si}}\right)^3 + 2R_c^3(f_c - 2f_{syo}) \cos\left(\frac{h}{R_c}\right)^3 - 2r^3(f_c - 2f_{syi}) \cos\left(\frac{h}{r}\right)^3 + 4f_{syo}R^3 \cos\left(\frac{h}{R}\right)^3 \right] \quad (134)$$

- Point D – maximum bending: The compression load N is equal to the resistance parcel of the total cross-section area of the “sandwich” concrete divided by two, and the moment M is the maximum bending considering the β angles and the neutral axis h as zero:

$$N_D = \frac{1}{2} f_c \pi (R_c^2 - r^2) \quad (135)$$

$$M_D = \frac{1}{3} \left[-4f_{syi}(r - t_{si})^3 + 2R_c^3(f_c - 2f_{syo}) - 2r^3(f_c - 2f_{syi}) + 4f_{syo}R^3 \right] \quad (136)$$

6.3.2 Proposed design method: confinement effect

The developed N-M interaction diagram for CFDST sections does not take into account the concrete confinement effect. It is well known the existence of confinement in the concrete-filled composite columns. However, both steel tubes' real confinement behaviour in the concrete in double-skin composite columns is not yet totally evident. Li *et al.* [91] consider the concrete confinement effect in CFDST columns to enhance the concrete strength due to the steel tubes. During the experiments, the strength of both steels tubes was measured by strain gauges, and the load carried by the concrete was taken as the total load subtracted by the loads carried by each steel tube in the same measured strain. A new compressive concrete strength f_{cc} can be obtained regarding the concrete confinement effect during the tests.

Li *et al.*'s [91] idea was then used in the present thesis considering enhancing the compressive concrete strength as f_{cc} . However, it was not possible to obtain these values experimentally or numerically from ABAQUS [16]. Therefore, values of a new compressive concrete strength f_{cc} were guessed for each studied cross-section to make the proposed $N_{u,pred}$ (Eq. 125) have the same value of the experiments and FE results presented before in this thesis. The ratio of the confined compressive concrete strength and the compressive concrete strength f_{cc}/f_c is presented in Figure 109 for all the experiments and FE results *versus* a) the confinement effect ξ (Han *et al.* [46]), b) the hollow ratio χ (Han *et al.* [46]), c) outer steel tube slenderness $\lambda_o = (D/t_{so}) \times (f_{syo}/235)$ and d) inner steel tube slenderness $\lambda_i = (d/t_{si}) \times (f_{syi}/235)$ (Eurocode 3 [22]).

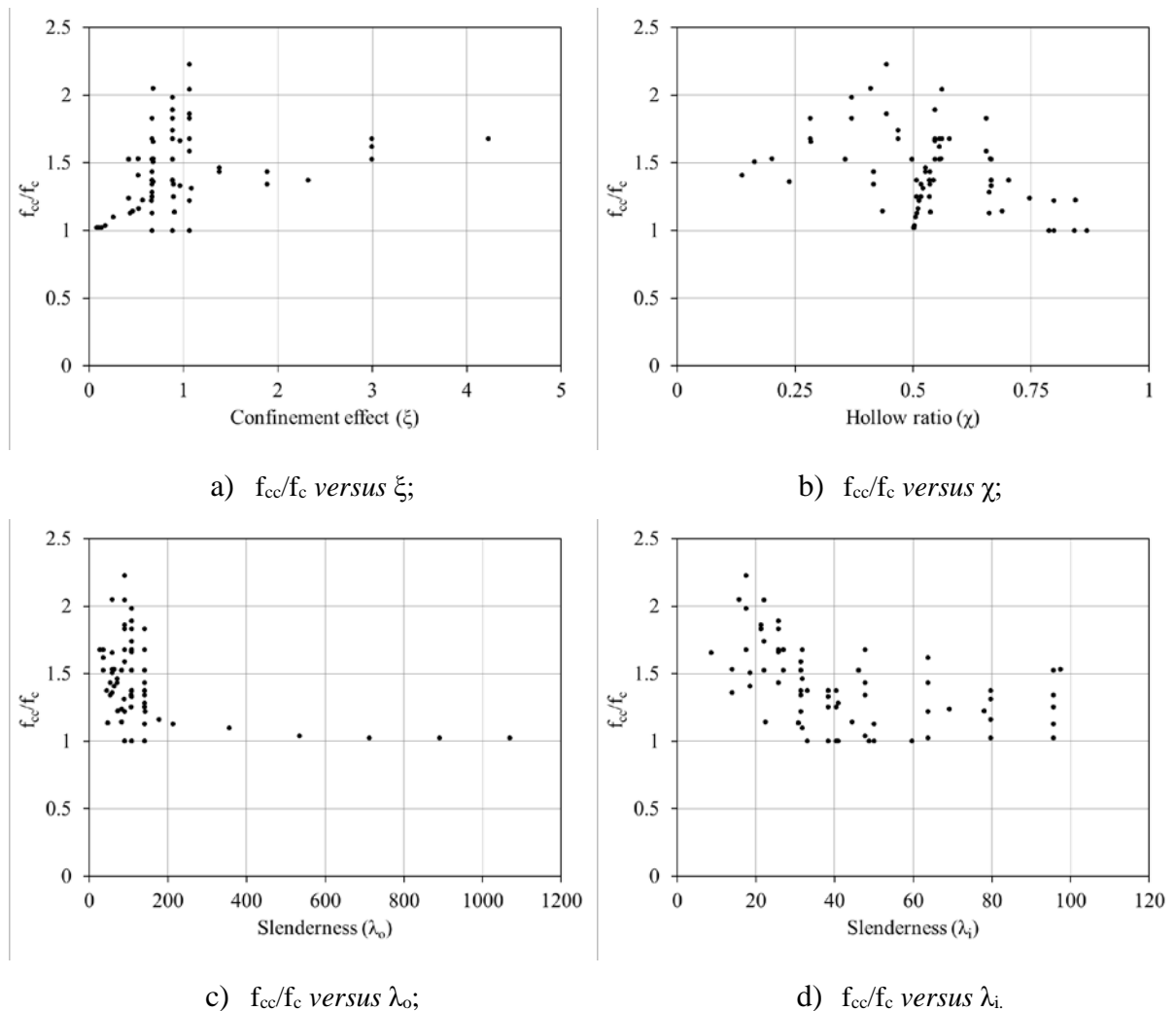


Figure 109 – Ratio of the confined compressive concrete strength and the compressive concrete strength f_{cc}/f_c *versus* important parameters.

The experiments and FE results presented all together in Figure 109 with the four parameters it is not possible to observe a trend to determine a concrete compressive strength enhancement. Therefore, after several tests, a new parameter is proposed to evaluate the confinement effect:

$$parameter = \xi \times \left(\frac{D}{t_{so}}\right)^{0.8} \times (1 - \chi) \times \sqrt{\frac{A_{si} \times f_{syi}}{A_{ce} \times f_c}} \quad (137)$$

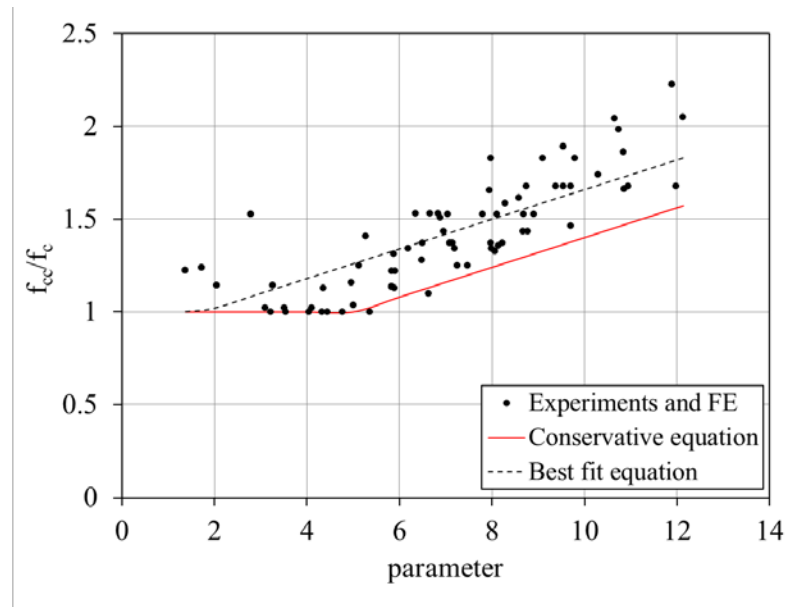


Figure 110 - Ratio of the confined compressive concrete strength and the compressive concrete strength f_{cc}/f_c versus the parameter.

Figure 110 shows the confined compressive concrete strength and the compressive concrete strength ratio f_{cc}/f_c versus the new parameter. The black points are the experiments and FE results previously presented in this thesis, being possible to plot a best-fit equation in the graph for these points. The red line represents this best-fit equation for conservative and safer values. A linear conservative equation can be now finally proposed for the ratio strength f_{cc}/f_c in terms of this proposed parameter, considering f_{cc}/f_c always ≥ 1.0 , since the concrete load-carrying should not be less than 1.0:

$$\frac{f_{cc}}{f_c} = 0.08 \times parameter + 0.06 \quad \text{since} \quad \frac{f_{cc}}{f_c} \geq 1.0 \quad (138)$$

The concrete confinement effect can be included in the procedure presented in Eqs. 126 to 136 replacing the f_c for the confined compressive concrete strength f_{cc} :

$$\begin{aligned}
N_{u,pred} = & f_{syi}(r - t_{si})^2 \sin(2\beta_{(i-t_{si})}) \\
& - \frac{R_c^2}{2} (f_{cc} - 2f_{sy0}) \sin(2\beta_c) + \frac{r^2}{2} (f_{cc} - 2f_{syi}) \sin(2\beta_i) \\
& - f_{sy0}R^2 \sin(2\beta_o) + [2(\beta_{(i-t_{si})} - \beta_i)f_{syi} + (\beta_i - \pi/2)f_{cc}]r^2 \\
& - 4f_{syi}rt_{si}\beta_{(i-t_{si})} + 2f_{syi}t_{si}^2\beta_{(i-t_{si})} + \frac{R_c^2}{2}(\pi - 2\beta_c)f_{cc} \\
& - 2f_{sy0}(R^2\beta_o - R_c^2\beta_c)
\end{aligned} \tag{139}$$

$$\begin{aligned}
M_{u,pred} = & \frac{1}{3} [-4f_{syi}(r - t_{si})^3 \cos \beta_{(i-t_{si})}^3 + 2R_c^3(f_{cc} - 2f_{sy0}) \cos \beta_c^3 \\
& - 2r^3(f_{cc} - 2f_{syi}) \cos \beta_i^3 + 4f_{sy0}R^3 \cos \beta_o^3]
\end{aligned} \tag{140}$$

- Point A:

$$N_A = f_{sy0}\pi(R^2 - R_c^2) + f_{cc}\pi(R_c^2 - r^2) + f_{syi}\pi(r^2 - r_{(i-t_{si})}^2) \tag{141}$$

$$M_A = 0 \tag{142}$$

- Point B:

$$N_B = 0 \tag{143}$$

$$\begin{aligned}
M_B = & \frac{1}{3} \left[-4f_{syi}(r - t_{si})^3 \cos \left(\frac{h}{r - t_{si}} \right)^3 + 2R_c^3(f_{cc} - 2f_{sy0}) \cos \left(\frac{h}{R_c} \right)^3 \right. \\
& \left. - 2r^3(f_{cc} - 2f_{syi}) \cos \left(\frac{h}{r} \right)^3 + 4f_{sy0}R^3 \cos \left(\frac{h}{R} \right)^3 \right]
\end{aligned} \tag{144}$$

$$h_B = \frac{1}{4} \frac{\pi f_{cc}(r^2 - R_c^2)}{[f_{cc}(r - R_c) + 2f_{sy0}(R_c - R) - 2f_{syi}t_{si}]} \tag{145}$$

- Point C:

$$N_c = 2N_D = f_{cc}\pi(R_c^2 - r^2) \tag{146}$$

$$M_c = M_B = \frac{1}{3} \left[-4f_{syi}(r - t_{si})^3 \cos\left(\frac{h}{r - t_{si}}\right)^3 + 2R_c^3(f_{cc} - 2f_{syo}) \cos\left(\frac{h}{R_c}\right)^3 - 2r^3(f_{cc} - 2f_{syi}) \cos\left(\frac{h}{r}\right)^3 + 4f_{syo}R^3 \cos\left(\frac{h}{R}\right)^3 \right] \quad (147)$$

- Point D:

$$N_D = \frac{1}{2} f_{cc} \pi (R_c^2 - r^2) \quad (148)$$

$$M_D = \frac{1}{3} \left[-4f_{syi}(r - t_{si})^3 + 2R_c^3(f_{cc} - 2f_{syo}) - 2r^3(f_{cc} - 2f_{syi}) + 4f_{syo}R^3 \right] \quad (149)$$

Figure 111 shows a) the pure compression ratio of the experiments and FE results and the proposed equation for N_u with the confinement effect f_{cc} ; b) and the pure bending ratio of the experiments and FE results and the proposed equation for M_u with the confinement effect f_{cc} . Almost all the results for pure compression are above the dotted line, which returns into safe values, however, for pure bending, there are some unsafe results below the dotted line, but still very close. Some plotted parametric results are class 4 for the outer steel tubes, and the results are more conservative in terms of pure bending. Table 35 also emphasizes that the proposed equations are in good agreement with the experiments and FE results since the CoV for pure compression is 7% and for pure bending is 9% considering class 4 outer steel tubes and 7% for pure compression and pure bending without considering class 4 outer steel tubes.

The developed concrete confinement parameter is not applicable for high strength concrete. In cases where the concrete compressive strength f_c is higher than 50 MPa, the confinement effect is reduced due to less concrete lateral expansion (poison effect) since the steel tubes reach their yielding strength before the concrete reach their compressive strength. Eurocode 2 [92] considers a reduction factor in defining the effective concrete strength in the concrete rectangular stress distribution:

$$\eta = 1.0; (f_c \leq 50MPa) \quad (150)$$

$$\eta = 1.0 - \frac{(f_c - 50)}{200}; (50 < f_c \leq 90MPa) \quad (151)$$

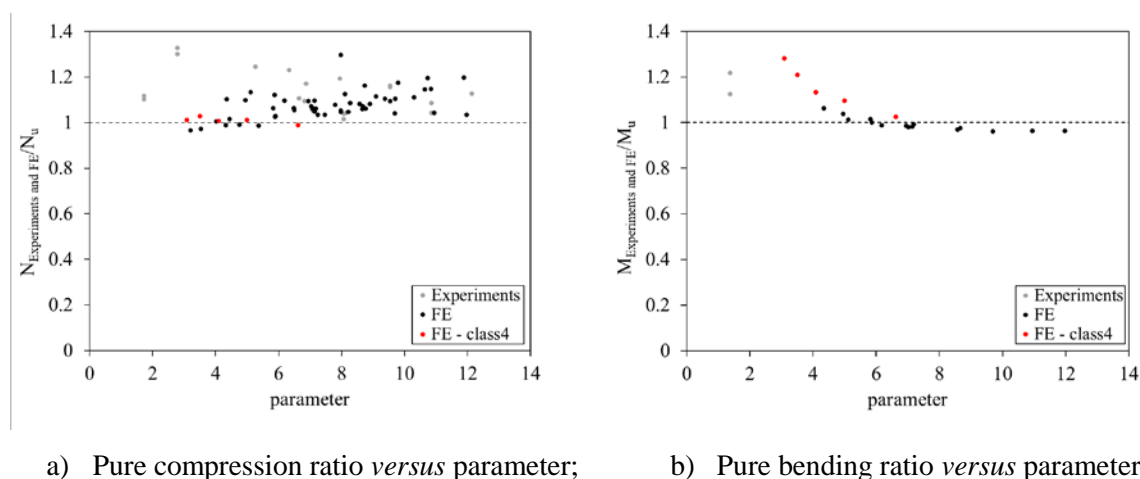
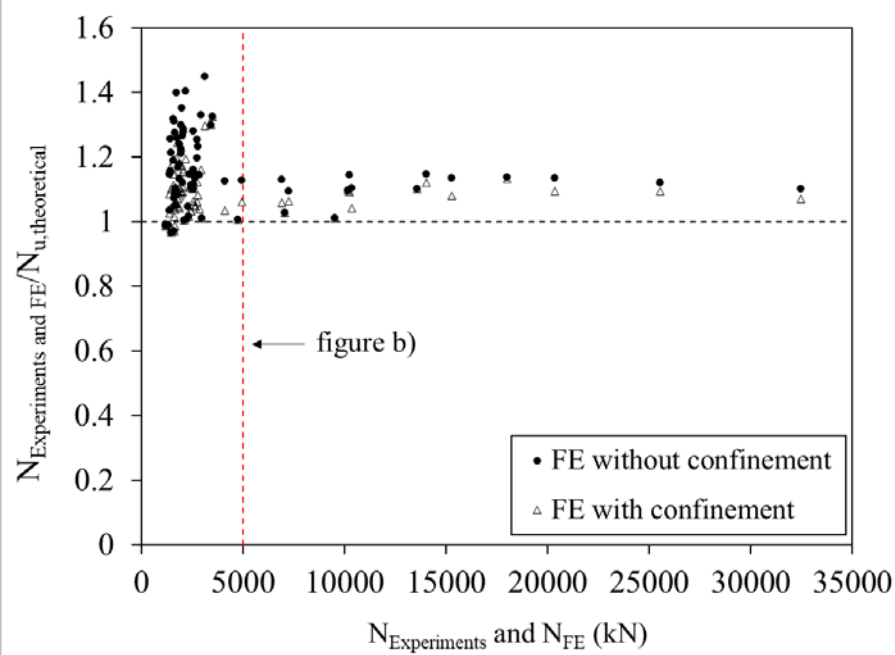


Figure 111 - Pure compression load and pure bending moment experiments and FE results divided by the proposed equations with confinement *versus* new parameter for $f_c \leq 50$ MPa.

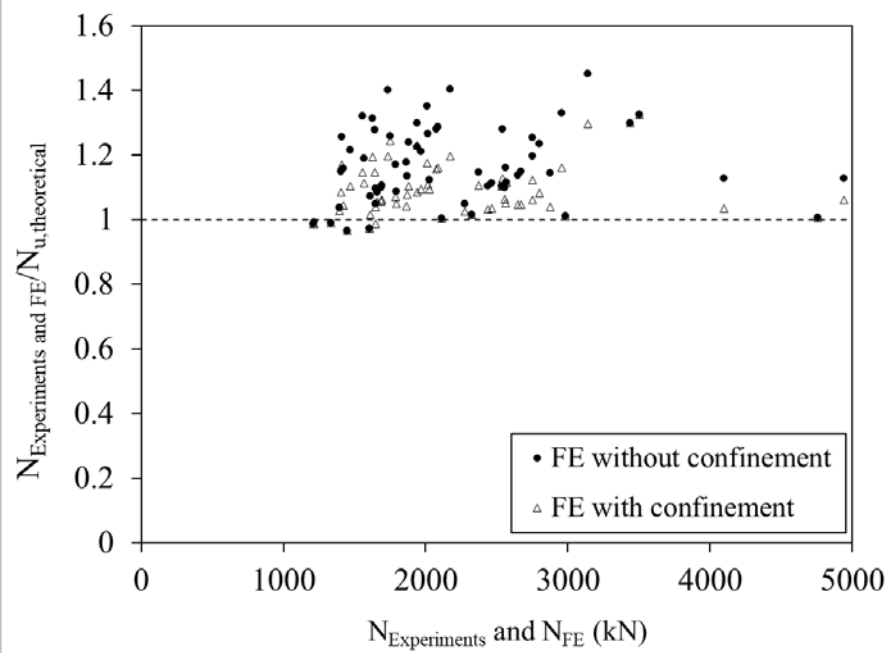
Table 35 - Coefficient of variation (CoV) of pure compression and pure bending proposed equations for $f_c \leq 50$ MPa.

	Total		Without class4	
	Pure compression (N_u)	Pure bending (M_u)	Pure compression (N_u)	Pure bending (M_u)
Average	1.087	1.044	1.093	1.013
Standard Deviation	0.075	0.093	0.074	0.067
CoV	0.069	0.089	0.068	0.066

Figure 112 presents the experiments and the FE results for CFDST columns submitted to concentric load divided by the compression load prediction *versus* the experiments and the FE results. a) is the total result of all the CFDST columns studied plotted until 35000 kN and b) is the partial result plotted only until 5000 kN. Figure 112 is divided in two series, the results for concentric load without considering the proposed confinement factor and considering the confinement factor. Figure 112 emphasizes Table 35 results, where it is possible to observe that the results using the confinement factor presents values closer to the dotted line, which represents the optimum value when $N_{\text{Experiments}}$ and/or N_{FE} is equal to the proposed concentric load equation $N_{u,\text{theoretical}}$.



a) $N_{\text{Experiments}}$ and N_{FE} - total results: plotted until 35000 kN;



b) $N_{\text{Experiments}}$ and N_{FE} - partial results: plotted until 5000 kN.

Figure 112 - $N_{\text{Experiments}}$ and N_{FE} divided by $N_{u,\text{theoretical}}$ versus $N_{\text{Experiments}}$ and N_{FE} for all the concentric load CFDST cross-sections studied with $f_c \leq 50\text{MPa}$.

Figure 113 shows a) the pure compression ratio of the FE results and the proposed equation for N_u with the reduction factor η in f_{cc} ; b) and the pure bending ratio of the FE results and the proposed equation for M_u with the reduction factor η in f_{cc} . All the results for pure compression and pure bending are above the dotted line, which returns into safe values. Some

plotted parametric results are class 4 for the outer steel tubes, and the results are more conservative, especially in terms of pure bending. Table 36 also emphasizes that the proposed equations are in good agreement with FE results since the CoV for pure compression is 2.4% considering class 4 outer steel tubes and 2.2 % without considering class 4 outer steel tubes. However, for pure bending, the CoV is 21% when the class 4 outer steel tubes are considered, and this value decreases considerably when the class 4 outer steel tubes are not considered, 9.7%.

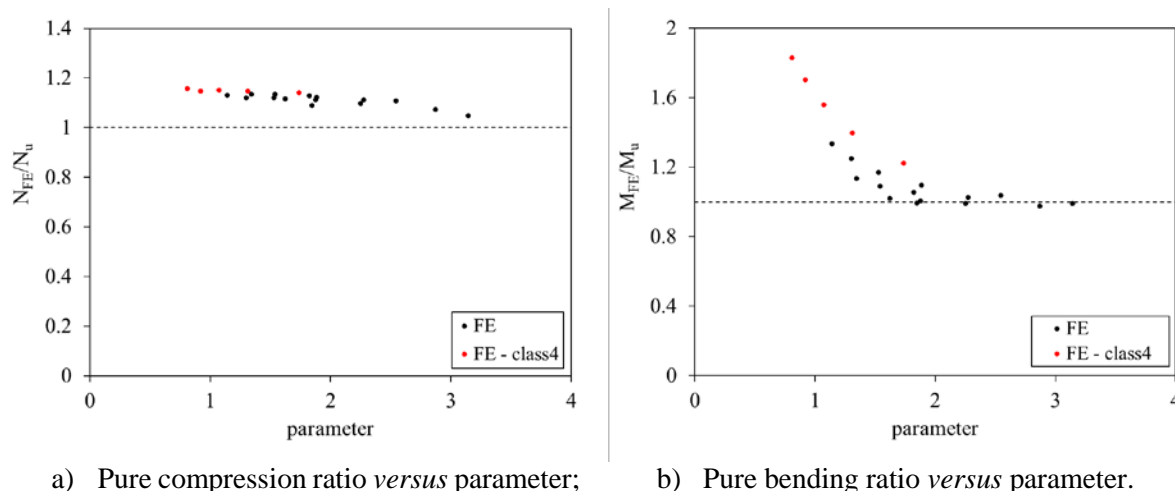


Figure 113 - Pure compression load and pure bending moment FE results divided by the proposed equations with η *versus* new parameter for $50 < f_c \leq 90$ MPa.

Table 36 - Coefficient of variation (CoV) of pure compression and pure bending proposed equations for $50 < f_c \leq 90$ MPa.

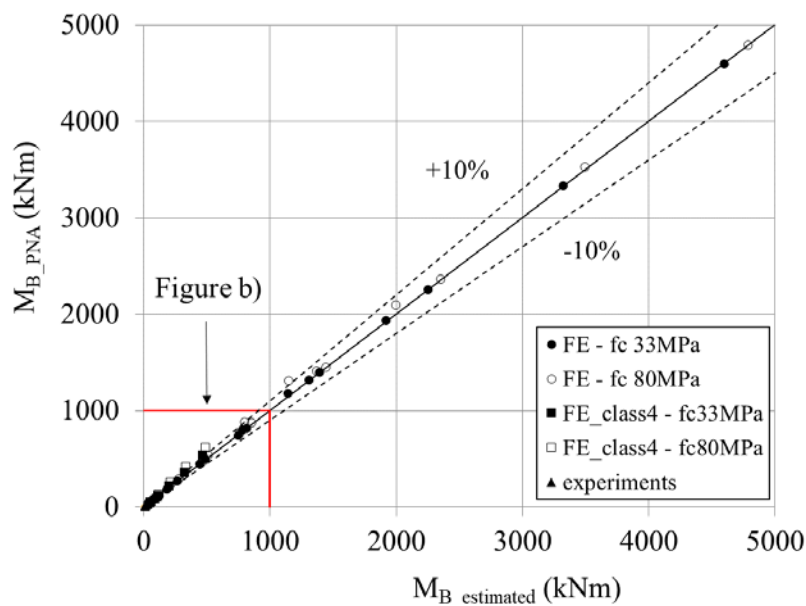
	Total		Without class4	
	Pure compression (N_u)	Pure bending (M_u)	Pure compression (N_u)	Pure bending (M_u)
Average	1.118	1.192	1.109	1.076
Standard Deviation	0.027	0.251	0.024	0.105
CoV	0.024	0.210	0.022	0.097

Finally, the pure bending proposed equation using the conservative approximation proposed by Fouché et al. [56] where $\sin(\beta) = \beta$ and $\cos(\beta) = 1$ is compared with the calculated pure bending equation by PNA varying the neutral axis. The confinement effect is also considered in both equations. Table 37 shows the results for all the cross-sections studied and for all the results without considering the class4 cross-sections. The CoV results, especially when the class4 cross-sections are not considered (5%), express that the estimated equation is in good agreement with the calculated by PNA varying the neutral axis.

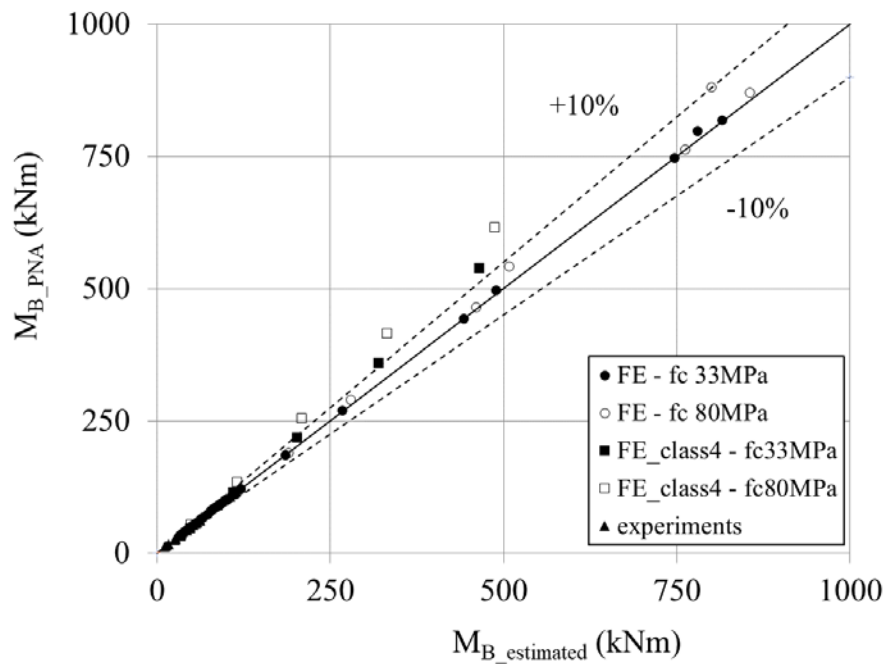
Table 37 - Coefficient of variation (CoV) for pure bending calculated by PNA and estimated.

	Total		Without class4	
	$h_{B_PNA}/h_{B_estimated}$	$M_{B_PNA}/M_{B_estimated}$	$h_{B_PNA}/h_{B_estimated}$	$M_{B_PNA}/M_{B_estimated}$
Average	0.948	1.026	0.952	1.022
Standard Deviation	0.066	0.053	0.064	0.050
CoV	0.070	0.051	0.068	0.049

Figure 114 depicts a comparison of the pure bending proposed equation using the conservative approximation where $\sin(\beta) = \beta$ and $\cos(\beta) = 1$ and the calculated pure bending equation by PNA varying the neutral axis. Figure 114 a) is the total studied cross-sections and b) partially studied cross-sections where it is possible to observe a higher value of results above 10% distant from the PNA pure bending. These values are from FE class 4 cross-sections studied, which is commonly expected since the effective area of the class 4 specimens was not considered in the calculations. However, there are still some class 4 specimens with the approximation equation in good agreement with the PNA equation which are: $D = 200$, $t_{so} = 1$, $d = 100$, $t_{si} = 5$ mm and $f_c = 33$ MPa, $D = 300$, $t_{so} = 1$, $d = 150$, $t_{si} = 5$ mm and $f_c = 33$ MPa and $D = 200$, $t_{so} = 1$, $d = 100$, $t_{si} = 5$ mm and $f_c = 80$ MPa. This might indicate that the Eurocode 4 [18] class 4 limitation ($D/t_{so} > 90\varepsilon^2$, where $\varepsilon^2 = f_{sy0}/235$) is too conservative for CFDST cross-sections and could be changed for $D/t_{so} > 150\varepsilon^2$, close to the limit of the cross-section $D = 300$, $t_{so} = 1$, $d = 150$, $t_{si} = 5$ mm.



a) CFDST cross-sections studied - total results: plotted until 5000 kNm;



b) CFDST cross-sections studied - partial results: plotted until 1000 kNm.

Figure 114 - Pure bending calculated through PNA and pure bending estimated formula accuracy assessment.

6.3.3 N-M interaction curve development

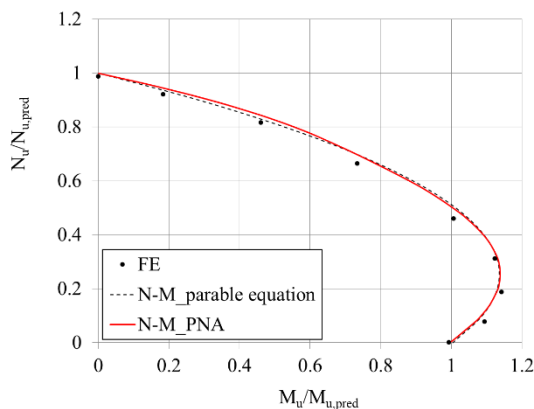
The simplified equations for compression ($N_{u,pred}$) and bending ($M_{u,pred}$) are used to calculate points A, B, C and D and consequently draw each cross-section N-M interaction curve. Moreover, the N-M interaction curve can be simplified, considering the curve as a parable format (Eqs. 152 and 153). The bending value M_u can be easily determined in terms of N_u and the maximum points N_D/N_A and M_D/M_B . The proposed equations and concrete confinement effect accuracy are evaluated through the ratios of experiments and the FE results to the predicted capacities of pure compression (N_u/N_A) and pure bending (M_u/M_B).

$$\frac{M_u}{M_B} = \left[\left(\frac{N_u}{N_A} - \frac{N_D}{N_A} \right)^2 + 2p \frac{M_D}{M_B} \right] / 2p \quad (152)$$

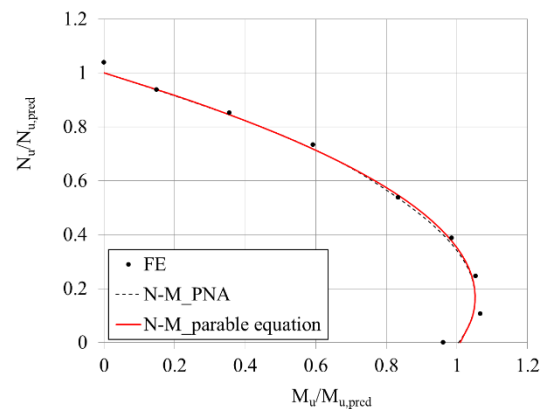
$$p(0,1) = \frac{-\left(1 - \frac{N_D}{N_A}\right)^2}{2 \frac{M_D}{M_B}} \quad (153)$$

where N_u and M_u are the experiments and FE results for load and bending capacities. N_A is the pure compression (Eq. 141), N_D is the maximum load of the N-M interaction curve (Eq. 148), M_B is the pure bending (Eq. 144), and M_D is the maximum bending of the N-M interaction curve (Eq. 149). p is the parable vertex where bending value is minimum equal to 0 and load is maximum equal to 1.

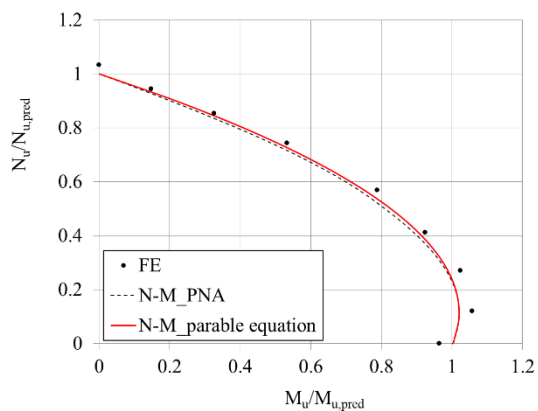
Figure 115 to Figure 117 illustrates the N-M interaction curve obtained using Eq. 139 and Eq. 140, varying the neutral axis h and the proposed parable equation (Eq. 152 and Eq. 153), as legend N-M_PNA and N-M_parable equation, respectively. Figure 115 and Figure 117, the proposed curves are compared with the FE results divided by the estimated equations for pure compression (Eq. 140) and pure bending (Eq. 143). Figure 116, the proposed curves are compared with the experiments from literature (Wang *et al.* [48], Han *et al.* [46], Tao *et al.* [5], Li *et al.* [77] and Zhao *et al.* [88]) also divided by the estimated equations for pure compression (Eq. 141) and pure bending (Eq. 144). Overall, all the cross-sections studied in the parametric analysis and experiments presented results in good agreement with both proposed N-M interaction curves. All the results are generally above both N-M interaction curves. The N-M_PNA curve is well represented by N-M parable equation, which is much simpler to be applied in engineering. The pure bending point is not very suitable since the equation used is estimated for small angles. Also, the curves are too conservative when the outer steel tube is class4 and/or has higher slenderness.



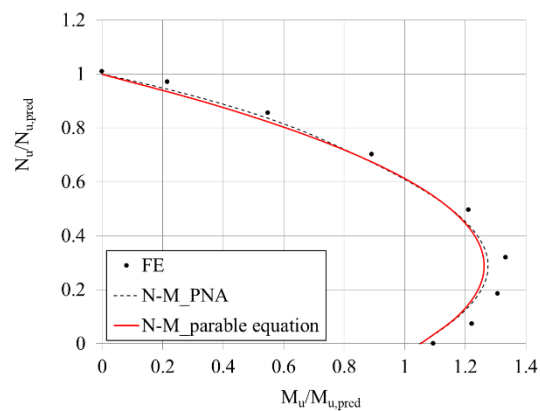
a) 200x1_100x5_class4;



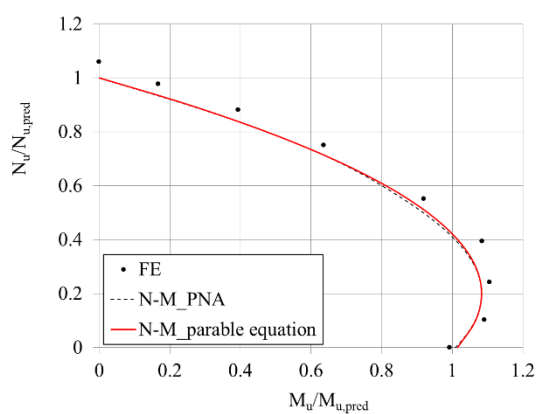
b) 200x5_100x5;



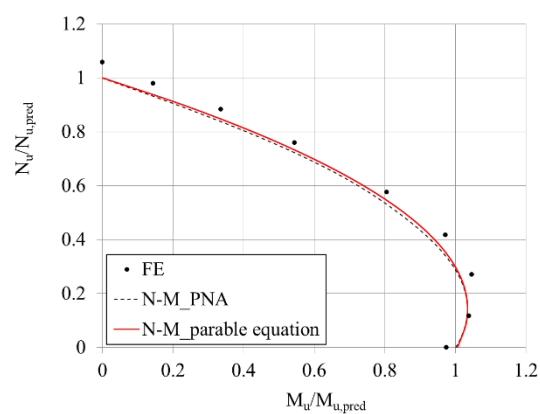
c) 200x10_100x5;



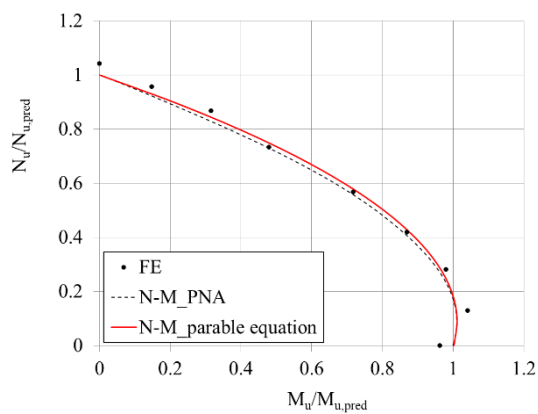
d) 300x1_150x5_class4;



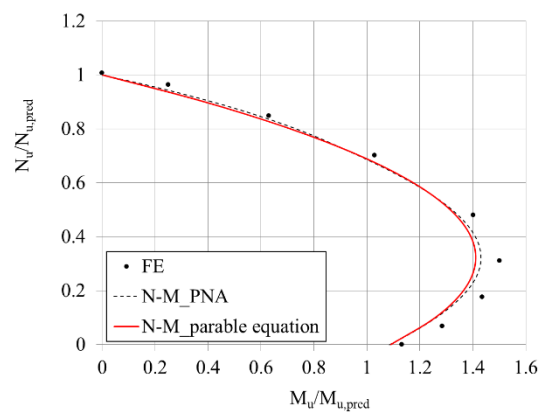
e) 300x5_150x5;



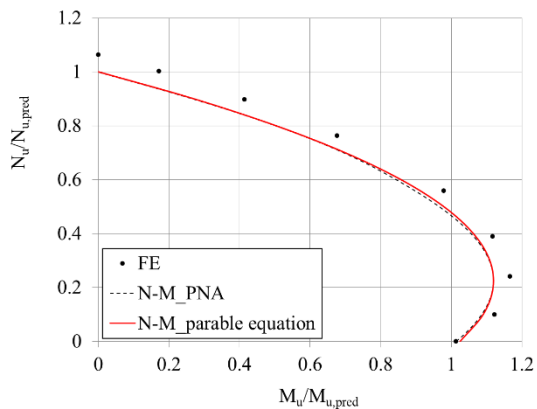
f) 300x10_150x5;



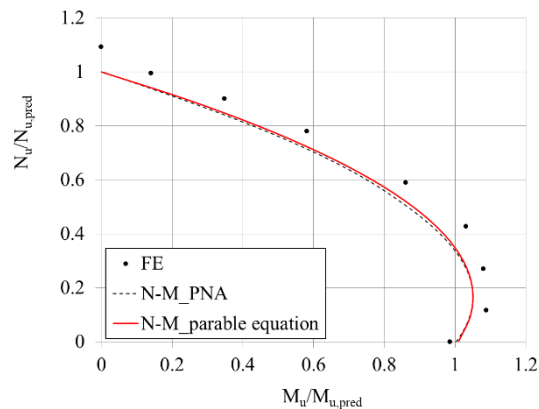
g) 300x20_150x5;



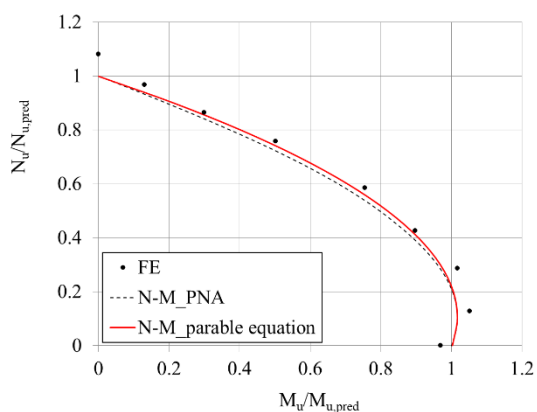
h) 400x1_200x5_class4;



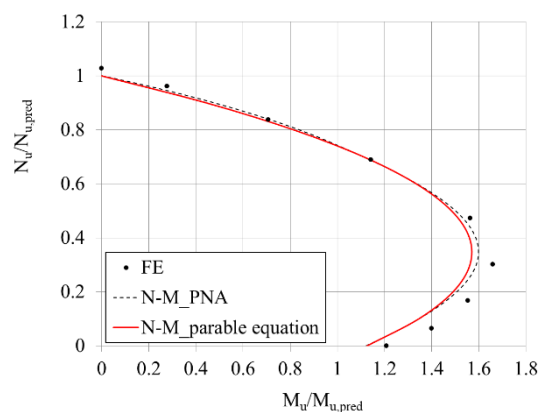
i) 400x5_200x5;



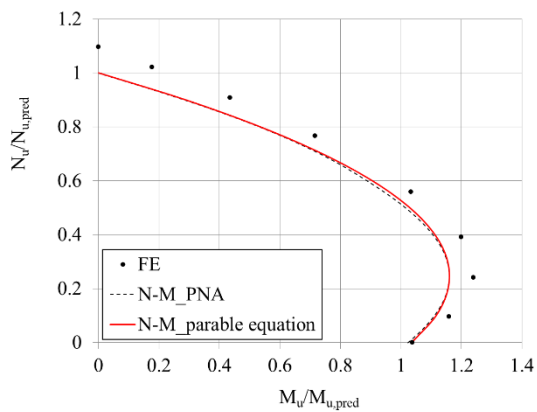
j) 400x10_200x5;



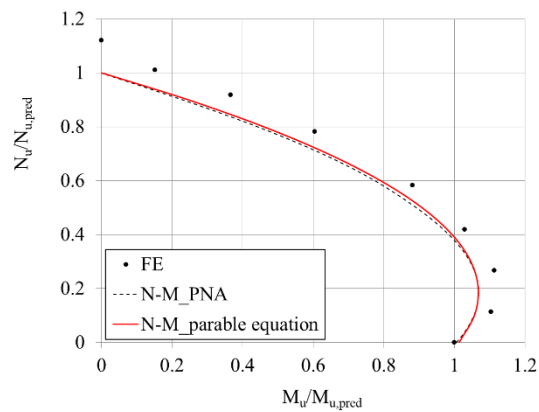
k) 400x20_200x5;



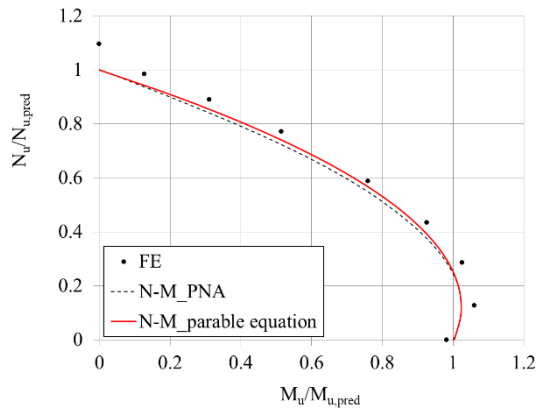
l) 500x1_250x5_class4;



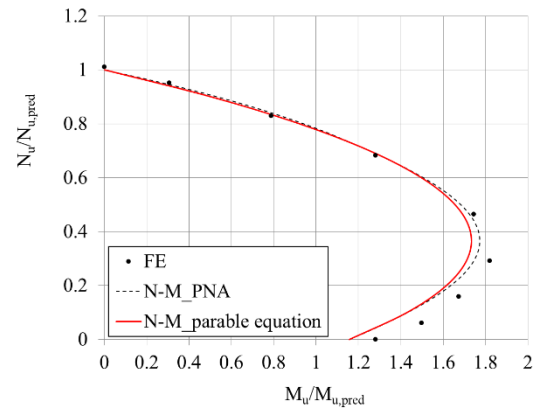
m) 500x5_250x5;



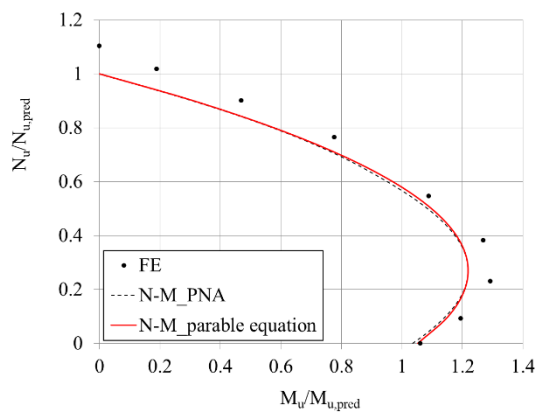
n) 500x10_250x5;



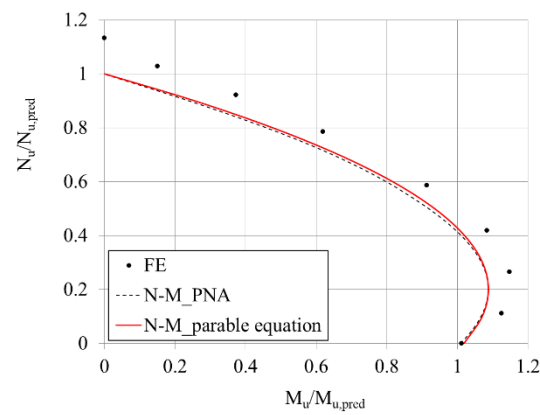
o) 500x20_250x5;



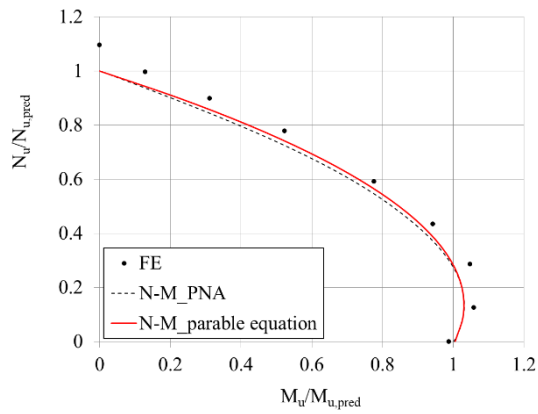
p) 600x1_300x5_class4;



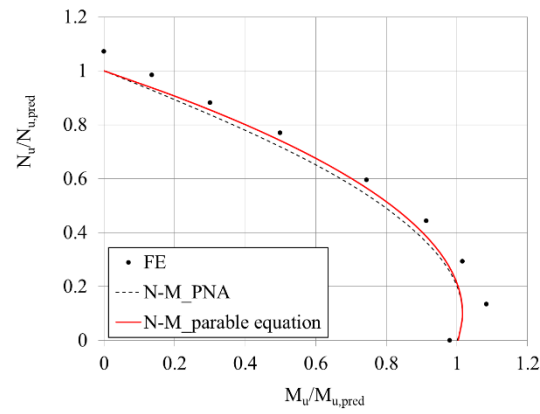
q) 600x5_300x5;



r) 600x10_300x5;

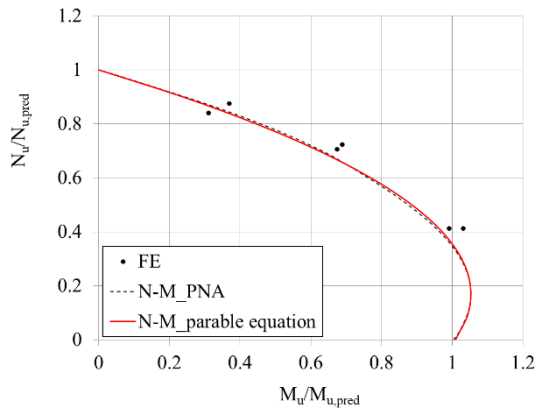


s) 600x20_300x5;

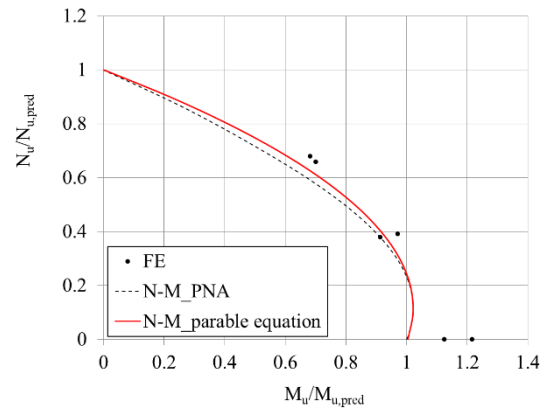


t) 600x30_300x5.

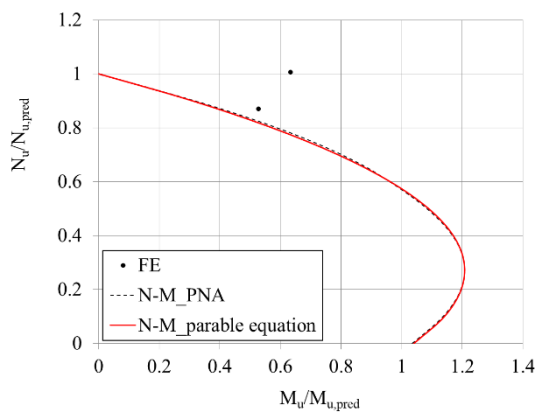
Figure 115 - Proposed N-M interaction curve and FE results for concrete strength (f_c) of 33 MPa.



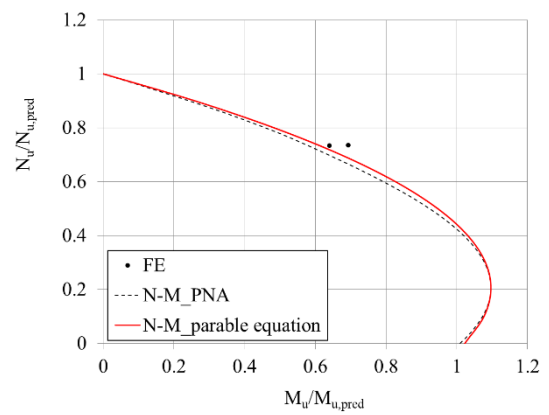
a) 114x3_58x3_Tao *et al.* [5];



b) 140x2.5_114x2_Li *et al.* [77];

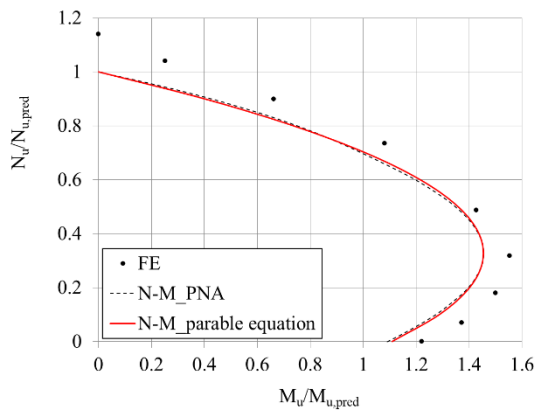


c) 114x1.88_48x2.52_Zhao *et al.* [88];

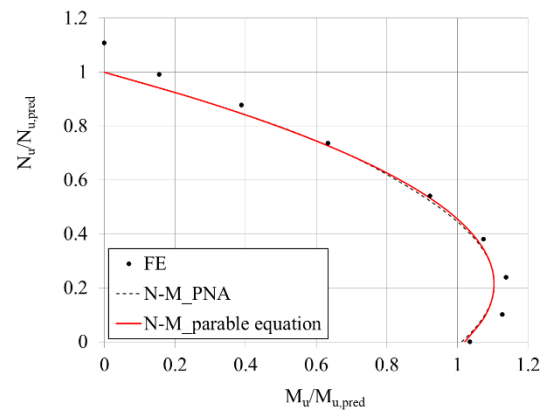


d) 114x1.88_76x2.01_Zhao *et al.* [88].

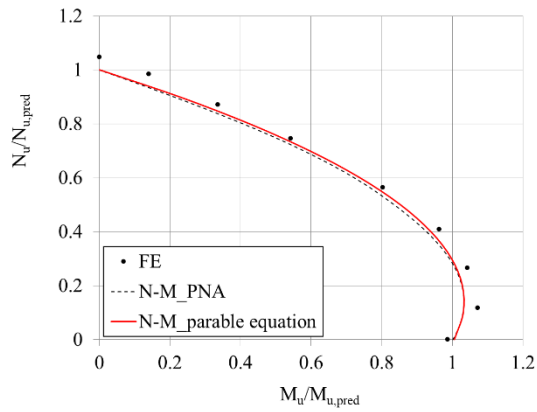
Figure 116 - Proposed N-M interaction curve and experiments from the literature.



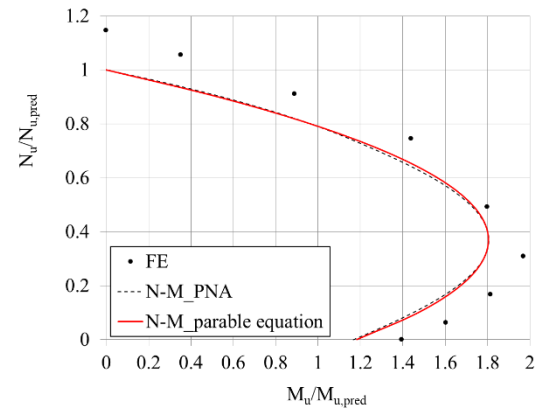
a) 200x1_100x5_class4;



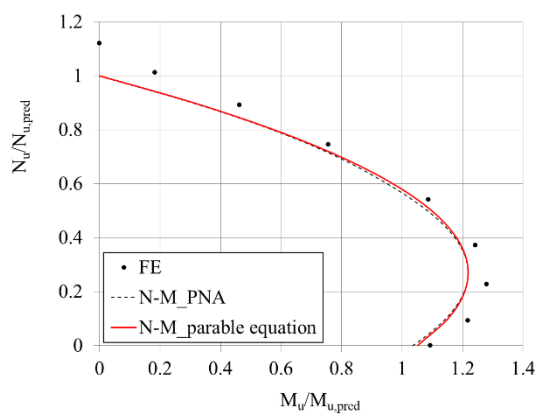
b) 200x5_100x5;



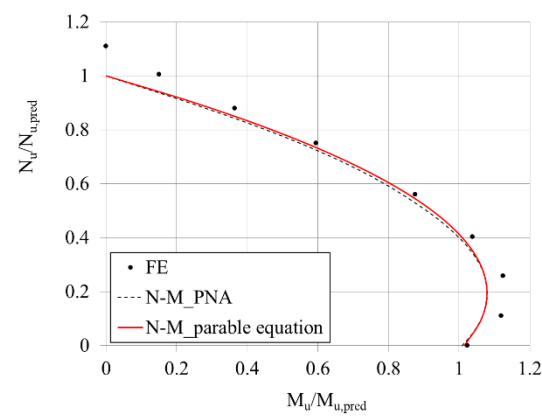
c) 200x10_100x5;



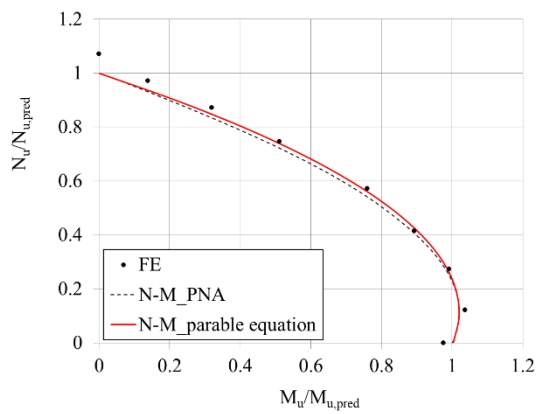
d) 300x1_150x5_class4;



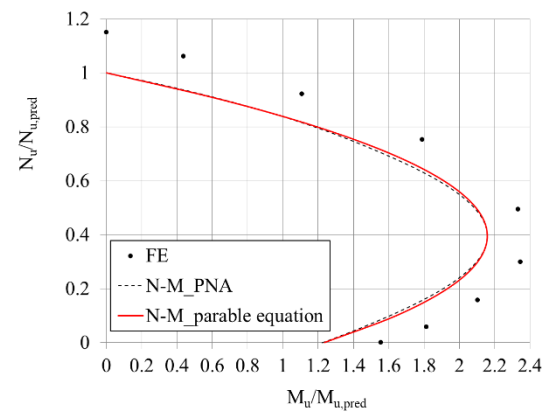
e) 300x5_150x5;



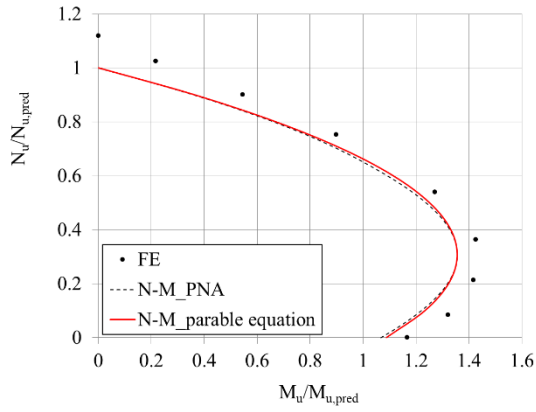
f) 300x10_150x5;



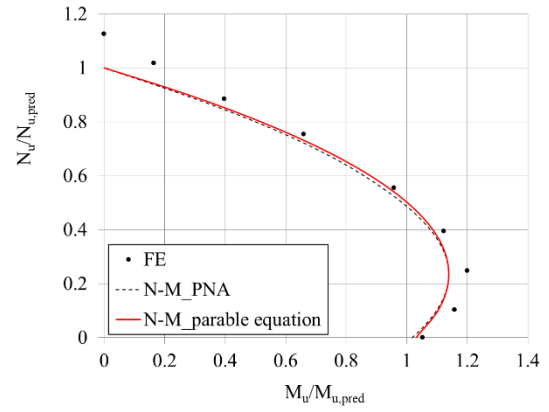
g) 300x20_150x5;



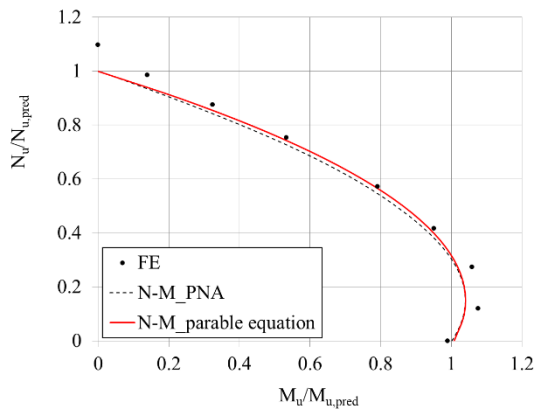
h) 400x1_200x5_class4;



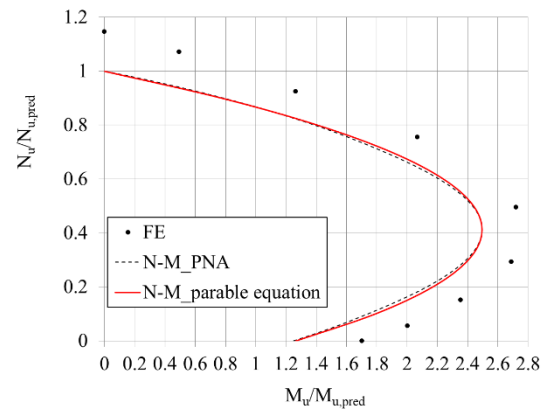
i) 400x5_200x5;



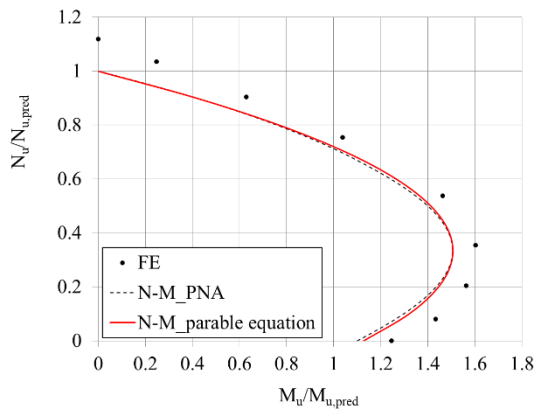
j) 400x10_200x5;



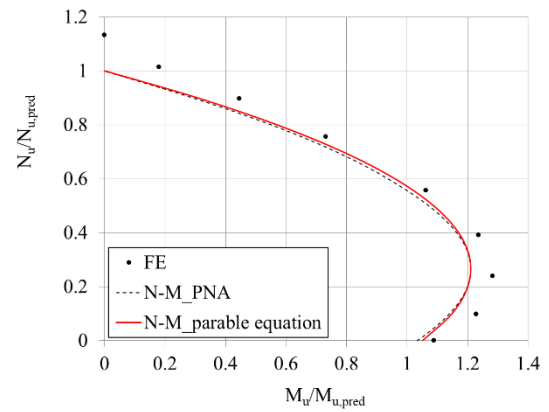
k) 400x20_200x5;



l) 500x1_250x5_class4;



m) 500x5_250x5;



n) 500x10_250x5;

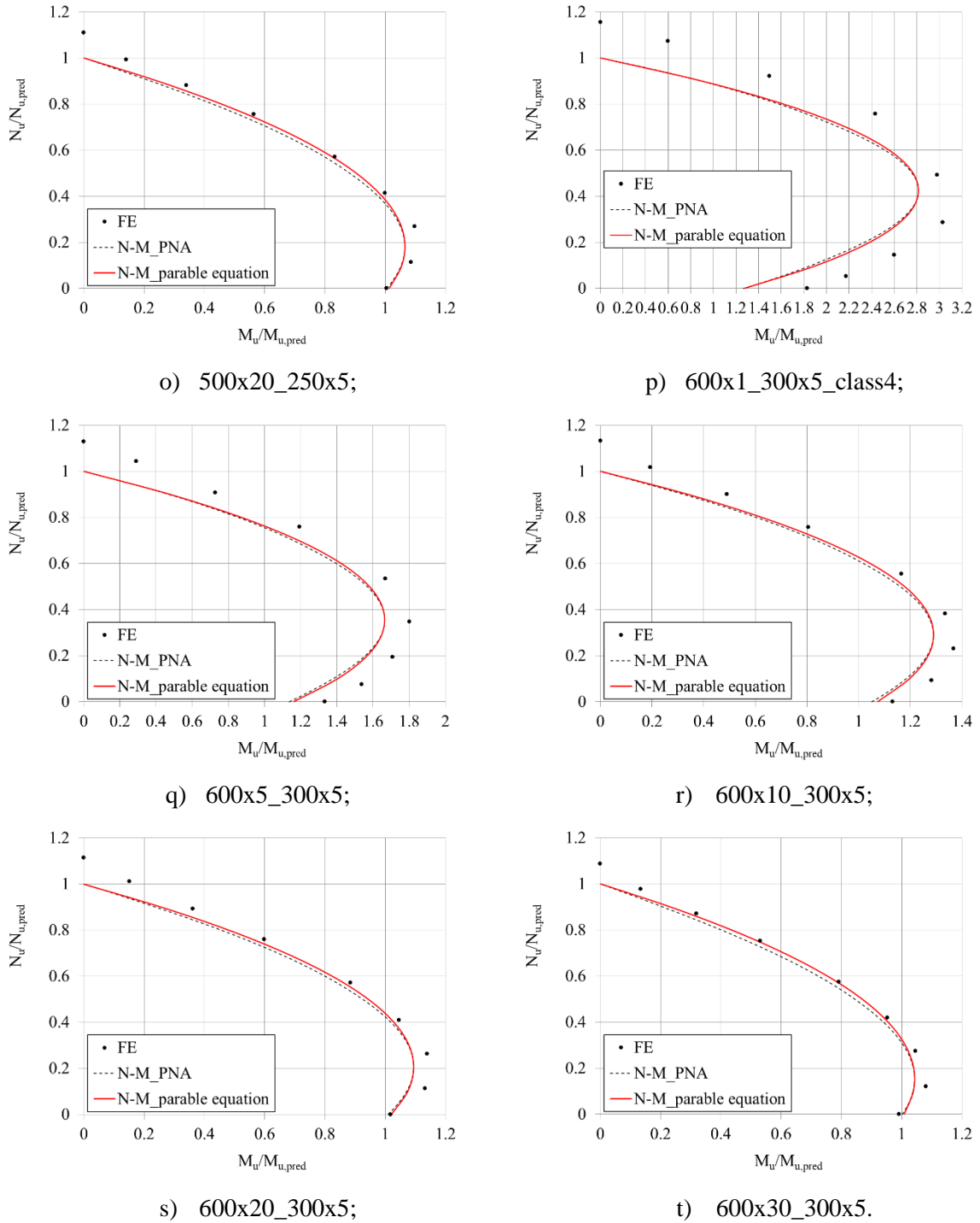


Figure 117 - Proposed N-M interaction curve and FE results for concrete strength (f_c) of 80 MPa.

The design prediction from the N-M_{parable} equation ($H_{u, pred}$) is compared with the cross-section resistances from the FE results and the experiments (H_u), as defined in Figure 118. As explained before, all the results are normalized by the pure compression (Eq. 141) and pure bending (Eq. 144) predictions. The equivalent eccentricity points from FE and experiments results were found in the N-M_{parable} equation and plotted in the graph as “Predicted

resistance”. For each FE, experiments and resistance points, a normalized N and M were found to calculate a hypotenuse H_u and $H_{u,pred}$, respectively. Finally, the accuracy of the proposed design can be found through the $H_u/H_{u,pred}$ ratio of the combining normal and bending predicted resistances $H_{u,pred}$ and FE and experiments results from H_u .

Table 38 to Table 42 present the average, the standard deviation and the coefficient of variation of the $H_u/H_{u,pred}$ ratio for the eccentricity parametric analysis with $f_c = 33$ MPa, experiments results, concentric parametric analysis with $f_c = 33$ MPa, parametric eccentricity analysis with $f_c = 80$ MPa and the total with all the FE and experiments results, respectively. In addition, the CoV from Table 38, Table 41 and Table 42 were also calculated considering the total cross-sections and without class4 cross-sections separately. The coefficients of variation varied from the minimum of 3.1% to the maximum of 10.6%. The proposed design was in good agreement with the FE and experiments results since the total CoV was 6.4% and the CoV without class4 cross-sections was 5.2%.

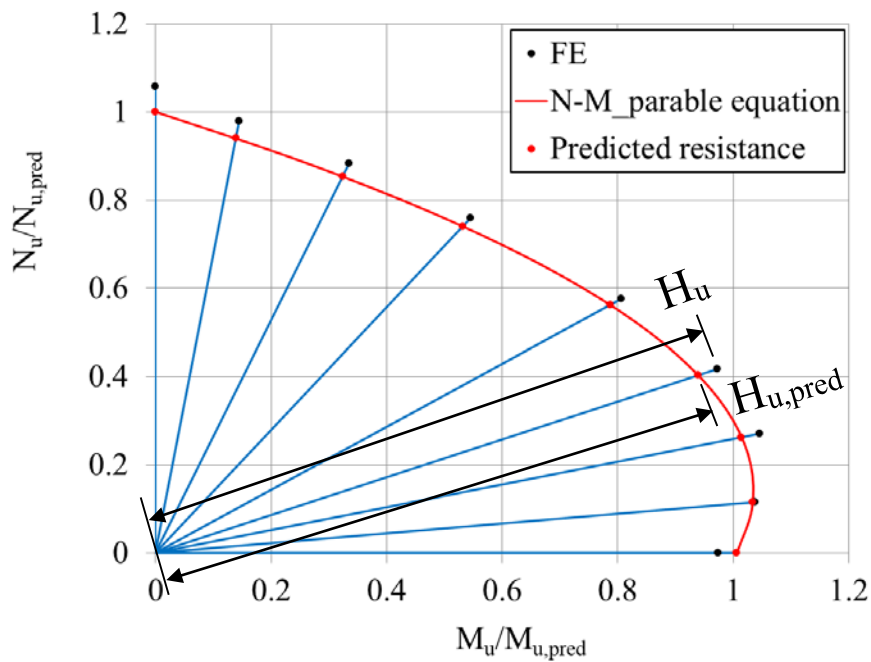


Figure 118 - Predicted capacity and definition of H_u and $H_{u,pred}$.

Table 38 - $H_u/H_{u,pred}$ coefficient of variation (CoV) for FE results of eccentricity parametric analysis with $f_c = 33$ MPa.

	Total	Without class4
	$H_u/H_{u,pred}$	$H_u/H_{u,pred}$

Average	1.032	1.035
Standard Deviation	0.032	0.032
CoV	0.031	0.031

Table 39 - $H_u/H_{u,pred}$ coefficient of variation (CoV) for experiments.

	$H_u/H_{u,pred}$
Average	1.065
Standard Deviation	0.113
CoV	0.106

Table 40 - $H_u/H_{u,pred}$ coefficient of variation (CoV) for FE results of concentric parametric analysis with $f_c = 33$ MPa.

	$H_u/H_{u,pred}$
Average	1.076
Standard Deviation	0.071
CoV	0.066

Table 41 - $H_u/H_{u,pred}$ coefficient of variation (CoV) for FE results of eccentricity parametric analysis with $f_c = 80$ MPa.

	Total	Without class4
	$H_u/H_{u,pred}$	$H_u/H_{u,pred}$
Average	1.074	1.047
Standard Deviation	0.074	0.038
CoV	0.069	0.037

Table 42 - $H_u/H_{u,pred}$ coefficient of variation (CoV) for all the FE and experiments results.

	Total	Without class4
	$H_u/H_{u,pred}$	$H_u/H_{u,pred}$
Average	1.056	1.047
Standard Deviation	0.067	0.055
CoV	0.064	0.052

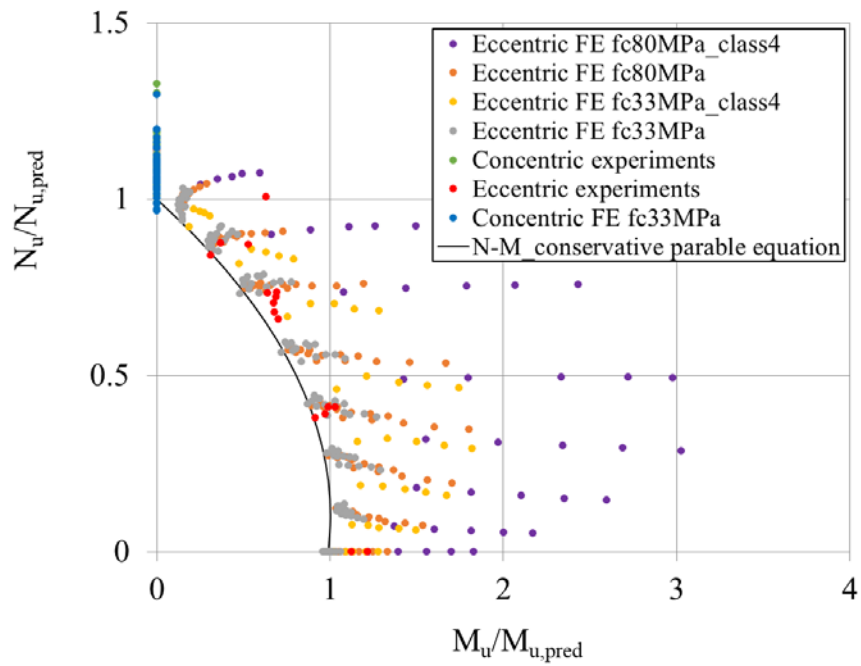


Figure 119 - Proposed conservative N-M interaction curve for all the FE and experiments evaluated.

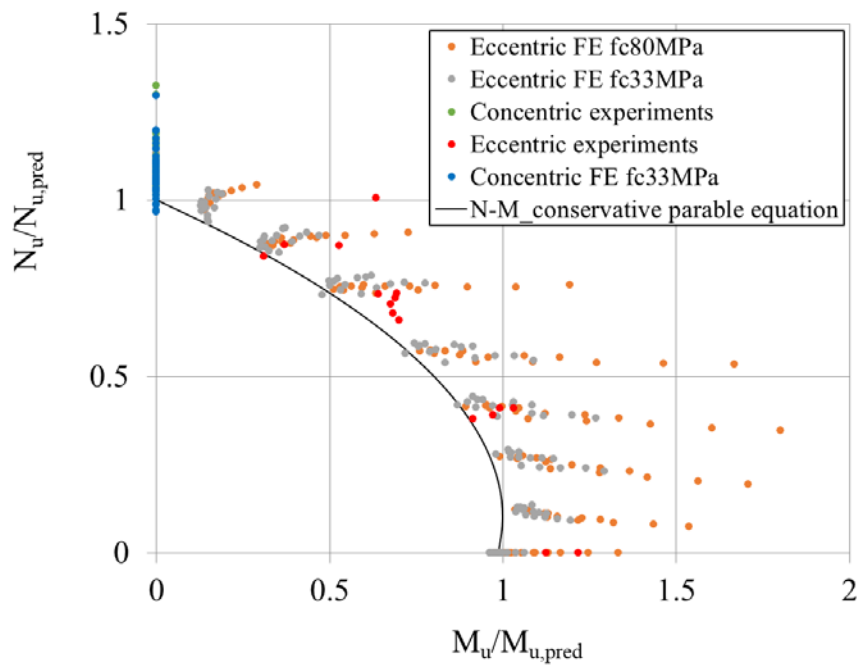


Figure 120 - Proposed conservative N-M interaction curve for all the FE and experiments evaluated without considered the studied class 4 cross-sections.

Table 43 - $H_u/H_{u,pred}$ coefficient of variation (CoV) for all the FE and experiments evaluated considering the proposed conservative N-M interaction curve.

	Total	Without class4
	$H_u/H_{u,pred}$	$H_u/H_{u,pred}$
Average	1.199	1.112
Standard Deviation	0.296	0.122
CoV	0.247	0.109

The design prediction from the N-M_{parable} equation can be even more simple to apply if the maximum parable values (N_D/N_A and M_D/M_B) were used as a fixed and conservative value. If $N_D/N_A = 0.1$ and $M_D/M_B = 1.0$ (Eqs. 154 and 155) the conservative N-M parable equation from Figure 119 and Figure 120 can be used for any cross-section value. Figure 119 and Figure 120 presents the $N_u/N_{u,pred}$ and $M_u/M_{u,pred}$ for all the examined cross-sections plotted by different colours. Figure 120 presents the same values from Figure 119, however, without the class 4 cross-sections. From Table 43, it is possible to observe that for some situations, for example, $f_c = 80$ MPa, especially for class 4 cross-sections, the proposed simplification in the N-M interaction curve is too conservative. However, it is in good agreement for all the class 3 cross-sections studied returning into a CoV of 11%.

$$\left(\frac{N_u}{N_A}\right)^2 - 0.2 \frac{N_u}{N_A} + 0.81 \frac{M_u}{M_B} = 0.8 \quad (154)$$

$$p(0,1) = -0.405 \quad (155)$$

6.3.4 Reliability analysis

A reliability analysis of the CFDST columns parametric results subjected to concentric load and eccentric axial compression will be presented in this section following both design codes: Eurocode 0 (EC0) [14] and AISI [15]. Table 44 and Table 45 presents the calculated key parameters for CFDST columns subjected to concentric axial compression, and Table 46

and Table 47 for CFDST columns subjected to eccentric axial compression for Eurocode 0 (EC0) [14] and AISI [15] methods.

The key parameters calculated for the Eurocode 0's method (EC0) [14] were: the design fractile factor $k_{d,n}$, the test or FE to design model resistance mean ratio b , the CoV of the tests or FE relative to the theoretical resistance V_δ and the partial safety factor γ_{M0} . The key parameters calculated for AISI's method [15] were: the professional factor P_m (test or FE resistance relative to the theoretical resistance ratio), the coefficient of variation V_P and the target reliability index β_0 . The calculated function to compare the tests or FE results to the predicted design ratio was the load resistance ($N_u/N_{u,pred}$) in CFDST columns under concentric axial compression and the hypotenuse from the load ($N_u/N_{u,pred}$) and bending ($M_u/M_{u,pred}$) predictions ($H_u/H_{u,pred}$) in CFDST columns under eccentric axial compression.

In Eurocode 0 (EC0) [14], the CoVs of the strength of stainless steel, concrete and carbon steel were adopted as 0.06 [94], $V_{fc} = 8/(1.64f_{cm})$ [95] and 0.0522 [95], respectively, while the corresponding CoVs of the geometric properties were also obtained from previous research and were taken as 0.05 [94], 0.01 [96] and 0.05 [95]. The mean to nominal yield stress ratios $f_{y,mean}/f_{y,nom}$ (i.e. the over-stress ratios for material yield stress) for the stainless steel was adopted as 1.30 [94]. The concrete [97] and the carbon steel [95] mean to nominal yield stress ratio ($f_{y,mean}/f_{y,nom}$) were calculated through the equations below:

$$f_c = f_{cm} - 1.64\delta \quad (156)$$

$$f_{ym} = f_y \alpha \exp(-kV_{fy}) - C \quad (157)$$

where f_{cm} is the concrete compressive strength in MPa, δ is the concrete compressive strength CoV taken as $V_{fc} = 8/(1.64f_{cm})$, f_y is the carbon steel yield stress in MPa, α is the spatial position factor ($\alpha = 1.0$ for other cases), k is a factor related to the fractile of the distribution used in describing the distance between the nominal and the mean value ($k = 2.95$ for S355M carbon steel [82]), V_{fy} is the carbon steel yield stress CoV taken as 0.0522 [95], and C is a reducing constant taken as 20 MPa to steel produced following [98].

In AISI [15], the resistance factor ϕ was taken as 0.85 [99]. In contrast, the mean values and CoVs for material and fabrication factors M_m , F_m , V_m , V_F and V_Q were considered as 1.10 for concentric axial compression and 1.05 for eccentric axial compression, 1.00, 0.10, 0.05 and 0.21, respectively. C_p is a correction factor based on the number of tests. C_ϕ is a calibration

coefficient adopted as 1.52. The target reliability index β_0 can be obtained from the equation below:

$$\phi = C_\phi (M_m F_m P_m) e^{-\beta_0 \sqrt{V_M^2 + V_F^2 + C_P V_P^2 + V_Q^2}} \quad (158)$$

To ensure the efficiency of the proposed design method, Eurocode 4's (EC4) [18], Uenaka *et al.*'s [54], Han *et al.*'s [46], Hassanein *et al.*'s [51], Fouché *et al.*'s [56] and Uenaka and Kitoh's [55] methods, the partial safety factors γ_{M0} from Eurocode 0 (EC0) [14] and the target reliability index β_0 from AISI [15] were compared with the calculated values presented from Table 44 to Table 47. The partial safety factor γ_{M0} in Eurocode 4 (EC4) [18] for composite columns is 1.0, whereas the calculated concentric axial compression is 1.086, and the eccentric axial compression is 1.074. The minimum limit target reliability index β_0 for structural members in AISI [15] is 2.5. The values calculated for the concentric axial compression was 3.104 and for the eccentric axial compression was 2.726, being in good agreement with the AISI [15] limit value. From the achieved results, the proposed design method can be considered to be in good agreement with Eurocode 0 (EC0) [14] and AISI [15] reliability analysis and presented better results than Eurocode 4's (EC4) [18], Uenaka *et al.*'s [54], Han *et al.*'s [46], Hassanein *et al.*'s, Fouché *et al.*'s [56] and Uenaka and Kitoh's [55] methods.

Table 44 - CFDST columns subjected to concentric axial compression evaluated by Eurocode 0 (EC0) [14].

Design	Sample type	Sample number	$k_{d,n}$	b	V_δ	γ_{M0}
Proposed design_class4	Test + FE	96	3.136	1.103	0.060	1.082
Proposed design	Test + FE	86	3.148	1.102	0.059	1.086
Eurocode 4's method_class4 [18]	Test + FE	96	3.136	0.898	0.082	1.322
Eurocode 4's method [18]	Test + FE	86	3.136	0.892	0.082	1.352
Uenaka <i>et al.</i> 's method_class4 [54]	Test + FE	83	3.152	0.829	0.103	1.465
Uenaka <i>et al.</i> 's method [54]	Test + FE	73	3.168	0.819	0.110	1.521
Han <i>et al.</i> 's method_class4 [46]	Test + FE	96	3.136	0.893	0.107	1.350
Han <i>et al.</i> 's method [46]	Test + FE	86	3.148	0.893	0.108	1.372
Hassanein <i>et al.</i> 's method [51]	Test + FE	44	3.263	0.979	0.083	1.310

Table 45 - CFDST columns subjected to concentric axial compression evaluated by AISI [15].

Design	Sample type	Sample number	Mean ($N_u/N_{u,pred}$)	CoV	P_m	V_P	β_0
Proposed design_class4	Test + FE	96	1.092	0.061	1.092	0.065	3.098
Proposed design	Test + FE	86	1.094	0.060	1.094	0.065	3.104
Eurocode 4's method_class4 [18]	Test + FE	96	0.991	0.083	0.991	0.083	2.644
Eurocode 4's method [18]	Test + FE	86	0.993	0.087	0.993	0.087	2.635
Uenaka <i>et al.</i> 's method_class4 [54]	Test + FE	83	0.944	0.101	0.944	0.101	2.388
Uenaka <i>et al.</i> 's method [54]	Test + FE	73	0.941	0.107	0.941	0.107	2.350
Han <i>et al.</i> 's method_class4 [46]	Test + FE	96	1.011	0.108	1.011	0.108	2.623
Han <i>et al.</i> 's method [46]	Test + FE	86	1.022	0.107	1.022	1.107	2.667
Hassanein <i>et al.</i> 's method [51]	Test + FE	40	0.927	0.094	0.927	0.094	2.335

Table 46 - CFDST columns subjected to eccentric axial compression evaluated by Eurocode 0 (EC0) [14].

Design	Sample type	Sample number	$k_{d,n}$	b	V_δ	γ_{M0}
Proposed design_class4	FE	376	3.061	1.030	0.054	1.089
Proposed design	FE	286	3.068	1.029	0.038	1.074
Fouché <i>et al.</i> 's method_class4 [56]	FE	376	3.061	0.917	0.107	1.271
Fouché <i>et al.</i> 's method [56]	FE	286	3.068	0.913	0.108	1.285
Uenaka and Kitoh's method_class4 [55]	FE	376	3.061	0.953	0.106	1.230
Uenaka and Kitoh's method [55]	FE	286	3.068	0.948	0.105	1.235

Table 47 - CFDST columns subjected to eccentric axial compression evaluated by AISI [15].

Design	Sample type	Sample number	Mean ($H_u/H_{u,pred}$)	CoV	P_m	V_P	β_0
--------	-------------	---------------	---------------------------	-----	-------	-------	-----------

Proposed design_class4	FE	376	1.052	0.057	1.052	0.065	2.758
Proposed design	FE	286	1.044	0.039	1.044	0.065	2.726
Fouché <i>et al.</i> 's method_class4 [56]	FE	376	0.983	0.121	0.983	0.121	2.294
Fouché <i>et al.</i> 's method [56]	FE	286	0.968	0.125	0.968	0.125	2.220
Uenaka and Kitoh's method_class4 [55]	FE	376	1.031	0.137	1.031	0.137	2.405
Uenaka and Kitoh's method [55]	FE	286	0.999	0.131	0.999	0.131	2.314

7 CONCLUSION AND RECOMMENDATIONS FOR FUTURE RESEARCH

7.1 Generalities

The design propositions development and the quality and quantity of research about concrete-filled double-skin tubular (CFDST) columns have increased the world interest in their use. Together with their advantages, especially high compressive load-carrying and construction costs and formwork requirements reduction due to fewer materials use, it makes CFDST columns an efficient and light structure. The addition of stainless steel and recycled aggregate concrete have made their use even more interesting due to environmental issues. The main objective of this thesis is to evaluate the use of recycled aggregate concrete (RAC) in CFDST columns and developed a design guideline for CFDST columns under concentric and eccentric load considering a concrete confinement factor and a parable N-M interaction curve.

Firstly, a literature review into the behaviour of CFT and CFDST columns was presented, followed by Chapter 2, focussing on the existing design methods for CFDST columns. Chapter 3 involves an experimental programme of CFDST columns with RAC and stainless and carbon steel tubes with a concentric load. A numerical investigation was then presented in Chapter 4, performed by the finite element (FE) program ABAQUS. The developed FE model was calibrated against the experiments presented in Chapter 3 and from experiments results from the literature review. In Chapter 5, an extended parametric analysis was conducted in ABAQUS with more than 360 FE models aiming to provide a higher range of CFDST columns under concentric and eccentric load and a meticulous evaluation of which parameter can be more significant in the CFDST columns and beam-columns behaviour. Finally, a simplified concrete confinement factor and parable N-M interaction curve is proposed for CFDST columns and beam-columns in Chapter 6, followed by reliability analysis.

7.2 Main conclusions

Based on the experiments presented in Chapter 3 it was possible to conclude that the specimens behaved similarly irrespective of the concrete type, with very comparable load-

displacement responses. For all specimens, the load-displacement behaviour was linear until reaching the first load peak. The RAC columns had a slightly stiffer response in the elastic range in all cases. All columns, irrespective of the concrete type, displayed reasonable ductility with some increase in the load-carrying capacity in the plastic range before the failure. In general, the CFDST columns with RAC presented similar load-carrying, ductility and deformed response, where sometimes presented even better result than the NAC CFDST columns. The RAC can be easily applied in CFDST columns when the recycled aggregate is original only from structural debris and treated before casting.

The FE model in Chapter 4 well express the results of the experiments, providing good load-displacement depiction, load-axial strain, moment-displacement response, the very similar deformed overall shape and failure modes, as well as the key behavioural aspects such as initial stiffness, yielding and capacity, with a mean $N_{u,FE}/N_{u,test}$ value of 1.00 and a coefficient of variation (CoV) of 0.11 for ultimate capacity.

For parametric analysis with concentric axial compression in Chapter 5, CFDST columns with the greater concrete area and outer tube diameter (D) presented higher strain hardening in the steel tubes and the concrete confinement effect. CFDST columns with small inner tube diameters and larger volumes of concrete infill provided the most conservative results for Han *et al.* [46] design expression. The load-carrying capacity and ductility of CFDST columns increases as the χ value decreases due to the higher concrete confining pressure. Han *et al.* [46] design expression is most conservative for columns with low hollow ratios and unconservative for χ values greater than 0.67. Smaller inner steel tube slenderness resulted in higher load-carrying capacity and ductility.

For parametric analysis with eccentric axial compression in Chapter 5, an identical behaviour during the elastic phase and different response after it was observed, mostly dependent on the outer tube diameter (D) value, where smaller D resulted in two load peaks with the second and ultimate load higher than the first, while greater D had only one peak load with very little strain hardening and ductility. The yielding stage proved to be higher for CFDST columns and beam-columns where D and the concrete confinement effect are significantly larger. The beam-column capacity increased for large D and A_c/A_{total} members due to the concrete infill confinement. The load-carrying capacity and ductility of CFDST beam-columns increased as the χ value decreased due to the higher concrete confining pressure. For all eccentricities, smaller $D/\varepsilon^2 t_{so}$ ratios and greater outer steel tube thickness (t_{so}) led to higher load-carrying capacities. The Eurocode 4 (EC4) [18] predictions provided safe design results for CFDST columns and unsafe design results for CFDST beam-columns. The load-carrying

capacities decrease as eccentricity applied increases, which is more accentuated for beam-columns with a large outer tube diameter (D) and thickness (t_{so}).

The proposed design methods for CFDST columns under concentric axial load from Eurocode 4 (EC4) [18], Uenaka *et al.* [54], Han *et al.* [46] and Hassanein *et al.* [51] methods are compared with the experiments and FE parametric analysis in Chapter 6. The results implied that all the design methods are unsafe for higher load capacities, where the methods are limited for higher concrete compressive strength (f_c) and outer tube slenderness. All the methods were only developed for NAC, while the concrete confinement effect was only considered induced by the outer steel tube.

The proposed design methods for CFDST columns under eccentric axial load from Eurocode 4 (EC4) [18], Uenaka and Kitoh [55], Han *et al.* [12] and Fouché *et al.* [56] methods are compared with the experiments and FE parametric analysis in Chapter 6. This followed by a proposed design method for CFDST column and beam-column considering a concrete confinement effect and the N-M interaction curve development. Han *et al.* [12] approach can be applied only for cross-sections with $D \geq 200$ mm, $4 \leq t_{so} \leq 20$ mm, $D/t_{so} \leq 135 \times 235/f_{syo}$, $0.0 \leq \chi \leq 0.75$, $0.6 \leq \xi \leq 4.0$ and concrete compressive strength $f_c \leq 33$ MPa. Uenaka and Kitoh's [55] diagram is only applied for $1 \leq t_{so} \leq 10$ mm due to the equation only considers the outer angle β_o and the inner angle β_i to calculate the areas. The concrete compressive strength (f_c) should not exceed at least the value of 33 MPa ($f_c \leq 33$ MPa). Fouché *et al.*'s [56] proposed design is not suitable for CFDST| beam-columns with an outer tube thickness (t_{so}) greater than 10 mm ($t_{so} \geq 10$ mm) due to the same angles approximation from Uenaka and Kitoh's [55]. This method is also not applicable in higher strength concrete.

Also, in Chapter 6, the N-M interaction diagram for CFDST sections was developed through the stress distribution varying the cross-section's neutral axis position. This procedure can be simplified for compression load N and bending M for each important point in the N-M interaction curve, as point A with pure compression and point B with pure bending. Point A is the total area of each material and point B the same conservative approximation proposed by Fouché *et al.* [56] where $\sin(\beta) = \beta$ and $\cos(\beta) = 1$ is considered. Next, a confinement parameter is incorporated into the equations for load and bending as an enhancement in the compressive concrete strength as f_{cc} when the concrete compressive strength $f_c \leq 50$ MPa and as a reduction in the concrete compressive strength when the concrete compressive strength is between $50 > f_c \geq 90$ MPa, as proposed in Eurocode 2 [92]. Finally, the N-M interaction curve can be simplified, considering the curve as a parable format. Finally, the accuracy of the proposed

design can be found through the $H_u/H_{u,pred}$ ratio of the combining normal and bending predicted resistances $H_{u,pred}$ and FE and experiments results from H_u . The proposed design agrees with the FE and experiments results with a CoV of 6.4% and without class4 cross-sections, a CoV of 5.2%. The reliability analysis of the CFDST columns parametric results calculated from Eurocode 4 (EC4) [18] is evaluated through the partial safety factor γ_{M0} , which was 1.086 for concentric axial compression and 1.074 the eccentric axial compression. The limit target reliability index β_o calculated from AISI [15] for the concentric axial compression was 3.104 and for the eccentric axial compression was 2.726.

7.3 Future research recommendations

Some suggestions for possible future research in this present subject are mentioned in this section:

- Perform experiments in CFDST stub columns with outer stainless steel tube, inner carbon steel tube and RAC with the same concrete properties mentioned in this thesis, under concentric and eccentric loading;
- Perform experiments in CFDST stub columns with outer stainless steel tube, inner carbon steel tube and RAC varying the concrete properties mentioned in this thesis under concentric and eccentric loading. Aiming to evaluate the influence of the recycled aggregate in the CFDST structural elements behaviour;
- Execute experiments in CFDST stub columns varying the cross-sections, focussing on the optimum hollow ratio (χ) value;
- Execute experiments in CFDST stub columns under eccentric load and pure bending;
- Accomplish experiments of CFDST slender columns and slender beam-columns;
- Accomplish experiments with a higher value of strain gauge in all the three elements aiming to observe the influence of each material in the final response of CFDST stub columns and beam-columns;
- Perform experiments evaluating the fire behaviour using RAC in CFDST columns.

REFERENCES

- [1] H. Shakir-Khalil, S. Illouli. Composite columns of concentric steel tubes, In: Proceeding of conference on Non-conventional structures and on the Design and Construction of Non-Conventional Structures, London, UK. (1987) 73-82.
- [2] S. Wei, S. T. Mau, C. Vipulanandan, S. K. Mantrala. Performance of New Sandwich Tube Under Axial Loading: Experiment, *Journal of Structural Engineering*. 121 (1995) 1806-1814.
- [3] L-H. Han, L. Wei, R. Bjorhovde. Developments and advanced applications of concrete-filled steel tubular (CFST) structures: Members, *Journal of Constructional Steel Research*. 100 (2014) 211-228.
- [4] W. Li, L-H. Han, X-L. Zhao. Axial strength of concrete-filled double skin steel tubular (CFDST) columns with preload on steel tubes, *Thin-Walled Structures*. 56 (2012) 9-20.
- [5] Z. Tao, L-H. Han, X-L. Zhao. Behaviour of concrete-filled double skin (CHS inner and CHS outer) steel tubular stub columns and beam-columns, *Journal of Constructional Steel Research*. 60 (2004) 1129-1158.
- [6] H-T. Hu and F-C. Su. Nonlinear analysis of short concrete-filled double skin tube columns subjected to axial compressive forces, *Marine Structures*. 24 (2011) 319-337.
- [7] H. Lu, L-H. Han, X-L. Zhao. Fire performance of self-consolidation concrete-filled double skin steel tubular columns: Experiments, *Fire Safety Journal*. 45 (2010) 106-115.
- [8] P. Ayough, N. H. Ramli Sulong, Z. Ibrahim. Analysis and review of concrete-filled double skin steel tubes under compression, *Thin-Walled Structures*. 148 (2020) 106495.
- [9] F. Wang, B. Young, L. Gardner. Experimental investigation of concrete-filled double-skin tubular stub columns with ferritic stainless steel outer tubes, 8th European Conference on Steel and Composite Structures, Copenhagen, Denmark. 1 (2017) 2-3.
- [10] F-C. Wang, L-H. Han, W. Li. Analytical behavior of CFDST stub columns with external stainless steel tubes under axial compression, *Thin-Walled Structures*. 127 (2018) 756-768.

- [11] F-C. Wang, L-H. Han. Analytical behavior of carbon steel-concrete-stainless steel double-skin tube (DST) used in submarine pipeline structure, *Marine Structures*. 63 (2019) 99-116.
- [12] L-H. Han, D. Lam, D.A. Nethercot. Design guide for concrete-filled double skin steel tubular structures. First edition. Boca Raton, Florida, USA: CRC Press Taylor & Francis Group, 2019.
- [13] Buildings Library. Available in:
<<https://www.ajbuildingslibrary.co.uk/projects/display/id/1336>> Accessed on 27 of January of 2021.
- [14] EN 1990: 2008. Eurocode 0, Basis of structural design. CEN, European Committee for Standardization, Brussels.
- [15] AISI S100-07. 2007. North American Specification for the Design of Cold-Formed Steel Structural Members. North American Cold-Formed Steel Specification, American Iron and Steel Institute. Washington, D.C, USA.
- [16] ABAQUS, ABAQUS/standard User's Manual. Version 6.17, Dassault Systemes Simulia Corp., USA, 2017.
- [17] L. Calado Estruturas Mistas de Aço e Betão. Third edition. Lisboa, Portugal: IST Press, 2015 (in Portuguese).
- [18] EN 1994-1-1: 2004. Eurocode 4, Design of Composite Steel and Concrete Structures, Part 1.1: General Rules and Rules for Buildings. CEN, European Committee for Standardization, Brussels.
- [19] J-L. Ma, T-M. Chan, B. Young. Material properties and residual stresses of cold-formed high strength steel hollow sections, *Journal of Constructional Steel Research*. 109 (2015) 152-165.
- [20] L. Gardner. The use of stainless steel in structures, *Progress in Structural Engineering and Materials*. 7 (2005) 45-55.
- [21] International Stainless Steel Forum. Brussels, Belgium. Available in:
<https://www.worldstainless.org/Files/issf/non-image-files/PDF/ISSF_The_Ferritic_Solution_English.pdf> Accessed in 31 of January of 2021.

- [22] EN 1993-1-1: 2005. Eurocode 3, Design of Steel Structures, Part 1.1: General Rules and Rules for Buildings. CEN, European Committee for Standardization, Brussels.
- [23] R.D. Silva. Estudo da aderência aço-concreto em pilares mistos preenchidos. Master Dissertation (Master's degree in civil engineering) – School of Engineering of São Carlos, University of São Paulo, São Carlos, São Paulo, 136 pages, 2006. (in Portuguese)
- [24] W. L. A. Oliveira, A. L. H. C. El Debs. Estudo da Efeito de Confinamento do Concreto em Pilares Mistos Preenchidos Curtos, *Cadernos de Engenharia de Estruturas*, São Carlos, 11, n 48, (2009) 39-53. (in Portuguese)
- [25] T. H. Han, J. M. Stallings, Y. J. Kang. Nonlinear concrete model for double-skinned composite tubular columns, *Construction and Buildings Materials*. 24 (2010) 2542-2553.
- [26] M. J. McGinnis, M. Davis, A. de la Rosa, B. D. Weldon, Y. C. Kurama. Strength and stiffness of concrete with recycled concrete aggregates, *Construction and Buildings Materials*. 154 (2017) 258-269.
- [27] R. V. Silva, J. de Brito, R. K. Dhir. Properties and composition of recycled aggregates from construction and demolition waste suitable for concrete production, *Construction and Buildings Materials*. 65 (2014) 201-217.
- [28] R. V. Silva, J. de Brito, R. K. Dhir. Establishing a relationship between modulus of elasticity and compressive strength of recycled aggregate concrete, *Journal of Cleaner Production*. 112 (2016) 2171-2186.
- [29] G. Wardeh, E. Ghorbel, H. Gomart. Mix Design and Properties of Recycled Aggregate Concretes. Applicability of Eurocode 2, *International Journal of Concrete Structures and Materials*. 9 (2014) 1-20.
- [30] Y-F. Yang, L-H. Han. Experimental behaviour of recycled aggregate concrete-filled steel tubular columns, *Journal of Constructional Steel Research*. 62 (2006) 1310-1324.
- [31] ACI 2014. Building Code Requirements for Structural Concrete, American Concrete Institute. Michigan, USA.
- [32] AIJ 2002. Standard for Structural Design of Reinforced Concrete Boxed-Shaped Wall Structures. Architectural Institute of Japan, Tokyo, Japan.
- [33] ANSI/AISC 360-10. 2010. An American National Standard. Specification for Structural Steel Buildings. American Institute of Steel Construction. Chicago, USA.

- [34] BS5400: British Standard 1978. Steel, concrete and composite bridges – Part 2: Specifications for loads. London, UK.
- [35] DBJ13-51 2003. Technical Specification for concrete-filled steel tubular structures. The Construction Department of Fujian Province, Fuzhou, China.
- [36] Y. Huang, J. Xiao, C. Zhang. Theoretical study on mechanical behavior of steel confined recycled aggregate concrete, *Journal of Constructional Steel Research*. 76 (2012) 100-111.
- [37] S. Zhong. The unified theory of concrete-filled steel tube. Tsinghua University Press, Beijing, China.
- [38] H. Mei, P. D. Kioussis, M. R. Ehsani, H. Saadatmanesh. Confinement effects on high-strength concrete, *ACI – Structural Journal*. 98 (2001) 548-553.
- [39] V. Azevedo. Avaliação experimental de colunas mistas curtas com núcleo de concreto reciclado. PhD thesis, PGECIV- Post Graduate Program in Civil Engineering, State University of Rio de Janeiro – UERJ, 2018 (in Portuguese)
- [40] A. He, A. Su, Y. Liang, O. Zhao. Experimental and numerical investigations of circular recycled aggregate concrete-filled stainless steel tube columns, *Journal of Constructional Steel Research*. 179 (2021) 106566.
- [41] L-H. Han, G-H. Yao, Z. Tao. Performance of concrete-filled thin-walled steel tubes under pure torsion, *Thin-Walled Structures*. 45 (2007) 24-36.
- [42] J. Xiao, J. Li, C. Zhang. Mechanical properties of recycled aggregate concrete under uniaxial loading, *Cement and Concrete Research*. 35 (2005) 1187-1194.
- [43] AS/NZS 5100.6-2017. Australian/New Zealand Standards, Bridge design, part 6: Steel and Composite Construction. Sydney, Australia, 2017.
- [44] K. Uenaka. CFDST stub columns having outer circular and inner square sections under compression, *Journal of Constructional Steel Research*. 120 (2016) 1-7.
- [45] Z. Tao and L-H. Han. Behaviour of concrete-filled double skin rectangular steel tubular beam-columns, *Journal of Constructional Steel Research*. 62 (2005) 631-646.
- [46] L-H. Han, Q-X. Ren, W. Li. Tests on stub stainless steel-concrete-carbon steel double-skin tubular (DST) columns, *Journal of Constructional Steel Research*. 67 (2011) 437-452.

- [47] G. Silva, E. Goulart, L. Lima, P. Vellasco. Tubular stainless and mild steel double-skin columns, In Proc. of Eurosteel 2014 – 5th European Conference on Steel and Composite Structures, Naples, Italy. 1 (2014) 10-12.
- [48] F. Wang, B. Young, L. Gardner. Compressive testing and numerical modelling of concrete-filled double skin CHS with austenitic stainless steel outer tubes, *Thin-Walled Structures*. 141 (2019) 345-359.
- [49] R. O. de Araújo. Avaliação de colunas tubulas mistas – aço inoxidável, concreto e aço carbono, MSc Dissertation, PGECIV – Post Graduate Program in Civil Engineering, State University of Rio de Janeiro – UERJ, 2016 (in Portuguese).
- [50] Ansys 12.0, ANSYS – Inc. Theory Reference, 2010.
- [51] M. F. Hassanein, O. F. Kharoob, Q. Q. Liang. Circular concrete-filled double-skin tubular short columns with external stainless steel tubes under axial compression, *Thin-Walled Structures*. 73 (2013) 252-263.
- [52] M. F. Hassanein and O. F. Kharoob. Analysis of circular concrete-filled double-skin tubular slender columns with stainless steel tubes, *Thin-Walled Structures*. 79 (2014) 23-37.
- [53] M. Pagoulatou, T. Sheehan, X. H. Dai, D. Lam. Finite element analysis on the capacity of circular concrete-filled double-skin steel tubular (CFDST) stub columns, *Engineering Structures*. 72 (2014) 102-112.
- [54] K. Uenaka, H. Kitoh, K. Sonoda. Concrete filled double skin circular stub columns under compression, *Thin-Walled Structures*. 48 (2010) 19-24.
- [55] K. Uenaka and H. Kitoh. Mechanical behaviour of concrete-filled double-skin tubular circular deep beams, *Thin-Walled Structures*. 49 (2011) 256-263.
- [56] P. Fouché, M. Bruneau and V. Chiarito. Dual-hazard blast and seismic behaviour of concrete-filled double-skin steel tubes bridge pier, *Journal of Structural Engineering*. 143 (2017) 1-22.
- [57] Architectural Institute of Japan. Standard for Structural Calculation of Steel Reinforced Concrete Structures, 2002 (in Japanese).

- [58] Q.Q. Liang and S. Fragomeni. Nonlinear analysis of circular concrete-filled steel tubular short columns under axial loading, *Journal of Constructional Steel Research*. 65 (2009) 2186-2196.
- [59] M.F. Hassanein, O.F. Kharoob, Q.Q. Liang. Behaviour of circular concrete-filled lean duplex stainless steel tubular short columns, *Thin-Walled Structures*. 68 (2013) 113-123.
- [60] M.F. Hassanein, O.F. Kharoob, Q.Q. Liang. Behaviour of circular concrete-filled lean duplex stainless steel-carbon steel tubular short columns, *Engineering Structures*. 56 (2013) 83-94.
- [61] Q.Q. Liang. Performance-based analysis of concrete-filled steel tubular beam-columns. Part I: theory and algorithms, *Journal of Constructional Steel Research*. 65 (2009) 363-373.
- [62] S. İpek and E.M. Güneyisi. Nonlinear finite element analysis of double skin composite columns subjected to axial loading, *Archives of Civil and Mechanical Engineering*. 20, (2020) 1-25.
- [63] J. Tang, S. Hino, I. Kuroda, T. Ohta. Modelling of stress-strain relationships for steel and concrete in concrete-filled circular steel tubular columns, *Steel Construction Engineering*. 3 (1996) 35-46.
- [64] M. Bruneau and J. Marson. Seismic design of concrete-filled circular steel bridge piers, *Journal of Bridge Engineering*. 9 (2004) 24-34.
- [65] P. F. Rodrigues. Avaliação experimental e numérica de colunas tubulares mistas CFDST (aço inoxidável-concreto-aço carbono), MSc Dissertation, PGECIV – Post Graduate Program in Civil Engineering, State University of Rio de Janeiro – UERJ, 2018 (in Portuguese).
- [66] B. N. T. de Macedo. Determinação do coeficiente de conformação superficial de barras de aço para uso em concreto armado, MSc Dissertation, PGECIV – Post Graduate Program in Civil Engineering, State University of Rio de Janeiro – UERJ, 2018 (in Portuguese).
- [67] ABNT NBR 7211 (2009) Agregados para concreto – Especificação. Associação Brasileira de Normas Técnicas - Rio de Janeiro, Brazil (in Portuguese).

- [68] ABNT NBR 7251 (1982) Agregados em estado solto – Determinação da massa unitária – Método de ensaio, Associação Brasileira de Normas Técnicas, Rio de Janeiro, Brazil (in Portuguese).
- [69] ABNT NBR NM 45 (2006) Agregados – Determinação da massa unitária e do volume de vazios, Associação Brasileira de Normas Técnicas, Rio de Janeiro, Brazil (in Portuguese).
- [70] ABNT NBR NM 52 (2002) Agregado miúdo – Determinação de massa específica e massa específica aparente, Associação Brasileira de Normas Técnicas, Rio de Janeiro, Brazil (in Portuguese).
- [71] R. V. Silva, J. de Brito, R. K. Dhir. The influence of the use of recycled aggregates on the compressive strength of concrete: a review, *European Journal of Environmental and Civil Engineering*. 19 (2015) 825-849.
- [72] EN 10002-1: 1990. Metallic materials – Tensile testing – Part 1: Method of test at ambient temperature. CEN, European Committee for Standardization, Brussels.
- [73] Y. Huang, B. Young. The art of coupon test, *Journal of Constructional Steel Research*. 96 (2014) 159-175.
- [74] P. B. Dinis, D. Camotim, N. Silvestre. On the mechanics of thin-walled angle column instability, *Thin-Walled Structures*. 52 (2012) 80-89.
- [75] I. A. Luquin. New approach for efficient design of stainless steel RHS and SHS elements. Barcelona, Spain: Universitat Politècnica de Catalunya; 2016 (Ph.D. thesis).
- [76] Z. Tao, Z-B. Wang, Q. Yu. Finite element modelling of concrete-filled steel stub columns under axial compression, *Journal of Constructional Steel Research*. 89 (2013) 121-131.
- [77] W. Li, D. Wang, L-H. Han. Behaviour of grout-filled double skin steel tubes under compression and bending: Experiments, *Thin-Walled Structures*. 116 (2017) 307-319.
- [78] C. W. Roeder, B. Cameron, C. B. Brown. Composite action in concrete-filled tubes, *J. Struct. Eng., ASCE*. 125 (1999) 477-484.
- [79] Chou S.M., Chai G.B and Ling L Finite element technique for design of stub columns, *Thin-Walled Structures* 37 (2000) 97-112.
- [80] A. Gholampour, A. H. Gandomi, T. Ozbakkaloglu. New formulations for mechanical properties of recycled aggregate concrete using gene expression programming, *Construction and Building Materials*. 130 (2017) 122-145.

- [81] W. Li, L-H. Han, T-M. Chan. Numerical investigation on the performance of concrete-filled double-skin steel tubular members under tension, *Thin-Walled Structures*. 79 (2014) 108-118.
- [82] FIP. CEB-FIP Model Code 1990. London: Thomas Telford Ltd. (1993).
- [83] X. Yun, L. Gardner. Stress-strain curves for hot-rolled steels, *Journal of Constructional Steel Research*. 133 (2017) 36-46.
- [84] G. B. dos Santos, L. Gardner, M. Kucukler. A method for the numerical derivation of plastic collapse loads, *Thin-Walled Structures*. 124 (2018) 258-277.
- [85] L. Gardner and X. Yun. Description of stress-strain curves for cold-formed steels. *Construction and Building Materials*. 189 (2018) 527-538.
- [86] K. J. R. Rasmussen. Full-range stress-strain curves for stainless steel alloys. *Journal of Constructional Steel Research*. 59 (2003) 47-61.
- [87] C. Ibañez, A. Piquer, D. Hernández-Figueirido, Ó. Martínez-Ramos. Experimental analysis of concrete-filled double-skin tubular columns subjected to eccentric loads, In *Proc. of Eurosteel 2017 – 8th European Conference on Steel and Composite Structures*, Copenhagen, Denmark. 1 (2017) 13-15.
- [88] H. Zhao, R. Wang, D. Lam, C-C. Hou, R. Zhang. Behaviours of circular CFDST with stainless steel external tube: Slender columns and beams. *Thin-Walled Structures*. 158 (2021) 107172.
- [89] ANSI/AISC 360-16. Specification for Structural and Steel Buildings. American Institute of Steel Construction, Chicago, USA, 2016.
- [90] MATLAB (Version 2020a), MathWorks (2020). The MathWorks inc.
- [91] Y. L. Li, X. L. Zhao, R. K. Singh Raman, X. Yu. Axial compression tests on seawater and sea sand concrete-filled double-skin stainless steel circular tubes. *Engineering Structures*. 176 (2018) 426-438.
- [92] EN 1992-1-1: 2004. Eurocode 2, Design of concrete structures, Part 1-1: General rules and rules for buildings. CEN, European Committee for Standardization, Brussels.
- [93] EN 1993-1-4: 2006. Eurocode 3, Design of Steel Structures, Part 1.4: General Rules and Supplementary Rules for Stainless Steels. CEN, European Committee for Standardization, Brussels.

- [94] S. Afshan, P. Francis, N.R. Baddoo, L. Gardner. Reliability analysis of structural stainless steel design provisions. *Journal of Constructional Steel Research*. 114 (2015) 293-304.
- [95] S. J. Hicks and A. Pennington. Partial factors for the design resistance of composite beams in bending. *Journal of Constructional Steel Research*. 105 (2015) 74-85.
- [96] R. Lu, Y. Luo, J.P. Conte. Reliability evaluation of reinforced concrete beams. *Structural Safety*. 14 (1994) 277-298.
- [97] C. Arya. *Design of Structural Elements*. Third Edition, Spon Press, London, 2009.
- [98] JCSS Probabilistic Model Code. Joint committee on structural safety, 2000.
- [99] J-H. Zhang and B. Young. Finite element analysis and design of cold-formed steel built-up closed section columns with web stiffeners. *Thin-Walled Structures*. 131 (2018) 223-237.